Synthese und Applikation von monodispersen mikrometergroßen Silica-Partikeln mit maßgeschneiderten Poren

Dissertation

der Mathematisch-Naturwissenschaftlichen Fakultät
der Eberhard Karls Universität Tübingen
zur Erlangung des Grades eines
Doktors der Naturwissenschaften
(Dr. rer. nat.)

vorgelegt von

M. Sc. Fabio Fait

aus Neustadt a. d. W.

Tübingen

2023

Gedruckt mit Genehmigung der Mathematisch-Naturwissenschaftlichen Fakultät der Eberhard Karls Universität Tübingen.

Tag der mündlichen Qualifikation:	22.09.2023
Dekan:	Prof. Dr. Thilo Stehle
1. Berichterstatter:	Prof. Dr. Hermann A. Mayer
2. Berichterstatter:	Prof. Dr. Reiner Anwander
3. Berichterstatter:	Prof. Dr. Andreas Kandelbauer

Die vorliegende Arbeit wurde im Zeitraum von November 2019 bis März 2023 am Institut für Anorganische Chemie der Universität Tübingen und dem Process Analysis & Technology Zentrum der Fachhochschule Reutlingen, unter der Anleitung von Prof. Dr. Hermann A. Mayer und Prof. Dr. Andreas Kandelbauer, durchgeführt.

Danksagung

An dieser Stelle möchte ich allen beteiligten Personen meinen großen Dank aussprechen, die mir bei der Anfertigung meiner Dissertation unterstützend und mit Ratschlägen ebenso wie mit Anregungen zur Seite standen.

Herrn Prof. Dr. Hermann A. Mayer, meinem Doktorvater, und Herrn Prof. Dr. Andreas Kandelbauer danke ich vielmals für die Möglichkeit dieser Promotion in ihrem Themenbereich und für die Aufnahme in ihre Arbeitskreise. Die fortwährende Betreuung der beiden und die zahlreichen Diskussionen rund um die verschiedensten Problemstellungen in diesem Projekt sowie die wissenschaftliche Freiheit, die mir bei der Bearbeitung und Ausführung zugetraut wurde, haben diese Arbeit erst ermöglicht. Des Weiteren danke ich dem Bundesministerium für Bildung & Forschung für die Finanzierung dieses Projekts.

Zudem danke ich Herrn Prof. Dr. Reiner Anwander für die Begutachtung meiner Dissertation und Prof. Dr. Carolin Huhn für die Auseinandersetzung mit dieser Arbeit im Rahmen der Disputation.

Der Firma Dr. Maisch GmbH, insbesondere Dr. Johannes Maisch, gilt ein besonderer Dank für die jahrelange enge Kooperation, den unerlässlichen wissenschaftlichen Austausch sowie der Unterstützung während meines gesamten Studiums.

Zugleich möchte ich nachstehenden Personen danken: Dr. Klaus Eichele, für die Einarbeitung in die Arbeitstechniken der NMR-Spektroskopie, Dr. Larysa Kutuzova in die der thermogravimetrischen Analyse und Mohammad Ghani, für die Aufnahmen der Elementaranalysen. Ein großer Dank für die zahlreichen REM-Aufnahmen wie auch für die unkomplizierte und gute Zusammenarbeit gilt vor allem Frau Elke Nadler.

Julia C. Steinbach danke ich für das bedeutende Zusammenwirken und die schöne gemeinsame Zeit während dieser Promotion. Die enge Zusammenarbeit und der persönliche sowie fachliche Austausch mit ihr haben die drei Jahre zu einer Bereicherung gemacht.

Meinen ehemaligen Kolleginnen und Kollegen Dr. Björn Brodbeck, Dr. Dennis Max Meisel, Dr. Tomasz Misztal und Dr. Stefanie Wagner sowie Corvin Lossin und Annika Stetter als auch dem Arbeitskreis Wesemann danke ich vielmals für all die fachlichen Diskussionen, die Hilfestellungen und das freundschaftliche Verhältnis.

Besonders meinen Freunden, namentlich Maximilian Auer, Victoria Graf, Cornelius Knappe, Tim Parker und Magda Zweigart, danke ich von Herzen für die motivierenden Worte, die konstruktive Kritik und eine unvergessliche Studienzeit.

Mein außerordentlicher Dank gilt meiner Frau Luisa Fait, für ihr stetiges Verständnis und ihr uneingeschränktes Engagement während meiner gesamten Studienzeit. Ausdrücklich bedanken möchte ich mich auch bei meiner Familie, ausschlaggebend bei meiner Mutter Diana Fait und meinen Großeltern Petra und Klaus Paul, welche meinen bisherigen Lebensweg unbegrenzt unterstützt und gefördert haben. Ich danke euch von ganzem Herzen.

Meiner Familie

Inhaltsverzeichnis

Abkürzungsverzeichnis . . . . . **III**

Chemische Formeln . . . . . **IV**

Symbole und mathematische Formelzeichen . . . . . **IV**

Zusammenfassung . . . . . **VI**

Summary . . . . . **VII**

Veröffentlichungen . . . . . **VIII**

Eigenleistung . . . . . **IX**

1 Zielsetzung **1**

2 Theorie **3**

3 Zusammenfassung der Ergebnisse **10**

3.1 Einfluss der Porosität und Grad der Funktionalisierung der *p*(GMA-*co*-EDMA)-Template 10

3.2 Einlagerung von Silica-Nanopartikeln über unterschiedliche Hydrolysegeschwindigkeiten 16

3.3 Verwendung von MPSM als stationäre Trennphase in der HPLC 26

4 Schlussfolgerung **29**

5 Unveröffentlichte Ergebnisse **30**

5.1 Polystyrol 30

5.2 Aminofunktionalisierungen von *p*(GMA-*co*-EDMA)-Templaten und *semi-batch*-Verfahren im Sol-Gel-Prozess 34

5.3 Synthese poröser Template auf Basis von Vinyltriethoxysilan 41

6 Publikation I **50**

7 Publikation II **66**

8 Publikation III **84**

9 Publikation IV **101**

10 Publikation V **117**

11 Publikation VI 139

12 Experimenteller Teil 170
12.1 Allgemeine Arbeits- und Analysemethoden 170
12.1.1 Ausrüstung und Arbeitstechniken 170
12.1.2 Chemikalien und Lösungsmittel 170
12.1.3 Charakterisierung der Partikeleigenschaften 171
12.2 Partikelnomenklatur 173
12.3 Synthesen 174
12.3.1 Synthese monodisperser Polystyrol-Partikel 174
12.3.2 Synthese poröser *p*(GMA-*co*-EDMA) Template 175
12.3.3 Aminofunktionalisierung von *p*(GMA-*co*-EDMA) Templaten 178
12.3.4 Sol-Gel-Prozess in Anwesenheit aminofunktionalisierter *p*(GMA-*co*-EDMA)-Template 181
12.3.5 Kalzinierung von *p*(GMA-*co*-EDMA)/SiO_2-Hybrid-Partikel 184
12.3.6 Funktionalisierung der mesoporösen Silica-Partikel 185
12.3.7 Synthese mesoporöser Silica-Partikel auf Basis von Vinyltriethoxysilan 186

13 Literatur 188

Abkürzungsverzeichnis

Abb.	Abbildung
BET	Brunauer, Emmet & Teller
BJH	Barret, Joyner & Halenda
bzw.	beziehungsweise
CP/MAS	*Cross Polarization / Magic Angle Spinning*
DRIFT	Diffuse Reflexions Infrarotspektroskopie
et al.	und andere
Fig.	Figur
Glg.	Gleichung
HB	Hybrid-Partikel
HPDEC	*High Power Decoupling*
HPLC	Hochleistungsflüssigkeitschromatographie (*High Performance Liquid Chromatography*
i-SEC	inverse Größenauschlusschromatographie (*inverse Size Exclusion Chromatography*)
Kap.	Kapitel
Meth.	Methode
Mo.	Monomer
MPSM	mesoporöse Silica-Partikel (*Mesoporous Silica Microspheres*)
NMR	Kernspinresonanz (Nuclear Magnetic Resonance)
P	Polymertemplat
Po.	Porogen
polym.	polymerisiert
PS	Polystyrol-Partikel
Publ.	Publikation
REM	Rasterelektronenmikroskop
RP-LC	Umkehrphasenchromatographie (*Reversed Phase Liquid Chromatography*)
SNP	Silica-Nanopartikel (*Silica Nanoparticles*)
Tab.	Tabelle
TGA	thermogravimetrische Analyse
unpolym.	unpolymerisiert
vgl.	vergleiche

Chemische Formeln

APTES	(3-Aminopropyl)triethoxysilan
C_{18}	Octadecyl-Rest
DBP	Dibutylphthalat
EDMA	Ethylenglycoldimethacrylat
GMA	Glycidylmethacrylat
p(GMA-*co*-EDMA)	*poly*(Glycidylmethacrylat-*co*-Ethylenglycoldimethacrylat)
$NaNO_2$	Natriumnitrit
$SiCl_4$	Siliciumtetrachlorid
SiO_2	Siliciumdioxid
Si-OH	Silanol
TBOS	Tetrabutoxysilan
TEOS	Tetraethoxysilan
TEPA	Tetraethylenpentamin
TMA	Trimethylammoniumchlorid
TMOS	Tetramethoxysilan
TPOS	Tetrapropoxysilan
VTEOS	Vinyltriethoxysilan
VTMOS	Vinyltrimethoxysilan

Symbole und mathematische Formelzeichen

$>$	größer
$\geq$	größer gleich
°C	Grad Celsius
a_{BET}	spezifische Oberfläche
Au	*arbitrary unit* (willkürliche Einheit)
β	*beta* (griechischer Buchstabe)
d_{50}	durchschnittlicher Partikeldurchmesser
Δ	*Delta* (griechischer Buchstabe)
g	Gramm
h	Stunde
m	Masse
m^2/g	Quadratmeter pro Gramm
µm	Mikrometer
min	Minuten
mL	Milliliter

mm	Millimeter
MPa	Megapascal
mV	Millivolt
M_w	Molekulargewicht
n	Stoffmenge
nm	Nanometer
Φ	Median der Porengrößenverteilung
R	Auflösung
$\approx$	ungefähr
t_r	Retentionszeit
v. %	Volumenprozent
V_P	Porenvolumen
wt. %	Gewichtsprozent
$\times$	-fache Vergrößerung

Zusammenfassung

In dieser Arbeit wurden monodisperse, mesoporöse Silica-Partikel (MPSM) im Mikrometerbereich mit maßgeschneiderten Partikel- und Porendesign hergestellt und charakterisiert. Die Applikation dieser Materialien erfolgte als Trennphasen in der Hochleistungsflüssigkeitschromatographie zur Separation verschiedener Biomoleküle. Die Synthese basiert auf der Einlagerung von Silica-Nanopartikeln (SNP) in porösen, organischen Templaten, welche anschließend bei 600 °C thermisch zersetzt wurden. Die kontrollierte Einstellung der Poreneigenschaften über den Sol-Gel-Prozess ermöglicht die zielgenaue Synthese von MPSM entsprechend der Trennproblematik und steigert die Qualität der HPLC.

Die Impfsuspensionspolymerisation von Polystyrol-Partikeln unter Verwendung von Glycidylmethacrylat (GMA), Ethylenglycoldimethacrylat (EDMA) und Porogenen erlaubt die Synthese hochgradig monodisperser, poröser *p*(GMA-*co*-EDMA)-Template. Die Einflussfaktoren (A) Monomer-Porogen-Verhältnis, (B) Monomerverhältnis und (C) Porogenzusammensetzung wurden systematisch untersucht und die Auswirkungen auf die Eigenschaften Porengröße, Porenvolumen und spezifische Oberfläche erläutert. Der Durchmesser der Template wird weitgehend von der Größe der Polystyrol-Partikel (PS) vorgegeben. Als Zwischenschritt in der Synthese von MPSM werden die Template aminofunktionalisiert, um eine Attraktivität der unpolaren Template gegenüber den SNP zu gewährleisten. Die Anbindung aminierter Substanzen erfolgt unter Ringöffnung der Epoxidgruppe von GMA. Im anschließenden basischen Sol-Gel-Prozess werden SNP aufgrund der Ladungsunterschiede in das funktionalisierte *p*(GMA-*co*-EDMA)-Templat eingelagert. Die Partikelgröße der SNP beeinflusst die Poreneigenschaften der MPSM maßgeblich. Die Größe der eingelagerten SNP hängt von drei Faktoren ab: (*i*) der Wachstumsgeschwindigkeit in der kontinuierlichen Phase, welche über die Einstellungen des Sol-Gel-Prozesses gesteuert wird, (*ii*) der Diffusionsrate, welche über die elektrostatische Anziehung gesteuert wird und von dem Grad der Funktionalisierung abhängt und (*iii*) der Porosität des Polymertemplats. Verschiedene Applikationen zur Auftrennung von Aminosäuren, Proteinen und Vitaminen wurden mit den MPSM nach erfolgreicher Modifikation mit Octadecylsilan etabliert. Die Trennperformance dieser Phasen erreicht gleichwertige Ergebnisse wie kommerziell verfügbare HPLC-Materialien. Jedoch ist es bei der vorgestellten Synthesestrategie möglich, aufgrund des schrittweise molekularen Aufbaus der mesoporösen Silica-Partikel, die stationäre Phase besser an die Trennproblematik zu adaptieren.

Summary

In this work, monodisperse micron-scale mesoporous silica particles (MPSM) with tailored particle and pore designs were prepared and characterized. These materials were applied as a separation phase in high performance liquid chromatography for the separation of different biomolecules. The synthesis was based on the incorporation of silica nanoparticles (SNP) into porous organic templates, which were subsequently removed at 600 °C by thermal degradation. The controlled adjustment of pore properties via the sol-gel process enables the precise synthesis of MPSM according to the separation problem and enhances the quality of HPLC.

Seed suspension polymerization of polystyrene particles using glycidyl methacrylate (GMA), ethylene glycol dimethacrylate (EDMA) and porogens allows the synthesis of highly monodisperse, porous *p*(GMA-*co*-EDMA) templates. The influencing factors of (A) monomer-to-porogen ratio, (B) monomer ratio, and (C) porogen composition were systematically investigated and the effects on the properties of pore size, pore volume, and specific surface area were explained. The diameter of the template is widely dictated by the size of the polystyrene particles (PS). As an intermediate step in the synthesis of MPSM, the templates are aminofunctionalized to provide attraction of the nonpolar templates to the SNP. Aminated substances are attached with ring opening of the epoxide group of GMA. In the subsequent basic sol gel process, SNP are incorporated into the functionalized *p*(GMA-*co*-EDMA) template due to the charge differences. The particle size of the SNP significantly affects the pore properties of the MPSM. The size of the embedded SNP depends on three factors: (*i*) the growth rate in the continuous phase, which is controlled by the settings of the sol gel process, (*ii*) the diffusion rate, which is controlled by the electrostatic attraction and depends on the degree of functionalization, and (*iii*) the porosity of the polymer template. Several applications for the separation of amino acids, proteins and vitamins have been established with the MPSMs after successful modification with octadecylsilane. The separation performance of these phases achieves equivalent results to commercially available HPLC materials. However, with the presented synthesis strategy, it is possible to better adjust the stationary phase to the separation problem based on the stepwise molecular design of the mesoporous silica particles.

Veröffentlichungen

Publikation I

F. Fait, J. C. Steinbach, A. Kandelbauer, H. A. Mayer, *Impact of porosity and surface functionalization of hard templates on the preparation of mesoporous silica microspheres*, Microporous and Mesoporous Materials, **2023**, *351*, 112482.[1]

Publikation II

J. C. Steinbach, F. Fait, S. Wagner, A. Wagner, M. Brecht, H. A. Mayer, A. Kandelbauer, *Rational Design of Pore Parameters in Monodisperse Porous Poly(glycidyl methacrylate-co-ethylene glycol dimethacrylate) Particles Based on Response Surface Methodology*, Polymers, **2022**, *14*, 382.[2]

Publikation III

F. Fait, J. C. Steinbach, A. Kandelbauer, H. A. Mayer, *Incorporation of silica nanoparticles into porous templates to fabricate mesoporous silica microspheres for high performance liquid chromatography applications*, Journal of Chromatography A, **2023**, *1705*, 464190.[3]

This article was published in „Journal of Chromatography A, 1705, F. Fait, J. C. Steinbach, A. Kandelbauer, H. A. Mayer, Incorporation of silica nanoparticles into porous templates to fabricate mesoporous silica microspheres for high performance liquid chromatography applications, 464190, 2023 © Elsevier“.

Publikation IV

F. Fait, S. Wagner, J. C. Steinbach, A. Kandelbauer, H. A. Mayer, *Tailoring the Morphology of Monodisperse Mesoporous Silica Particles Using Different Alkoxysilanes as Silica Precursors.*, International Journal of Molecular Sciences, **2023**, *24*, 11729.[4]

Publikation V

J. C. Steinbach, F. Fait, H. A. Mayer, A. Kandelbauer, *Monodisperse Porous Silica/ Polymer Nanocomposite Microspheres with Tunable Silica Loading, Morphology and Porosity*, International Journal of Molecular Sciences, **2022**, *23*, 14977.[5]

Publikation VI

J. C. Steinbach, F. Fait, H. A. Mayer, A. Kandelbauer, *Sol-Gel-Controlled Size and Morphology of Mesoporous Silica Microspheres Using Hard Templates*, ACS Omega, **2023**, *8*, 30273 − 30284.[6]

Eigenleistung

Publikation I

Alle Synthesen wurden vom Autor geplant und umgesetzt. Entsprechende Analytik und Auswertung der Partikel (Partikelgrößenauswertung, Thermogravimetrische Analyse, Stickstoffsorptionsmessungen, Infrarotspektroskopie, HPLC-Messungen) wurden vom Autor und Julia C. Steinbach durchgeführt. Die multivariate Datenanalyse der IR-Spektren wurde von Julia C. Steinbach ausgewertet. Die HPLC-Säulen wurden vom Autor gepackt. Das Manuskript wurde vom Autor und Julia C. Steinbach verfasst.

Die Rasterelektronenmikroskopie-Aufnahmen wurden von Elke Nadler und die Elementaranalysen von Mohammad Ghani an der Universität Tübingen aufgenommen.

Publikation II

Die Synthesen wurden von Julia C. Steinbach und dem Autor geplant und umgesetzt. Entsprechende Analytik und Auswertung der Partikel (Partikelgrößenauswertung, Infrarotspektroskopie, HPLC-Messungen) wurden von Julia C. Steinbach und dem Autor durchgeführt. Die statistische Versuchsplanung wurde von Julia C. Steinbach ausgewertet. Die HPLC-Säulen für die *i*-SEC wurden vom Autor gepackt. Das Manuskript wurde von Julia C. Steinbach verfasst.

Die Rasterelektronenmikroskopie-Aufnahmen wurden von Elke Nadler an der Universität Tübingen aufgenommen.

Publikation III

Alle Synthesen wurden vom Autor geplant und umgesetzt. Entsprechende Analytik und Auswertung der Partikel (Partikelgrößenauswertung, Thermogravimetrische Analyse, Stickstoffsorptionsmessungen, Infrarotspektroskopie, HPLC-Messungen) wurden vom Autor und Julia C. Steinbach durchgeführt. Die ^{13}C- und ^{29}Si-Festkörper-NMR-Spektren wurden vom Autor aufgenommen und ausgewertet. Die HPLC-Säulen wurden vom Autor gepackt. Das Manuskript wurde vom Autor verfasst.

Die Rasterelektronenmikroskopie-Aufnahmen wurden von Elke Nadler und die Elementaranalysen von Mohammad Ghani an der Universität Tübingen aufgenommen.

Publikation IV

Alle Synthesen wurden vom Autor und Dr. Stefanie Wagner geplant und umgesetzt. Entsprechende Analytik und Auswertung der Partikel (Partikelgrößenauswertung, Thermogravimetrische Analyse, Stickstoffsorptionsmessungen, Infrarotspektroskopie, HPLC-Messungen) wurden vom Autor und Julia C. Steinbach durchgeführt. Die HPLC-Säulen wurden vom Autor gepackt. Das Manuskript wurde vom Autor verfasst.

Die Rasterelektronenmikroskopie-Aufnahmen wurden von Elke Nadler an der Universität Tübingen aufgenommen.

Publikation V

Alle Synthesen wurden von Julia C. Steinbach geplant und umgesetzt. Entsprechende Analytik und Auswertung der Partikel (Partikelgrößenauswertung, Thermogravimetrische Analyse, Stickstoffsorptionsmessungen) wurden vom Autor und Julia C. Steinbach durchgeführt. Die statistische Versuchsplanung wurde von Julia C. Steinbach ausgewertet. Das Manuskript wurde von Julia C. Steinbach verfasst.

Die Rasterelektronenmikroskopie-Aufnahmen wurden von Elke Nadler an der Universität Tübingen aufgenommen.

Publikation VI

Alle Synthesen wurden vom Autor und Julia C. Steinbach geplant und umgesetzt. Entsprechende Analytik und Auswertung der Partikel (Partikelgrößenauswertung, Stickstoffsorptionsmessungen, HPLC-Messungen) wurden vom Autor und Julia C. Steinbach durchgeführt. Die HPLC-Säulen wurden vom Autor gepackt. Das Manuskript wurde von Julia C. Steinbach verfasst.

Die Rasterelektronenmikroskopie-Aufnahmen wurden von Elke Nadler an der Universität Tübingen aufgenommen.

1 Zielsetzung

Heutzutage ermöglicht die seit 1980 stetig weiterentwickelte Sol-Gel-Chemie ein breites Anwendungsfeld von Siliziumdioxid in unterschiedlichen Bereichen der Forschung und Industrie. Der Einsatz als Wirkstofftransportmittel für Medikamente,[7–10] zur Herstellung von Zement,[11,12] die Darstellung anorganischer/organischer Hybridmaterialien zur Verbesserung chemischer und thermischer Eigenschaften[13,14] oder die Nutzung als Trägermaterial in der analytischen Chemie[15–19] sind verschiedene Einsatzgebiete von Silica-Materialien. Durch die fortdauernde Optimierung industrieller Prozesse werden die Anforderungen für zuverlässige Kontroll- und Analyseverfahren immer anspruchsvoller. Effizienz, Flexibilität und Reproduzierbarkeit sind hierbei entscheidende Kriterien.

Die Synthese sphärischer Silica-Partikel erfolgt durch das Verbrennen von $SiCl_4$ oder dem von Stöber, Fink und Bohn entwickelten Stöber-Prozess.[20,21] Hierbei werden anorganische Silicate oder Alkoxysilane basenkatalysiert umgesetzt und bilden über Hydrolyse- und Kondensationsreaktionen nicht poröse sphärische Silica-Partikel im unteren Mikrometerbereich.[20] Mit Hilfe spezieller Techniken oder Additiven von Alkalisalzen kann der Partikeldurchmesser weiter erhöht werden.[22–25] Die Prozesse sind chemisch gut kontrollierbar und gewähren über die systematische Einstellung der Reaktionsparameter präzise Partikelgrößen. Zur Darstellung poröser Silica-Partikel werden Template benötigt.[26–28] Grundsätzlich werden zwischen „weichen“ Templaten, sogenannten *soft templates* und „harten“ Templaten, den *hard templates*, unterschieden. *Soft template*-Methoden beruhen auf molekularen Wechselwirkungen unter Zugabe von nicht kovalent bindenden organischen Reagenzien, wie Cetyltrimethylammoniumbromid oder Blockpolymeren, wie Pluronic P123. Die Größe der porösen Silica-Partikel liegt entweder im Nanometerbereich oder führt zu einer uneinheitlichen Partikelgröße im Mikrometerbereich.[27,29–31] Die Verwendung poröser organischer Polymerpartikel als *hard templates* ermöglicht eine definierte Größenverteilung der Silica-Partikel im Mikrometerbereich.[32] Die Einlagerung von Silica-Nanopartikeln in den Poren der Template führt, nach erfolgreicher Entfernung des organischen Polymers, zu monodispersen Silica-Materialien mit regulierbarer Porenstruktur.[33–37] Die Einstellung von Parametern wie Porengröße und spezifische Oberfläche der mikrometergroßen Silica-Partikel wird über den Durchmesser der Silica-Nanopartikel realisiert und kann durch den Sol-Gel-Prozess gesteuert werden.

Die Hochleistungsflüssigkeitschromatographie (HPLC) ist eine der bekanntesten Methoden zur Analyse von Komponenten und Auftrennung von Gemischen. Sphärische Silica-Partikel dienen häufig als Trägermaterial, da sie eine hohe mechanische Stabilität aufweisen und weitestgehend chemisch inert sind. Zusätzlich besitzen die Partikel an der Oberfläche reaktive Spezies, an denen beliebige Moleküle immobilisiert werden kön-

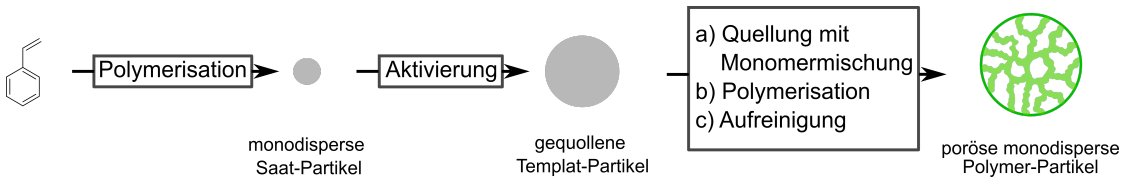
nen.[38–40] Die chromatographischen Kenngrößen, wie Analysezeit, Bodenzahl, Selektivität und Gegendruck, können über die Partikelgröße und deren Größenverteilung sowie der Porenstruktur und Oberflächenfunktionalisierung gezielt beeinflusst werden.[41–43] Enge Partikelgrößenverteilungen und große spezifische Oberflächen ermöglichen eine hohe Trenneffizienz. Durch die Verkleinerung der Partikelgröße nimmt die relative Oberfläche zu, jedoch erhöht sich dadurch der Gegendruck, was besondere und kostspielige Anforderungen an das HPLC-Equipment stellt.[44,45] Die Einführung von Poren in Silica-Partikeln erzielt eine Reduktion des Gegendrucks und stellt gleichzeitig eine hohe Oberfläche zur Verfügung, welche gute Wechselwirkungen in diffusionskontrollierten Prozessen ermöglicht. Die stationären Phasen in der HPLC werden entsprechend der Trennproblematik ausgewählt.[45,46] Die Synthese dieser Trennphasen mit definierten Porenparametern, maßgeschneidert zu den Trennproblemen, stellt weiterhin eine große Herausforderung dar. Biomoleküle, darunter Proteine, Peptide und Aminosäuren, sind wesentliche Bestandteile in der pharmazeutischen und medizinischen Diagnostik. Beispielweise ermöglichen der Einsatz von therapeutischen Proteinen und Peptiden Behandlungsalternativen für bestimmte Krankheiten wie Diabetes, Krebs- oder Coronaerkrankungen.[47,48] Die zuverlässige Analyse der Biomoleküle ist hierbei unerlässlich. Oftmals bestehen Proteine und Peptide aus komplizierten Aminosäuresequenzen, deren Verunreinigungen sich minimal in ihrer Sequenzabfolge unterscheiden. Neben der Kapillarelektrophorese[49] und biophysikalischen Trenntechniken[50–52] haben sich verschiedene Arten der Flüssigkeitschromatographie als Analysetool etabliert. Größenauschlusschromatographie (*size exclusion chromatography*, SEC), Ionenaustauschchromatographie (*ion exchange chromatography*, IEC) und Umkehrphasenchromatographie (*reversed-phase liquid chromatography*, RP-LC) werden zur Auftrennung von Biomolekülen genutzt.[53,54]

Ziel dieser Arbeit ist die kontrollierte Entwicklung monodisperser, mesoporöser Silica-Partikel im Mikrometermaßstab unter Verwendung aminofunktionalisierter organischer Template. Die Darstellung poröser Polymerpartikel mit unterschiedlichen Porendesign bildet hierbei die Grundlage. Modifizierte Syntheserouten der *hard template*-Methode und deren Einfluss auf die resultierenden Porenparameter der Silica-Materialien werden umfangreich untersucht und diskutiert. Eine anschließende C_{18}-Funktionalisierung ermöglicht die Applikation als leistungsstarke Trennphase für Biomoleküle wie Aminosäuren, Peptide oder Proteine in der Hochleistungsflüssigkeitschromatographie.

2 Theorie

Die kommerzielle Herstellung vieler wichtiger Polymere, wie Polyvinylchlorid (PVC), Polymethylmethacrylat (PMMA) oder expandierendes Polystyrol (EPS, Styropor®), erfolgt über Heterophasenpolymerisationen ihrer Monomere. Die Anwendungsmöglichkeiten der Polymere erstrecken sich, ähnlich wie bei Silicamaterialien, von Bau- und Füllstoffen[55] über die medizinische Diagnostik[56,57] bis hin zum Trägermaterial in der HPLC.[58–61] Die präzise Kontrolle der Partikel- und Porengrößen sowie die Stabilität über den gesamten pH-Bereich sind ein großer Vorteil gegenüber den Silica-Partikeln.[62]
Radikalische Polymerisationen basieren auf dem Zerfall eines Initiators, der eine Kettenreaktion der Monomere auslöst, bis diese aufgebraucht sind. Mit Hilfe der Dispersionspolymerisation können monodisperse, sphärische, nicht poröse Partikel im Größenbereich zwischen 0.1 µm und 10 µm realisiert werden. Die Monomere wachsen bis zu einer kritischen Kettenlänge und fallen als Keime in der kontinuierlichen Phase aus. Die Wachstumsphase der Keime endet, sobald die Monomere aufgebraucht sind.[63,64] Suspensionspolymerisationen ermöglichen Partikelgrößen zwischen 20 µm und wenigen Millimetern. Durch Zugabe eines Porogens können poröse Polymerpartikel erzielt werden. Der Initiator ist in den Monomeren löslich. Nach Initiation des Kettenwachstums werden die Monomertröpfchen durchpolymerisiert. Die Tröpfchengröße der Monomere wird über die Rührgeschwindigkeit definiert und bestimmt die finale Partikelgröße. Aufgrund dessen gehen Suspensionspolymerisationen mit einer breiten Partikelgrößenverteilung einher.[65,66]

Die Kombination beider Methoden bildet die mehrstufige Impfsuspensionspolymerisation, bei welcher Saatpartikel (Seeds) als formgebende Schablone fungieren und zu monodispersen, porösen Partikeln aufgequollen werden. Ugelstad entwickelte einen zweistufigen Prozess, welcher eine enorme Volumenvergrößerung der Saatpartikel ermöglichte (Schema 1).[67–69] Als Ausgangsmaterial dienen monodisperse Polystyrolpartikel, die über die herkömmlichen Polymerisationsprozesse erhalten werden. Im ersten Schritt werden die Seeds mit einer wasserunlöslichen Verbindung, wie Dibutylphthalat (DBP) oder 1-Chlordecan, gequollen und aktiviert.[70,71] Dabei wird die Substanz als fein dispergierte wässrige Emulsion mit den Saatpartikel umgesetzt. Sobald das Aktivierungsreagenz vollständig aufgenommen wurde, folgt im zweiten Schritt die weitere Quellung und Polymerisation der Partikel. Eine wässrige Emulsion aus Monomer, Quervernetzer, Porogenen, Initiator und Stabilisator wird mit den aktivierten Saatpartikeln umgesetzt und nach der vollständigen Quellung die Polymerisation thermisch initiiert. Nach der Polymerisation werden nicht umgesetzte Monomere sowie die Porogene und der Stabilisator ausgewaschen. Vorerst basierten die hydrophoben Polymerpartikel auf Grundlage von Styrol und Divinylbenzol. Mit der Verwendung von Glycidylmethacrylat (GMA) als Monomer erweiterten Šmigol und Švec die Einsatzgebiete der Polymere, da sie nun auch für hydrophile Anwendungen zugänglich wurden.[72] Die nachträgliche



Schema 1: Schematische Darstellung der Herstellung poröser Polymerpartikel nach Ugelstad.[67–69]

Umsetzung der Epoxidfunktion ermöglichte eine anwendungsspezifische Funktionalisierung und machte die *poly*(Glycidylmethacrylat-*co*-Ethylenglycoldimethacrylat)-Partikel (*p*(GMA-*co*-EDMA)) zu einem vielseitigen Ausgangsmaterial. Die Arbeitsgruppe um Fréchet rehydroxylierte die Epoxidfunktion zur Ausbildung eines Diols für die Normalphasen- und wässrige Größenauschlusschromatographie.[73,74] Hradil *et al.*,[75] Švec *et al.*[76] und Gong *et al.*[77] veröffentlichten die Modifizierung mit Alkylamin- bzw. Bernsteinsäurederivaten für den Einsatz als Anionen- und Kationenaustauscher in der Ionenaustauschchromatographie. Die Anbindung von Kronenethern oder β-Cyclodextrinen ermöglicht den Einsatz als chirale Phase in der HPLC.[78,79]
Die Ausbildung des Porennetzwerks erfolgt aufgrund der Phasenseparation während der Polymerisation in Anwesenheit inerter, wasserunlöslicher Porogene. Bei den Porogenen handelt es sich um Lösungsmittel oder lineare Polymere, die mit den Monomeren mischbar sind, aber das gebildete Polymer nicht auflösen. Da die Monomere während des Polymerisationsprozesses zu polymeren Strukturen reagieren, erreichen die Monomerketten sowohl das kritische Molekulargewicht sowie den Vernetzungsgrad und trennen sich von der Lösung als neue Phase. Sie wachsen aufgrund der, in der umgebenden Lösung vorhandenen, Monomere weiter. Die Löslichkeit des Polymers im inerten Lösungsmittel und damit auch der Zeitpunkt der Phasentrennung beeinflussen die Porenstruktur der entstehenden Polymerpartikel. Grundsätzlich werden die Porogene über ihren Hansen-Löslichkeitsparameter definiert und in drei Kategorien unterteilt.[80] Thermisch gute Lösemittel weisen eine geringe Differenz gegenüber dem gebildetem Polymer (hier: *p*(GMA-*co*-EDMA)) auf. Beispiele hierfür sind Toluol, n-Butylacetat oder Cyclohexanol. Es tritt eine späte Phasenseparation der Polymerpartikel auf, welche Mikro- und Mesoporen, ein geringes Porenvolumen und eine hohe spezifische Oberfläche zur Folge hat. Dodecanol ist ein Beispiel für thermodynamisch schlechte Lösemittel. Bei ihnen liegt eine große Differenz zwischen gebildetem Polymer (hier: *p*(GMA-*co*-EDMA)) und Löslichkeitsparameter vor. Eine frühe Phasenseparation und Meso- bis Makroporen, hohes Porenvolumen und geringe spezifische Oberfläche sind das Resultat. Die dritte Kategorie bilden lineare Polymere wie Polystyrol. Sie induzieren eine extrem frühe Phasenseparation und bilden makroporöse Strukturen mit geringer Oberfläche.[70,81] Die Kombination der drei Porogenklassen erlaubt eine gezielte Einstellung der Poreneigenschaften.

Bereits seit 1968 ist die Methode zur Darstellung sphärischer, monodisperser Silica-Partikel etabliert. Die basisch induzierte Umsetzung von Tetraalkylorthosilicaten, im alkoholischen Milieu, zu unporösen Silica-Partikeln, in der Größenordnung von 0.05 µm bis 1.70 µm, ist weitreichend untersucht und unter dem Namen *Stöber-Prozess* bekannt.[20] Die Ausbildung dreidimensionaler Siloxannetzwerke erfolgt über Hydrolyse- und Kondensationsreaktionen von Alkoxysilanen (Glg. 2.1). Die einzelnen Teilreaktionen können als nukleophile Substitutionsreaktionen betrachtet werden, deren Geschwindigkeit von der chemischen Umgebung des Si-Atoms, dem angreifenden Nukleophil, der Abgangsgruppe des Silicium-Precursors sowie den Reaktionsbedingungen abhängig ist.[82–85]

$$\mathrm{Si(OR)_4 + 2\ H_2O \xrightarrow[\text{Alkohol}]{\mathrm{OH^-}} SiO_2 + 4\ ROH} \tag{2.1}$$

Die Hydrolyse, bei welcher die nukleophile Substitution eines Hydroxid-Ions zur Bildung eines Silanols stattfindet, bildet den geschwindigkeitsbestimmenden Schritt der Reaktionsabfolge (Glg. 2.1.1). Die anschließende Kondensation zu Siloxanen erfolgt über die nukleophile Substitution eines Silanolat-Ions. Die Reaktion mit einem Silanol (Glg. 2.1.2) oder einem Alkoxysilan (Glg. 2.1.3) führt zum Polymerwachstum und zur Ausbildung des Siloxannetzwerks. Die Rückreaktion, die Hydrolyse der Siloxanbindung, dient zur Umstrukturierung des Netzwerks und kann im Extremfall zur vollständigen Depolymerisation führen (Ostwald-Reifung).[84]

$$\mathrm{(RO)_3Si{-}OR + OH^- \rightleftharpoons (RO)_3Si{-}OH + RO^-} \tag{2.1.1}$$

$$\mathrm{(RO)_3Si{-}O^- + (RO)_3Si{-}OH \rightleftharpoons (RO)_3Si{-}O{-}Si(OR)_3 + OH^-} \tag{2.1.2}$$

$$\mathrm{(RO)_3Si{-}O^- + (RO)_3Si{-}OR \rightleftharpoons (RO)_3Si{-}O{-}Si(OR)_3 + RO^-} \tag{2.1.3}$$

Wie oben genannt, ist die Kinetik der Teilreaktionen abhängig von der chemischen Umgebung des Si-Atoms. Im Ablauf des Sol-Gel-Prozesses ändert sich diese fortlaufend. Die Abnahme der Elektronendichte und die geringere sterische Hinderung begünstigen mit zunehmenden Hydrolysegrad einen nukleophilen Angriff am Si-Atom entsprechend $\mathrm{Si(OR)_4 < Si(OR)_3(OH) < Si(OR)_2(OH)_2 < Si(OR)(OH)_3 < Si(OH)_4}$.[82] Mit zunehmenden Kondensationsgrad wächst die sterische Abschirmung der Siloxan-Reste und erschwert weitere nukleophile Angriffe.

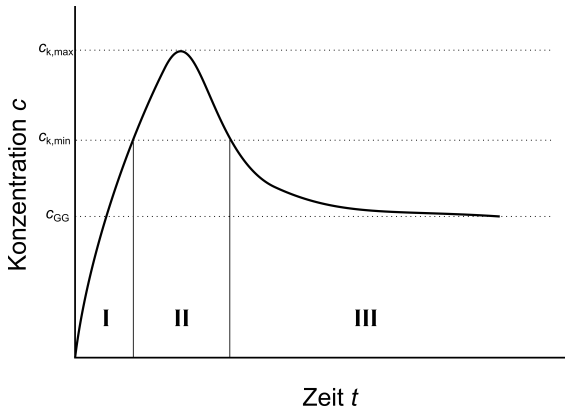


Abbildung 1: Konzentrationsprofil aktivierter Monomere nach LaMer und Dinegar[86] in Abhängigkeit der Zeit: (**I**) Induktionsphase, (**II**) Keimbildungsphase, (**III**) Wachstumsphase.

Die Ausbildung kolloidaler Silica-Partikel ereignet sich aufgrund der Phasenseparation kontinuierlich wachsender Monomere. Das von LaMer und Dinegar[86] veröffentliche Modell (Abb. 1) für die Wachstumsphasen von Schwefelkeimen beschreibt den Konzentrationsverlauf aktivierter Monomere und kann für das Polymerwachstum von Alkoxysilanen übernommen werden. In der Induktionsphase steigt die Konzentration hydrolysierter Silica-Spezies rapide über die Gleichgewichtskonzentration an. Überschreitet diese die kritische Konzentration $c_{k,min}$, übersättigt die Lösung und Keime werden gebildet. Die Keimbildungsphase endet, sobald die Konzentration $c_{k,min}$ unterschritten wird. Die Restkonzentration an aktivierter Monomere trägt zum Wachstum der Keime bei und nähert sich der Gleichgewichtskonzentration an. Die Differenz Δc_k und damit die Dauer der Keimbildungsphase steuert die finale Partikelgröße. In der Literatur werden verschiedene Modelle bezüglich des Mechanismus der Wachstumsphase diskutiert. Unabhängig der Abfolge beschreiben beide vorgestellten Modelle zunächst die Ausbildung von Keimen. Das Monomer-Additions-Modell von Matsoukas und Gulari[87,88] beruht auf der Hydrolyse und beschreibt das Wachstum als Kondensation einzelner Monomere mit der Partikeloberfläche. Bereits die Bildung dimerer Alkoxysilane wird als Keim betrachtet. Die Keimbildungsrate wird über die Hydrolysegeschwindigkeit bestimmt und bildet den geschwindigkeitsbestimmenden Schritt. Bogush und Zukoski[89,90] erläutern das Wachstum als Aggregation instabiler Partikel mit sich selbst oder stabilen Partikeln. Die Polykondensation führt zu einer Erhöhung des Molekulargewichts und einer Verdichtung der Partikel-Spezies, welche die Löslichkeit überschreiten und als Keime ausfallen.[89–91]

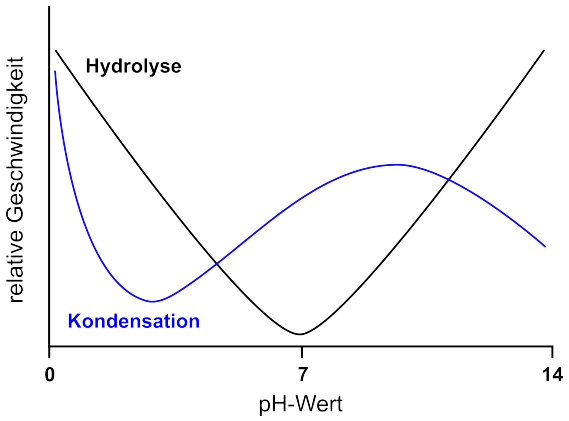


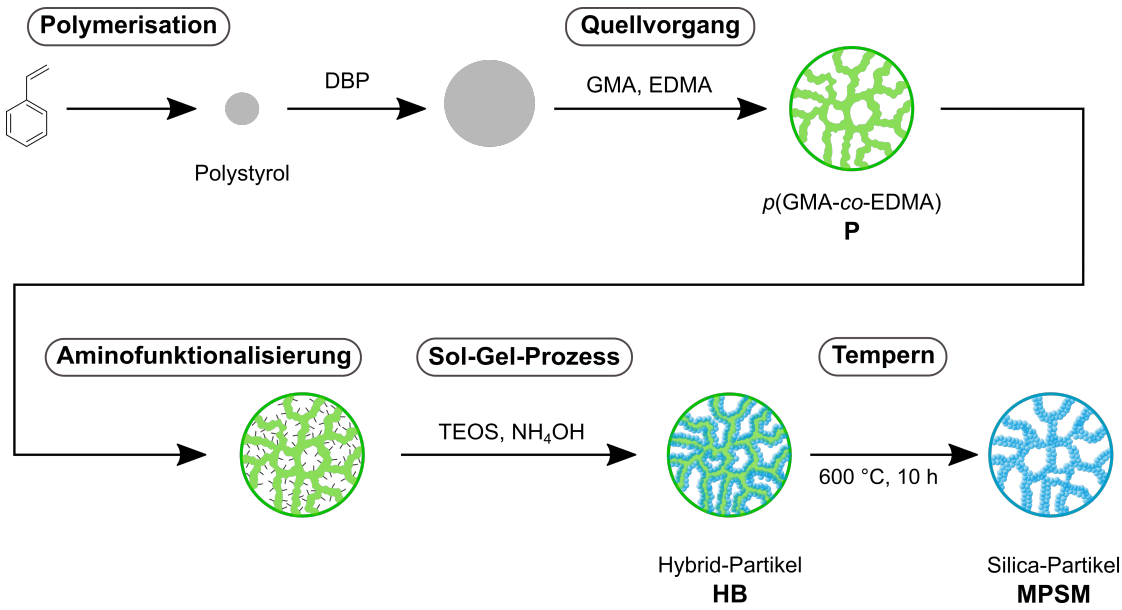
Abbildung 2: Relative Geschwindigkeiten der Hydrolyse und Konzentration in Abhängigkeit des pH-Werts.

Die Einstellungen der Reaktionsbedingungen im Sol-Gel-Prozess ermöglichen die Steuerung der Hydrolyse- und Kondensationsgeschwindigkeiten und damit die finale Partikelgröße. Zu den in dieser Arbeit verwendeten Parametern gehören:

- Kettenlänge und -verzweigung des alkoholischen Lösungsmittels,
- Konzentration von Ammoniak,
- Alkylkettenlänge des Alkoxysilans,
- Verhältnis n(H_2O)/n(TEOS),
- Zugabemethode der Precursoren.

Alkoholische Lösungsmittel haben sich als geeignetes Medium für die Synthese von Stöber-Partikel etabliert. Neben der Mischbarkeit von Tetraalkylorthosilicaten und H_2O beeinflusst das Lösungsmittel die Geschwindigkeitskonstanten der Hydrolyse und Kondensation. Mit zunehmender Kettenlänge und -verzweigung des Alkohols steigt die Hydrolysegeschwindigkeit und resultiert in größeren Partikeldurchmessern.[20,82,83,92–95] Längerkettige Alkohole $\geq C_5$ bilden nicht-sphärische Partikel.[96] Die Rückreaktion der Siloxane (Rückveresterung) kann zu einem Austausch der Alkoxygruppen mit dem Lösungsmittel führen. Die relativen Geschwindigkeiten der Hydrolyse und Kondensation sind stark pH-Wert-abhängig (Abb. 2). Dieser wird über die Konzentration von Ammoniak reguliert und legt die Anzahl der gebildeten Ionen fest. Die Oberfläche von Stöber-Partikeln ist, aufgrund des niedrigen isoelektrischen Punkts (pH = 2), bei pH-Werten > 7 negativ geladen. In beiden Reaktionen reagieren Anionen (Hydrolyse: Hydroxid-Ionen; Kondensation: Silanolat-Ionen) als Nukleophile und beeinflussen die Lage der Gleichgewichtsreaktionen. Zusätzlich schirmen Ammonium-Ionen die negative Oberflächenladung unter Ausbildung einer STERN-Doppelschicht ab.[20,82,83,87,95,97–100] Die Alkylreste der Alkoxysilane erhöhen mit zunehmender Kettenlänge und -verzweigung den sterischen Anspruch und die

Elektronendichte am Si-Atom, was einen nukleophilen Angriff erschwert. Die Hydrolysegeschwindigkeit nimmt ab und kleinere Partikeldurchmesser sind die Folge.[20, 82, 83, 97–99, 101] Die Anwesenheit von Wasser ist für den Sol-Gel-Prozess essenziell und beeinflusst die Gleichgewichtslage von Hydrolyse und Kondensation. Eine erhöhte Wasserkonzentration begünstigt die Hydrolyse (vgl. Glg. 2.1.1) und hemmt die Kondensation (vgl. Glg. 2.1.2). Infolgedessen erfahren die Partikelgrößen, in Abhängigkeit der Wasserkonzentration bzw. dem Verhältnis n(H_2O)/n(TEOS), meist ein Optimum.[20, 82, 83, 87, 91, 95, 97, 99, 100] Die Zugabe der Alkoxysilane erfolgt in den meisten Fällen vollständig (*batch*-Verfahren) oder stufenweise (*semi-batch*-Verfahren). Die Konzentration an hydrolysierten Monomeren ist in den *semi-batch*-Verfahren gering, was eine reduzierte Anzahl an Keimen zur Folge hat. Diese wachsen aufgrund der stetigen Zugabe der Monomere an und resultieren in größeren Partikeldurchmessern als in *batch*-Verfahren.[24, 25]



Schema 2: Synthese mesoporöser Silica-Partikel mit Hilfe organischer *p*(GMA-*co*-EDMA) Templaten.[33]

Poröse *p*(GMA-*co*-EDMA)-Partikel (**P**) fungieren neben dem Einsatz als stationäre Phase auch hervorragend als organisches *hard template* zur Synthese von monodispersen mesoporösen Silica-Partikeln (Schema 2). Als Ausgangsmaterial wird Styrol über die gängigen Polymerisationsarten zu monodispersen Saatpartikeln polymerisiert. Diese werden mit Dibutylphthalat aktiviert und anschließend mit GMA und EDMA als Monomere sowie Toluol und Cyclohexanol als Porogene umgesetzt. Wird der Sol-Gel-Prozess in Anwesenheit funktionalisierter *p*(GMA-*co*-EDMA)-Partikel durchgeführt, lagern sich Silica-Nanopartikel (SNP) in den Poren des Templats an und bilden organische/anorganische Hybrid-Partikel (**HB**). Durch thermische Zersetzung wird das organische Templat entfernt und monodisperse mesoporöse Silica-Partikel (**MPSM**) bleiben über.

Meyer *et al.* erläuterte die Notwendigkeit von Hydroxy- oder Aminogruppen zur Einlagerung von Siliciumprecursoren in organischen Templaten.[32] In den letzten Jahren wurden vermehrt aminofunktionalisierte *p*(GMA-*co*-EDMA)-Partikel zur Herstellung mesoporöser Silica-Partikel verwendet, da diese eine erhöhte Affinität gegenüber den SNP aufweisen. He *et al.* nutzten ethylendiamin-funktionalisierte *p*(GMA-*co*-EDMA)-Partikel im Sol-Gel-Prozess in Gegenwart von Tetramethylammoniumhydroxid oder Tetra-*n*-butylammoniumbromid in 2-Propanol. Die Zugabe einer 10 % TEOS-Lösung erfolgte tropfenweise. Sie erzielten eine Abbildung des Templats, jedoch mit geringer Ausbeute.[34] Xia *et al.* und Bai *et al.* verwendeten Tetraethylenpentamin als Funktionalisierungsreagenz und erreichten eine vollständige Abbildung der Partikelgröße mit adäquaten Ausbeuten.[35,37,102] Chen *et al.* untersuchten die Zeta-Potentiale der funktionalisierten Template und verglichen Ethylendiamin, (3-Aminopropyl)triethoxysilan und Trimethylammoniumchlorid miteinander. Aufgrund der höchsten Potentialdifferenz zwischen den TMA funktionalisierten Polymerpartikeln (0.321 mV) und TEOS im Reaktionsmedium (− 3.35 mV), favorisierten sie diese für die Darstellung poröser Silica-Partikel.[36] Die unterschiedlichen Funktionalisierungsmöglichkeiten beeinflussen die Einlagerung der SNP und damit die Partikel- und Poreneigenschaften der Silica-Partikel massiv.

3 Zusammenfassung der Ergebnisse

Die Darstellung mesoporöser Silica-Partikel mit Hilfe von *p*(GMA-*co*-EDMA)-Templaten wurde in den letzten Jahren genauer untersucht.[34–37,102] Bisherige Arbeitsgruppen verglichen den Einfluss verschiedener Funktionalisierungsreagenzien auf die Größe und Morphologie sowie den Porenparametern der resultierenden Silica-Materialien. Die Partikelgrößen der eingelagerten Silica-Nanopartikel unterscheiden sich dabei je nach funktionalisiertem Templat. Ein genauerer Fokus auf den Sol-Gel-Prozess zur Steuerung der Größe und Einlagerung der Silica-Nanopartikel blieb bisher aus. Eine Übersicht der in dieser Arbeit diskutierten Veröffentlichungen ist in Abbildung 3 dargestellt.

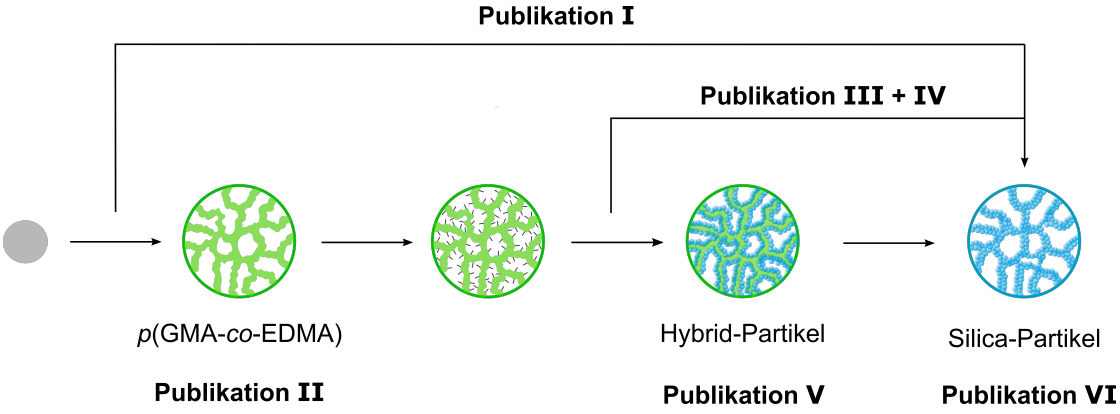


Abbildung 3: Übersicht der in dieser Arbeit veröffentlichten Publikationen in Bezug auf die *hard template*-Methode zur Herstellung mesoporöser Silica-Partikel.[1,2,5]

Die Nomenklatur der *p*(GMA-*co*-EDMA)-Template (**P**), der Hybrid-Partikel (**HB**) und der Silica-Partikel (**MPSM**) werden in der Zusammenfassung fortlaufend nummeriert und stimmen mit den Bezeichnungen in den Veröffentlichungen nicht überein. Eine Zuordnung der einzelnen Partikel ist in Kapitel 12.2 dokumentiert.

3.1 Einfluss der Porosität und Grad der Funktionalisierung der *p*(GMA-*co*-EDMA)-Template

Die physikalischen Eigenschaften organischer Template, wie Partikeldurchmesser, Porengrößenverteilung, Porenvolumen und spezifische Oberfläche, können über physikochemische und hydrodynamische Parameter während der Impfsuspensionspolymerisation gesteuert werden. Reaktionsparameter, wie das Verhältnis der kontinuierlichen und dispergierten Phase, Wahl und Konzentration des Stabilisators, Rührgeschwindigkeit oder Rührtyp, wirken sich auf die finale Partikelgröße des Templats aus. Die porösen Eigenschaften werden von den physikochemischen Einstellungen beeinflusst. Zu diesen zählen die Art und der prozentuale Anteil der Monomere, Quervernetzer, Initiator und inerten porogenen Lösungsmittel sowie Temperatur und Dauer der Polymerisation. Die Variati-

on der Reaktionsparameter ermöglicht verschiedene poröse *p*(GMA-*co*-EDMA)-Template unterschiedlicher chemischer, prozentualer Zusammensetzungen. Die Verhältnisse von A: Monomere zu Porogenen (Publ. **I** + **II**), B: GMA zu EDMA (Publ. **I** + **II**) und C: die Porogenzusammensetzung von Toluol und Cyclohexanol (Publ. **II**) wurden variiert und deren Einfluss auf die physikalischen Eigenschaften der *p*(GMA-*co*-EDMA)-Template untersucht.
Die Partikeldurchmesser der Polymertemplate (d_{50}) sind von der Masse (m) und Größe (d) der Seeds und dem Anteil an organischer Phase (M) gemäß Gleichung 3.1 abhängig.[103] Innerhalb der Versuchsreihe von **P1** - **P6** wurde eine Batch an Polystyrol-Partikel und die gleiche Volumenmenge an organischer Phase eingesetzt (Publ. **I**).

$$log(d_{50}) = log(d) + \frac{1}{3} log\Big(\frac{M+m}{m}\Big) \tag{3.1}$$

Die resultierenden Partikeldurchmesser der *p*(GMA-*co*-EDMA)-Template ändern sich minimal zwischen 7.3 µm und 7.9 µm (Abb. 4a). Ein zunehmender GMA-Anteil und höhere Porogenkonzentrationen bewirken eine Vergrößerung der Poren (Abb. 4b). Gleichzeitig nehmen die Porenvolumina und die spezifischen Oberflächen der Polymerpartikel bei zunehmenden GMA-Anteil ab. Eine hohe Porogenkonzentration (**P5**) hat ein erhöhtes Porenvolumen und größere Oberflächen, während eine hohe Monomerkonzentration (**P6**) ein geringes Porenvolumen und niedrigere Oberflächen zur Folge hat (Abb. 4c und 4d). Je mehr GMA in der organischen Phase vorliegt, desto weniger EDMA ist vorhanden und desto geringfügiger sind die Polymerpartikel vernetzt. Zusätzlich setzt die Phasenseparation bei zunehmenden GMA-Gehalt früher ein. Beide Effekte führen zu einer Vergrößerung der Poren und einer Erniedrigung der spezifischen Oberfläche.

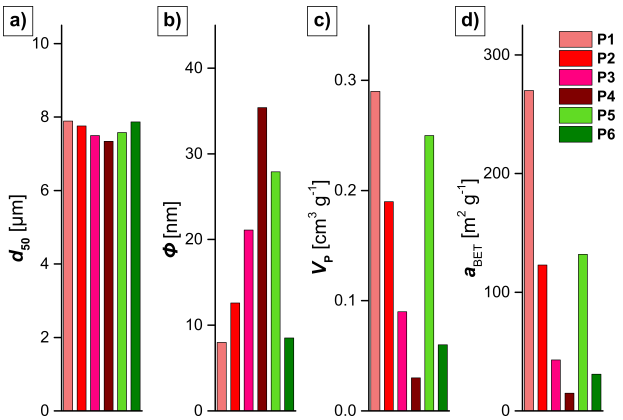


Abbildung 4: Partikelgrößen und Porenparameter der *p*(GMA-*co*-EDMA)-Template **P1** - **P6**.

	GMA/EDMA [v.%/v.%]	Mo./Po. [v.%/v.%]
P1	20/80	50/50
P2	40/60	50/50
P3	60/40	50/50
P4	80/20	50/50
P5	40/60	25/75
P6	40/60	75/25

Die Varianzanalyse der statistischen Versuchsplanung ermöglicht die Identifizierung komplexer Wechselwirkungen zwischen Faktoren in einem System. Im Fall der Impfsuspen-

sionpolymerisation der *p*(GMA-*co*-EDMA)-Template konnten die Zusammenhänge bezüglich der oben genannten Verhältnisse erläutert werden (Publ. **II**). Dafür wurde ein Probenset von 19 Polymerbatches dargestellt und auf ihre Porenparameter untersucht. Das Porenvolumen der Polymerpartikel wird maßgeblich von der Art und dem Anteil der Porogene bestimmt. Die Differenz der HILDEBRANDT-Löslichkeitsparameter von Toluol ($18.2\,\mathrm{MPa}^{1/2}$)[80] und Cyclohexanol ($22.4\,\mathrm{MPa}^{1/2}$)[80] gegenüber *p*(GMA-*co*-EDMA) ($24.0\,\mathrm{MPa}^{1/2}$)[104] bestimmt den Zeitpunkt der Phasenseparation. Die Zusammensetzung der Porogenmischung aus Toluol und Cyclohexanol resultiert bei zunehmender Konzentration an Cyclohexanol in niedrigeren Porenvolumina. Aufgrund der geringeren Differenz der HILDEBRANDT-Löslichkeitsparameter ist Cyclohexanol das bessere Lösungsmittel und führt zu einer späteren Phasenseparation. Bei konstanter Porogenzusammensetzung wird mit erhöhtem GMA-Anteil eine Erniedrigung des Porenvolumens beobachtet (Publ. **II**, Kap. 3.4.). Die Porengröße hängt von den Parametern GMA/EDMA und Toluol/Cyclohexanol ab. Insgesamt werden bei zunehmenden GMA-Verhältnis Polymernetzwerke mit größeren Poren gebildet. Dieser Effekt verstärkt sich, wenn die Porogenzusammensetzung zunehmend aus Toluol besteht (Publ. **II**, Kap. 3.5.). Die spezifische Oberfläche umfasst ein Zusammenspiel aus Porenvolumen und Porengröße.[105] Je größer das Porenvolumen und kleiner die Poren der Partikel sind, desto größer die erhaltenden Oberflächen. Da beide Effekte über das Verhältnis von GMA zu EDMA bestimmt werden, resultieren bei zunehmenden GMA-Anteil geringere Oberflächen (Publ. **II**, Kap. 3.6.). Insgesamt gilt: Je höher der Anteil an Porogenen, desto größer die Porenparameter der Polymerpartikel. Die Ergebnisse der statistischen Versuchsplanung (Publ. **II**) korrelieren mit den Erkenntnissen der Versuchsreihe **P1** - **P6** (Publ. **I**).

Die Funktionalisierung der *p*(GMA-*co*-EDMA)-Template mit Aminoreagenzien erzeugt eine positive Oberflächenladung unter STÖBER-Bedingungen und ermöglicht die Einlagerung von negativ geladenen nicht porösen Silica-Nanopartikeln (SNP). Der Grad der Aminierung und folgend die Anzahl positiver Ladungen, ist von dem Anteil des eingebauten GMAs abhängig. Die Etablierung eines *partial least square*-Regressionsmodells (PLS-R) zur Vorhersage der relativen Anzahl an eingebauten Epoxidgruppen konnte erfolgreich demonstriert werden (Publ. **II**, Kap. 3.3.). Das Modell basiert auf den asymmetrischen und symmetrischen Banden ($845\,\mathrm{cm}^{-1}$ und $910\,\mathrm{cm}^{-1}$)[106] und der C-O Streckschwingung ($1250\,\mathrm{cm}^{-1}$)[106] von Epoxiden. Die Umsetzung der Polymerpartikel **P1** - **P6** erfolgt durch Ringöffnung der Epoxidgruppen mit Tetraethylenpentamin unter Ausbildung eines Aminoalkohols (Schema 2). Im Vergleich zur restlichen Masse der funktionalisierten Polymerpartikel **P1@TEPA** - **P6@TEPA** findet die Aminierung nur oberflächlich statt, sodass eine Änderung des Stickstoffgehalts in den Elementaranalysen nicht detektiert wird. Alternativ wurde der Grad der Aminierung indirekt über die Abnahme der Bandenintensität der Epoxidgruppen bestimmt. Dieser steigt mit zunehmenden Verhältnis von GMA zu EDMA (**P1@TEPA** $<$ ... $<$ **P4@TEPA**) und bleibt bei Änderung des Monomer-zu-

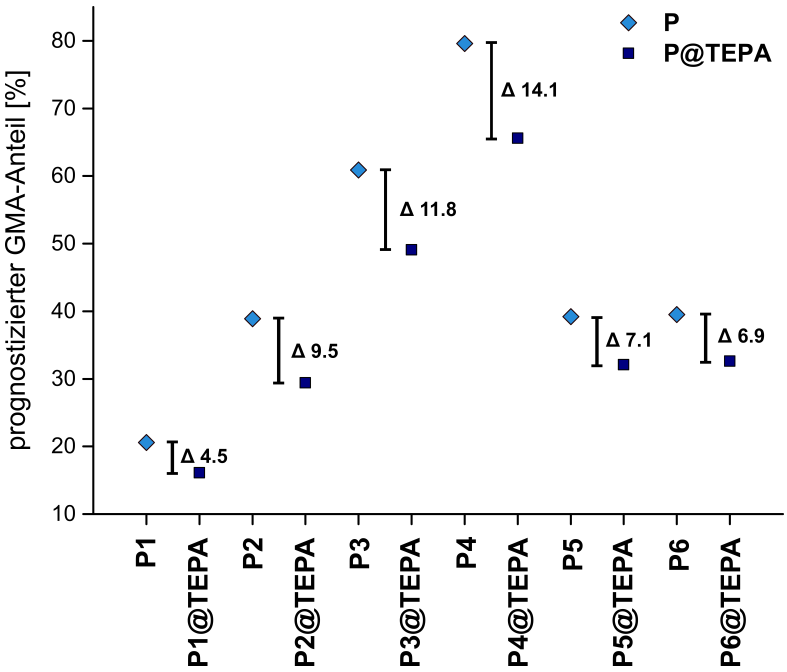
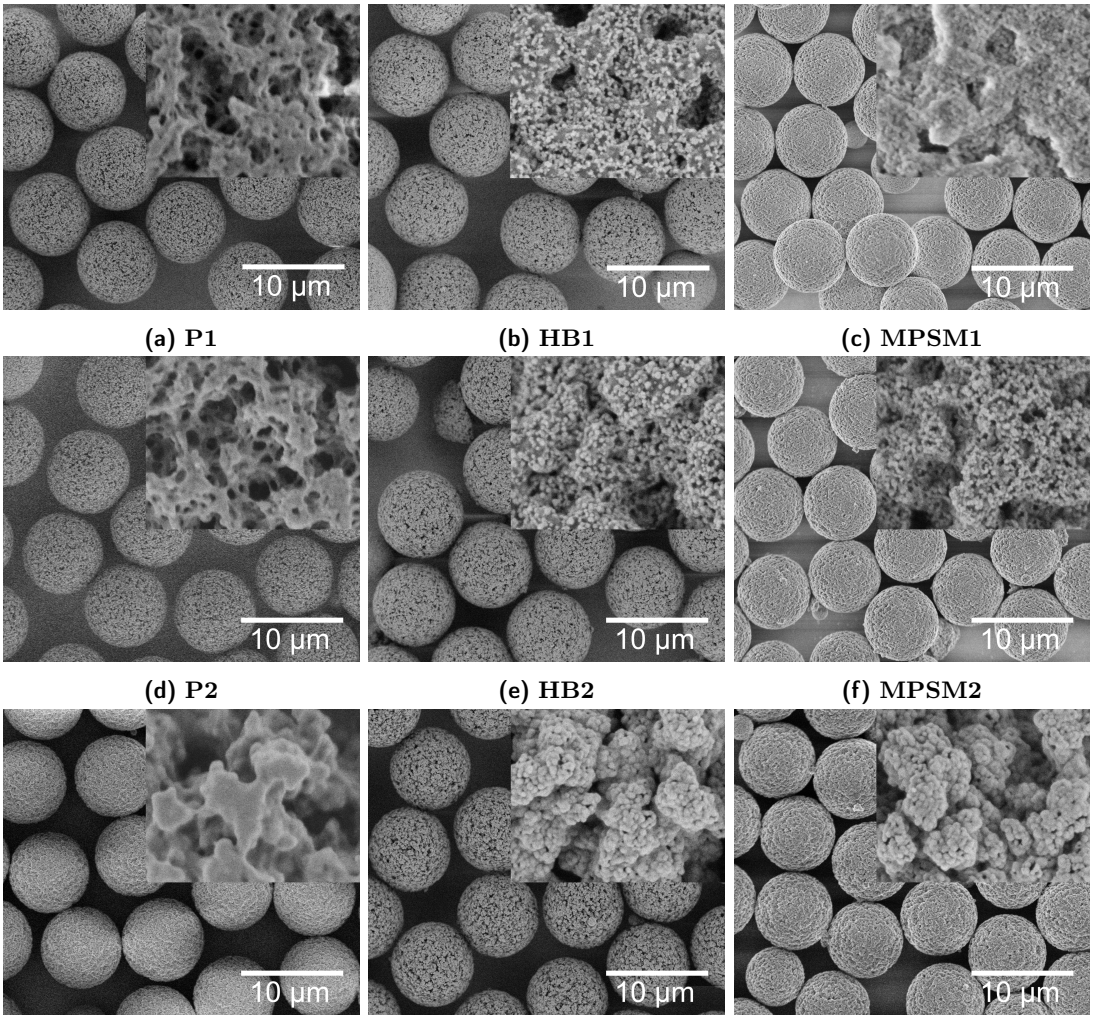


Abbildung 5: Differenz Δ der prognostizierten relativen Anteile an Epoxidgruppen in *p*(GMA-*co*-EDMA)-Partikeln **P** und aminofunktionalisierten Polymerpartikeln **P@TEPA**.

Porogen-Verhältnisses nahezu gleich (**P5@TEPA** ∼ **P2@TEPA** ∼ **P6@TEPA**).
Die funktionalisierten **P1-6@TEPA**-Partikel wurden als *hard templates* in einem basenkatalysierten Sol-Gel-Prozess verwendet und bildeten Polymer/SiO_2-Hybrid-Partikel **HB1** - **HB6**. Nach Entfernen des Polymers wurden die monodispersen Silica-Materialien **MPSM1** - **MPSM6** erhalten. Die Größe der Silica-Partikel unterscheidet sich je nach Grad der Funktionalisierung und steigt mit zunehmenden Anteil an Aminogruppen gemäß Abbildung 5. Die Porenparameter der **MPSM1** - **MPSM5** nehmen im Vergleich zu ihren korrespondierenden *p*(GMA-*co*-EDMA)-Templaten zu. Das Entfernen des Polymers eröffnet mehr Platz, sodass Porengröße, Porenvolumen und spezifische Oberfläche ansteigen. Die Trends der Porenparameter von **MPSM1** - **MPSM4** verhalten sich analog zu ihren Polymeren **P1** - **P4**. Während **P5** im Vergleich zu den anderen Templaten die zweithöchste Porengröße vorweist, besitzt **MPSM5** die geringste.

Anhand der REM-Aufnahmen in Abbildung 6 wird deutlich, dass die MPSMs aus angelagerten SNP bestehen. Die Größe der SNPs korreliert ebenfalls mit dem Grad der Aminierung und steigt mit zunehmenden GMA-Anteil. Bei hoher elektrostatischer Anziehung werden bereits kleine negativ geladene Silica-Nanopartikel in das Templat eingelagert. Aufgrund ihres hohen Ladung-zu-Größe-Verhältnisses sind diese reaktiv und aggregieren zu größeren Spezies (Abb. 6k). Im Fall von **MPSM6** verschlossen die SNP das funktionalisierte Polymer aufgrund der geringen Porosität und bildeten eine Schicht um das Templat. Nach der Kalzinierung verblieb eine hohle Hülle (Abb. 6r). Bei geringerer An-

ziehung wachsen die SNPs in der kontinuierlichen Phase bereits heran und diffundieren langsamer in das funktionalisierte Templat. Diese sind unreaktiver, lagern sich in den Poren des Templats an und behalten ihre Größe bei.
Thermogravimetrische Analysen von **HB1** - **HB5** ergaben für alle Hybrid-Materialien einen SiO_2-Massenanteil von $\sim$ 30 wt.%, unabhängig der Zusammensetzung des Templats. Die Größe der eingelagerten SNP hängt folglich von drei Faktoren ab: (*i*) der Wachstumsgeschwindigkeit der SNPs, die über die Sol-Gel-Parameter gesteuert werden, (*ii*) der Diffusionsrate der SNPs, welche über die elektrostatische Anziehung gesteuert wird und von der Funktionalisierung abhängt und (*iii*) der Porosität des Polymertemplats.



(a) P1 **(b) HB1** **(c) MPSM1**

(d) P2 **(e) HB2** **(f) MPSM2**

(g) P3 **(h) HB3** **(i) MPSM3**

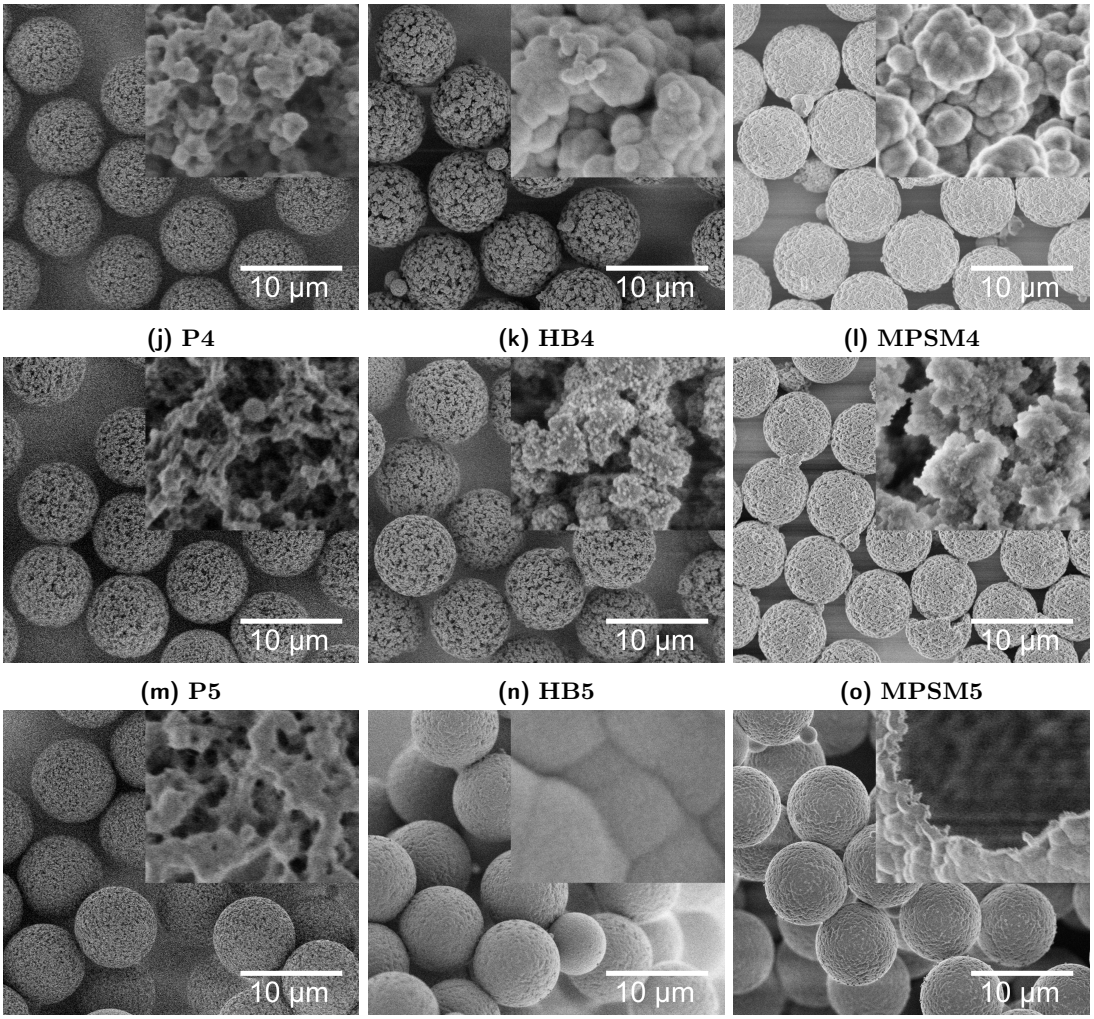


Abbildung 6: REM-Aufnahmen der *p*(GMA-*co*-EDMA)-Template **P1** - **P6** (links), Polymer/SiO_2 Hybrid-Partikel **HB1** - **HB6** (mittig) und Silica-Partikel **MPSM1** - **MPSM6** (rechts). Entsprechende Oberflächen sind im rechten oberen Quadranten abgebildet. REM-Konditionen: 2,000 ×; 50,000 ×.

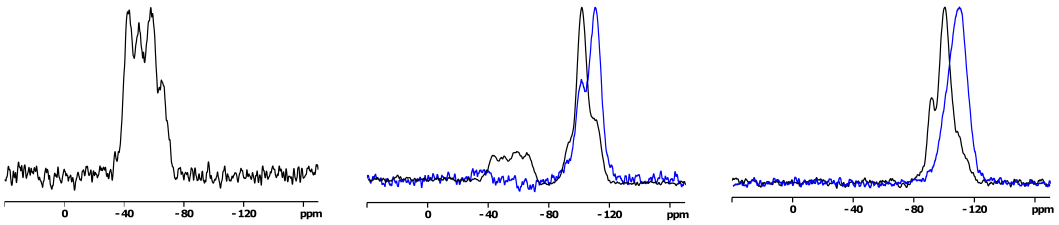
Die Einlagerung von Silica-Nanopartikeln in porösen *p*(GMA-*co*-EDMA)-Templaten zur Darstellung mesoporöser Silica-Partikel konnte erfolgreich demonstriert werden (Publ. **I**). Die Größe der eingebetteten SNP steuert die Porengrößen der finalen MPSM. Große SNP führen zu großen Poren, wohingegen kleine SNP in kleinen Poren resultieren. Die Partikelgröße der SNP hängt, neben der Wachstumsgeschwindigkeit in der kontinuierlichen Phase, auch von der Funktionalisierung und der Porosität des Templats ab. Daher wurde ein modellhafter Zusammenhang entwickelt, welcher das Verhältnis zwischen Monomeren, der Porogenzusammensetzung und dem Verhältnis von Monomeren zu Porogenen verdeutlicht (Publ. **II**). Dieser ermöglicht die gezielte Einstellung der Porosität der *p*(GMA-*co*-EDMA)-Template.

3.2 Einlagerung von Silica-Nanopartikeln über unterschiedliche Hydrolysegeschwindigkeiten

Die Bildung nicht poröser monodisperser Silica-Partikel im alkoholischen Medium erfolgt über eine basenkatalysierte Kaskade von Hydrolyse- und Kondensationsreaktionen. In Anwesenheit aminofunktionalisierter poröser Polymertemplate lagern sich Silica-Nanopartikel in den Poren des Templats an und generieren Polymer/SiO_2-Hybrid-Partikel **HB**. Die Reaktionsparameter des Sol-Gel-Prozesses steuern die Wachstumsgeschwindigkeit der SNP in der kontinuierlichen Phase. Zu diesen zählen die Alkylkettenlänge und -verzweigung der alkoholischen Lösungsmittel (Publ. **III**), die Alkylkettenlänge der eingesetzten Alkoxysilane (Publ. **IV**) und die Konzentration von Alkoxysilan, NH_3 und H_2O (Publ. **V**).

In Publ. **III** werden (3-Aminopropyl)triethoxysilan (APTES) funktionalisierte Polymerpartikel als *hard template* mit TEOS im Sol-Gel-Prozess eingesetzt. Hierbei wurde der Einfluss alkoholischer Lösungsmittel (MeOH (**HB7**), EtOH (**HB8**), 2-PrOH (**HB9**) und n-BuOH (**HB10**)) zur Kontrolle der Größe und Steuerung der Porenparameter der mesoporösen Silica-Partikel untersucht.
APTES als Funktionalisierungsreagenz für *p*(GMA-*co*-EDMA)-Template ermöglicht, im Vergleich zu TEPA, neben der positiven Ladung der Amingruppe, die Anbindung von SNP über die Kondensation der Triethoxysilanfunktion mit Silanol-Gruppen. Die erfolgreiche Synthese von **P7@APTES**-Partikeln konnte über Elementaranalysen (N: 1.6 %) und thermogravimetrische Analysen (SiO_2: 6.6 %) nachgewiesen werden. Die Größe, Dispersität und Morphologie der Partikel ändern sich im Vergleich zu den Polymertemplaten **P7** nicht. Die Einlagerung von SNP reduzieren das Porenvolumen der Hybrid-Materialien **HB7** – **HB10** und führen zu einem Anstieg der Partikelgröße um 600 - 800 nm. REM-Aufnahmen der Hybrid-Partikel zeigen, dass die Morphologien und die Größe der SNP sich, je nach verwendetem Alkohol, unterscheiden (Abb. 8). In Methanol lagern sich die kleinsten SNP im Templat an, in 1-Butanol die größten (Abb. 8a u. Abb. 8g). Die Morphologien werden dabei partikulärer, je größer die eingelagerten Silica-Nanopartikel sind. TGA-Messungen von **HB7** – **HB10** belegen einen zunehmenden SiO_2-Gehalt mit zunehmender SNP-Größe. Nach der Entfernung des Polymers behalten die MPSM ihre generierten Morphologien bei. Die Morphologie und Porenparameter der Silica-Partikel **MPSM7** – **MPSM10** werden durch die Größe der unporösen SNP bestimmt. Hierbei steuert die Wahl des Lösungsmittels das *in situ*-Wachstum der SNP[85, 93, 94] und damit die Partikeleigenschaften der finalen MPSM. Aufgrund der geringen Hydrolyse- und Kondensationsgeschwindigkeit von TEOS in MeOH, wird ein geringerer Anteil an SiO_2 in das Templat eingebaut, was nach der Kalzinierung zu kleineren Partikelgrößen von **MPSM7** führt. Das Verbrennen der organischen Vorlage führt zu einer Kondensation der kleinen SNP miteinander

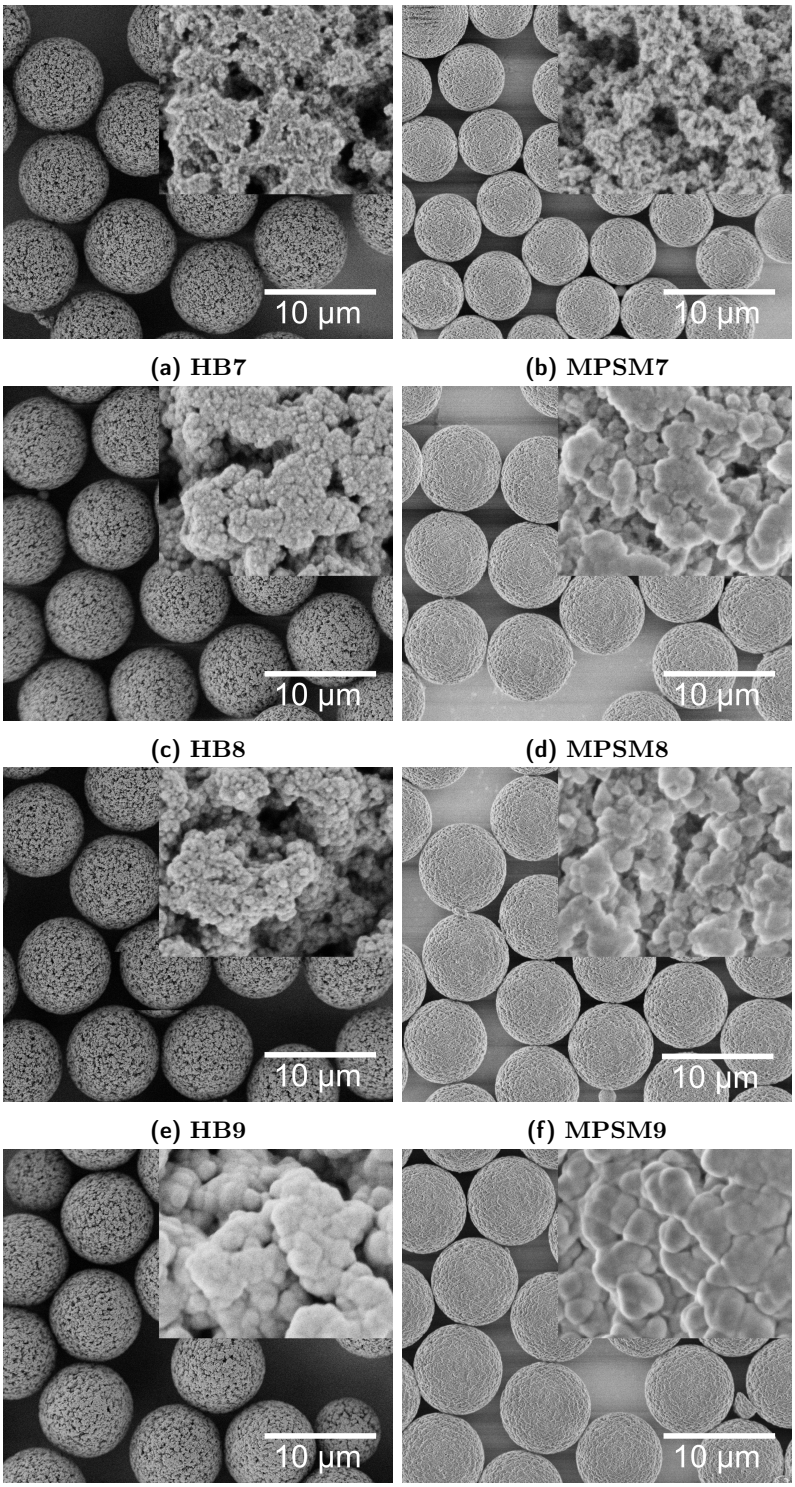
und einem Schrumpfen des SiO_2-Netzwerks. Mesoporen mit einem Median von 4.7 nm bleiben über. In EtOH, 2-PrOH und BuOH werden die SNP größer und bilden **MPSM8**, **MPSM9** und **MPSM10** mit größeren Poren. Aufgrund der Einlagerung größerer SNP und folglich mehr SiO_2 in den Poren des Templats, bilden **MPSM8** – **MPSM10** das Polymer vollständig ab und die mediane Porengröße steigt auf bis zu 23.8 nm an.



(a) P@APTES **(b) HB** **(c) MPSM**

Abbildung 7: ^{29}Si-CP/MAS- (schwarz) und ^{29}Si-HPDEC-NMR-Spektren (blau) von APTES funktionalisierten *p*(GMA-*co*-EDMA)-Templaten **P@APTES**, daraus resultierende Polymer/SiO_2-Hybrid-Partikel **HB** und Silica-Partikel **MPSM**.

Die Festkörper-NMR Spektren von P@APTES, HB und MPSM gewähren einen Zugriff auf die chemischen und strukturellen Zusammensetzungen der Partikel (Abb. 7). Das ^{29}Si-CP/MAS-NMR-Spektrum von P@APTES weist vier Signale im Bereich von -40 bis -80 ppm auf und kann nicht hydrolysierter (T^0), teilweise hydrolysierter (T^1,T^2) und vollständig hydrolysierter (T^3) Alkoxysilan-Spezies zugeordnet werden (Abb. 7a). Während der Funktionalisierung der *p*(GMA-*co*-EDMA)-Template wird die Triethoxysilangruppe zu einem gewissen Grad hydrolysiert und kondensiert. Die erfolgreiche Einlagerung von SNP in das funktionalisierte Templat werden über Q^2-, Q^3- und Q^4-Gruppen zwischen -90 und -110 ppm im ^{29}Si-CP/MAS-NMR-Spektrum der Hybrid-Partikel nachgewiesen (Abb. 7b). Das Signalmuster der T-Gruppen der HB erfährt, im Vergleich zu dem Spektrum von P@APTES, keine Änderung. Die *in situ* gebildeten SNP füllen lediglich die Poren und binden nicht kovalent an das Templat. In den ^{29}Si-HPDEC-NMR-Spektren wird ersichtlich, dass das Siloxannetzwerk der HB und MPSM hauptsächlich aus Q-Gruppen besteht. Als Folge der Kalzinierung werden die T-Gruppen vollständig in Q-Gruppen umgewandelt (Abb. 7c).



(a) HB7 **(b) MPSM7**

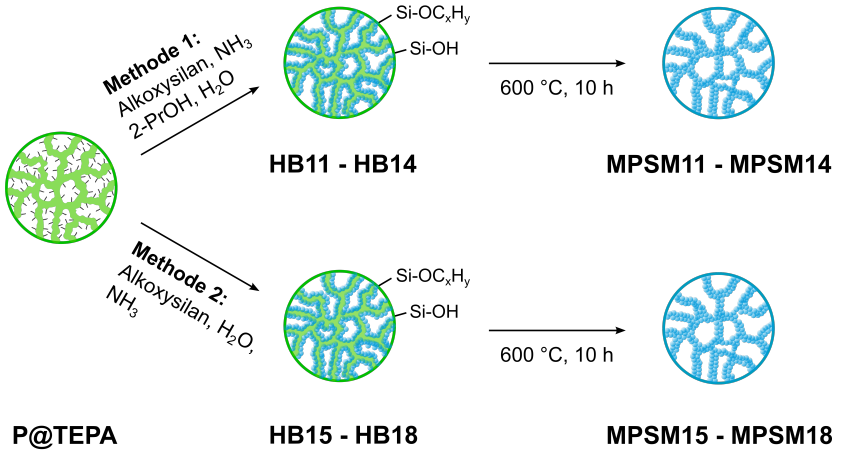
(c) HB8 **(d) MPSM8**

(e) HB9 **(f) MPSM9**

(g) HB10 **(h) MPSM10**

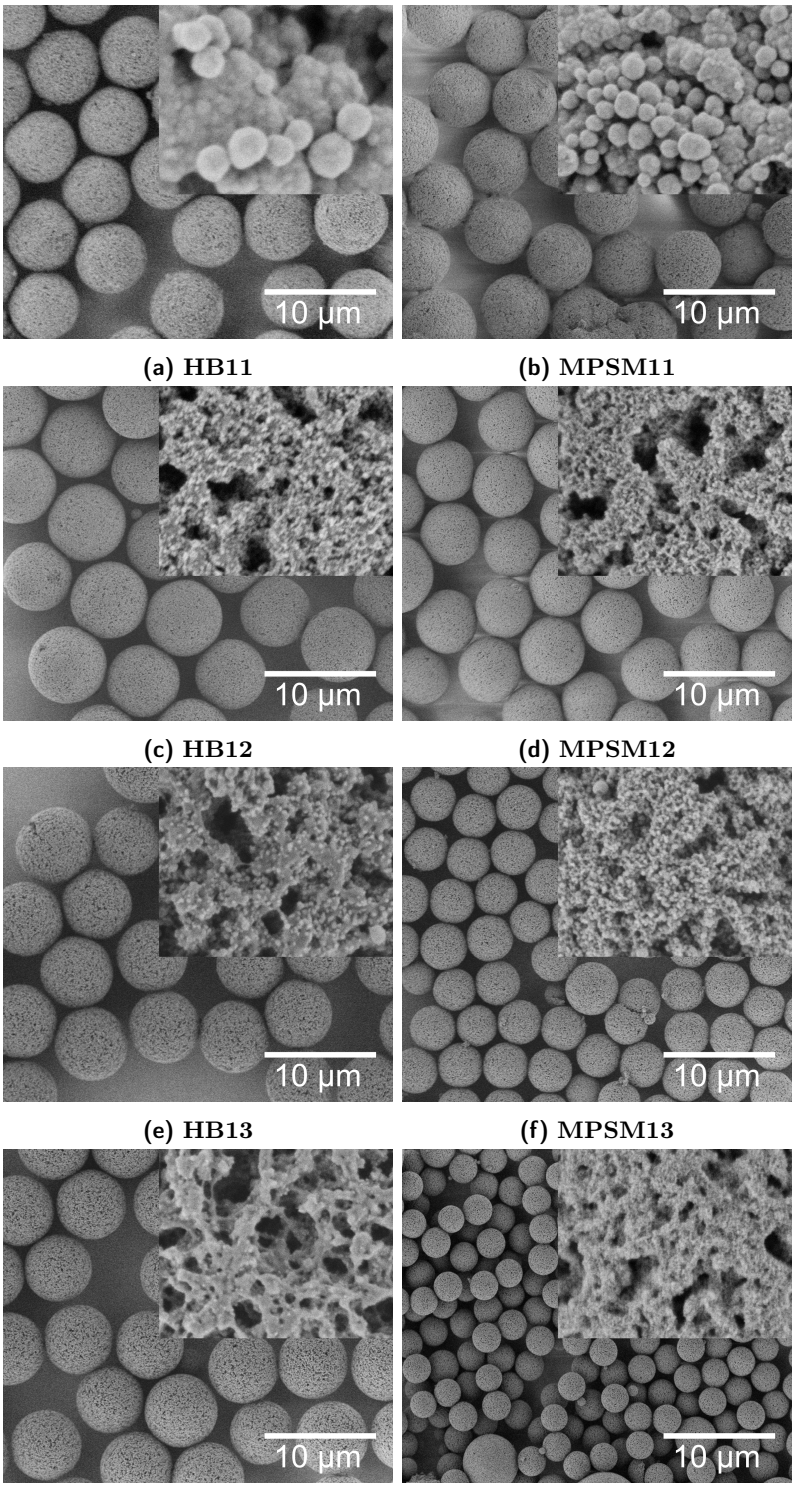
Abbildung 8: REM-Aufnahmen der Polymer/SiO_2-Hybrid-Partikel **HB7** – **HB10** (links) und Silica-Partikel **MPSM7** – **MPSM10** (rechts). Entsprechende Oberflächen sind im rechten oberen Quadranten abgebildet. REM-Konditionen: 2,000 ×; 50,000 ×.

Ein weiterer Sol-Gel-Parameter ist die chemische Umgebung des Si-Atoms der Precursoren. Eine Zunahme der Kettenlänge der Alkylgruppen des Alkoxysilans führt zu einer Abnahme der Hydrolysegeschwindigkeit. Die zunehmende sterische Hinderung und die induktiven Effekte der Alkylgruppen erhöhen die Elektronendichte am Silicium-Atom und hemmen einen nukleophilen Angriff. Darüber hinaus kann die abnehmende Polarität der Alkoxysilane, je nach Lösungsmittel, zu einer Phasentrennung führen.



Schema 3: Vergleich der Synthesemethoden zur Einlagerung von SNP in **P@TEPA**-funktionalisierte Partikel (Publ. **IV**).

In Publ. **IV** wurde die Hydrolysegeschwindigkeit der SNP über die Reste der eingesetzten Alkoysilane gesteuert. Die Precursoren TMOS (**HB11**), TEOS (**HB12**), TPOS (**HB13**) und TBOS (**HB14**) wurden in Anwesenheit von 2-Propanol, H_2O und NH_3 mit **P8@TEPA**-Partikeln umgesetzt (Schema 3, Meth. 1). Die Hybrid-Partikel wachsen um 300 nm gegenüber dem *p*(GMA-*co*-EDMA)-Templat **P8**. REM-Aufnahmen der Hybrid-Partikel zeigen kleiner werdende anlagernde SNP bei abnehmender Hydrolysegeschwindigkeit gemäß **HB11** > **HB12** > **HB13** > **HB14** (Abb. 9). Die Wachstumsgeschwindigkeit der SNP für TMOS ist dabei so hoch, dass sich Sekundärpartikel unterschiedlicher Größen ($\sim$ 60 nm) an das Templat lagern und nicht in die Poren diffundieren (Abb. 9a). Für TEOS ist die Hydrolysegschwindigkeit bereits viermal langsamer,[101] sodass einheitliche SNP in die Poren des Templats diffundieren. TGA-Messungen der Hybrid-Partikel bestätigen, dass bei zunehmender Alkylkettenlänge der Precursoren weniger SiO_2 in das Templat eingelagert wird. Nach Entfernung des organischen Polymers bleiben monodisperse Silica-Partikel über. Die Partikelgröße und die mediane Porengröße nehmen von **MPSM11** zu **MPSM14** ab. Während **MPSM11** und **MPSM12** das Templat **P8** noch zu 100 % bzw. 92 % (6.0 µm bzw. 5.5 µm) abbilden, schrumpfen **MPSM13** und **MPSM14** auf 60 % bzw. 37 % (3.6 µm bzw. 2.2 µm) zusammen. Die mediane Porengröße der Silica-Partikel nimmt von 23.6 nm auf 4.0 nm ab. Die Abnahme der Partikel-



(a) HB11 **(b) MPSM11**

(c) HB12 **(d) MPSM12**

(e) HB13 **(f) MPSM13**

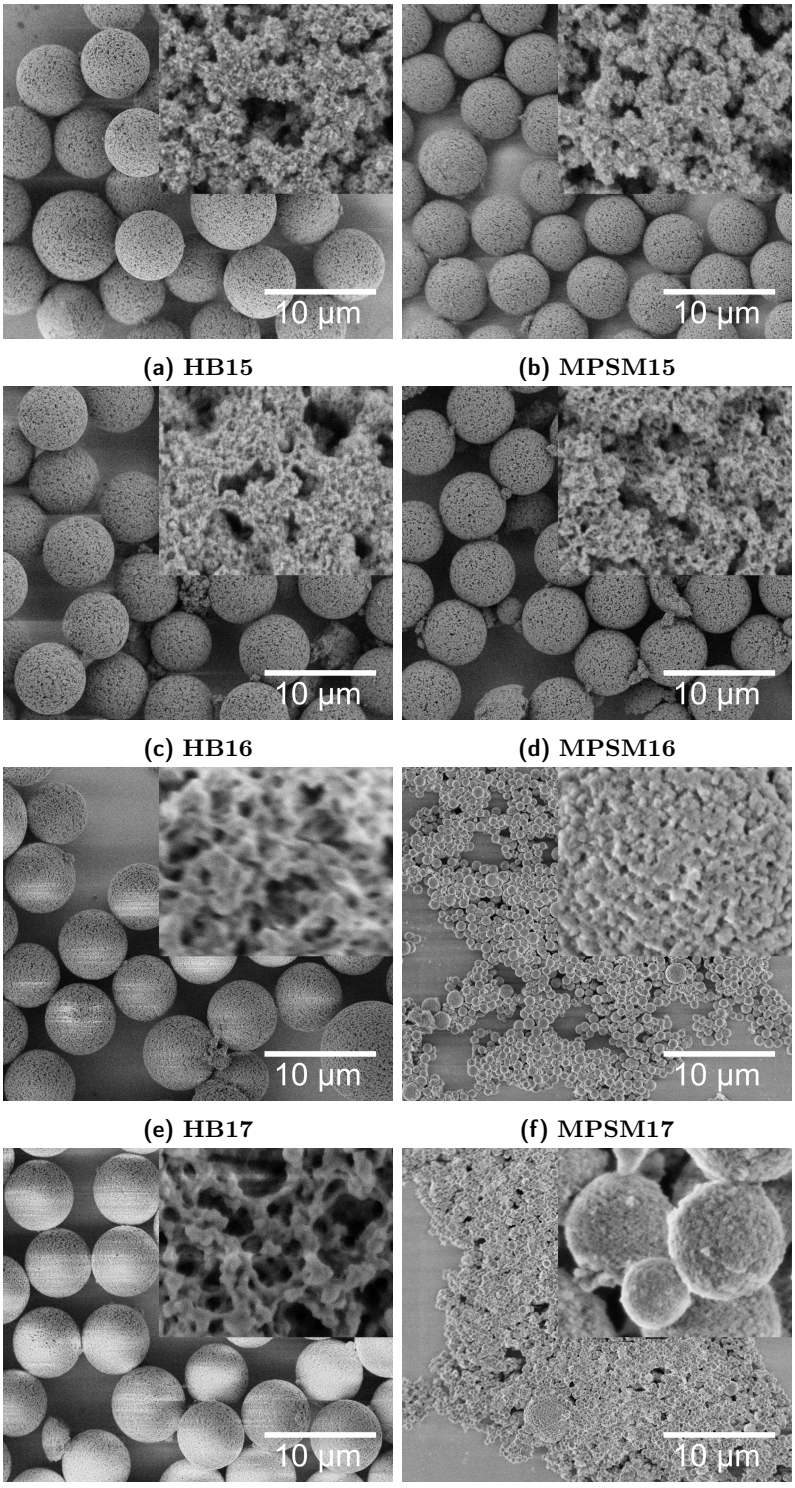
(g) HB14 **(h) MPSM14**

Abbildung 9: REM-Aufnahmen der Polymer/SiO_2-Hybrid-Partikel **HB11** – **HB14** (links) und Silica-Partikel **MPSM11** – **MPSM14** (rechts). Entsprechende Oberflächen sind im rechten oberen Quadranten abgebildet. REM-Konditionen: 2,000 ×; 50,000 ×.

und Porengrößen korrelieren mit der abnehmenden Größe der angelagerten SNP bei geringerer Hydrolysegeschwindigkeit. Die Morphologie der HB wird auf die MPSM übertragen (Abb. 9).

Die Bildung unporöser Silica-Nanopartikel, welche in das Templat diffundieren und sich dort anlagern, findet bereits in der kontinuierlichen Phase statt. Im Stöber-Prozess werden meist alkoholische Lösungsmittel als Reaktionsmedium eingesetzt, da diese die Mischbarkeit der unpolaren Alkoxysilane mit Wasser ermöglichen. Die Konzentration von H_2O forciert die Gleichgewichtslage der Hydrolyse auf die Seite der Produkte und die Kondensation auf die Seite der Edukte. Sowohl die Hydrolyse als auch die Kondensation verlaufen in reinem H_2O extrem langsam. Um die Partikelbildung außerhalb des Templats zu unterdrücken, wurden die Precursoren TMOS (**HB15**), TEOS (**HB16**), TPOS (**HB17**) und TBOS (**HB18**) mit **P8@TEPA**-Partikeln ausschließlich in Wasser vorgelegt (Schema 3, Meth. 2). NH_3 als Katalysator wird 24 h später zugegeben. Aufgrund der Polaritätsunterschiede zwischen den Precursoren und dem Reaktionsmedium, diffundieren die Monomere in das aminofunktionalisierte Templat. Erst bei Zugabe von NH_3 startet die Kondensation der hydrolysierten Precursoren in den Poren des Templats. Aufgrund der unterdrückten Kondensation sind die Hydrolysegeschwindigkeiten von TMOS und TEOS nahezu gleich. Die Partikel **HB15** weisen keine Sekundärpartikel an der Oberfläche des Templats auf (Abb. 10a). Insgesamt wird eine kantigere Morphologie für die Hybrid-Partikel **HB15** und **HB16** erzeugt. **HB17** und **HB18** zeigen keine Änderung der Partikelgröße und Morphologie gegenüber dem Templat auf. Nach der Kalzinierung resultieren monodisperse poröse Silica-Partikel mit einer Größe von 6.0 µm für **MPSM15** und **MPSM16**. Die kantige Morphologie der Partikel bleibt erhalten. Die Umsetzung von TPOS und TBOS erfolgt deutlich langsamer. Als Folge bleiben polydisperse MPSM mit einer durchschnittlichen Partikelgröße von 0.8 µm (**MPSM17**) bzw. 0.5 µm (**MPSM18**) über. Interessanterweise zeigen **HB16** mit TEOS als Precursor minimal größere SNP und einen höheren SiO_2-Gehalt gegenüber **HB15**. Dieser spiegelt sich in den größeren Poren von **MPSM16** im Vergleich zu **MPSM15** wider.

Die Kombination verschiedener Precursoren ermöglicht die Steuerung der morphologischen Eigenschaften sowie das Verhindern unerwünschter Effekte. In 2-PrOH/H_2O ist die Hydrolysegeschwindigkeit von TMOS zu schnell, sodass sich Sekundärpartikel bilden, während bei TPOS diese zu langsam ist, um das Templat vollständig abzubilden. Die Kombination von TMOS und TEOS (**HB19**) bzw. TPOS und TEOS (**HB20**) ist in Abbildung 11 dargestellt. Für **HB19** und daraus resultierend **MPSM19** werden keine angelagerten Sekundärpartikel beobachtet. Die Morphologie ist partikulär und die Porengröße von **MPSM19** beträgt 23.4 nm (vgl. **MPSM11**: 23.6 nm). Mit einer Größe von 5.0 µm bildet **MPSM20** zu 84 % (vgl. **MPSM13**: 60 %) das Templat ab. Die spezifische Oberfläche von **MPSM20** befindet sich im Bereich von **MPSM12** und **MPSM13**, während die Porengröße auf 17.1 nm ansteigt.



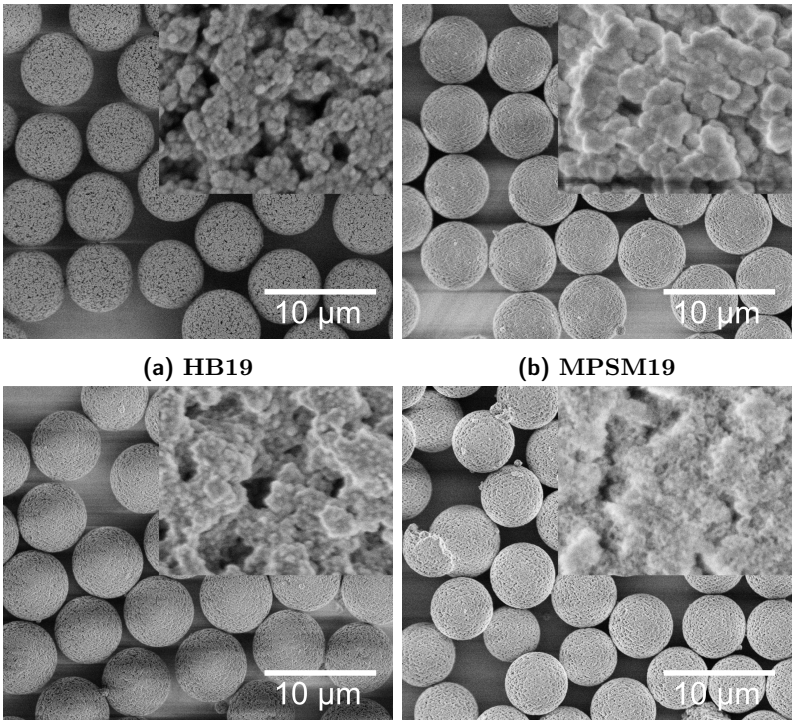
(a) HB15 **(b) MPSM15**

(c) HB16 **(d) MPSM16**

(e) HB17 **(f) MPSM17**

(g) HB18 **(h) MPSM18**

Abbildung 10: REM-Aufnahmen der Polymer/SiO_2-Hybrid-Partikel **HB15** – **HB18** (links) und Silica-Partikel **MPSM15** – **MPSM18** (rechts). Entsprechende Oberflächen sind im rechten oberen Quadranten abgebildet. REM-Konditionen: 2,000 ×; 50,000 ×.



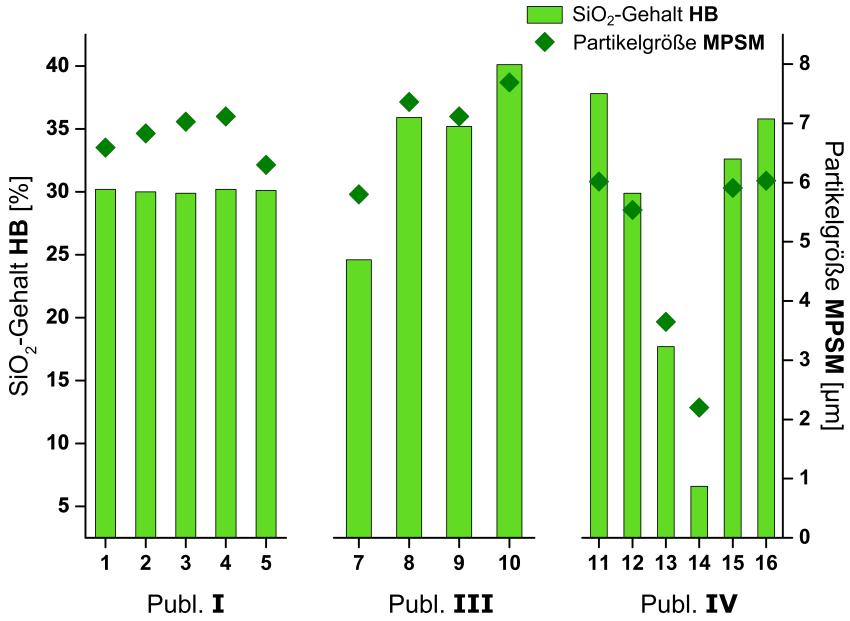
(a) HB19 **(b) MPSM19**

(c) HB20 **(d) MPSM20**

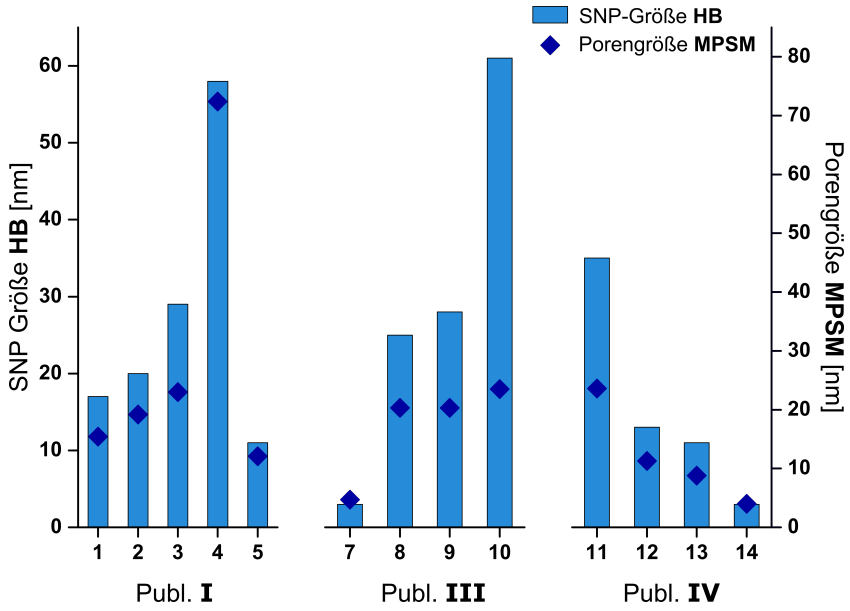
Abbildung 11: REM-Aufnahmen der Polymer/SiO_2-Hybrid-Partikel **HB19** und **HB20** (links) sowie Silica-Partikel **MPSM19** und **MPSM20** (rechts). Entsprechende Oberflächen sind im rechten oberen Quadranten abgebildet. REM-Konditionen: 2,000 ×; 50,000 ×.

Die Partikelgröße, die Morphologie sowie die Porenparameter der MPSMs hängen von der Größe der SNP und folglich von den Einstellungen des Sol-Gel-Prozesses ab. Diese werden in der Synthese der Hybrid-Partikel eingestellt. Die Größe der eingelagerten SNP kann über die Hydrolysegeschwindigkeit der Alkoxysilane in der kontinuierlichen Phase gesteuert werden. In diesen Arbeiten wurden der Einfluss von alkoholischen Lösungsmitteln (Publ. **III**) und die Kettenlänge der eingesetzten Precursoren (Publ. **IV**) untersucht. Bei zunehmender Kettenlänge und -verzweigung der Alkohole steigt die Hydrolysegeschwindigkeit an und größere SNP werden in das Templat eingebaut. Längerkettige Alkoxygruppen der Precursoren führen zu einer Abnahme der Hydrolysegeschwindigkeit. Folglich werden kleinere SNP gebildet und eine geringere Menge an SiO_2 eingelagert. Anhand von REM-Aufnahmen und TGA-Messungen konnten diese Trends bestätigt werden. Die Kontrolle der Hydrolysegeschwindigkeit ist essenziell zur Abbildung der Partikelgröße des Templats. Erhöhte Hydrolyseraten führen zu SNP, die zu groß sind, um in das funktionalisierte Polymer zu diffundieren. Im Gegensatz dazu wird das Templat bei langsameren Hydrolysegeschwindigkeiten nicht vollständig abgebildet.

Die Partikelgröße der Silica-Nanopartikel spielt eine entscheidende Rolle für die Morphologie und die Porenparameter der MPSM. Je größer die eingelagerten SNP, umso größer die Poren der MPSM und desto ausgeprägter ist die partikuläre Morphologie (Abb. 12). Die Bildung von SNP in der kontinuierlichen Phase konnte unterdrückt werden, indem der Sol-Gel-Prozess nur in H_2O durchgeführt wird. Silica-Partikel synthetisiert mit Tetramethyl- und Tetraethylorthosilikat, bilden bei dieser Methode das Templat vollständig ab und haben eine kantige Morphologie. Die Kombination von TMOS und TPOS mit TEOS führt zur Verhinderung ihrer unerwünschten Effekte und der Abbildung des Templats mit unterschiedlichen Morphologien.
^{29}Si-Festkörper-NMR-spektroskopische Aufnahmen der Hybrid-Partikel zeigen, dass die SNP nicht kovalent an die Triethoxysilanfunktionen der P@APTES-Partikel binden (Publ. **III**). Die Alkoxysilane werden in der kontinuierlichen Phase hydrolysiert und kondensiert, diffundieren in das Templat und lagern sich an den Porenwänden an.
Die Abhängigkeit der Eigenschaften der MPSM von der Menge und Größe an eingelagertem SiO_2 wurde in den Publikationen **V** und **VI** ebenfalls beobachtet. Je nach Konzentrationen von NH_3 und dem Verhältnis $^{n(H_2O)}/_{n(TEOS)}$ werden SNP verschiedener Größen eingebaut. Die Charakterisierung der Hybrid- und Silica-Partikel erlaubt die Unterteilung der Hydrolysegeschwindigkeiten in drei Reaktionsbereiche. Geringe Hydrolyseraten bilden kleine SNP, die in das Templat diffundieren und die Porenwände des funktionalisierten Templats überziehen (Publ. **V**, Fig. 7a). Die resultierenden MPSM schrumpfen auf einen Bruchteil der Templatgröße zusammen und weisen kleine Poren mit einer hohen Oberfläche auf (Publ. **VI**). Moderate Hydrolysegeschwindigkeiten füllen das Templat vollständig mit SiO_2 und erzeugen mesoporöse Silica-Partikel entsprechend der Templatgröße (Publ. **V**, Fig. 7b). Überschreitet das Wachstum neuer SiO_2-Spezies die Diffusionsgeschwindigkeit der SNP in das Templat, werden diese zu groß und füllen die Poren komplett. Nachträglich gebildete SNP verbleiben in der kontinuierlichen Phase und wachsen zu unporösen Sekundärpartikeln weiter (Publ. **V**, Fig. 7c). Diese müssen im Aufreinigungsschritt entfernt werden. Entsprechend der zunehmenden Größe der SNP nimmt die Porengröße der MPSM zu und die Porenvolumina und spezifische Oberfläche ab (Publ. **VI**).



(a) Abhängigkeit der Partikelgröße der MPSM vom eingebauten SiO_2-Gehalt.

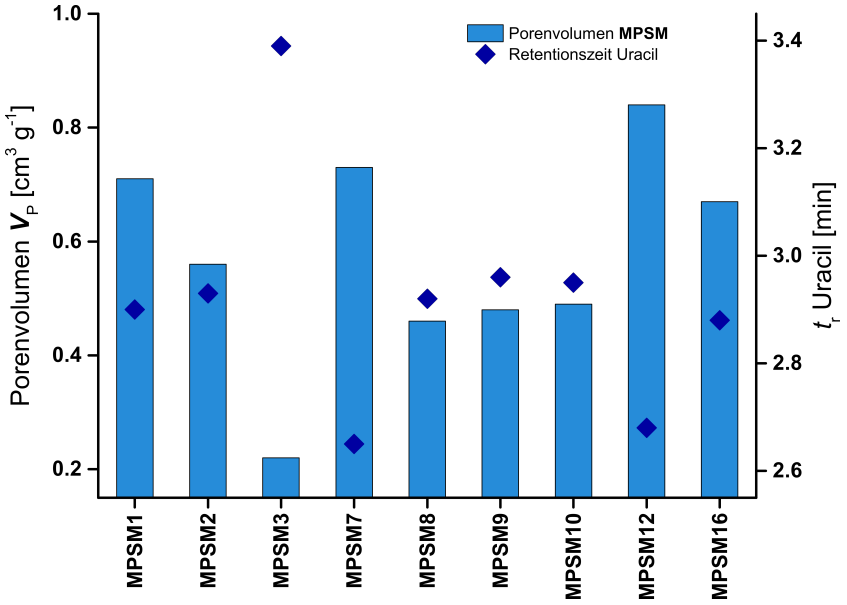


(b) Abhängigkeit der Porengröße der MPSM von den eingelagerten SNP.

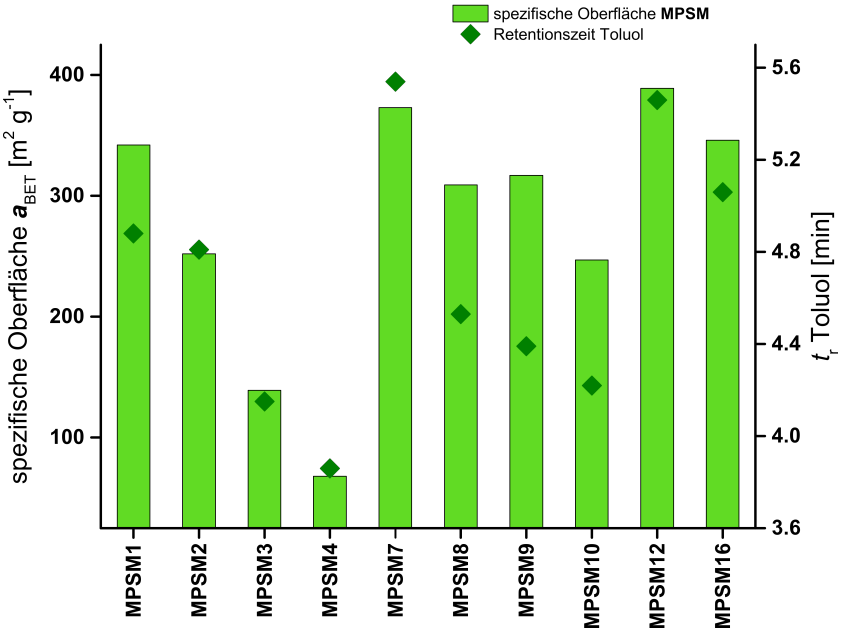
Abbildung 12: Korrelation zwischen dem eingebauten SiO_2-Gehalt im HB (hellgrüne Balken) und der Partikelgröße der MPSM (dunkelgrüne Punkte) sowie der eingelagerten SNP-Größe im HB (hellblaue Balken) und der Porengröße der MPSM (dunkelblaue Punkte).

3.3 Verwendung von MPSM als stationäre Trennphase in der HPLC

Mit der Zulassung synthetisch hergestellten Insulins 1982, gewann die Analyse von Biomolekülen wie Aminosäuren, Peptiden und Proteinen für viele pharmazeutische Betriebe an enormem Interesse.[107,108] Die Kopplung analytischer Trenntechniken, wie RP-LC/MS, ermöglichen die Aufarbeitung komplexer Probengemische, deren Verunreinigungen sich oft nur in wenigen Aminosäuren unterscheiden.[108–110] Während kleine Moleküle aufgrund der Wechselwirkung mit der Oberfläche der stationären Phase getrennt werden, benötigen große Moleküle, wie Proteine, poröse Strukturen als stationäre Phase. Mesoporöse C_{18}-modifizierte Silica-Partikel haben sich als bewährte Trennphase in der RP-LC etabliert.[45,46] Zur Untersuchung der vorgestellten MPSM wurden ausgewählte Materialien mit Octadecyltrimethoxysilan funktionalisiert und in 250 x 4.6 mm Säulen gepackt. Die Qualität der Säulenpackung wurde mit einem Testgemisch aus Uracil und Toluol evaluiert. Zusätzlich korrelieren beide Analyten mit den Porenparametern der stationären Phase. Uracil dient als Totzeitmarker in der RP-LC und eluiert entsprechend dem Porenvolumen. Toluol wechselwirkt mit den unpolaren Alkylketten der C_{18}-Funktionalisierung und spiegelt die spezifische Oberfläche wider. In Abbildung 13 sind die Porenvolumina und spezifischen Oberflächen der MPSM sowie die Retentionszeiten t_r von Uracil und Toluol auf den funktionalisierten Materialien dargestellt.



(a) Porenvolumina der unfunktionalisierten **MPSM** (hellblaue Balken) und Retentionszeiten von Uracil (dunkelblaue Punkte) auf den entsprechenden C_{18}-funktionalisierten Materialien als RP-Trennphase.



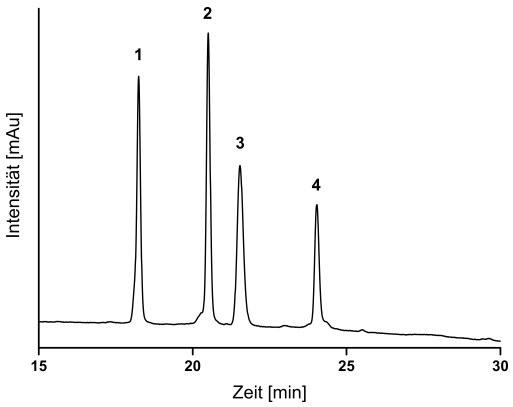
(b) Spezifische Oberflächen der unfunktionalisierten **MPSM** (hellgrüne Balken) und Retentionszeiten von Toluol (dunkelgrüne Punkte) auf den entsprechenden C_{18}-funktionalisierten Materialien als RP-Trennphase.

Abbildung 13: Korrelation zwischen den Porenparametern der Silica-Partikel **MPSM** und den chromatographischen Eigenschaften der entsprechenden C_{18}-funktionalisierten RP-Trennphasen.

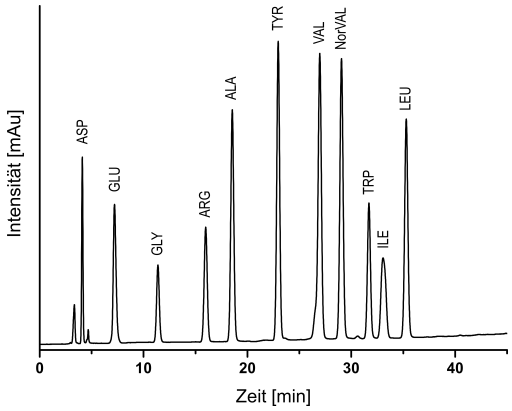
Die späteren Retentionszeiten von Uracil bei höheren Porenvolumina der MPSM sind nur bedingt erkennbar. Die Belegung der Silica-Materialien mit Octadecyl-Gruppen scheint nicht vollständig stattgefunden zu haben. Als Resultat verbleiben polare Si-OH-Gruppen an der Oberfläche, welche mit Uracil wechselwirken. Dies kann trotz geringerem Porenvolumen zu einer erhöhten Retentionszeit führen. Die Korrelation der verkürzten Retentionszeit von Toluol, bei abnehmender spezifischer Oberfläche der MPSM, wird in Abb. 13b ersichtlich.

Zur Auftrennung einer Proteinmixtur, bestehend aus Ribonuklease A, Cytochrome C, Holo-Transferin und Apomyoglobin, wurden die Silica-Partikel **MPSM1-C_{18}** – **MPSM4-C_{18}** verwendet (Publ. **I**). Die hergestellten Materialien weisen eine vergleichbar hohe Trenneffizienz gegenüber einer kommerziell erwerblichen Säule auf. Alle Proteine werden mit einer Auflösung von $R \geq 2$ Basislinien getrennt. Die Auftrennung von Proteinen fundiert neben den hydrophoben Wechselwirkungen auf dem Größenausschluss, gesteuert durch die Porengröße der stationären Phase. Die Auflösung steigt von **MPSM1-C_{18}** zu **MPSM3-C_{18}** mit zunehmender Porengröße. Trotz größerer Poren von **MPSM4-C_{18}** führt die verschlossene Morphologie zur Signalverbreiterung und folglich zu einer geringeren Auflösung. Die Trennung von elf verschiedenen Aminosäuren wurde auf den Materialien **MPSM7-C_{18}** – **MPSM10-C_{18}** erzielt (Publ. **III**). Eine Basislinientren-

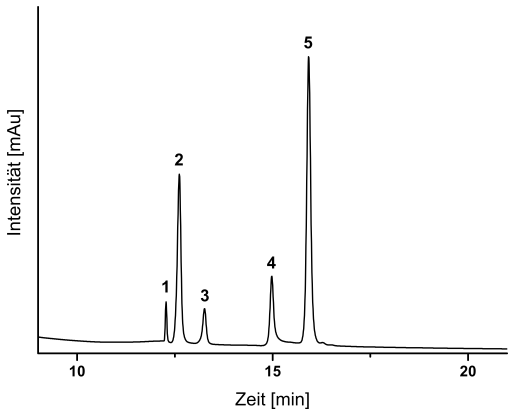
nung aller Aminosäuren konnte mit **MPSM8-C**$_{18}$ und **MPSM9-C**$_{18}$ erreicht werden. Die chromatographischen Eigenschaften beider Phasen sind vergleichbar, da sich ihre Partikelgröße und Porenparameter ähneln. Die Auflösung zwischen Arginin und Alanin ist bei **MPSM9-C**$_{18}$ erhöht, was auf die größere Oberfläche zurückzuführen ist. Auf **MPSM7-C**$_{18}$ und **MPSM10-C**$_{18}$ eluieren die letzten fünf Aminosäuren ineinander. Infolge der hohen spezifischen Oberfläche von **MPSM7** interagieren die Analyten länger mit der stationären Phase, was zu einer unvollständigen Trennung führt. Die agglomerierte Morphologie von **MPSM10** erschwert die Diffusion der Aminosäuren in die Poren und verbreitert die einzelnen Signals. Verschiedene wasserlöslichen Vitamine konnte mit Hilfe der Trennphase **MPSM12-C**$_{18}$ separiert werden (Publ. **IV**).



(a) Trennung von Ribonuklease A (**1**), Cytochrom C (**2**), holo-Transferrin (**3**) und Apomyoglobin (**4**).



(b) Trennung verschiedener Aminosäuren.



(c) Trennung von Vit. B_1 (**1**), B_3 (**2**), B_5 (**3**), B_9 (**4**) und B_{12} (**5**).

Abbildung 14: Beispielhafte Chromatogramme verschiedener Biomoleküle auf den synthetisierten Trennphasen. Chromatographische Einstellungen siehe: (**a**) Publ. **I**, (**b**) Publ. **III** und (**c**) Publ. **IV**.

4 Schlussfolgerung

Die mehrstufige Synthese mesoporöser Silica-Partikel im Mikrometermaßstab (*mesoporous silica microspheres*, MPSM), unter Verwendung der *hard template*-Methode, bietet verschiedene Einstellungsmöglichkeiten zur Steuerung der Partikel- und Poreneigenschaften. Die Ausgangsmaterialien bilden monodisperse *p*(GMA-*co*-EDMA)-Polymertemplate in denen, nach erfolgreicher Aminofunktionalisierung, Siliciumdioxid eingelagert wird. Das Entfernen der Organik erfolgt über Kalzinierung und übrig bleiben monodisperse MPSM. Die Porosität der *p*(GMA-*co*-EDMA), deren Funktionalisierungsgrad und die Einlagerung von SiO_2 unter verschiedenen Sol-Gel-Bedingungen mit Auswirkung auf die Eigenschaften der Silica-Materialien wurden genauer untersucht.

Die Poreneigenschaften der *p*(GMA-*co*-EDMA) werden über die Verhältnisse GMA:EDMA, Monomer:Porogen und Toluol:Cyclohexanol eingestellt. Mit Hilfe der statistischen Analyse wurde ein quantitatives Modell erstellt, welches die komplexen Wechselwirkungen der Verhältnisse zur Kontrolle der Porosität aufzeigt. Dadurch können *p*(GMA-*co*-EDMA)-Template mit gewünschten Poreneigenschaften maßgeschneidert hergestellt werden. Der Grad der Funktionalisierung und damit die Attraktivität der Polymertemplate gegenüber SiO_2 ist von der Anzahl an Epoxidgruppen abhängig. Die Einlagerung von Siliciumdioxid erfolgt durch die Anlagerung von Silica-Nanopartikeln (SNP) in den Poren. NMR-Spektroskopische Untersuchungen zeigen, dass der Partikelaufbau nicht in den Poren des Templats stattfindet. Die SNP werden in der kontinuierlichen Phase gebildet und von den Sol-Gel-Parametern Lösungsmittel, Alkoxysilan, Ammoniakkonzentration oder dem Verhältnis $^{n(H_2O)}/_{n(TEOS)}$ beeinflusst. Die Größe der eingebauten SNP steuert die Poreneigenschaften der resultierenden MPSM und hängt von folgenden Faktoren ab: (*i*) der Porosität der *p*(GMA-*co*-EDMA)-Template, (*ii*) der Diffusionsrate, welche über die elektrostatische Anziehung gesteuert wird und vom Grad der Funktionalisierung abhängt, und (*iii*) der Wachstumsgeschwindigkeit der SNP in der kontinuierlichen Phase.

Die Verwendung der Materialien als Trennphase in der Umkehrphasenchromatographie zur Separation von diversen Biomolekülen wurde erfolgreich dargelegt. Das Verständnis der Einflussfaktoren auf die Partikeleigenschaften der MPSM ermöglicht die Herstellung maßgeschneiderter poröser Silica-Partikel. Die individuelle Einstellung der Porenparameter eröffnet die Option, die Synthese entsprechend der gewünschten Applikation anzupassen.

5 Unveröffentlichte Ergebnisse

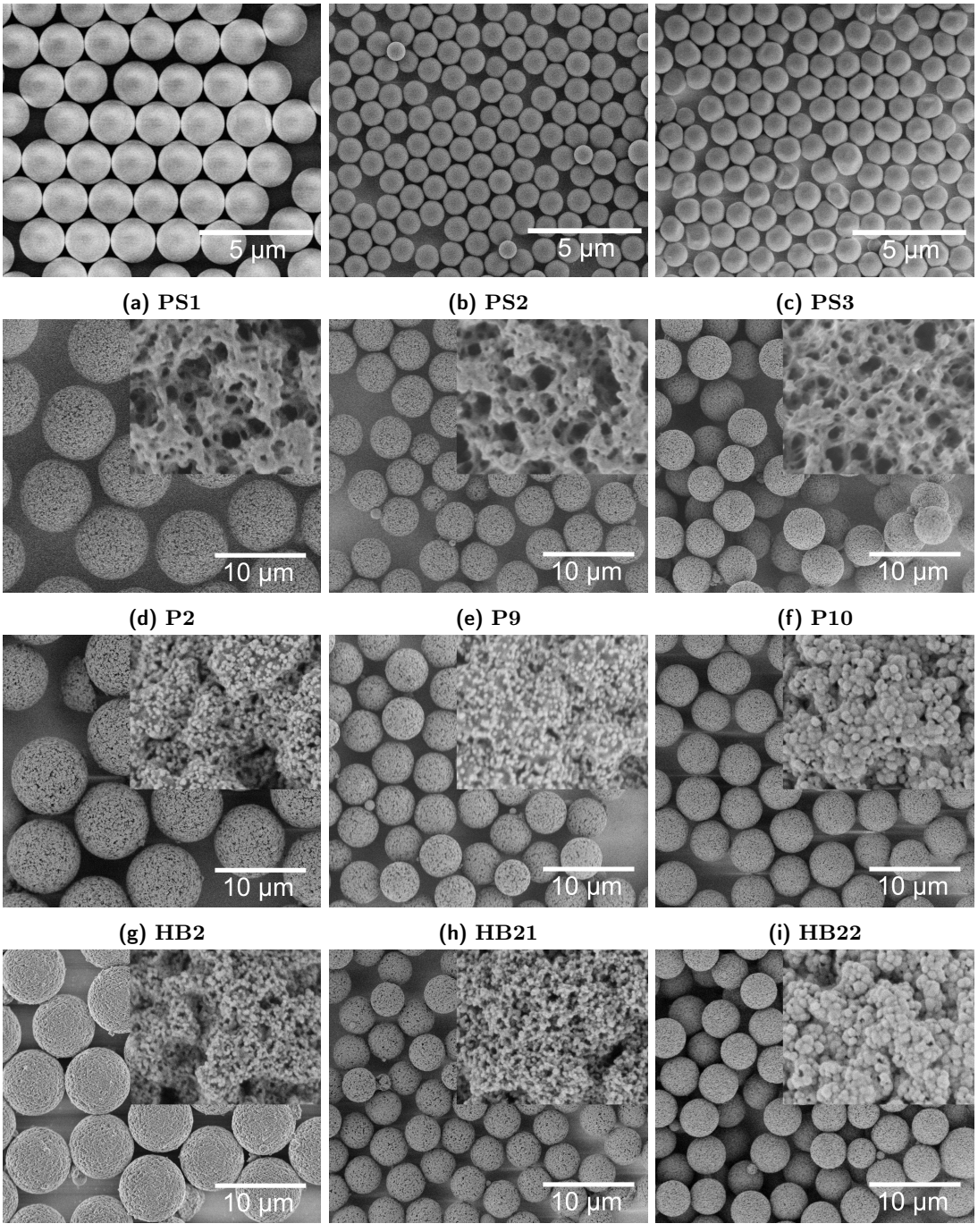
5.1 Polystyrol

Zur Darstellung monodisperser *p*(GMA-*co*-EDMA)-Template werden Polystyrol-Partikel (**PS**) mit einer engen Größenverteilung benötigt. Diese dienen als Saat-Partikel in Impfsuspensionspolymerisationen und beeinflussen die Partikeldurchmesser der Polymertemplate gemäß Gleichung 3.1. Insbesondere die Größe und die Dispersität der Polystyrol-Partikel haben direkten Einfluss auf die hergestellten *p*(GMA-*co*-EDMA)-Template. Neben der Größenvorgabe fungieren die Polystyrol-Partikel, als lineares Polymer, auch als Porogen in der vorgestellten Synthese der Polymertemplate.[70,81] Da die Partikelgröße und Porenstruktur der *p*(GMA-*co*-EDMA)-Template in direktem Zusammenhang mit den finalen MPSM stehen, beeinflusst bereits die Wahl der Saat-Partikel die Eigenschaften der resultierenden Silica-Partikel. Dispersionspolymerisationen ermöglichen monodisperse Saat-Partikel im Größenbereich von 0.1 µm und 10 µm. Die Polymerisation von Styrol erfolgt unter Verwendung eines Reaktionsgemischs, bestehend aus Monomer, Initiator und Stabilisator in der kontinuierlichen Phase. In den meisten Fällen werden Alkohole oder ein Gemisch aus Alkohol und H_2O als Reaktionsmedium eingesetzt. Die Einstellung der Syntheseparameter steuert die Größe und Dispersität der Polystyrol-Partikel. In diesem Abschnitt werden drei verschiedene Polystyrol-Batches (**PS1 − PS3**) unterschiedlicher Syntheseeinstellungen miteinander verglichen sowie der Einfluss auf die *p*(GMA-*co*-EDMA)-Template und die resultierenden MPSM diskutiert.

Tabelle 1: Partikeleigenschaften der Polystyrol-Partikel **PS1 − PS3** und die daraus resultierenden *p*(GMA-*co*-EDMA)-Template **P**.

	d_{50} [µm]	d_{90}/d_{10}	M_w [$\frac{g}{mol}$]		d_{50} [µm]	d_{90}/d_{10}	Φ [nm]	V_P [$\frac{mL}{g}$]	a_{BET} [$\frac{m^2}{g}$]
PS1	1.94	1.06	53329	**P2**	7.76	1.17	12.6	0.19	123
PS2	1.06	1.12	65457	**P9**	4.54	1.08	13.1	0.18	107
PS3	1.07	1.17	14929[33]	**P10**	4.07	1.19	11.2	0.21	131

Die statistische Untersuchung der Reaktionsbedingungen mit Einfluss auf die Größe und Dispersität der Polystyrol-Partikel wurde in Zusammenarbeit mit Steinbach getätigt und ausführlich erläutert.[111] Die verschiedenen Reaktionsbedingungen für **PS1**, **PS2** und **PS3** führen zu unterschiedlichen Molekulargewichten und Partikeldurchmessern (Abb. 15a − c). Die Größen und Molekulargewichte der Polystyrol-Partikel sind in Tabelle 1 aufgelistet. Die Umsetzung der Saat-Partikel zu *p*(GMA-*co*-EDMA)-Templaten wurde unter den gleichen Reaktionsbedingungen durchgeführt. Alle Polymertemplate quellen auf circa die vierfache Größe ihrer Polystyrol-Partikel an und weisen poröse Strukturen auf (Abb. 15d − f).



(a) PS1 **(b) PS2** **(c) PS3**

(d) P2 **(e) P9** **(f) P10**

(g) HB2 **(h) HB21** **(i) HB22**

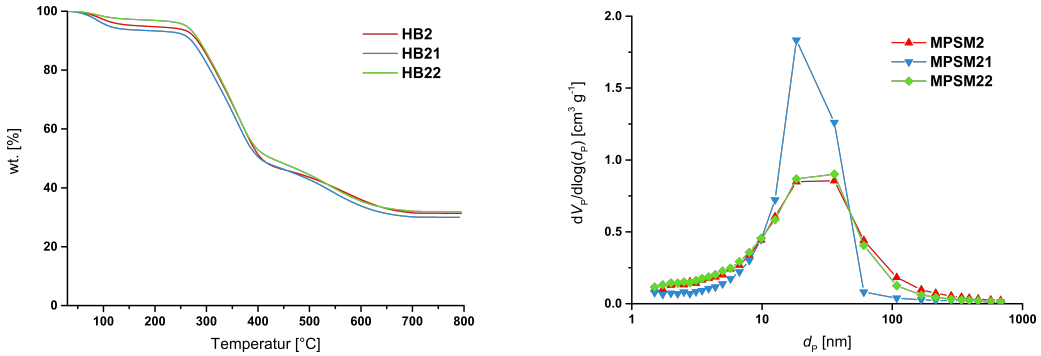
(j) MPSM2 **(k) MPSM21** **(l) MPSM22**

Abbildung 15: REM-Aufnahmen der Polystyrol-Partikel **PS1** – **PS3** und daraus resultierende *p*(GMA-*co*-EDMA)-Template **P**, Hybrid-Partikel **HB** und Silica-Partikel **MPSM**. Entsprechende Oberflächen sind im rechten oberen Quadranten abgebildet. REM-Konditionen: 2,000 × (**P**, **HB**, **MPSM**) bzw. 5,000 × (**PS**); 50,000 ×.

Tabelle 2: Fortsetzung von **Tabelle 1**. Partikeleigenschaften der Hybrid- (**HB**) und Silica-Partikel (**MPSM**).

	d_{50} [µm]	d_{90}/d_{10}	SiO_2 wt. [%]		d_{50} [µm]	d_{90}/d_{10}	Φ [nm]	V_P [$\frac{mL}{g}$]	a_{BET} [$\frac{m^2}{g}$]
HB2	8.31	1.05	30.0	**MPSM2**	6.83	1.24	19.2	0.56	252
HB21	4.38	1.11	31.3	**MPSM21**	3.85	1.19	17.4	0.81	265
HB22	4.62	1.13	31.8	**MPSM22**	3.97	1.17	18.2	0.56	285

Die Porengrößen der Template **P2**, **P9** und **P10** unterscheiden sich um wenige Nanometer, das Porenvolumen sowie die spezifische Oberfläche liegen im ähnlichen Größenbereich (Tabelle 1). Die Morphologie der *p*(GMA-*co*-EDMA)-Template ähnelt den bisherigen Beobachtungen der Polymer-Partikel. Nach erfolgreicher Funktionalisierung mit TEPA erfolgte die Einlagerung von SiO_2 in einem basisch katalysierten Sol-Gel-Prozess in 2-PrOH und H_2O. Die Anlagerung der *in situ* gebildeten SNP ist für alle drei funktionalisierten Template optisch erkennbar (Abb. 15g − i). Aufgrund der Anlagerung nehmen die Partikelgrößen der Hybrid-Partikel zu. Thermogravimetrische Analysen von **HB2**, **HB21** und **HB22** zeigen, dass unabhängig vom Polymer, 30 % SiO_2 eingelagert wird (Abb. 16a). Interessanterweise variiert die Größe der SNP je nach verwendetem *p*(GMA-*co*-EDMA)-Templat. Die Hybrid-Partikel **HB2** und **HB21** weisen Silica-Nanopartikel mit einer Größe von $\sim$ 20 nm auf, während für **HB22** Silica-Nanopartikel der Größe von $\sim$ 38 nm beobachtet werden. Nach der Kalzinierung verbleiben sphärische mesoporöse Silica-Materialien (Abb. 15j − l). Die Partikel **MPSM2** und **MPSM21** schrumpfen auf 85 % ihrer ursprünglichen Templatgröße zusammen. **MPSM22** behält zu 98 % die Größe von **P10** bei. Die Porenparameter der MPSM steigen im Vergleich zu den *p*(GMA-*co*-EDMA)-Templaten drastisch an (Tab. 1 und Tab. 2). Die finalen Silica-Partikel besitzen Porengrößen zwischen 17 − 19 nm mit engen Porengrößenverteilungen und spezifischen Oberflächen von 250 − 285 m^2/g (Abb. 16b). Das Porenvolumen von **MPSM2** und **MPSM22** erhöht sich auf 0.56 mL/g, während es für **MPSM21** auf 0.81 mL/g ansteigt. Die polymeren Strukturen der Porenwände der *p*(GMA-*co*-EDMA)-Template verschwinden bei der Kalzinierung und bilden neue Hohlräume zwischen den angelagerten SNP. Diese neu generierten Zwischenräume führen zu einem Anstieg im Porenvolumen.



(a) Thermogravimetrische Analysen der Hybrid-Partikel **HB2**, **HB21** und **HB22**.

(b) Porengrößenverteilung der Silica-Partikel **MPSM2**, **MPSM21** und **MPSM22**.

Abbildung 16: TGA-Messungen der Hybrid-Partikel **HB2**, **HB21** und **HB22** (links) und Porengrößenverteilungen der Silica-Partikel **MPSM2**, **MPSM21** und **MPSM22** (rechts) ausgewertet nach BJH-Methode.

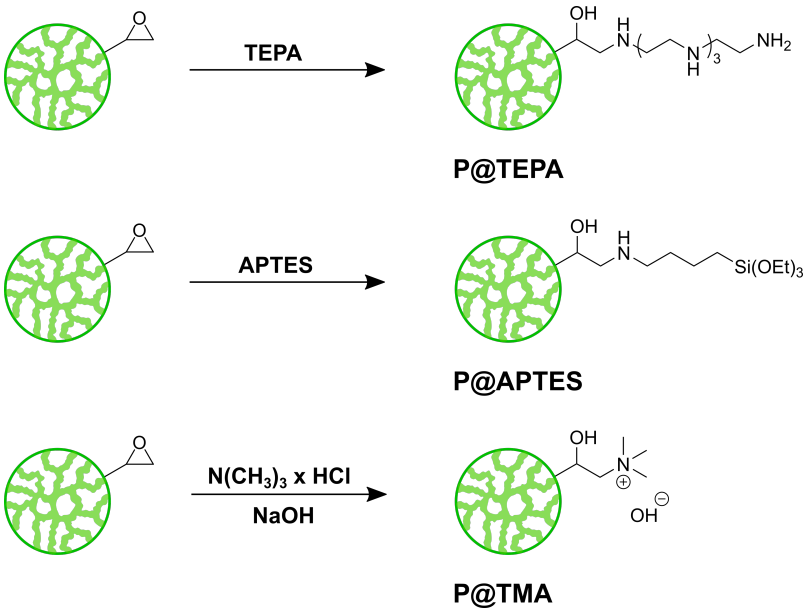
Schlussfolgerung

Bereits die Wahl der Saat-Partikel hat großen Einfluss auf die Partikeleigenschaften der MPSM. Mit Hilfe verschiedener Synthesetechniken kann die Größe der Polystyrol-Partikel gezielt gesteuert werden. Wie bereits in den Arbeiten von Wagner[33] festgestellt, gibt der Partikeldurchmesser der Saat-Partikel die Größe der *p*(GMA-*co*-EDMA)-Template vor. Der Einfluss von Polystyrol als Porogen verhält sich bei den verwendeten Reaktionsbedingungen gering. Trotz unterschiedlicher Molekulargewichte der PS liegen die Porenparameter der Polymertemplate in der gleichen Größenordnung. Die daraus resultierenden mesoporösen Silica-Partikel bilden ihre Template nahezu vollständig ab. Folgend kann festgehalten werden, dass insbesondere die Partikelgröße der finalen Silica-Materialien mit der Wahl der Polystyrol-Partikel definiert wird.

5.2 Aminofunktionalisierungen von *p*(GMA-*co*-EDMA)-Templaten und *semi-batch*-Verfahren im Sol-Gel-Prozess

Die Funktionalisierung von *p*(GMA-*co*-EDMA)-Templaten erfolgt durch einen nukleophilen Angriff auf die Glycidylfunktion der Partikel. Bisherige Ergebnisse von verschiedenen Arbeitsgruppen zeigen erfolgreiche Abbildungen der porösen Polymertemplate mit aminofunktioneller Oberfläche als Zwischenstufe, in der Synthese von porösen Silica-Materialien.[33–37, 102] Die Epoxidfunktionen der *p*(GMA-*co*-EDMA)-Template werden durch Ringöffnungsreaktionen zu Aminoalkoholen umgesetzt. Die Funktionalisierung mit Aminoreagenzien erhöht die Polarität der Polymertemplate und gewährt eine Affinität gegenüber den *in situ* gebildeten SNP. Unter basischen Bedingungen liegen die Aminogruppen teilweise protoniert vor und weisen eine positive Oberflächenladung auf. Die negativ geladenen Silica-Spezies diffundieren aufgrund der elektrostatischen Anziehung in die Poren des funktionalisierten Templats und lagern sich an. Die Diffusionsgeschwindigkeit der SNP wird über die Potentialdifferenz von aminofunktionalisierten Templaten und in Lösung entstehenden Silica-Spezies gesteuert. Der Einfluss von verschiedenen Funktionalisierungen auf die Einlagerung von SiO_2 und Auswirkungen auf die Porenparameter der MPSM werden im Nachfolgenden diskutiert. Als Reagenzien wurde die bereits in der Literatur untersuchten Tetraethylenpentamin (TEPA), (3-Aminopropyl)triethoxysilan (APTES) und Trimethylammoniumchlorid (TMA) verwendet (Schema 4).[36, 37] Der darauffolgende Sol-Gel-Prozess wurde mit einer einmaligen Zugabe von TEOS in Anwesenheit der aminofunktionalisierten Template (**P2@TEPA**, **P9@APTES**, **P11@TMA**) durchgeführt und bildete die Hybrid-Partikel **HB2**, **HB9** und **HB23**. Alternativ wurde die stufenweise Zugabe einer verdünnten TEOS-Lösung (10 v.% in 2-PrOH) als *semi-batch*-Verfahren untersucht. Hierfür wurde das *p*(GMA-*co*-EDMA)-Templat **P11** als Ausgangsmaterial verwendet und analog zu den anderen Materialien aminofunktionalisiert. Aus **P11@TEPA**, **P11@APTES** und **P11@TMA** resultieren die Hybrid-Partikel **HB24** − **HB26**.

Die erfolgreiche Synthesen von **P11@TEPA**, **P11@APTES** und **P11@TMA** konnten über diffuse Reflexions-Fouriertransformationsinfrarotspektroskopie (DRIFT), Festkörper-NMR-Spektroskopie und Elementaranalysen nachgewiesen werden. Die DRIFT-Spektren der funktionalisierten *p*(GMA-*co*-EDMA)-Template zeigen eine Abnahme der Intensität der Bande um 908 cm^{-1}, welche charakteristisch für die Epoxidgruppe ist (Abb. 17). Durch Funktionalisierung der Epoxidfunktion entstandene Aminoalkohole weisen Banden bei 1160 cm^{-1} und 1265 cm^{-1} auf, welche den Schwingungen der C−N-Bindung zugeordnet werden können. Die intensiven Banden zwischen 3700 cm^{-1} und 3100 cm^{-1} resultieren aus den Schwingungen benachbarter OH- und NH-Gruppen (Abb. 17).[33, 112] Die Methylgruppen der Trimethylammonium-Funktionalisierung führen zu einer intensiveren Bande bei 1480 cm^{-1}.[36] Während die Methingruppe der Epoxidfunktion im ^{13}C-CP/MAS-NMR-Spektrum bei 48.3 ppm für das unfunktionalisierte Templat noch



Schema 4: Schematische Darstellung verschiedener Funktionalisierungen von *p*(GMA-*co*-EDMA)-Templaten mit entsprechender aminierter Oberfläche.

deutlich zu erkennen ist, nimmt die Intensität des Signals nach der Funktionalisierung ab (Abb. 17). Insgesamt ähneln sich die Spektren, da die chemische Zusammensetzung der Template bis auf die Funktionalisierung gleich ist. Die Signale der Methylengruppen von **P11@TEPA** liegen unterhalb der bereits vorhandenen Signale des *p*(GMA-*co*-EDMA)-Templats. Für **P11@APTES** ist die CH_2-Gruppe der Propylkette, welche direkt am Si-Atom liegt, schwach bei 9.8 ppm zu erkennen. Die positive Ladung am Stickstoff-Atom für **P11@TMA** führt zu einer chemischen Verschiebung der Methylgruppen von TMA zu 54.6 ppm. Im Fall von **P11@APTES** sind die T-Gruppen Signale der Triethoxysilan-Funktion im ^{29}Si-CP/MAS-Spektrum wieder zu finden (Abb. 17). Die Elementaranalysen der Partikel zeigen einen Stickstoffanteil von 2.75 % (**P11@TEPA**), 1.04 % (**P11@APTES**) und 1.85 % (**P11@TMA**) und indizieren ebenfalls eine erfolgreiche Anbindung der Aminoreagenzien. Das Messen der Zeta-Potentiale, als Nachweis der positiven Oberflächenladung der funktionalisierten Template, konnte wegen der schnellen Sedimentation der Partikel nicht durchgeführt werden. Aufgrund dessen werden die von Bai *et al.* veröffentlichten Werte für **P@TEPA** (4.42 mV), **P@APTES** (1.99 mV), **P@TMA** (3.52 mV) und SNP (− 2.84 mV) als Orientierung verwendet.[37]

Die Anlagerung der im Reaktionsmedium gebildeten SNP erfolgt aufgrund der Potentialdifferenz zwischen reaktiven Silica-Spezies und funktionalisiertem Templat. Die Zeta-Potentiale nehmen von **P@TEPA** > **P@TMA** > **P@APTES** ab. Aufgrund der gleichen Reaktionsbedingungen zur Herstellung des Polymertemplats und während des Sol-Gel-Prozesses, wird die Einlagerung von SiO_2 über die Funktionalisierung gesteuert. Entgegen der Beobachtungen von Chen *et al.*[36] und Bai *et al.*[37] lagern sich bei dem

Tabelle 3: Partikel- und Poreneigenschaften der Hybrid- (**HB**) und Silica-Partikel (**MPSM**).

	d_{50} [µm]	d_{90}/d_{10}	SiO_2 wt. [%]		d_{50} [µm]	d_{90}/d_{10}	Φ [nm]	V_P $[\frac{mL}{g}]$	a_{BET} $[\frac{m^2}{g}]$
HB2	8.31	1.05	30.0	**MPSM2**	6.83	1.24	19.2	0.56	252
HB9	8.34	1.07	28.6	**MPSM9**	7.12	1.21	20.3	0.48	314
HB23	8.09	1.18	32.8	**MPSM23**	7.67	1.10	17.4	0.73	441
HB24	8.55	1.07	28.6	**MPSM24**	6.84	1.10	16.3	0.69	348
HB25	8.28	1.07	32.0	**MPSM25**	7.14	1.12	16.8	0.66	420
HB26	8.22	1.14	30.2	**MPSM26**	7.10	1.16	14.3	0.86	530

(3-Aminopropyl)triethoxysilan funktionalisierten Templat, trotz des geringsten Zeta-Potentials, die größten SNP mit einer Größe von ∼28 nm an (**HB9**, Abb. 18e). Die Größe der SNP mit **P2@TEPA** als Ausgangstemplat beträgt ∼20 nm (**HB2**, Abb. 18a) und für **P11@TMA** ∼14 nm (**HB23**, Abb. 18i). Aufgrund der Ein- und Anlagerung von SNP nimmt die Größe der Hybrid-Partikel im Vergleich zum Polymertemplat zu.
Der eingelagerte SiO_2-Gehalt wurde mittels thermogravimetrischen Analysen bestimmt und liegt für die hier vorgestellten Hybrid-Partikel bei ca. 30 % (Tabelle 3). Dies ist auf die gleichen Reaktionsbedingungen des Sol-Gel-Prozesses zurückzuführen. Die nach der Kalzinierung resultierenden Silica-Partikel **MPSM2**, **MPSM9** und **MPSM23** liegen monodispers vor. Während der Kalzinierung werden vorhandene Silanol-Gruppen zu Siloxanen verknüpft, das zu einem Schrumpfen der Silica-Partikel führt. Verglichen mit dem jeweiligen Polymer bildet **MPSM23** das Templat zu 96 %, **MPSM9** zu 93 % und **MPSM2** zu 88 % ab. Die Größe der eingelagerten Silica-Nanopartikel beeinflusst die Poreneigeschaften der MPSM. Im Vergleich zu den anderen weist **MPSM9** die größten Poren mit 20.3 nm und das geringste Porenvolumen mit 0.48 $^{mL}/_{g}$ auf. Entsprechend der abnehmenden Silica-Nanopartikelgröße nehmen die Porengrößen von **MPSM2** (19.2 nm) und **MPSM23** (17.4 nm) ab und die Porenvolumina (0.56 $^{mL}/_{g}$ bzw. 0.73 $^{mL}/_{g}$) zu. Die spezifischen Oberflächen setzen sich aus den Parametern Porengröße und Porenvolumen zusammen. Kleine Poren und hohes Porenvolumen führen zu einer großen Oberfläche, wohingegen große Poren und niedrige Volumina in geringen Oberflächen resultieren. Folglich besitzt **MPSM23** die größte spezifische Oberfläche, gefolgt von **MPSM9** und **MPSM2**.

Semi-batch-Verfahren werden im Sol-Gel-Prozess verwendet, um größere Silica-Partikel zu generieren. Aufgrund der fortlaufenden Zugabe von Alkoxysilanen wird die Anzahl an Si-Oligomer-Keimen gering gehalten, sodass diese ein stärkeres Wachstum erfahren. In Anwesenheit der aminofunktionalisierten Template werden die gebildeten Silica-Spezies zu einem frühen Stadium der kontinuierlichen Phase entnommen und lagern sich im Templat an. Eine 10 %-ige TEOS in 2-PrOH wurde mit 0.2 $^{mL}/_{min}$ zu den funktionalisierten

Partikeln **P11@TEPA**, **P11@APTES** und **P11@TMA** dosiert. Die Hybrid-Partikel **HB24**, **HB25** und **HB26** zeigen die sich anlagernden Silica-Nanopartikel in Abb. 18b, 18f und 18j. Die Hybrid-Partikel weisen erneut einen SiO_2-Gehalt von $\sim 30\,\%$ auf (Tab. 3). Die Partikelgröße der SNP ist im Vergleich zu der einmaligen Zugabe geringer und folgt dem zuvor beobachteten Trend der Aminoreagenzien. Wie bereits zuvor steuern die eingelagerten SNP die Porenparameter der nach der Kalzinierung entstandenen Silica-Partikel. Aufgrund der geringeren Größe fallen die Porengrößen von **MPSM24** – **MPSM26** kleiner aus. Im Gegensatz dazu steigen die Volumina auf bis zu $0.86\ {}^{\mathrm{mL}}/_{\mathrm{g}}$ und die spezifischen Oberflächen auf $530\ {}^{\mathrm{m}^2}/_{\mathrm{g}}$.

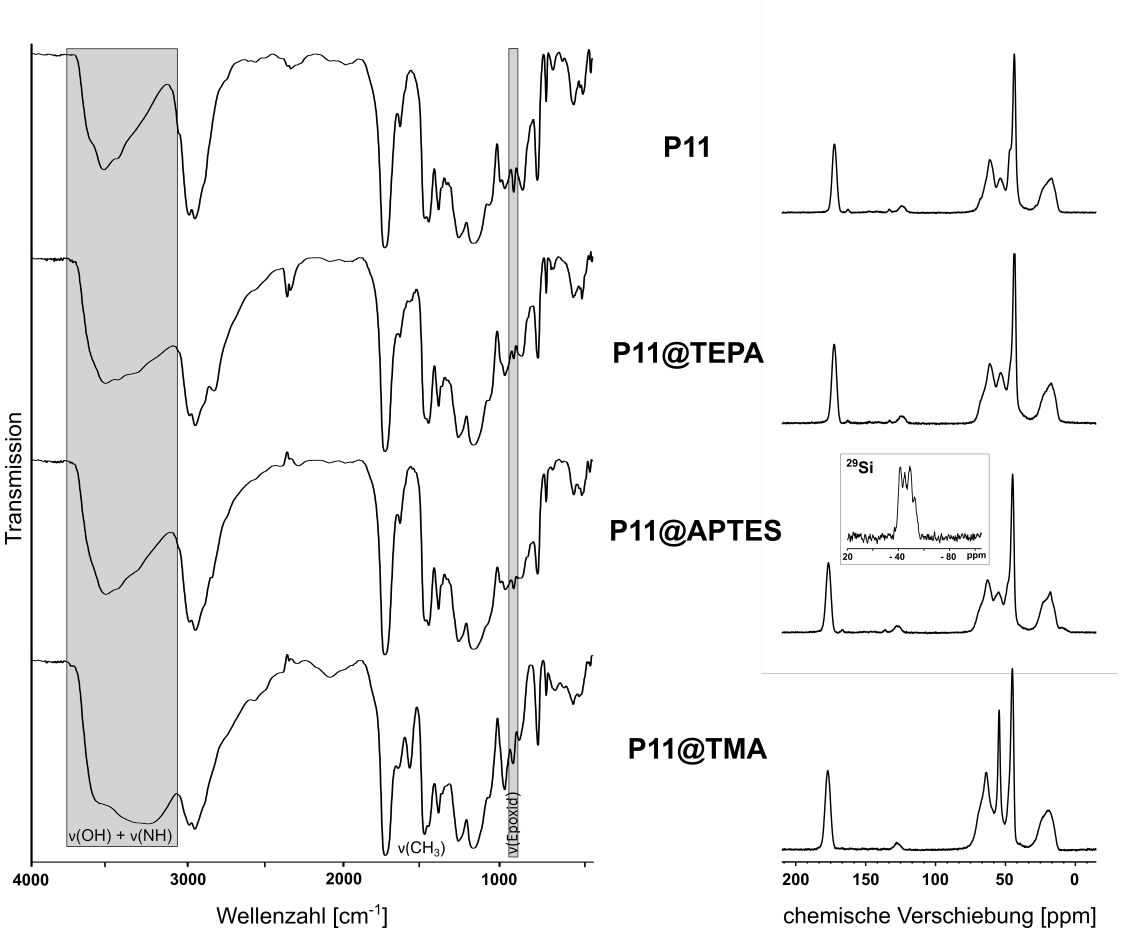
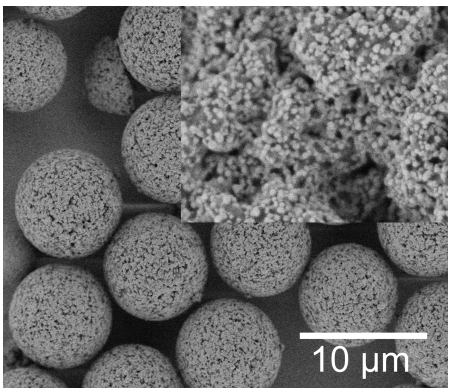
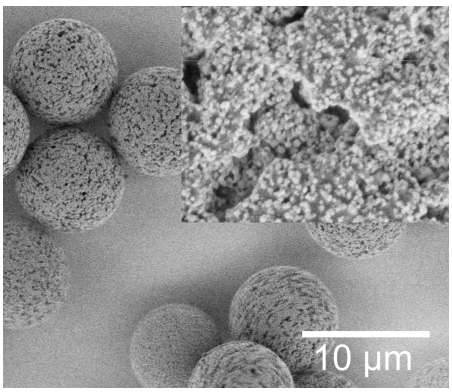


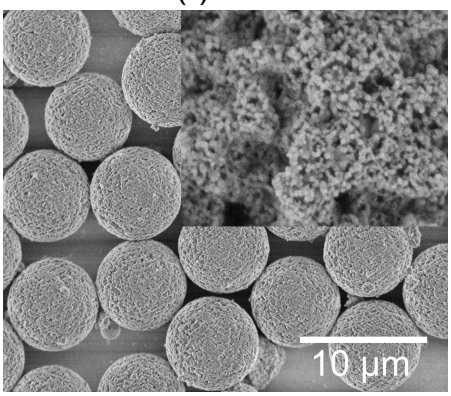
Abbildung 17: DRIFT- (links) und ^{13}C-CP/MAS-NMR-Spektren (rechts) der *p*(GMA-*co*-EDMA)-Template **P11**, **P11@TEPA**, **P11@APTES** und **P11@TMA**. Abnahme der Epoxidbande ($908\,\mathrm{cm}^{-1}$) und Zunahme der OH- und NH-Schwingungen ($3700\,\mathrm{cm}^{-1} - 3000\,\mathrm{cm}^{-1}$) in den DRIFT-Spektren grau hinterlegt.



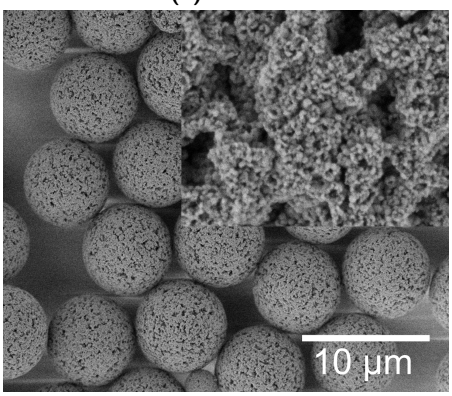
(a) HB2



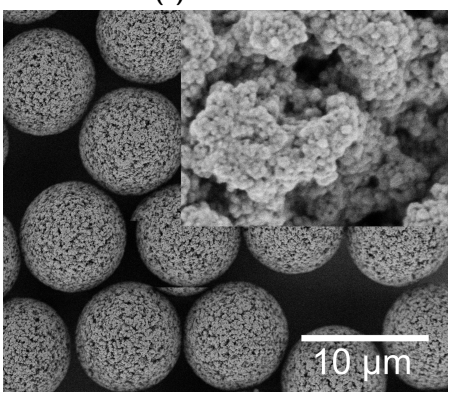
(b) HB24



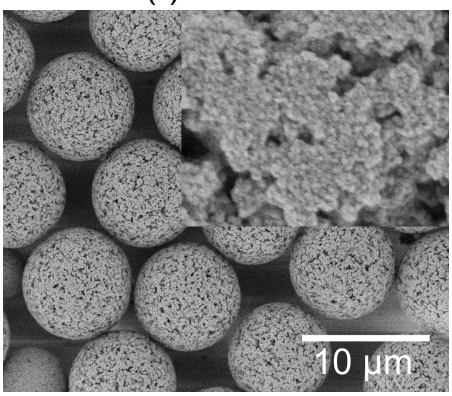
(c) MPSM2



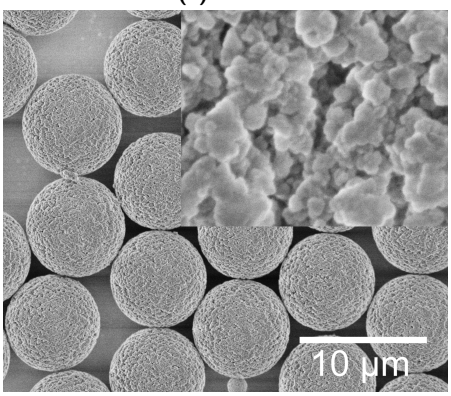
(d) MPSM24



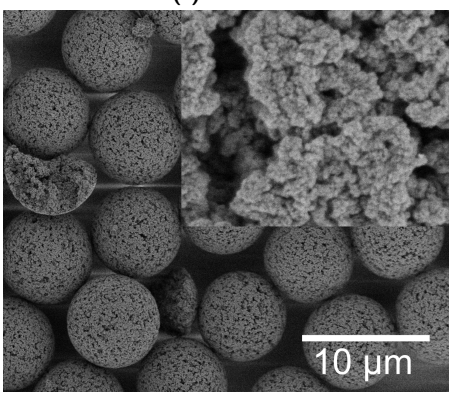
(e) HB9



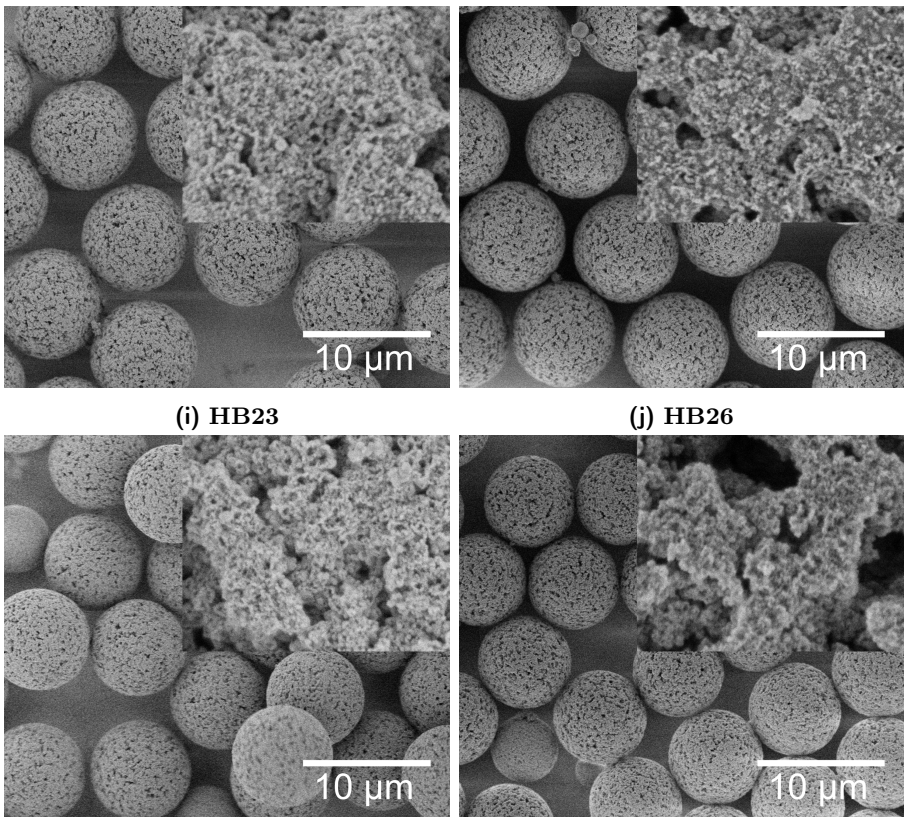
(f) HB25



(g) MPSM9



(h) MPSM25



(i) HB23 **(j) HB26**

(k) MPSM23 **(l) MPSM26**

Abbildung 18: REM-Aufnahmen der Hybrid-Partikel **HB2**, **HB9**, **HB23** – **HB26** und daraus resultierende Silica-Partikel **MPSM2**, **MPSM9**, **MPSM23** – **MPSM29**. Entsprechende Oberflächen sind im rechten oberen Quadranten abgebildet. REM-Konditionen: 2,000 ×; 50,000 ×.

Ohne vorherige Funktionalisierung der *p*(GMA-*co*-EDMA)-Template weisen diese keine Attraktivität gegenüber den SNP auf. Als Folge wachsen die Nanopartikel in der kontinuierlichen Phase $> 100\,\text{nm}$ und lagern sich vereinzelt an die Außenfläche des Templats an. Nach der Kalzinierung verbleiben instabile hohle Hüllen bestehend aus großen SNP. Die Hydroxylierung der Epoxidfunktion mit Schwefelsäure erzeugt Diole an der Oberfläche. Meyer *et al.* berichtet von der Notwendigkeit von Hydroxy- oder Aminogruppen zur Einlagerung von SiO_2 in Polymerpartikeln basierend auf Polystyrol und Divinylbenzol.[32] Im Fall von rehydroxylierten *p*(GMA-*co*-EDMA)-Templaten wird das gleiche Phänomen wie bei unfunktionalisierten Polymertemplaten beobachtet (Abb. 19). Die Anziehungskraft der rehydroxylierten Template reicht nicht aus, um die gebildeten SNP aufzunehmen. Die zu groß gewachsenen Silica-Nanopartikel können nicht mehr aufgenommen werden und bilden eine Schicht um das Templat. Resultierend daraus entstehen ebenfalls leere Hüllen nach der Entfernung der Organik.

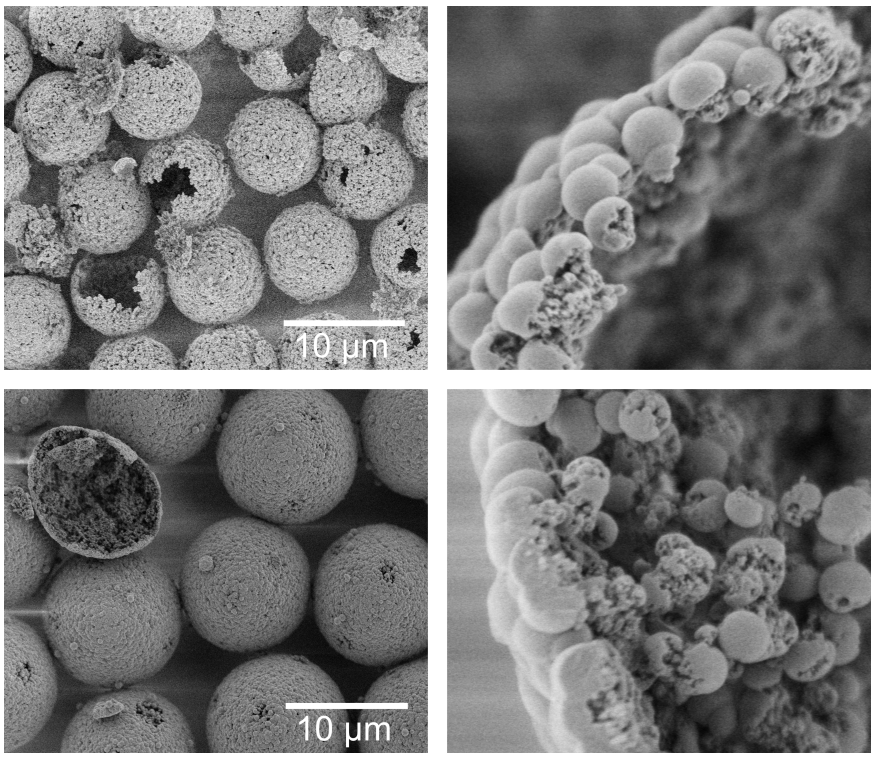


Abbildung 19: REM-Aufnahmen von Silica-Partikeln nach Durchführung des Sol-Gel Prozesses in Anwesenheit unfunktionalisierter *p*(GMA-*co*-EDMA)-Template (obere Reihe) und hydroxylierter *p*(GMA-*co*-EDMA)-Template (untere Reihe). REM-Konditionen: 2,000 ×; 50,000 ×.

Schlussfolgerung

Die Funktionalisierung der *p*(GMA-*co*-EDMA)-Template mit Aminoreagenzien zur Einlagerung von SiO_2 in Form von Silica-Nanopartikeln ist essenziell. Unter basischen Bedingungen besitzen die funktionalisierten Polymere eine positives Zeta-Potential, während die gebildeten SNP negativ vorliegen. Aufgrund der Potentialdifferenz diffundieren diese in die Poren des Templats und lagern sich an. Mit den verwendeten Funktionalisierungsreagenzieren ist eine monodisperse Abbildung des porösen Templats als mesoporöse Silica-Partikel möglich. Hingegen der Erwartung korreliert die Größe der eingebauten SNP nicht mit den Potentialunterschieden. In (3-Aminopropyl)triethoxysilan funktionalisierte *p*(GMA-*co*-EDMA)-Template werden die größten SNP eingebaut, gefolgt von Tetraethylenpentamin und Trimethylammoniumchlorid. Resultierend aus der SNP-Größe werden die größten Poren und das geringste Porenvolumen bei **MPSM9** beobachtet. Die stufenweise Zugabe von TEOS als *semi-batch*-Verfahren führt zu insgesamt kleineren angelagerten SNP und folglich zu geringeren Porenparametern der MPSM. Die Abbildung des porösen Templats ist weiterhin gewährleistet. Der Einbau von SiO_2 in unfunktionalisierte bzw. als Diol vorliegende *p*(GMA-*co*-EDMA)-Template blieb erfolglos.

5.3 Synthese poröser Template auf Basis von Vinyltriethoxysilan

Die Synthese von mesoporösen Silica-Partikeln auf Grundlage von *p*(GMA-*co*-EDMA)-Templaten benötigt als Zwischenschritt die Aminofunktionalisierung der Epoxidfunktion, um die Attraktivität gegenüber Silica-Nanopartikeln zu ermöglichen. Eine Substitution von Glycidylmethacrylat, durch eine Verbindung mit entsprechender funktioneller Gruppe zur Polymerisation und Attraktivität gegenüber SNP, verkürzt das Syntheseschema der MPSM. Erste innovative Versuche mit Vinyltrimethoxysilan (VTMOS) zeigten vielversprechende Ergebnisse.[33] Die Polymerisation mit EDMA kann mittels der Vinyl-Gruppe erzielt werden, während die Trimethoxysilan-Funktion als Linker für Silica-Spezies fungieren soll. Nach dem Quellvorgang werden eine Vielzahl unerwünschter poröser Sekundär-Partikel beobachtet. Diese entstehen aufgrund der Hydrolyse und Kondensation von VTMOS, welche als Nebenreaktionen während dem Quellprozess ablaufen.[33]
Im folgenden Abschnitt wird der Quellvorgang mit Vinyltriethoxysilan (VTEOS) als Monomer analog zu den *p*(GMA-*co*-EDMA)-Templaten (VTEOS/EDMA: 40 v.%/60 v.%; Monomer/Porogen: 50 v.%/50 v.%) durchgeführt und die resultierenden Polymer-Partikel (**V-PB**) charakterisiert. Die Erweiterung der Alkoxygruppen des Vinylsilans um eine CH_2-Gruppe reduziert die Hydrolysegeschwindigkeit des Monomers und soll die Hydrolyse und Kondensation von VTEOS unterdrücken. Zusätzlich wurde eine Versuchsreihe mit der Zugabe von Natriumnitrit durchgeführt. Dieses dient als Radikalfänger in der wässrigen Phase und soll erneute Polymerisationen außerhalb der Saat-Partikel verhindern. Abbildung 20 zeigt die erfolgreiche Herstellung poröser Polymer-Partikel (**V-PB1**) auf Basis von VTEOS. Das Templat besitzt überwiegend einen Durchmesser von 7.73 µm und erreicht damit vergleichbare Werte wie das GMA-Analogon. Zusätzlich werden einige kleinere poröse Partikel beobachtet, welche im Folgenden als Sekundärpartikel bezeichnet werden.

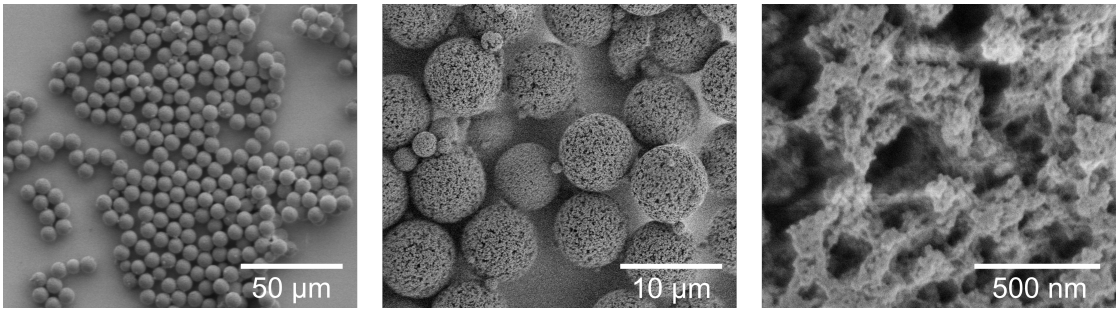


Abbildung 20: REM-Aufnahmen von porösen Polymer-Partikeln **V-PB1** auf Basis von Vinyltriethoxysilan. REM-Konditionen: 400 ×; 2,000 ×; 50,000 ×.

Mit der Einführung der Triethoxysilan-Funktion entfällt die notwendige Funktionalisierung der Polymertemplate, sodass der basenkatalysierte Sol-Gel-Prozess in Anwesenheit von **V-PB1** durchgeführt werden kann. Die dadurch entstehenden Hybrid-Partikel **V-HB1** weisen die Anlagerung einer Vielzahl an nicht porösen Silica-Nanopartikel auf (Abb. 21). Der Partikeldurchmesser von **V-HB1** bleibt im Vergleich zum Templat gleich. Die zuvor beobachteten Sekundärpartikel zeigen gleichermaßen die Anlagerung von SNP. Die thermogravimetrischen Analysen von **V-PB1** und **V-HB1** bestätigen den erfolgreichen Einbau der SNP durch einen Anstieg des SiO_2-Gehalts von 5 % auf 33 % (Abb. 22a). Nach der Kalzinierung verbleiben die porösen Silica-Materialien **V-MPSM1** und schrumpfen weitgehend auf 5.45 µm zusammen. Die Morphologie von **V-MPSM1** besteht aus einer Vielzahl von SNP (Abb. 23). Kleinere poröse Silica-Partikel, resultierend aus den Sekundärpartikeln, die während der Impfsuspensionspolymerisation von **V-PB1** entstehen, können ebenfalls beobachtet werden. Anschließende Aufreinigungstechniken, wie Zentrifugation oder Sedimentation in 2-Propanol zum Entfernen der Sekundärpartikel, blieben ohne Erfolg. Aufgrund der Polydispersität von **V-MPSM1** ergibt sich eine breite bimodale Verteilung des Porennetzwerks (Abb. 22b).

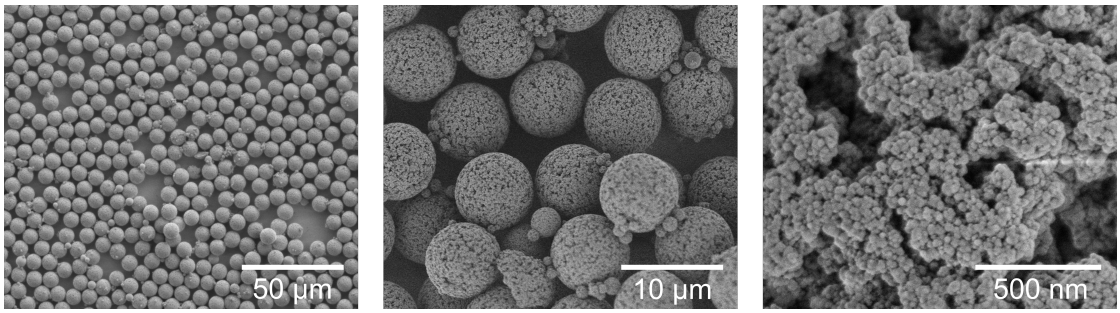
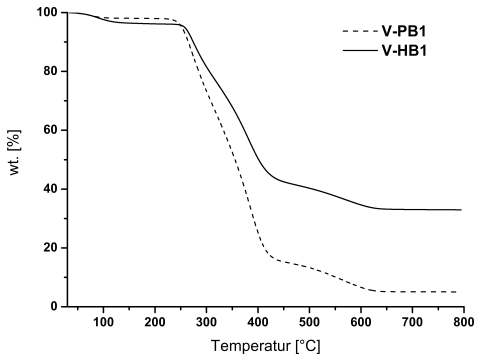
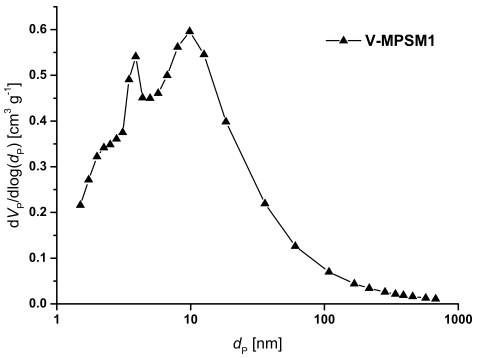


Abbildung 21: REM-Aufnahmen der Hybrid-Partikel **V-HB1** resultierend aus dem Sol-Gel Prozess in Anwesenheit von **V-PB1**. REM-Konditionen: 400 ×; 2,000 ×; 50,000 ×.



(a) Thermogravimetrische Analysen der Partikel **V-PB1** und **V-HB1**.



(b) Porengrößenverteilung der Silica-Partikel **V-MPSM1**.

Abbildung 22: TGA-Messungen der Polymer- u. Hybrid-Partikel **V-PB1** u. **V-HB1** (links) und Porengrößenverteilung der Silica-Partikel **V-MPSM1** (rechts) ausgewertet nach BJH-Methode.

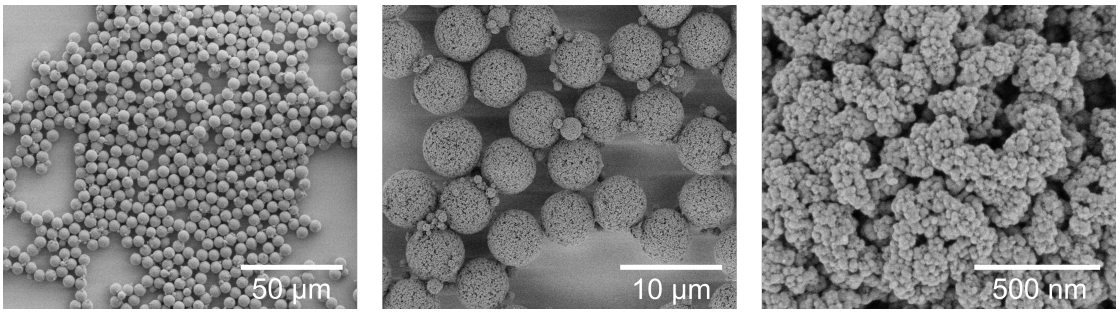


Abbildung 23: REM-Aufnahmen der Silica-Partikel **V-MPSM1** nach Kalzination von **V-HB1**. REM-Konditionen: 400 ×; 2,000 ×; 50,000 ×.

Abbildung 24 zeigt das ^{13}C-CP/MAS-NMR-Spektrum von **V-PB1**. Das polymere Gerüst der Partikel äußert sich in den Signalen bei 18 ppm (**3**), 45 ppm (**1**) und 56 ppm (**2**). Die chemische Verschiebung der Methylengruppen von EDMA liegen bei 59 ppm (**5**) und fallen mit dem quartären C-Atom des Polymergerüsts zusammen. Die Carbonylgruppen unterscheiden sich jeweils in ihrer chemischen Umgebung. Die Carbonylgruppe, welche direkt am polymeren Rückgrat hängt, bildet ein intensives Signal bei 177 ppm (**4**), während das andere Carbonyl ein schwaches Signal bei 167 ppm (**6**) aufweist. Die Umgebung besteht aus der unpolymerisierten Doppelbildung, welche bei 128 ppm (**8**) und 137 ppm (**7**) erkennbar ist. Die Ethoxyreste von eingebautem Vinyltriethoxysilan ergeben Signale bei 22 ppm (**10**) und 62 ppm (**9**). Während die CH_2-Gruppe deutlich sichtbar ist, liegt die CH_3-Gruppe unter dem Polymergerüst. Als Nebenreaktion findet die Hydrolyse und Kondensation des Silans statt, sodass die Signale von **7** und **8** auch unpolymerisiertem Vinyltriethoxysilan zugeordnet werden können, welches über Siloxanbindungen eingebaut wurde.

Diese Nebenreaktion kann in den ^{29}Si-NMR-Spektren von **V-PB1** beobachtet und belegt werden. Zwischen -40 und -60 ppm sind die T-Gruppen von Vinyltriethoxysilan mit polymerisierter Doppelbindung wieder zu finden (Abb. 25a). Zusätzlich erscheinen Signale bei -71 ppm und -79 ppm. Anhand von Silica-Partikeln auf VTEOS-Basis als Referenz (Abb. 25a, rotes Spektrum) konnten diese Signale kondensierter Spezies von Vinyltriethoxysilan mit intakter Doppelbindung zugeordnet werden. Die Hydrolyse und Kondensation von VTEOS während des Polymerisationsprozesses konnte durch die Erweiterung der Alkylkette nicht verhindert werden. Nach der Einlagerung von SiO_2 dominieren die Q-Gruppen Signale das Spektrum (Abb. 25b). Eine Veränderung der Intensitäten der T-Gruppen zwischen -40 und -60 ppm ist nur bedingt erkennbar. Folglich erfolgt keine kovalente Anbindung der angelagerten SNP an das Templat. Die vorliegenden T-Gruppen mit intakter Doppelbindung kondensieren während des Sol-Gel-Prozesses weiter, sodass diese weitestgehend als T^3-Gruppen vorliegen. Die SNP bestehen nahezu ausschließlich aus Q^3- und Q^4-Gruppen. Während der Kalzinierung kondensieren die Si-Spezies weiter und die vorhandene Organik wird entfernt. Als Folge werden die restlichen T-Gruppen in Q-Gruppen umgesetzt (Abb. 25c).

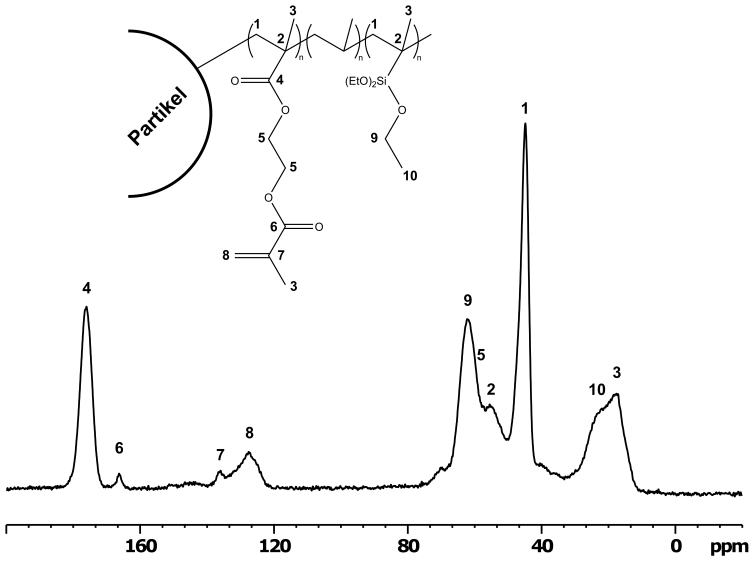
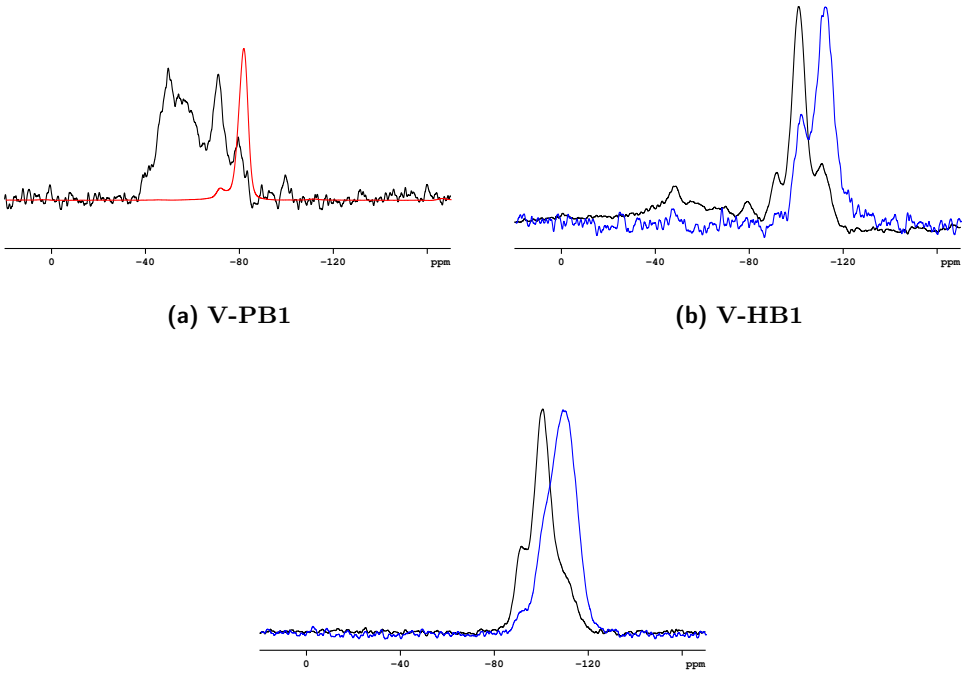


Abbildung 24: ^{13}C-CP/MAS-Festkörperspektrum von Polymer-Partikeln **V-PB1**.

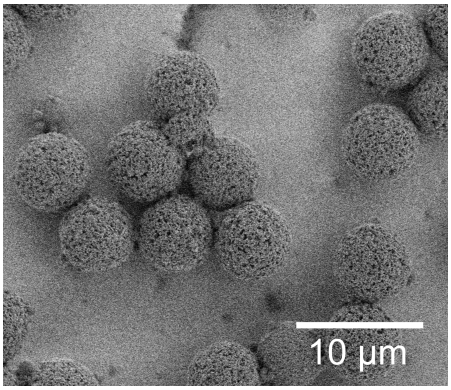


(a) V-PB1 **(b) V-HB1**

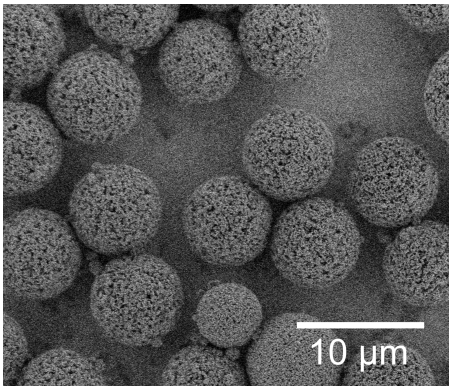
(c) V-MPSM1

Abbildung 25: ^{29}Si-CP/MAS- (schwarz) und ^{29}Si-HPDEC-NMR-Spektren (blau) der Polymer-Partikel **V-PB1** sowie Hybrid-Partikel **V-HB1** und **V-MPSM1**. ^{29}Si-CP/MAS-Spektrum von VTEOS-Silica-Partikeln als Referenz (rot).

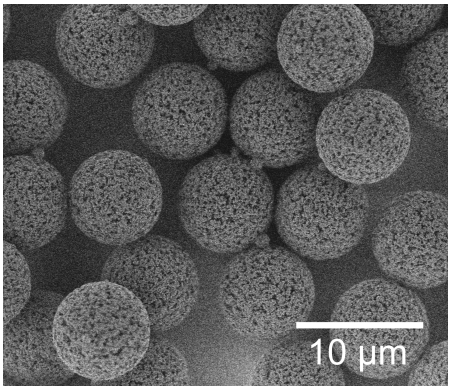
Die Entstehung der Sekundärpartikel erfolgt bereits im Polymerisationsschritt und resultiert in polydispersen porösen Silica-Partikeln. Um den Zeitpunkt der Bildung der Sekundärpartikel identifizieren zu können und um das Wachstum der Polymer-Partikel genauer zu verstehen, wurden während des Polymerisationsprozesses von **V-PB2** Proben zu verschiedenen Zeitpunkten entnommen und mit Hilfe der Rasterelektronenmikroskopie untersucht. Die Proben wurden mit einer $NaNO_2$-Lösung (0.3 $^{mg}/_{mL}$) gequentscht. Bereits zu Beginn der Polymerisation beim Erreichen von 70 °C hat **V-PB2** eine Größe von 5.8 µm (Abb. 26a). Im Anschluss erfahren die Polymer-Partikel ein exponentielles Wachstum innerhalb der ersten 60 min (Abb. 26l). Anschließend flacht das Wachstumsverhalten ab und die Partikel erreichen eine Größe von 7.7 µm nach sechs Stunden. 24 h nach Beginn der Polymerisation liegen die Partikel mit einer Größe von 8.3 µm vor. Nach 60 min können erste kleinere Partikel an der Oberfläche der Polymer-Partikel beobachtet werden (Abb. 26e) und nach 90 min ist zudem eine Verbreiterung der Partikelgrößenverteilung sichtbar. Theoretisch wäre ein Abbruch der Polymerisation zur Verhinderung der Sekundärpartikel möglich, da sich die Partikelgröße bereits nach 120 min der finalen Partikelgröße sehr stark annähert, jedoch ist unklar, inwieweit die Partikel zu dem Zeitpunkt quer vernetzt sind und folglich instabil wären.



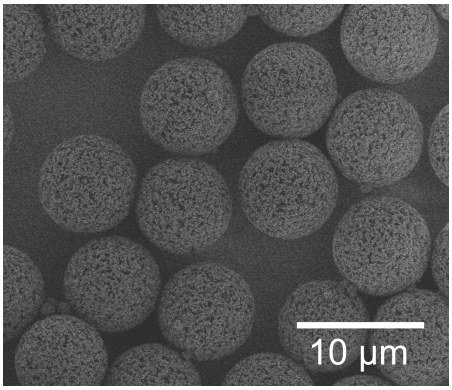
(a) 0 min



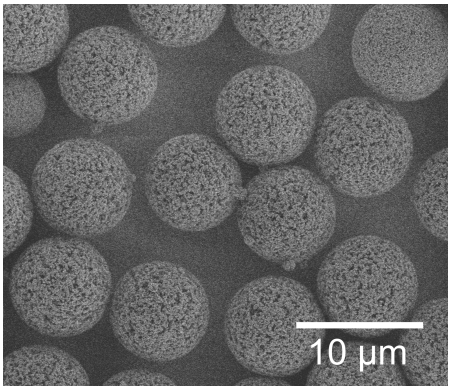
(b) 10 min



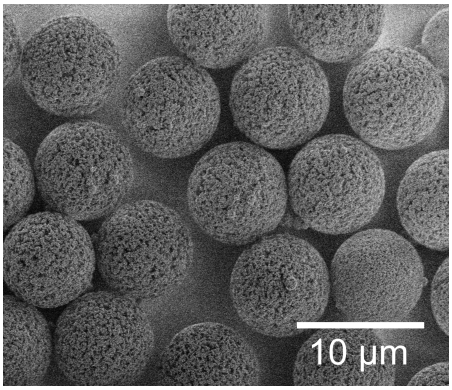
(c) 30 min



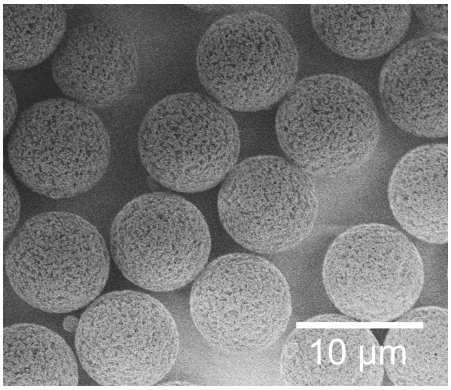
(d) 45 min



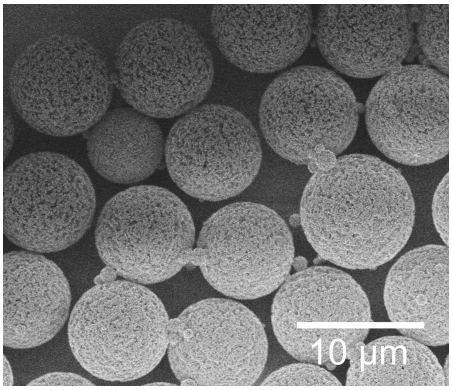
(e) 60 min



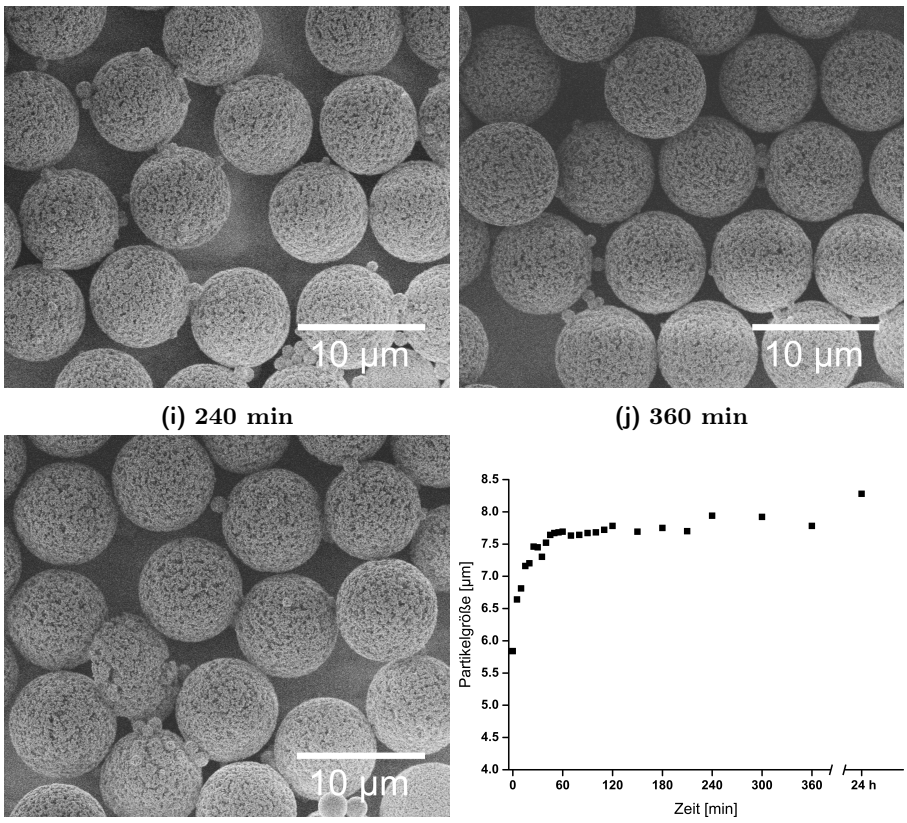
(f) 90 min



(g) 120 min



(h) 180 min

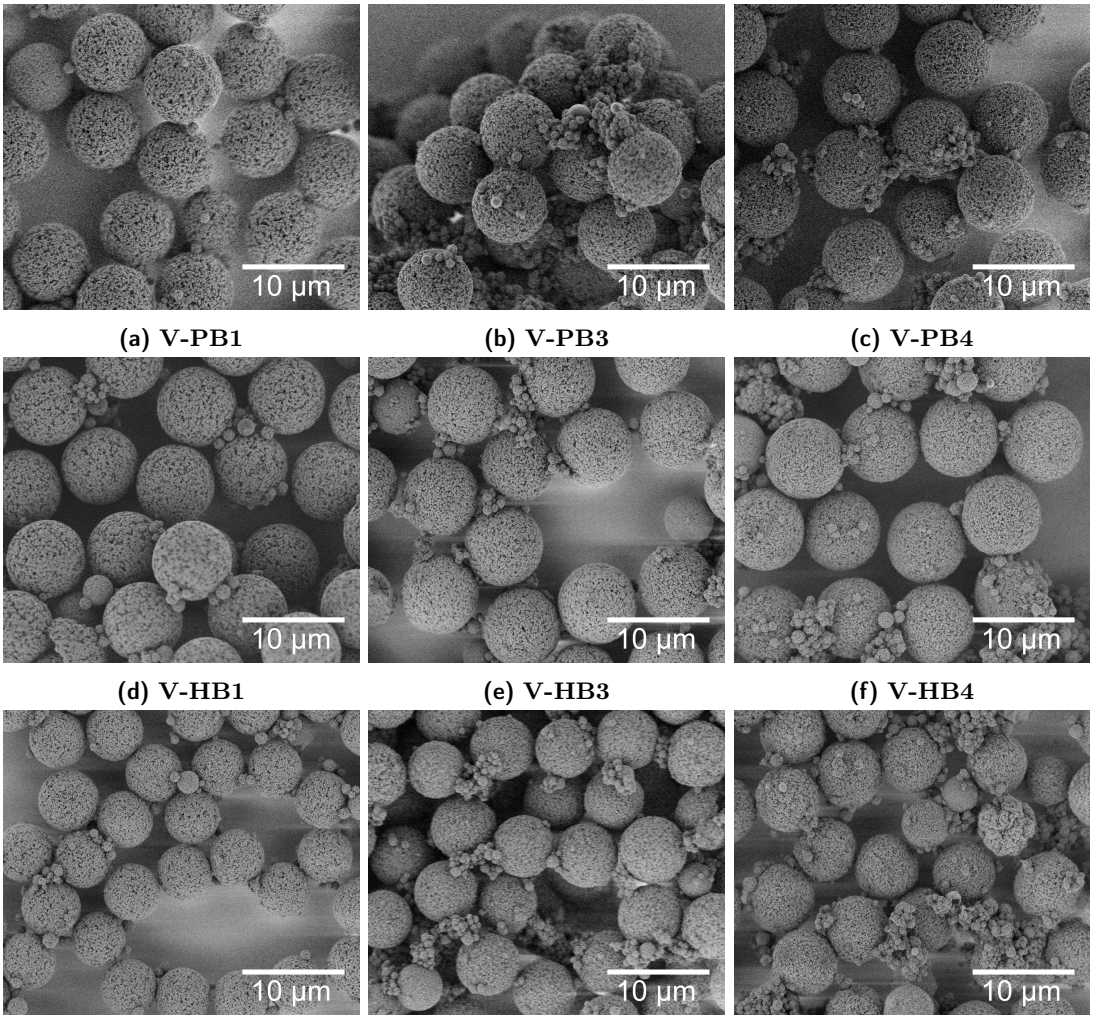


(i) 240 min **(j) 360 min**

(k) 24 h **(l)** Wachstumsverlauf von **V-PB2**.

Abbildung 26: REM-Aufnahmen von **V-PB2** zu unterschiedlichen Zeitpunkten während der Polymerisationsphase und deren Wachstumsverlauf. REM-Konditionen: 2,000 ×.

Eine geringe Wasserlöslichkeit der Monomere kann zu einer Polymerisation in wässriger Lösung führen. Unpolymerisierte Edukte versuchen die Verschiebung des Gleichgewichts zu kompensieren und diffundieren aus den gequollenen Partikeln zurück in die kontinuierliche Phase. Als Folge starten sekundäre Polymerisationen außerhalb der Saat-Partikel. Der Zusatz von Natriumnitrit als Radikalfänger kann potentielle Polymerisationen in der wässrigen Phase verhindern. Wang *et al.* erzielten größere Partikeldurchmesser in der Lösungspolymerisation von Methylmethacrylat aufgrund des geringeren Monomerverlusts bei Zugabe von $NaNO_2$.[113] Zur Unterdrückung der Sekundärpartikel wurden verschiedene Konzentrationen von $NaNO_2$ (0.0 $^{mg}/_{mL}$ (**V-PB1**), 0.3 $^{mg}/_{mL}$ (**V-PB3**) und 0.6 $^{mg}/_{mL}$ (**V-PB4**)) vor der Polymerisationsphase zugegeben. Das Ergebnis ist in Abbildung 27 dargestellt. Trotz der Zugabe des Natriumnitrits entstehen bei den drei Versuchen unerwünschte Sekundärpartikel. Hingegen der Erwartungen steigt die Anzahl an kleinen Partikeln mit der Zugabe an $NaNO_2$. Eine Abtrennung der Sekundärpartikel mit Hilfe von Zentrifugation blieb erfolglos. Daraus resultierend verbleiben kleine poröse Silica-Partikel nach der Kalzination und die Dispersität steigt an.



(a) V-PB1 **(b) V-PB3** **(c) V-PB4**

(d) V-HB1 **(e) V-HB3** **(f) V-HB4**

(g) V-MPSM1 **(h) V-MPSM3** **(i) V-MPSM4**

Abbildung 27: REM-Aufnahmen von Polymer-Partikeln mit Zugabe von 0.0 $^{mg}/_{mL}$ (**V-PB1**), 0.3 $^{mg}/_{mL}$ (**V-PB3**) und 0.6 $^{mg}/_{mL}$ (**V-PB4**) $NaNO_2$. Entsprechend unterhalb die zugehörigen Hybrid-Partikel **V-HB1**, **V-HB3**, **V-HB4** sowie den resultierenden Silica-Partikeln **V-MPSM1**, **V-MPSM3** und **V-MPSM4**. REM-Konditionen: 2,000 ×.

Schlussfolgerung

Die alternative Herstellung von porösen Polymertemplaten auf Basis von Vinylsilanen konnte erfolgreich demonstriert werden. Eine Substitution von Glycidylmethacrylat durch Vinyltriethoxysilan als Monomer im Polymerisationsprozess erzielt sphärische Polymertemplate mit vergleichbarer Partikelgröße. Diese können direkt in einem basenkatalysierten Sol-Gel-Prozess umgesetzt werden und bilden nach der Kalzinierung poröse Silica-Materialien. Während des Polymerisationsprozesses entstehen kleinere Sekundärpartikel, welche über gängige Trenntechniken nicht entfernt werden konnten. Als Folge werden in die Sekundärpartikel ebenfalls SNP eingelagert, was eine zunehmende Dispersität der

Silica-Partikel zur Folge hat. ^{29}Si-CP/MAS-NMR-spektroskopische Untersuchungen von **V-PB1** zeigen zweierlei Spezies von polymerisiertem Vinyltriethoxysilan. Einerseits wird das Monomer wie gewünscht über die Doppelbindung polymerisiert und eingebaut, andererseits wird unpolymerisiertes Monomer, welches über Hydrolyse und Kondensation der Alkoxygruppe verknüpft wird, beobachtet. Eine Zeitreihe des Polymerisationsprozesses zeigt die Bildung von Sekundärpartikeln bereits 120 min nach Polymerisationsstart. Die Zugabe von $NaNO_2$, als Radikalfänger zur Unterdrückung unerwünschter Nebenpolymerisationen, erzielte keinen Erfolg.

6 Publikation I

Microporous and Mesoporous Materials 351 (2023) 112482

Contents lists available at ScienceDirect

Microporous and Mesoporous Materials

journal homepage: www.elsevier.com/locate/micromeso

Impact of porosity and surface functionalization of hard templates on the preparation of mesoporous silica microspheres

Fabio Fait [a,b,1], Julia C. Steinbach [a,b,1], Andreas Kandelbauer [b,c], Hermann A. Mayer [a,*]

[a] Institute of Inorganic Chemistry, University of Tübingen, Auf der Morgenstelle 18, 72076, Tübingen, Germany
[b] Process Analysis and Technology (PA&T), Reutlingen Research Institute, Reutlingen University, Alteburgstrasse 150, 72762, Reutlingen, Germany
[c] Institute of Wood Technology and Renewable Materials, Department of Material Sciences and Process Engineering (MAP), University of Natural Resources and Life Sciences, Gregor-Mendel-Straße 33, 1180, Vienna, Austria

ARTICLE INFO

Keywords:
Glycidylmethacrylate (GMA)
Ethylenglycol dimethacrylate (EDMA)
Mesoporous silica microspheres (MPSM)
Hard template method
High performance liquid chromatography (HPLC)

ABSTRACT

Mesoporous silica microspheres (**MPSMs**) find broad application as separation materials in high liquid chromatography (HPLC). A promising preparation strategy uses *p*(GMA-*co*-EDMA) as hard templates to control the pore properties and a narrow size distribution of the MPMs. Here six hard templates were prepared which differ in their porosity and surface functionalization. This was achieved by altering the ratio of GMA to EDMA and by adjusting the proportion of monomer and porogen in the polymerization process. The various amounts of GMA incorporated into the polymer network of **P1**-**6** lead to different numbers of tetraethylene pentamine in the *p*(GMA-*co*-EDMA) template. This was established by a partial least squares regression (PLS-R) model, based on FTIR spectra of the templates. Deposition of silica nanoparticles (SNP) into the template under Stoeber conditions and subsequent removal of the polymer by calcination result in **MPSM1**-**6**. The size of the SNPs and their incorporation depends on the pore parameters of the template and degree of TEPA functionalization. Moreover, the incorporated SNPs construct the silica network and control the pore parameters of the **MPSMs**. Functionalization of the **MPSMs** with trimethoxy (octadecyl) silane allows their use as a stationary phase for the separation of biomolecules. The pore characteristics and the functionalization of the template determine the pore structure of the silica particles and, consequently, their separation properties.

1. Introduction

Silica based materials serve as platforms in a wide range of applications e.g. in coatings, as filler materials, in catalysis, in chemical sensors and in separation methods or medical diagnostics [1–6]. Furthermore, porous silica microspheres are widely used due to their high specific surface area, chemical stability and the possibility to vary their properties by surface functionalization [7–9]. Especially in high performance liquid chromatography (HPLC), porous silica microspheres are employed in column materials as stationary phases. With the continuous progress of HPLC and the ever-increasing demands on separation methods, further improvement of column materials is essential.

A high surface area is beneficial for separation efficiency in HPLC applications. As the relative surface area increases with decreasing particle diameter, this can be achieved by reducing the sizes of the particles. Unfortunately, this increases the backpressure which demands special and costly requirements for the HPLC equipment [10,11]. This challenge can be overcome by introducing mesopores and/or macropores into micron sized silica particles, which allow for good effective interaction of the liquid phase with the surface of the stationary phase in diffusion-controlled processes such as HPLC [12].

Currently, micron sized mesoporous silica particles are produced in industrial scale by emulsion process or spray drying [13–15]. These methods generate high yields but result in a broad particle size distribution. Processing and separation techniques such as sieving, sedimentation or air classification are necessary to obtain monodisperse particle distributions. These are costly and time-consuming.

The method presented by Stoeber et al. for the preparation of monodisperse silica particles posed a fundamental development in sol-gel chemistry. Under basic conditions the hydrolysis and condensation of alkoxysilane precursors in alcoholic media form spherical silica species. However, their size is limited to a range of 50–800 nm [16,17].

* Corresponding author.
E-mail address: hermann.mayer@uni-tuebingen.de (H.A. Mayer).
[1] Fabio Fait and Julia C. Steinbach equally contributed to this work.

https://doi.org/10.1016/j.micromeso.2023.112482
Received 3 January 2023; Received in revised form 31 January 2023; Accepted 2 February 2023
Available online 6 February 2023
1387-1811/© 2023 The Authors. Published by Elsevier Inc. This is an open access article under the CC BY license (http://creativecommons.org/licenses/by/4.0/).

Although special techniques allow to expand the particle size into the micrometer range, they remain non-porous [18–20].

The preparation of porous silica materials with discrete sizes can be achieved by different template methods [21–23]. A hard template method has been demonstrated to be suitable for the targeted synthesis of mesoporous silica microspheres (**MPSMs**) with a narrow size distribution [24–26]. Thus amino-functionalized porous organic co-polymers based on glycidyl methacrylate and ethylene glycol dimethacrylate (*p*(GMA-*co*-EDMA)) thermosets were successfully applied as hard templates in the preparation of **MPSMs** [27–29]. In the presence of these polymer templates, the hydrolysis and condensation of alkoxysilanes under Stoeber conditions generate silica nanoparticles (SNP) which accumulate in the pores of the polymer network. The SNPs aggregate in the pores and build a new silica network, which is interpenetrating the organic template. The organic polymer can be removed via calcination, leaving **MPSMs** (Scheme 1). Their morphology and pore properties are selectively controlled while maintaining a spherical shape with a narrow size distribution [24–26,30].

We reported earlier the systematic evaluation of process parameters in seeded suspension polymerization of GMA and EDMA [31]. The particle and pore properties of the polymer were controlled in targeted manner by variation of the GMA to EDMA ratio, the monomer to porogen ratio and the composition of the porogens. For *p*(GMA-*co*-EDMA) templates, higher proportions of GMA resulted in larger pores and smaller surface areas [31].

Here we demonstrate that the pore structures of the hard polymer template affect the size and pore properties of the mesoporous silica microspheres which have implications on their performance in HPLC.

2. Materials and methods

2.1. Chemicals

Polyvinyl alcohol (PVA, 87–89% hydrolyzed, mean average 88,000–97,000 g mol^{-1}), tetraethyl orthosilicate (TEOS) and trimethoxy (octadecyl) silane (ODTMS) were acquired from abcr GmbH. Ethyleneglycol dimethacrylate (EDMA) was bought from Acros Organics and ammonia (28–30% aqueous solution) was obtained from Alfa Aesar. Cyclohexanol and sodium dodecyl sulfate (SDS) were purchased from Carl Roth. Dibenzoyl peroxide (BPO), dibutyl phthalate (DBP), ethanol (EtOH), glycidyl methacrylate (GMA), hydrochloric acid, methanol (MeOH), 2-propanol, triethylamine, trifluoroacetic acid (TFA) and the protein test mixture H2899 (ribonuclease A, cytochrome C, holotransferrin and apomyoglobin) were obtained from Sigma-Aldrich. Acetonitrile (ACN, HPLC grade), tetraethylene pentamine (TEPA), and water (HPLC grade) were bought from fisher scientific. Toluene and deionized water were cleaned through a solvent purification system (SPS-800, MBraun).

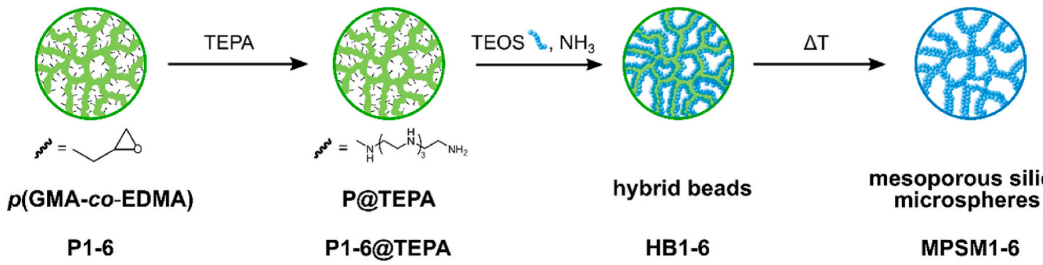
2.2. Characterizations

Scanning electron microscopy (SEM) images were taken with a Hitachi SU8030 instrument and used to determine the size, dispersity, and morphology of the particles. The size and dispersity of the particles were assessed by evaluating at least 400 particles per batch. Thermogravimetric studies of the hybrid beads were performed on a Mettler Toledo TGA/DSC I. For this purpose, the samples were calcined in an alumina crucible with a heating rate of 5 K min^{-1} under synthetic air (50 mL min^{-1}). The remaining mass corresponds to the amount of silica.

Infrared (IR) spectra were acquired using a Frontier 2 FTIR (PerkinElmer) with an attenuated total reflection accessory. Each sample was measured five times in a spectral range from 4000 cm^{-1} to 500 cm^{-1} with a spectral resolution of 2 cm^{-1} and four scans. A partial least squares regression model (PLS-R) was built similar to previous work [31]. To increase model quality, another two *p*(GMA-*co*-EDMA) templates with 50:50 GMA:EDMA from previous work (central points, CPs) were added for model building. The spectra were preprocessed by smoothing with a Savitzky-Golay filter (polynomial order: 2., over eleven points) and a subsequent removal of multiplicative scattering effects using a standard normal variate transformation. The analyzed spectral range was 1750–700 cm^{-1}. The spectra of the *p*(GMA-*co*-EDMA) templates (five spectra of **P1**–**4**, two spectra from **P5** and **P6** and seven spectra from the CPs) were used as test set and were validated externally (three spectra of **P5** and **P6**, as well as three spectra of the central points from our previous work). For spectral preprocessing and the multivariate data analysis, the software Unscrambler-X (CAMO Software AS) was used. The PLS-R model was applied for the prediction of GMA content for all particles **P1**–**6** and **P1**–**6@TEPA**, to assess the change in epoxy groups after amination as indicative measure for the degree of amination.

To determine the pore size, volume, and specific surface area of the particles, N_2 adsorption-desorption measurements were performed on a BELSORP MiniX from Microtrac Retsch GmbH. The samples were preheated with a BELSORP VACII to remove possible physisorbed substances and to establish a reproducible equilibrium state. At a final vacuum of $2 \bullet 10^{-2}$ mbar, polymer samples were evacuated at 30 °C for 24 h, and silica samples were pretreated at 300 °C for 3 h, respectively. Nitrogen adsorption measurements were performed at 77 K. BELMaster 7 software was used to evaluate the isotherms. The specific surface area of the particles was determined according to the method of Brunauer, Emmett, and Teller (BET). The pore size distributions were obtained by applying the Barrett-Joyner-Halenda (BJH) method to the desorption and adsorption isotherms for the polymer templates and desorption isotherms for the silica particles. This was done taking into account that the peaks around 4 nm (Fig S3, S.I.) are the result of the tensile strength effect rather than a bimodal pore size distribution [32]. The median of the pore sizes differs hardly between adsorption and desorption isotherms (Table 1). This is the reason why the pore size distributions of the adsorption isotherms are shown in Fig. 3 for the polymer templates. The pore volume was estimated from a single point adsorption at p/p_0 of 0.95.

Analytical high performance liquid chromatography was performed on an Agilent 1100 series system (Agilent Technologies, Waldbronn, Germany) equipped with a quaternary pump with degasser, an auto



Scheme 1. Synthesis of mesoporous silica microspheres with different *p*(GMA-*co*-EDMA) polymer templates.

Table 1
Particle properties of *p*(GMA-*co*-EDMA) microspheres **P1**–**6** prepared with varying GMA/EDMA and monomer/porogen ratios.

	GMA/EDMA	monomer/porogen	particle size	dispersity	median pore size		pore volume	specific surface area
	v./v.	v./v.	[μm]	d_{90}/d_{10}	[nm][a]	[nm][b]	[$cm^3\ g^{-1}$]	[$m^2\ g^{-1}$]
P1	20/80	50/50	7.9	1.1	6.1	8.0	0.29	270
P2	40/60	50/50	7.8	1.2	12.2	12.6	0.19	123
P3	60/40	50/50	7.5	1.1	20.6	21.1	0.09	43
P4	80/20	50/50	7.3	1.2	35.5	35.4	0.03	15
P5	40/60	25/75	7.6	1.2	26.7	27.9	0.25	132
P6	40/60	75/25	7.9	1.2	15.1	8.5	0.06	31

[a] From adsorption isotherm.
[b] From desorption isotherm.

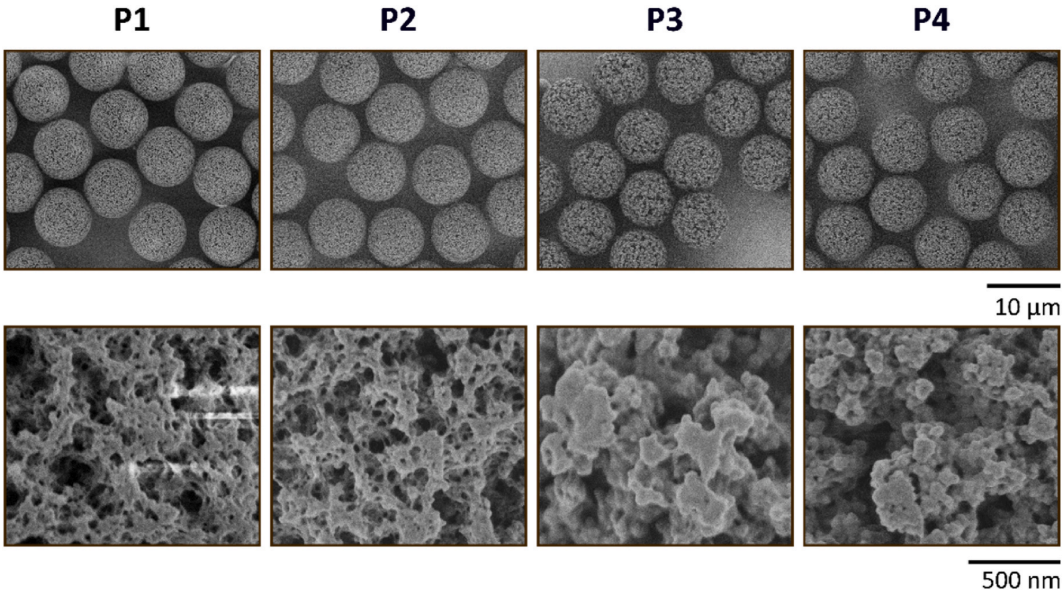


Fig. 1. SEM images of *p*(GMA-*co*-EDMA) templates **P1**–**4** with increasing GMA to EDMA ratio (from left to right). 2,000 (top row) and 50,000 (bottom row) magnification.

sampling system, column oven and a diode array detector. Instrument control, data acquisition and automated data analysis was performed by the Chem-Station software (B.04.03, Agilent Technologies, Waldbronn, Germany). A gradient elution was performed using water with 0.1% TFA (eluent A) and acetonitrile with 0.08% TFA (eluent B) with a gradient starting at 20% B to 85% B within 25 min. 5 μL of the protein mixture H2899 (1 mg mL^{-1} each protein in 90/10 A/B) were injected and detected at a wavelength of 215 nm. A commercially available column (ProSphere C18, 300 Å, 10 μm, 250 × 4.6 mm) was used as reference column. The prepared particles were packed into stainless-steel columns (250 × 4.6 mm).

2.3. Synthesis

2.3.1. Preparation of porous p(GMA-co-EDMA) particles *P1–6*

Monodisperse polystyrene (PS) microspheres with diameters of 1.9 ± 0.1 μm were prepared as reported earlier (Fig S1, S.I.) [24].

0.3 g of polystyrene particles and 5 mL of an aqueous SDS solution (0.25 wt%) were dispersed in a 250 mL flask. 2 mL of DBP were emulsified in 150 mL of an aqueous SDS solution (0.25 wt%) with a homogenizer at 4500 rpm for 15 min and then added to the polystyrene suspension. The mixture was stirred for 24 h at 200 rpm. Depending on the experiment the volume ratios of GMA and EDMA and the monomer to porogen ratios were varied according to Table 1. As porogen a mixture of toluene and cyclohexanol (73/27 v./v.) was applied. In all experiments a total volume of 30 mL of the organic phase was maintained. The monomer and porogen mixture, 0.4 g of BPO and 150 mL of an aqueous SDS solution (0.25 wt%) were emulsified with a homogenizer at 4500 rpm for 15 min. This emulsion and the activated polystyrene particles were transferred to a 500 mL three-necked flask and stirred for 24 h at 200 rpm. 150 mL of an aqueous PVA solution (2.3 wt %) was added to the reaction and Argon was passed into the reaction mixture for 30 min and then heated to 70 °C for 24 h. The particles were separated from the solution, washed three times with EtOH and three times with H_2O and dried at 65 °C for 16 h.

2.3.2. Preparation of mesoporous silica microspheres *MPSM1–6*

5 g of particles **P1**–**6** were dispersed in 200 mL of H_2O, 7.5 mL of tetraethylene pentamine were added and the solution was stirred for 24 h at 80 °C (200 rpm). The **P1**–**6@TEPA** particles were washed three times with H_2O and EtOH, each and dried at 65 °C for 16 h.

5 g of **P1**–**6@TEPA** particles were dispersed in 270 mL of 2-propanol and 30 mL of H_2O. Then 12.5 mL of TEOS and 1.25 mL of an ammonia solution were added and stirred at room temperature (130 rpm) for 24 h. The particles were separated from the solution, washed three times with H_2O and EtOH, each and dried at 65 °C for 16 h. After calcination at 600 °C for 10 h mesoporous silica microspheres **MPSM1**–**6** remained.

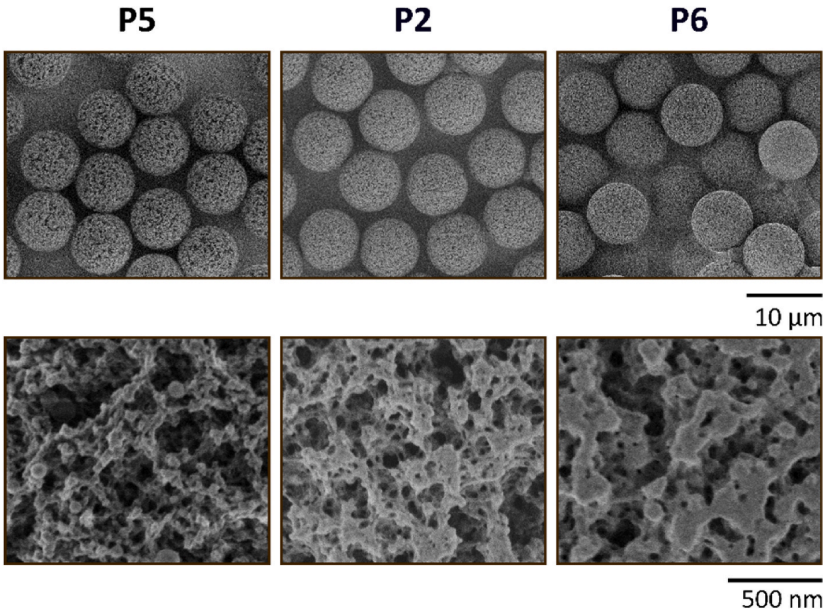


Fig. 2. SEM-images of *p*(GMA-*co*-EDMA) templates **P5**, **P2** and **P6** with increasing monomer to porogen ratio (from left to right). 2,000 (top row) and 50,000 (bottom row) magnification.

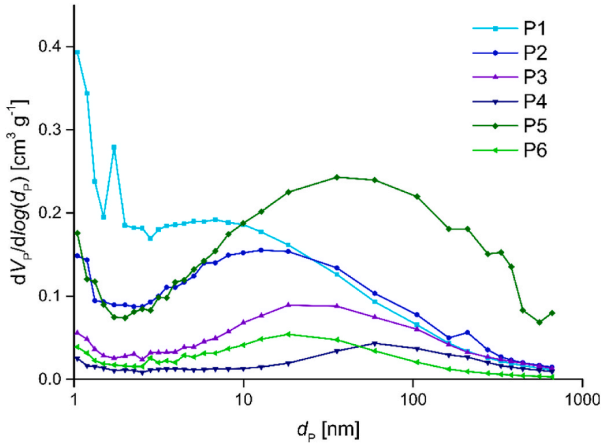


Fig. 3. Pore size distributions from the adsorption isotherms of the *p*(GMA-*co*-EDMA) templates **P1–6**.

*2.3.3. Octadecyl functionalization of **MPSM1–4** for chromatographic measurements*

5 g of **MPSM1–4** were dispersed in 600 mL of hydrochloric acid (3.7%) and stirred for 3 h at 100 °C (130 rpm). The particles were separated from the solution, washed with EtOH and H_2O until neutral and dried at 65 °C for 16 h. The particles were then dispersed in 75 mL of toluene, 25 mL of trimethoxy (octadecyl) silane (ODTMS) and 0.5 mL of triethylamine were added, and the mixture was stirred at 100 °C (130 rpm) for 6 h. The particles were separated from the solution, washed three times with toluene, three times with EtOH and twice with MeOH and dried at 65 °C for 16 h.

The functionalized particles were packed in a slurry with acetone and MeOH/H_2O (85/15 v./v.) as pressure medium.

3. Results and discussion

3.1. Modification of p(GMA-co-EDMA) microspheres with different GMA and EDMA ratios

The spherical porous *p*(GMA-*co*-EDMA) polymer particles **P1–6** were prepared by a seeded swelling suspension polymerization of monodisperse polystyrene (PS) microspheres [24]. PS with a diameter of 1.9 ± 0.1 µm (Fig S1, S.I.) were applied as seeds in the polymerization of glycidyl methacrylate and ethylene glycol dimethacrylate as crosslinker as well as toluene and cyclohexanol as porogens. The amount of GMA and EDMA (v./v.) and the ratio of monomers to porogens (v./v.) were varied according to Table 1.

The size and morphology of the *p*(GMA-*co*-EDMA) templates were characterized with scanning electron microscopy (SEM) (Figs. 1 and 2). The particle sizes of **P1–4** slightly decrease from 7.9 to 7.3 µm which correlates with the increasing amount of GMA (Table 1). As the density of GMA is lower than that of EDMA the swelling factor is reduced when the amount of GMA is increased at the expense of EDMA [33]. Changing the proportion of monomers to porogens at a constant GMA/EDMA ratio, increases the particle size of the template with increasing monomer content (**P5** < **P2** < **P6**, Table 1). This is attributed to the increased number of swelling monomers. All templates show a smooth morphology with different porous networks. Independent of the ratio of GMA to EDMA and the ratio of monomer to porogen uniform porous polymer templates with a narrow size distribution are obtained (Table 1, Figs. 1 and 2).

Specific surface areas, pore sizes and pore volumes of **P1–6** were determined from nitrogen adsorption isotherms (Fig. 3 and Fig S2, S.I.). All *p*(GMA-*co*-EDMA) templates (**P1–6**) display a broad pore size distribution between 5 and 100 nm (Fig. 3). In addition, contrary to the rest of the templates, **P1** shows a proportion of small pores (2 nm). With increasing amounts of monomer GMA the median pore size increases from 6 to 35 nm. Consequently, the surface areas of the particles decrease from 270 $m^2 g^{-1}$ to 15 $m^2 g^{-1}$ in the same order (**P1** > **P2** > **P3** > **P4**, Table 1).

The more GMA is applied the less EDMA is present, which leads to fewer branches and thus a lower degree of cross-linkage. As a result, the

pores become larger. On the other hand, a higher amount of GMA leads to earlier phase separation, which also results in larger pores [31]. The finer network structure, resulting from a higher cross-linking degree with higher EDMA ratios is also visible in the morphology of the polymer particles (Fig. 1). With increasing GMA content from **P1** to **P4**, the surface texture becomes rougher. The pore volume of the particles decreases with higher amount of GMA. Comparing the templates **P5**, **P2** and **P6** the pore parameters decrease with higher amount of monomer and consequently lesser amount of porogen. Since during the polymerization a lower proportion of porogens is present, this results in smaller pores and a smaller pore volume.

3.2. Spectral analysis of p(GMA-co-EDMA) and P@TEPA microspheres

The functionalization of the *p*(GMA-*co*-EDMA) polymer particles with amino groups provides a positive surface charge which supports the deposition of negatively charged silica species into the polymer network under sol-gel conditions [25,34]. To introduce amino functions, the porous templates **P1**–**6** were treated with tetraethylene pentamine to generate **P1**–**6@TEPA** particles via ring opening reactions of the epoxy groups (Scheme 1). As the degree of amination at the polymer surface depends on the amount of GMA incorporated into the template the number of TEPA groups and, thus, the positive charges differ in the **P1**–**6@TEPA** particles. Unfortunately, the amount of TEPA in the **P1**–**6@TEPA** particles is rather small compared to their bulk compositions, so that any changes of nitrogen content falls below the limit of detection via elemental analyses (Table S1, S.I.).

Thus, a partial least squares regression (PLS-R) model, based on FTIR spectra of the particles, which predicts the decrease in the GMA ratio through amination of polymers **P1**–**6** was applied as indirect and indicative measure. The aim is to assess differences in degrees of amination for the **P1**–**6@TEPA** particles in dependence of the initial relative GMA content.

The intensities of characteristic IR frequencies which vary with the amount of GMA are those of the symmetric and asymmetric ring vibration of the epoxide at 845 and 910 cm^{-1}, respectively [35]. The *C*–O stretching vibration of the epoxide ring at 1270 cm^{-1} also responds to changes in GMA ratio (Fig S4d, S.I.). The established PLS-R model, based on four regression coefficients, has a high predictive power with an $R^2_{pred} = 0.9922$ and a low error with RMSEP = 0.6% and can hence be used to effectively determine the relative ratio of GMA in **P1**–**6@TEPA** (Fig S4a-c, S.I.).

After the functionalization with TEPA, the vibrations corresponding to the epoxide groups decrease in absorbance. Consequently, the intensities of the vibrations from the epoxy groups decrease within increasing functionalization of the particles (Fig. 4a). The established PLS-R was used for the prediction of the GMA content of **P1**–**6** and **P1**–**6@TEPA** particles. The predicted values are given in Fig. 4b. The low deviations of predicted values from the actual values of the polymers and the small standard deviation for each prediction indicate a high model accuracy (Table 2, Fig. 4b).

The predicted residual GMA ratios for the amino functionalized particles **P1@TEPA** to **P6@TEPA**, respectively, correspond to a decrease in epoxy ratio during amination, respectively (Table 2). The degree of TEPA functionalization follows the order **P1** < **P5** ~ **P6** < **P2** < **P3** < **P4**.

3.3. Preparation of mesoporous silica microspheres (MPSM1–6)

The **P1**–**6@TEPA** particles were applied as hard templates in a base catalyzed sol-gel process. In the presence of 2-propanol and H_2O, the corresponding amino functionalized polymer templates, and tetraethyl orthosilicate (TEOS) formed polymer/silica hybrid beads (**HB1**–**6,** Scheme 1, and Figs. S5 and S6 and Table S2, S.I.). Calcination of the **HB1**–**6** at 600 °C for 10 h removed the organic polymer which leaves the mesoporous silica particles **MPSM1**–**6** (Scheme 1 and Figs. 5 and 6) (see

Table 2
Actual and predicted GMA ratios of **P1**–**6** and **P1**–**6@TEPA**.

	actual GMA ratio of *p*(GMA-*co*-EDMA)	predicted GMA ratio		predicted GMA ratio of P@TEPA	Δ *p*(GMA-*co*-EDMA) – P@TEPA
P1	20	20.6	**P1@TEPA**	16.1	4.5
P2	40	38.9	**P2@TEPA**	29.4	9.5
P3	60	60.9	**P3@TEPA**	49.1	11.8
P4	80	79.6	**P4@TEPA**	65.6	14.1
P5	40	39.2	**P5@TEPA**	32.1	7.1
P6	40	39.5	**P6@TEPA**	32.6	6.9

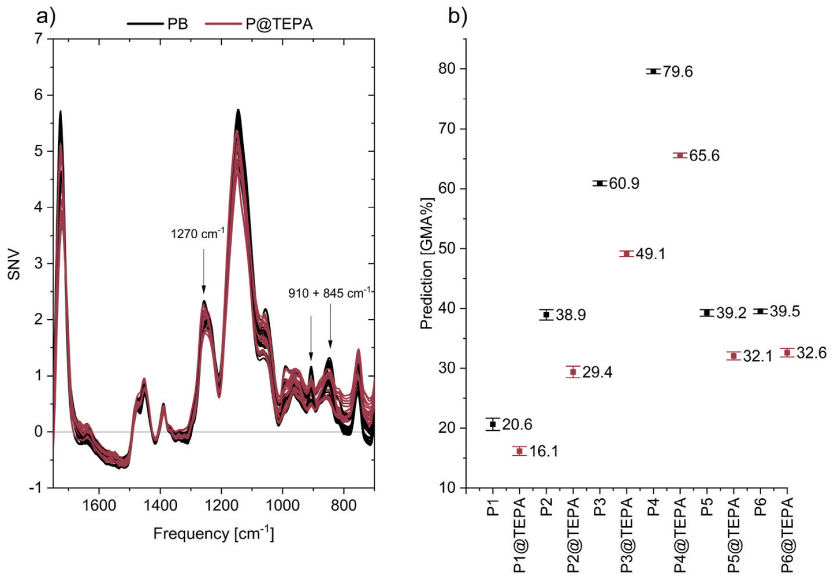


Fig. 4. a) Spectra of **P1–6** and **P1–6@TEPA** templates after spectral preprocessing with standard normal variate transformation and b) predicted values of mean epoxy content with standard deviation across all spectra used for prediction. **P1–6** are depicted in black and **P1–6@TEPA** templates in red.

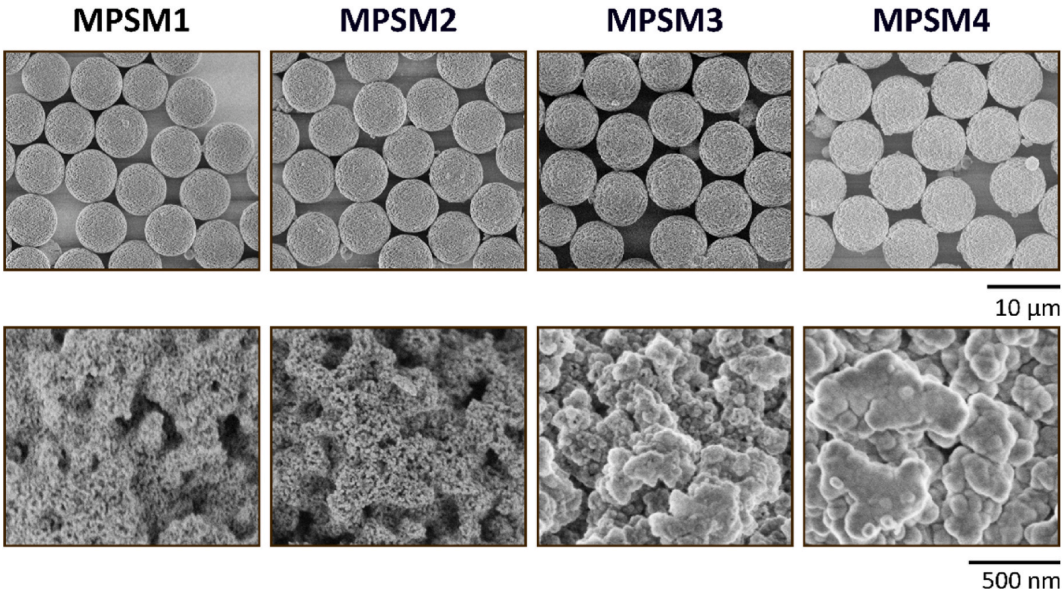


Fig. 5. SEM images of mesoporous silica microspheres **MPSM1**–**4** using polymer templates with different amount of GMA. 2,000 (top row) and 50,000 (bottom row) magnification.

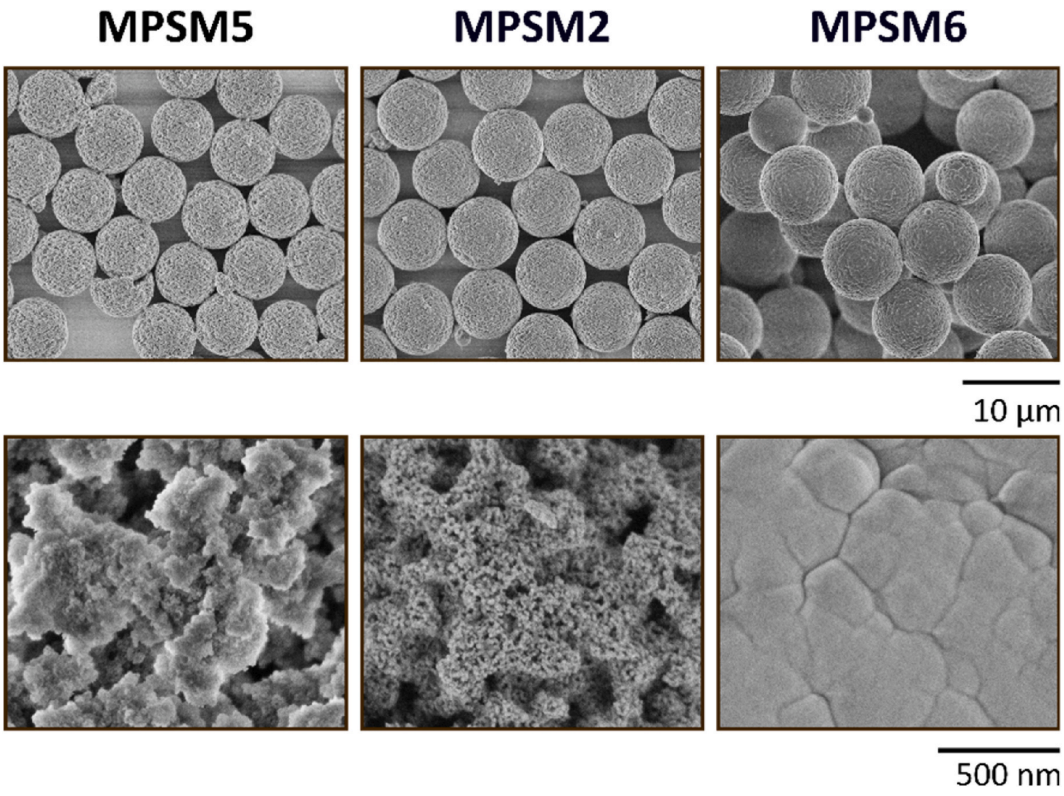


Fig. 6. SEM images of mesoporous silica microspheres **MPSM2,5,6** using polymer templates with different monomer to porogen ratio. 2,000 (top row) and 50,000 (bottom row) magnification.

Fig. 7).

An evaluation of the SEM images of **MPSM1**–**6** show that the high monodispersity as specified by the template particles is maintained (Figs. 5 and 6, Tables 1 and 3). Although the diameters of the templates **P1**–**6@TEPA** differ by only 0.6 µm (Table 1), the range of silica particle size is extended to 1.6 µm (Table 3). The smallest silica particles **MPSM1**

Table 3
Properties of mesoporous silica microspheres **MPSM1–6**.

	particle size	dispersity	median pore size	pore volume	specific surface area
	[µm]	d_{90}/d_{10}	[nm][a]	[$cm^3\ g^{-1}$]	[$m^2\ g^{-1}$]
MPSM1	6.6	1.2	15.4	0.71	342
MPSM2	6.8	1.2	19.2	0.56	252
MPSM3	7.0	1.2	23.0	0.22	139
MPSM4	7.1	1.2	72.4	0.12	68
MPSM5	6.3	1.1	12.1	0.88	382
MPSM6	8.2	1.1	–	–	–

[a] From desorption isotherms.

and **MPSM5** with a particle size of 6.3 and 6.6 µm, respectively, result from those templates which contain the smallest amount of TEPA (**P1@TEPA** and **P5@TEPA**). With increasing amount of TEPA in the templates (Table 2) the silica materials become larger (**MPSM2**, **MPSM3** and **MPSM4**). Interestingly, **MPSM6** with a particle size of 8.2 µm is larger than the corresponding **P6@TEPA** template (Tables 1 and 3). In this case also non-porous secondary nanoparticles with a size of 230 nm were found in the filtrate of the washing procedure (Fig S7, S.I.). The morphology of **HB6** and **MPSM6** (Fig S5 and Fig. 6) indicate that the pores of the template are closed, and large silica nanoparticles aggregate to a shell around the template. SEM images of purposely destroyed **MPSM6** show that the particles are hollow and a shell of silica remains after calcination (Fig S8, S.I.) The silica network of **MPSM1** and **MPSM2** is made up of small nanometer-sized silica particles which create many small pores and a rough surface (Fig. 5). With increasing amount of TEPA the SNPs become larger (**MSMP3** and **MSMP4**), the number of small particles is declining and the surface becomes smoother (Fig. 5).

Removing the organic template leaves more space behind so that the median pore sizes, pore volumes and specific surface areas of **MPSM1**–**5** increase compared to those of the corresponding polymer particles **P1**–**5** (Table 2). Moreover, the pore parameters of **MPSMs** follow the same course as those of the polymer particles. Based on the t-plots of the adsorption isotherms, the MPSMs do not exhibit microporosity and possess pre-dominantly mesopores.

The mesoporous silica microspheres **MPSM1**–**6** are composed of non-porous silica nanoparticles of different size and shape. The size of the SNPs and their deposition into the template depends on three factors: (i) the rate of the growth of the SNPs in the continuous phase which is based on the sol-gel parameters, (ii) the diffusion rate of the SNPs into the template which is controlled by the ability of the template to attract negatively charged SNPs from the solution and (iii) the pore parameters of the template. For all experiments the sol-gel process parameters are the same and thus the rates of the SNP growth are comparable. This agrees with the overall amount of deposited silica (30 wt%) into the porous polymer network independent of the polymer composition (Fig. S9, S.I.).

Under the present reaction conditions the amino groups of the attached TEPA functions are still partly protonated which provides the template surface with a positive charge. A higher amount of TEPA generates a higher positive charge. Templates with higher TEPA content extract negatively charged silica species from the reaction mixture at an early state of the SNP growth. Small silica particles are deposited in the pores of the template where they aggregate and form larger SNPs. This is the case for **MPSM4** and **6**. Furthermore, the larger pore structure of the **P4@TEPA** template provides more space for agglomeration resulting in larger SNPs. In case of **P6@TEPA** the combination of small pores and large SNPs closed the pores at the surface of the template. A silica shell around the polymer is observed. At a lower TEPA content, the attraction of SNPs is weaker, so that they diffuse into the template at a later state of the growth process. Consequently, the SNPs are larger when they are incorporated into the silica network and maintain their size as they are more stable than the smaller SNPs. In the case of **MPSM1**, a particle size of the SNPs of about 15 nm is observed.

*3.4. Protein separation using C_{18}-functionalized **MPSM1–4** as stationary phases*

Functionalization of silica materials to generate reverse stationary phases with trimethoxy (octadecyl) silane is an established method that is widely used [36]. Thus the **MPSM1-4** with different pore parameters were functionalized with trimethoxy (octadecyl) silane (C_{18}) and packed into 250 × 4.6 mm stainless steel columns using the slurry method. **MPSM5** and **MPSM6** were too fragile and broke during the packing process. The resulting reversed phase columns **MPSM1-C_{18}**-**MPSM4-C_{18}**, and the commercially available column ProSphere C18, (300 Å, 10 µm, 250 × 4.6 mm) as reference, were applied for the separation of a protein mixture consisting of ribonuclease A, cytochrome C, holo-transferrin and apomyoglobin. The chromatograms in Fig. 8 show a baseline separation of the proteins with all prepared C_{18} columns. Thus, the prepared packing materials show a separation efficiency comparable to those of the commercial column. Also, the resolutions (Table 4) between the protein peaks are comparable or even better than that of the commercially available column. Overall, the separation efficiency increases from **MPSM1-C_{18}** to **MPSM3-C_{18}**. This correlates well with the increase in median pore size of the **MPSM** packing material, as the accessibility for bigger proteins is facilitated. Especially the resolution between cytochrome C and holo-transferrin ($R_{2\text{-}3}$, Table 4) increase with increasing GMA ratio in the polymeric template which corresponds well to the increased pore sizes of **MPSM3**. Also, the overall peak symmetry is improved. For **MPSM4** the larger SNPs at the surface and the nearly closed morphology restrict the diffusion into the pores, resulting in broader peaks and decreasing column performance.

4. Conclusion

Non-porous SNPs are the building blocks of the mesoporous silica microspheres (**MPSM1-6**) prepared by the hard template assisted approach. Both pore properties and degree of amino-functionalization of the templates have a strong impact on the size of the deposited SNPs. A low proportion of GMA with small pores (**P1**) and large pores (**P5**) leads to small inserted SNPs. A high proportion of GMA with small pores (**P6**) results in the formation of a hollow silica shell. If the pores are large enough as in **P4** large SNPs can be incorporated. Thus the particle and pore properties of the **MPSM1-6** are controlled by the size of the SNPs. Small nanoparticles generate small pore sizes and high specific surface

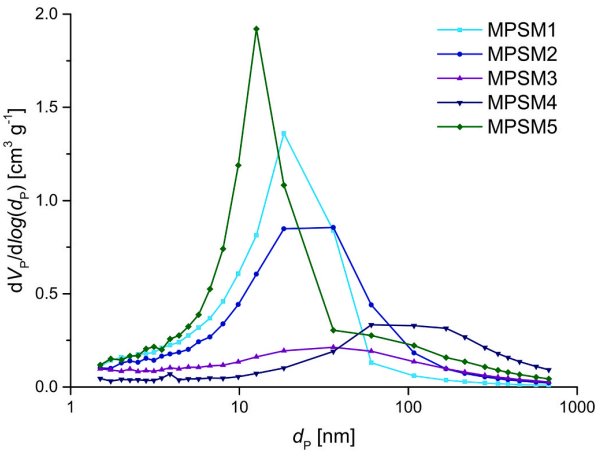


Fig. 7. Pore size distributions from the desorption isotherms of the mesoporous silica microspheres **MPSM1–5**.

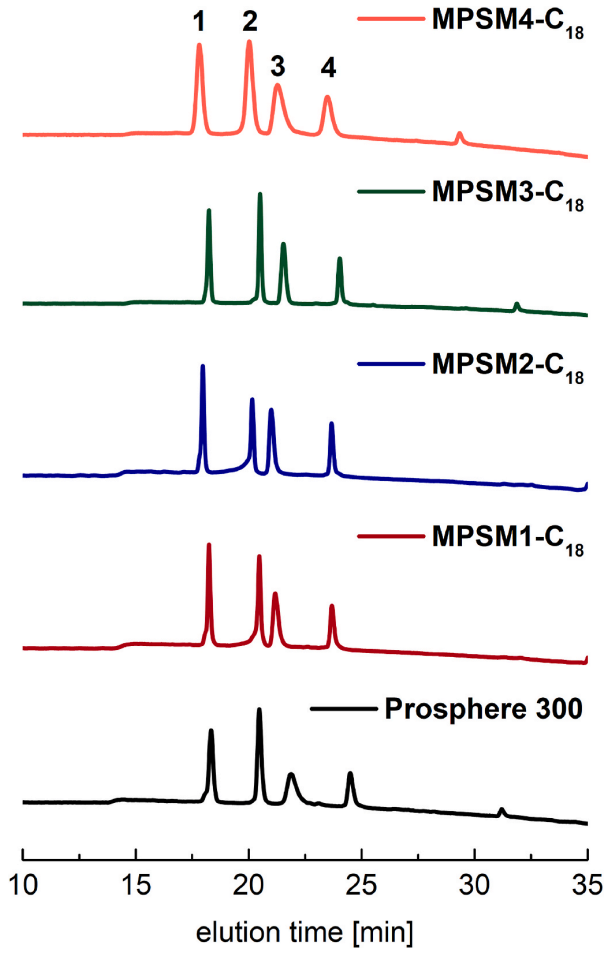


Fig. 8. Chromatograms of protein mixture H2899 separation with the prepared C_{18} functionalized stationary phases and a commercially available ProSphere 300. Chromatographic settings: column dimension: 250 × 4.6 mm; mobile phase A: H_2O with 0.1% TFA, mobile phase B: ACN with 0.08% TFA; gradient from 20% B to 85% B within 25 min; test mixture: 4 mg mL^{-1} (each 1 mg mL^{-1}) with 5 µL injection volume, 1 – ribonuclease A, 2 – cytochrome C, 3 – holotransferrin, 4 – apomyoglobin; column temperature: 30 °C; detection wavelength: 215 nm.

Table 4
Column performance for separation of protein mixture H2899 of the **MPSM-C_{18}** columns and a commercially available column.

	Resolution R_{1-2}	Resolution R_{2-3}	Resolution R_{3-4}
MPSM1-C_{18}	9.39	1.97	6.56
MPSM2-C_{18}	9.39	2.67	8.20
MPSM3-C_{18}	9.74	3.37	7.63
MPSM4-C_{18}	4.10	1.74	2.88
ProSphere 300	6.24	2.49	4.36

areas, while larger nanoparticles lead to larger pores and lower surface areas of **MPSMs**. Interestingly, the GMA to EDMA ratio and the monomer to porogen ratio in the preparation of the template control the pore parameters of the final **MPSMs**. This allows access to stationary phases for specific separation problems in HPLC.

CRediT authorship contribution statement

Fabio Fait: Writing – original draft, Visualization, Methodology, Investigation, Data curation. **Julia C. Steinbach:** Visualization, Methodology, Investigation, Formal analysis, Data curation, Writing – original draft. **Andreas Kandelbauer:** Writing – review & editing, Supervision, Project administration, Funding acquisition, Conceptualization. **Hermann A. Mayer:** Writing – review & editing, Supervision, Resources, Project administration, Funding acquisition, Data curation, Conceptualization.

Declaration of competing interest

The authors declare that they have no known competing financial interests or personal relationships that could have appeared to influence the work reported in this paper.

Data availability

Data will be made available on request.

Acknowledgments

This research was funded the by Bundesministerium für Bildung und Forschung (BMBF, grant number 13FH647IX6) and the Bundesministerium für Wirtschaft und Energie (AiF/ZIM, grant number ZF4019203SL8). Furthermore, we would like to thank our cooperation partner Dr. Maisch GmbH for their support in preparing the columns. We thank Elke Nadler for contributing the SEM measurements.

Appendix A. Supplementary data

Supplementary data to this article can be found online at https://doi.org/10.1016/j.micromeso.2023.112482.

References

[1] G.P. Bierwagen, Sol–gel coatings on metals for corrosion protection, Prog. Org. Coating 64 (2009) 327–338.
[2] J.J. Chruściel, E. Leśniak, Modification of epoxy resins with functional silanes, polysiloxanes, silsesquioxanes, silica and silicates, Prog. Polym. Sci. 41 (2015) 67–121.
[3] C.M. Crudden, M. Sateesh, R. Lewis, Mercaptopropyl-Modified mesoporous silica: a remarkable support for the preparation of a reusable, heterogeneous palladium catalyst for coupling reactions,, J. Am. Chem. Soc. 127 (2005) 10045–10050.
[4] J. Wei, Z. Sun, W. Luo, Y. Li, A.A. Elzatahry, A.M. Al-Enizi, Y. Deng, D. Zhao, New insight into the synthesis of large-pore ordered mesoporous materials, J. Am. Chem. Soc. 139 (2017) 1706–1713.
[5] K.W. Gallis, J.T. Araujo, K.J. Duff, J.G. Moore, C.C. Landry, The use of mesoporous silica in liquid chromatography, Adv. Mater. 11 (1999) 1452–1455.
[6] B.M. Wagner, S.A. Schuster, B.E. Boyes, J.J. Kirkland, Superficially porous silica particles with wide pores for biomacromolecular separations, J. Chromatogr. A 1264 (2012) 22–30.
[7] J.J. Kirkland, F.A. Truszkowski, C.H. Dilks, G.S. Engel, Superficially porous silica microspheres for fast high-performance liquid chromatography of macromolecules, J. Chromatogr. A 890 (2000) 3–13.
[8] L.F. Giraldo, B.L. López, L. Pérez, S. Urrego, L. Sierra, M. Mesa, Mesoporous silica applications, Macromol. Symp. 258 (2007) 129–141.
[9] M. Ide, E. Wallaert, I. Van Driessche, F. Lynen, P. Sandra, P. Van Der Voort, Spherical mesoporous silica particles by spray drying: doubling the retention factor of HPLC columns, Microporous Mesoporous Mater. 142 (2011) 282–291.
[10] K.K. Unger, R. Skudas, M.M. Schulte, Particle packed columns and monolithic columns in high-performance liquid chromatography-comparison and critical appraisal, J. Chromatogr. A 1184 (2008) 393–415.
[11] R. Hayes, A. Ahmed, T. Edge, H. Zhang, Core–shell particles: preparation, fundamentals and applications in high performance liquid chromatography, J. Chromatogr. A 1357 (2014) 36–52.
[12] M.C. Kimling, R.A. Caruso, Sol–gel synthesis of hierarchically porous TiO2 beads using calcium alginate beads as sacrificial templates, J. Mater. Chem. 22 (2012) 4073.
[13] W. Liu, C. Selomulya, W. Wu, X.D. Chen, A single step assembly of uniform microparticles for controlled release applications,, Soft Matter 7 (2011) 3323.
[14] I.V. Melnyk, B. Alonso, Y.L. Zub, E. Véron, D. Massiot, T. Cacciaguerra, Spray-dried mesoporous silica microspheres with adjustable textures and pore surfaces

homogenously covered by accessible thiol functions, J. Mater. Chem. 18 (2008) 1368.
[15] K. Waldron, Z. Wu, W.D. Wu, W. Liu, D. Zhao, X.D. Chen, C. Selomulya, Formation of uniform large SBA-15 microspheres via spray drying, J. Mater. Chem. 2 (2014) 19500–19508.
[16] W. Stöber, A. Fink, E. Bohn, Controlled growth of monodisperse silica spheres in the micron size range, J. Colloid Interface Sci. 26 (1968) 62–69.
[17] N. Plumeré, A. Ruff, B. Speiser, V. Feldmann, H.A. Mayer, Stöber silica particles as basis for redox modifications: particle shape, size, polydispersity, and porosity, J. Colloid Interface Sci. 368 (2012) 208–219.
[18] S.-L. Chen, P. Dong, G.-H. Yang, J.-J. Yang, Characteristic aspects of formation of new particles during the growth of monosize silica seeds, J. Colloid Interface Sci. 180 (1996) 237–241.
[19] K. Nozawa, H. Gailhanou, L. Raison, P. Panizza, H. Ushiki, E. Sellier, J.P. Delville, M.H. Delville, Smart control of monodisperse stöber silica Particles: effect of reactant addition rate on growth process, Langmuir 21 (2005) 1516–1523.
[20] H. Nakabayashi, A. Yamada, M. Noba, Y. Kobayashi, M. Konno, D. Nagao, Electrolyte-added one-pot synthesis for producing monodisperse, micrometer-sized silica particles up to 7 μm, Langmuir 26 (2010) 7512–7515.
[21] C.T. Kresge, M.E. Leonowicz, W.J. Roth, J.C. Vartuli, J.S. Beck, Ordered mesoporous molecular sieves synthesized by a liquid-crystal template mechanism, Nature 359 (1992) 710–712.
[22] N.K. Raman, M.T. Anderson, C.J. Brinker, Template-based approaches to the preparation of amorphous, nanoporous silicas, Chem. Mater. 8 (1996) 20.
[23] L. Zhang, L. Jin, B. Liu, J. He, Templated growth of crystalline mesoporous materials: from soft/hard templates to colloidal templates, Front. Chem. 7 (2019) 22.
[24] H. Xia, G. Wan, J. Zhao, J. Liu, Q. Bai, Preparation and characterization of monodisperse large-porous silica microspheres as the matrix for protein separation, J. Chromatogr. A 1471 (2016) 138–144.
[25] J. Chen, L. Zhu, L. Ren, C. Teng, Y. Wang, B. Jiang, J. He, Fabrication of monodisperse porous silica microspheres with a tunable particle size and pore size for protein separation, ACS Appl. Bio Mater. 1 (2018) 604–612.
[26] J. Bai, Q. Zhu, C. Tang, J. Liu, Y. Yi, Q. Bai, Synthesis and application of 5 μm monodisperse porous silica microspheres with controllable pore size using polymeric microspheres as templates for the separation of small solutes and proteins by high-performance liquid chromatography, J. Chromatogr. A 1675 (2022) 463165.
[27] V. Šmigol, F. Švec, Synthesis and properties of uniform beads based on macroporous copolymer glycidyl methacrylate–ethylene dimethacrylate: a way to improve separation media for HPLC,, J. Appl. Polym. Sci. 46 (1992) 1439–1448.
[28] S. Grama, D. Horák, Preparation of monodisperse porous silica particles using poly (glycidyl methacrylate) microspheres as a template, Physiol. Res. (2015) 11–17.
[29] L.C. Costa, R.C. Monteiro, H.M.A. Castro, T.S. Ribeiro, M.A. Oliveira, E.C. C. Torquato, M.E. Arcanjo, M.R.C. Marques, Glycidyl methacrylate-ethylene glycol dimethacrylate copolymers with varied pore structures prepared with different reaction parameters, Mat. Res. 23 (2020), e20190550.
[30] J. He, C. Yang, X. Xiong, B. Jiang, Preparation and characterization of monodisperse porous silica microspheres with controllable morphology and structure, J. Polym. Sci. Polym. Chem. 50 (2012) 2889–2897.
[31] J.C. Steinbach, F. Fait, S. Wagner, A. Wagner, M. Brecht, H.A. Mayer, A. Kandelbauer, Rational design of pore parameters in monodisperse porous poly (glycidyl methacrylate-co-ethylene glycol dimethacrylate) particles based on response surface methodology, Polymers 14 (2022) 382.
[32] J.C. Groen, L.A.A. Peffer, J. Pérez-Ramírez, Pore size determination in modified micro- and mesoporous materials. Pitfalls and limitations in gas adsorption data analysis, Microporous Mesoporous Mater. 60 (2003) 1–17.
[33] K. Hosoya, J.M.J. Fréchet, Influence of the seed polymer on the chromatographic properties of size monodisperse polymeric separation media prepared by a multi-step swelling and polymerization method, J. Polym. Sci. Polym. Chem. 31 (1993) 2129–2141.
[34] J.C. Steinbach, F. Fait, H.A. Mayer, A. Kandelbauer, Monodisperse porous silica/polymer nanocomposite microspheres with tunable silica loading, morphology and porosity, Int. J. Mol. Sci. 23 (2022) 14977.
[35] G. Socrates, Infrared and Raman Characteristic Group Frequencies: Tables and Charts, third ed., John Wiley & Sons Inc, 2004.
[36] H.A. Claessens, M.A. van Straten, Review on the chemical and thermal stability of stationary phases for reversed-phase liquid chromatography, J. Chromatogr. A 1060 (2004) 23–41.

Supporting Information

Impact of porosity and surface functionalization of the hard templates on the preparation of mesoporous silica microspheres

Fabio Fait[a,b,†], Julia C. Steinbach[a,b,†], Andreas Kandelbauer[b,c] and Hermann A. Mayer[a,*]

[a]Institute of Inorganic Chemistry, University of Tübingen, Auf der Morgenstelle 18, 72076 Tübingen, Germany
[b]Process Analysis and Technology (PA&T), Reutlingen Research Institute, Reutlingen University, Alteburgstrasse 150, 72762 Reutlingen, Germany
[c]Institute of Wood Technology and Renewable Materials, Department of Material Sciences and Process Engineering (MAP), University of Natural Resources and Life Sciences, Gregor-Mendel-Straße 33, 1180 Vienna, Austria

*Correspondence: hermann.mayer@uni-tuebingen.de
†These authors contributed equally.

Chemicals

Polyvinylpyrrolidone K_{30} (PVP, mean average 40000 g mol^{-1}) was purchased from abcr GmbH. Styrene was obtained by Fisher Chemicals. Dibenzoyl peroxide (BPO) was bought from Sigma-Aldrich.

Synthesis of polystyrene

Monodisperse polystyrene particles with diameters of 1.9 ± 0.1 µm were prepared as reported earlier (**Figure S1**) [1].

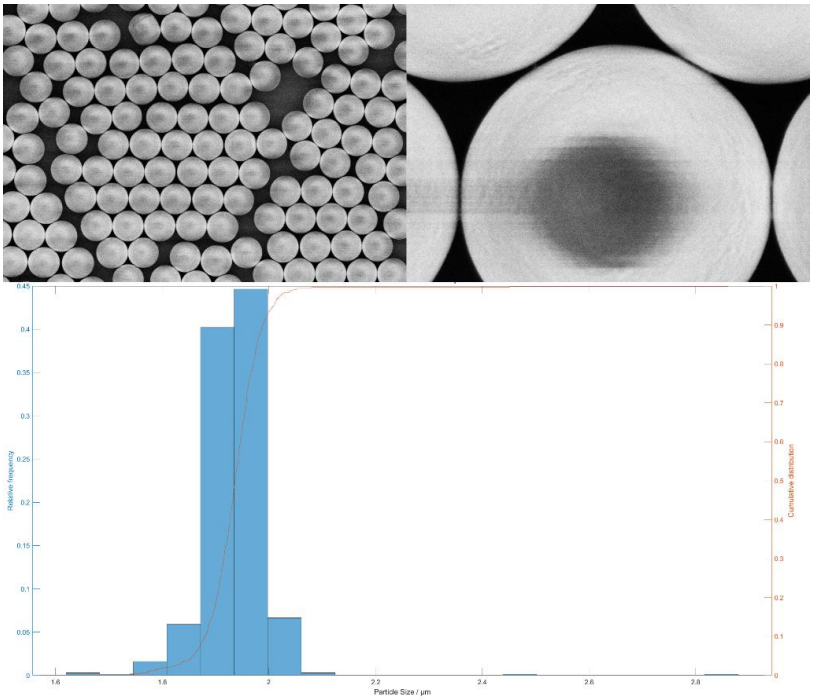


Figure S1. SEM images of applied polystyrene particles (top) and their particle size distribution (bottom).

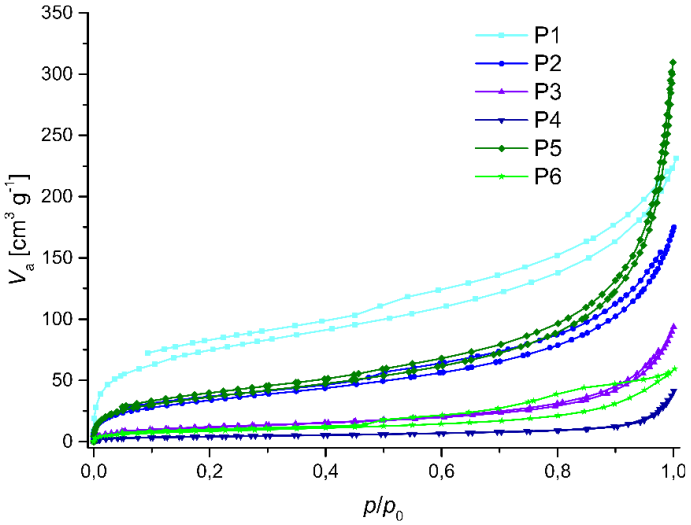


Figure S2. Isotherms of *p*(GMA-*co*-EDMA) templates.

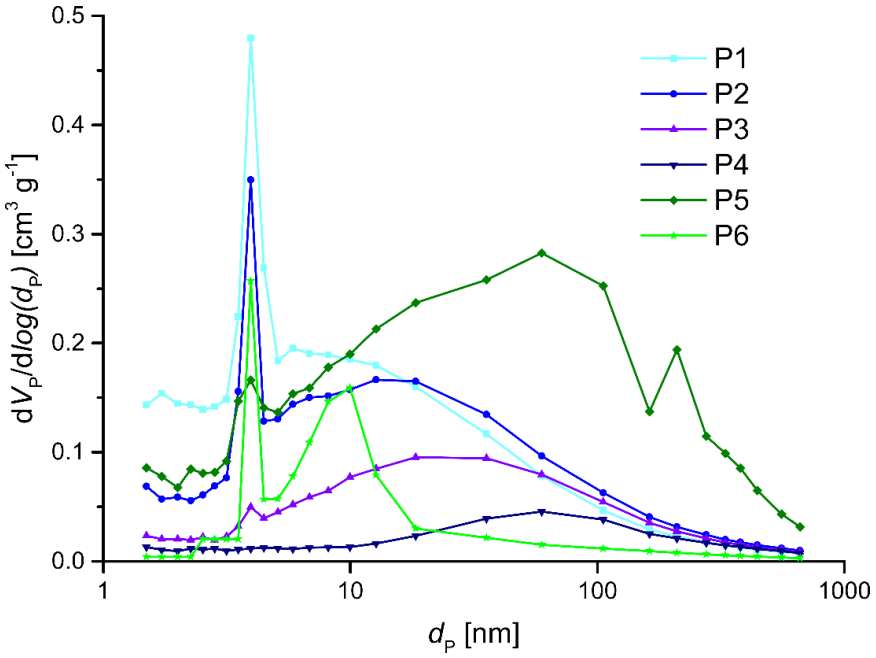


Figure S3. Pore size distributions from the desorption isotherms of the *p*(GMA-*co*-EDMA) templates **P1–6**.

Table S1. Elemtar analysis of **P1-6@TEPA**.

	H [%]	C [%]	N [%]
P1@TEPA	7.63	57.14	2.06
P2@TEPA	7.70	56.74	2.43
P3@TEPA	7.59	56.70	2.12
P4@TEPA	7.72	55.42	2.14
P5@TEPA	7.79	56.99	2.50
P6@TEPA	7.65	57.24	2.24

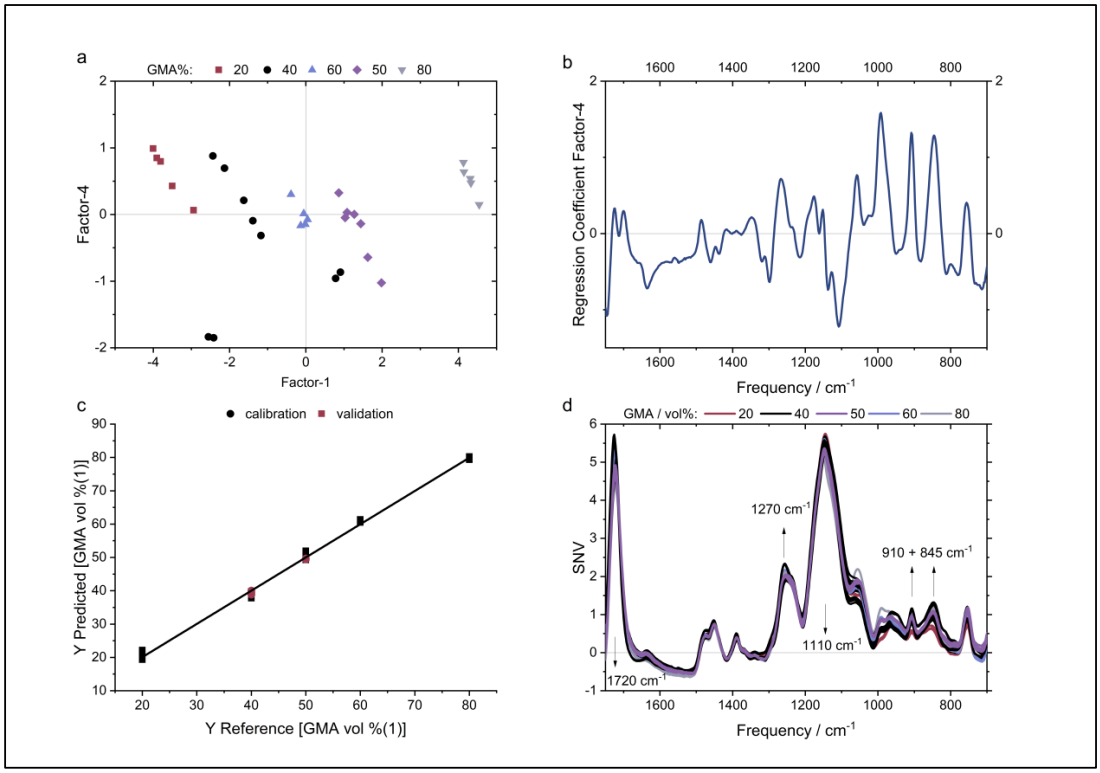


Figure S4. PLS-R model for the determination of GMA% from IR spectra. a) Scores plot of Factor-1 and Factor-4 with groups colored according to the GMA% used in preparation of the PBs. b) Regression coefficient of Factor-4 giving the importance of each frequency for the model. c) Predicted versus reference plot for the GMA% and d) shows the SNV pretreated spectra used for model building with important frequencies highlighted.

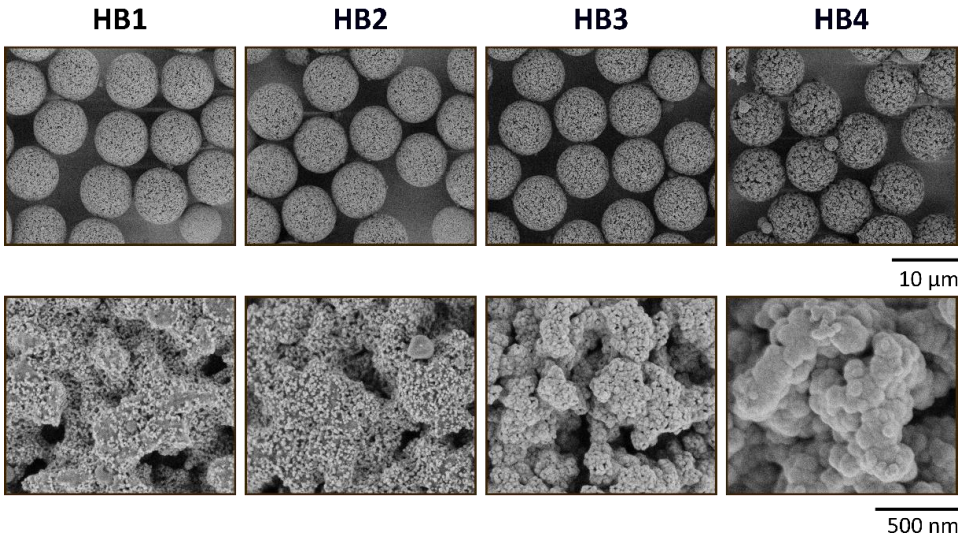


Figure S5. SEM images of polymer/SiO_2 hybrid beads with varying GMA to EDMA ratio. 2,000 (top row) and 50,000 (bottom row) magnification.

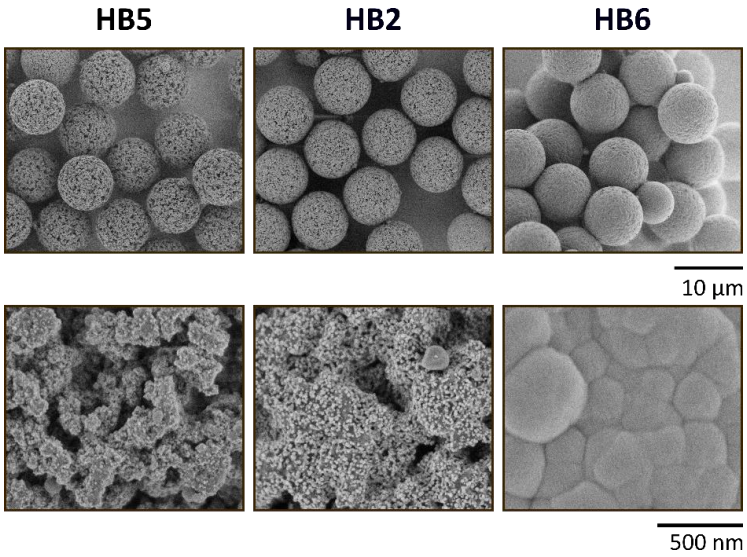


Figure S6. SEM images of polymer/SiO_2 hybrid beads with varying monomer to porogen ratio. 2,000 (top row) and 50,000 (bottom row) magnification.

Table S2. Properties of hybrid beads **HB1-6** using different polymer templates with different amounts of GMA.

	P		**HB**		**MPSM**	
	particle size [µm]	change [µm]	particle size [µm]	change [µm]	particle size [µm]	shrinkage [% µm³]
HB1	7.9	+ 0.3	8.2	- 1.6	6.6	47.9
HB2	7.8	+ 0.5	8.3	- 1.5	6.8	45.0
HB3	7.5	+ 0.6	8.1	- 1.1	7.0	35.5
HB4	7.3	+ 0.9	8.2	- 1.1	7.1	35.1
HB5	7.6	+ 0.6	8.2	- 1.9	6.3	54.6
HB6	7.9	+ 0.9	8.8	- 0.6	8.2	19.1

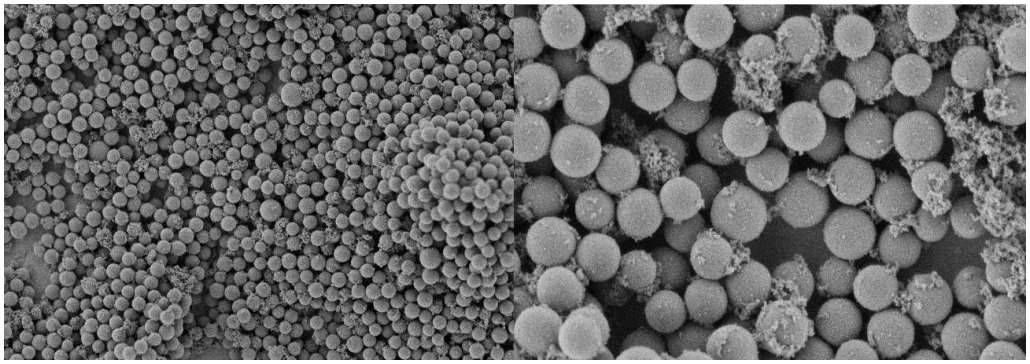


Figure S7. SEM images of filtrate of polymer/SiO_2 hybrid bead **HB6** after washing process.

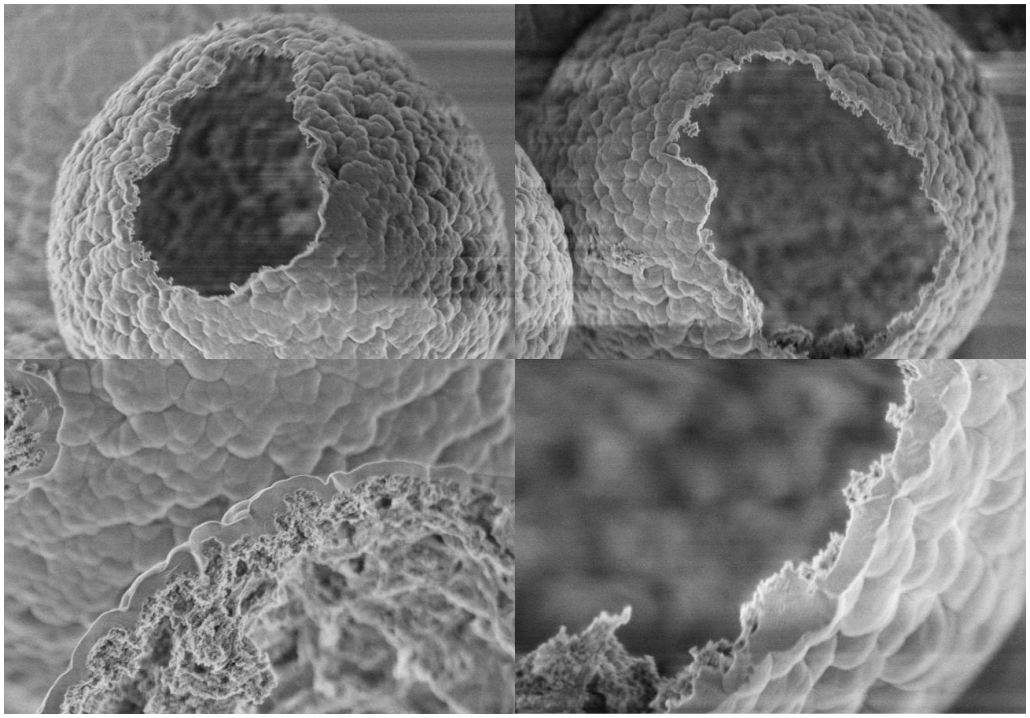


Figure S8. SEM images of broken silica microspheres of **MPSM6**.

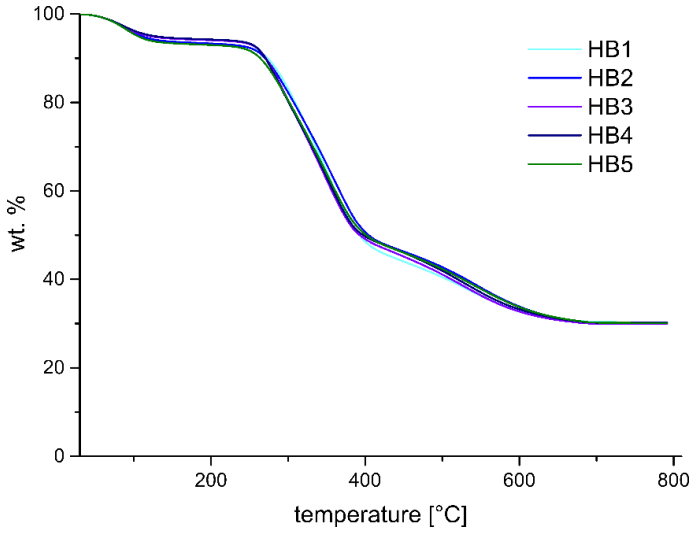


Figure S9. TGA curves of the hybrid beads **HB1-5**.

References

[1] H. Xia, G. Wan, J. Zhao, J. Liu, Q. Bai, Preparation and characterization of monodisperse large-porous silica microspheres as the matrix for protein separation, J. Chrom. A 1471 (2016) 138–144.

7 Publikation II

polymers

MDPI

Article

Rational Design of Pore Parameters in Monodisperse Porous Poly(glycidyl methacrylate-*co*-ethylene glycol dimethacrylate) Particles Based on Response Surface Methodology

Julia C. Steinbach [1,2,†], Fabio Fait [1,2,†], Stefanie Wagner [2], Alexandra Wagner [1,3], Marc Brecht [1,3], Hermann A. Mayer [2] and Andreas Kandelbauer [1,4,*]

[1] Process Analysis & Technology, Reutlingen Research Institute, Reutlingen University, Alteburgstraße 150, 72762 Reutlingen, Germany; Julia.Steinbach@Reutlingen-University.de (J.C.S.); Fabio.Fait@Reutlingen-University.de (F.F.); Alexandra.Wagner@Reutlingen-University.de (A.W.); Marc.Brecht@Reutlingen-University.de (M.B.)
[2] Institute of Inorganic Chemistry, University of Tübingen, Auf der Morgenstelle 18, 72076 Tübingen, Germany; stefaniewagnersb@googlemail.com (S.W.); hermann.mayer@uni-tuebingen.de (H.A.M.)
[3] Institute of Physical and Theoretical Chemistry, University of Tübingen, Auf der Morgenstelle 18, 72076 Tübingen, Germany
[4] Department of Material Sciences and Process Engineering (MAP), Institute of Wood Technology and Renewable Materials, University of Natural Resources and Life Sciences, Gregor-Mendel-Straße 33, 1180 Vienna, Austria
* Correspondence: Andreas.Kandelbauer@Reutlingen-University.de; Tel.: +49-(0)7-12-1271-2009
† These authors contributed equally to this work.

check for updates

Citation: Steinbach, J.C.; Fait, F.; Wagner, S.; Wagner, A.; Brecht, M.; Mayer, H.A.; Kandelbauer, A. Rational Design of Pore Parameters in Monodisperse Porous Poly(glycidyl methacrylate-*co*-ethylene glycol dimethacrylate) Particles Based on Response Surface Methodology. *Polymers* **2022**, *14*, 382. https://doi.org/10.3390/polym14030382

Academic Editor: José António Covas

Received: 30 December 2021
Accepted: 17 January 2022
Published: 19 January 2022

Publisher's Note: MDPI stays neutral with regard to jurisdictional claims in published maps and institutional affiliations.

Copyright: © 2022 by the authors. Licensee MDPI, Basel, Switzerland. This article is an open access article distributed under the terms and conditions of the Creative Commons Attribution (CC BY) license (https://creativecommons.org/licenses/by/4.0/).

Abstract: Monodisperse porous poly(glycidyl methacrylate-*co*–ethylene glycol dimethacrylate) particles are widely applied in different fields, as their pore properties can be influenced and functionalization of the epoxy group is versatile. However, the adjustment of parameters which control morphology and pore properties such as pore volume, pore size and specific surface area is scarcely available. In this work, the effects of the process factors monomer:porogen ratio, GMA:EDMA ratio and composition of the porogen mixture on the response variables pore volume, pore size and specific surface area are investigated using a face centered central composite design. Non-linear effects of the process factors and second order interaction effects between them were identified. Despite the complex interplay of the process factors, targeted control of the pore properties was possible. For each response a response surface model was derived with high predictive power (all $R^2_{predicted} > 0.85$). All models were tested by four external validation experiments and their validity and predictive power was demonstrated.

Keywords: porous microspheres; design of experiment; seed swelling polymerization; p(GMA-*co*-EDMA); particles; monodisperse; pores; morphology; process optimization

1. Introduction

Porous polymer particles have attracted considerable interest in various applications ranging from clinical diagnostics [1], immobilization support for biocatalysts [2], separation processes like chromatography [3–6], ion exchange phases [7] to applications as adsorption materials [8,9] or as hard-templates [10–12] for inorganic materials with defined structures. In particular, porous poly(glycidyl methacrylate-*co*-ethylene glycol dimethacrylate) (p(GMA-*co*-EDMA)) has been widely used, as the epoxy ring of GMA can be derivatized in various ways by ring opening reactions [2,13–15]. This allows application-specific functionalization and makes the p(GMA-*co*-EDMA) a versatile platform polymer. p(GMA-*co*-EDMA) particles have been used as chromatographic column material [4,16], as carriers for biocatalysts [17], for solid phase extraction [8] or as hard template for porous silica particles with defined pore structure [11].

For many applications involving particles, a small size distribution is advantageous. Monodispersity in these porous microspheres can be achieved through seeded swelling polymerization [18,19]. This approach allows one not only to influence the dispersity and size of the microspheres, but also to tailor the surface properties [20]. Thereby the increase in size is mainly dependent of the ratio of the organic phase to the amount of seed particles [21,22]. It has been reported that the specific surface area, porosity and pore volume depend on the composition of the organic phase of seeded swelling polymerization [21,23–28]. The organic phase usually consists of the monomers, here EDMA as crosslinker and GMA as monomer with a functional epoxide ring, and the porogen mixture, which are inert solvents, here cyclohexanol and toluene.

However, due to the high complexity of the system and the dependency on the different solubilities of the components, previous studies have been rather confined to semi quantitative statements from considerations of isolated process factors ("one-factor-at-a-time", OFAT), which do not allow a specific control of the synthesis and the pore and surface properties. In contrast to the common OFAT approach, in response surface methodology (RSM) multiple process factors are simultaneously and systematically varied and their effects are analyzed using a statistical approach. RSM provides not only insight in the effect strengths of single process factors but also allows to detect the presence of non-linear behavior and synergistic interactions between multiple process factors. This provides a detailed causal model of the studied process. [29–31] Currently, to the best of our knowledge, there is no predictive causal model available that is actually based on the numerical effects of the process factors on the morphological properties of porous p(GMA-*co*-EDMA) particles and thus allow for demand-driven control of particle properties.

The present study aims at demonstrating a valid and robust model allowing for tailored modification of pore parameters in porous p(GMA-*co*-EDMA) particles using RSM. For this purpose, the statistical significance and effect strengths of the process factors involved in the synthesis (a) monomer:porogen ratio, (b) GMA:EDMA ratio and (c) composition of the porogen mixture (toluene:cyclohexanol) were determined with respect to the responses pore volume, pore size and specific surface area using a face centered central composite experimental design. The pore properties were analyzed using inverse size exclusion chromatography (iSEC). To enable further application-specific functionalization, the conversion of the epoxide groups in the particles was studied by FTIR in combination with multivariate calibration by partial least squares regression (PLSR). Additional particles were prepared using four sets of factor level combinations as external validation experiments and characterized to verify the robustness and validity of the response surface models (RSM) established. The RSM approach has offered a better understanding of the seeded swelling polymerization for porous p(GMA-*co*-EDMA) and has provided valid, predictive models for the pore volume, pore size and specific surface area, which allow targeted adjustment of these quantities.

2. Materials and Methods

2.1. Chemicals

Styrene (99%), and ethylene glycole dimethacrylate (EDMA, 98%) were purchased from Fisher Scientific GmbH (Schwerte, Germany). Polyvinylpyrrolidone K30 (PVP), benzoyl peroxide (BPO, 75%), dibutyl phthalate (DBP, 99%) and glycidyl methacrylate (GMA, ≥97%) were purchased from Sigma-Aldrich Chemie GmbH (Taufkirchen, Germany). Polyvinyl alcohol (PVA, hydrolyzed 86–89%) was purchased from abcr GmbH (Karlsruhe, Germany). Sodium dodecyl sulfate (SDS, ≥99%) was purchased from Carl Roth GmbH + Co. KG (Karlsruhe, Germany). Ethanol 96% was purchased from VWR Chemicals (Darmstadt, Germany). All chemicals were used as delivered.

For the iSEC analysis tetrahydrofuran 99.9% was purchased from Carl Roth GmbH + Co. KG (Karlsruhe, Germany) and the polystyrene (PS) standards were purchased from PSS Polymer Standards Service GmbH (Mainz, Germany).

2.2. Instrumentation

An Ultra-Turrax T50 (IKA®-Werke GmbH & CO. KG, Staufen, Germany) was used for homogenization of the prepared emulsions.

iSEC measurements were carried out using an Agilent 1100 series system (Agilent Technologies, Waldbronn, Germany) equipped with a quaternary pump with degasser, an auto sampling system, 6-port valve for column selection and a DAD detector (254 nm). Instrument control, data acquisition and automated data analysis was performed by the Chem-Station software (B.04.03, Agilent Technologies, Waldbronn, Germany).

Spectral characterization was performed using a Frontier 2 FTIR (PerkinElmer LAS GmbH, Rodgau, Germany) with an attenuated total reflection accessory. The resolution was 2 cm^{-1} with 4 scans. For data processing the spectral region was reduced to the region from 1750 to 700 cm^{-1} which carried the highest amount of relevant information. The spectra were smoothed using a Savitzky-Golay filter and were treated with standard normal variate transformation, to remove multiplicative scattering interferences [32,33].

A partial least square regression model (PLSR, kernel algorithm) was applied for multivariate calibration of the relative GMA ratio. A total of 155 spectra from particles Std1–19 were used for modelling. From the 24 spectra of particles Val1–4 the predictive power of the model was verified. The processing software Unscrambler-X (CAMO Software AS, version 10.5.1, Oslo, Norway) was employed for spectral preprocessing, spectral analysis and multivariate data analysis.

2.3. Seeded Suspension Polymerization of Porous p(GMA-co-EDMA) Particles

The porous p(GMA-*co*-EDMA) particles were synthesized by seeded suspension polymerization using toluene and cyclohexanol as porogens. The polystyrene (PS) seeds were prepared according to the procedure provided in the Appendix A. 0.3 g PS seeds and 5 mL of a 2.0 $g{\cdot}L^{-1}$ SDS solution were sonicated for 10 min. An emulsion containing 2.0 mL of the activator DBP and 150 mL of SDS (2.53 $g{\cdot}L^{-1}$) were homogenized for 10 min at 5000 rpm and added to the seed particle suspension. The mixture was stirred for 24 h at 200 rpm at room temperature. Thereafter an emulsion (10 min, 5000 rpm) containing 150 mL of SDS (3.33 $g{\cdot}L^{-1}$), initiator BPO (0.4 g), porogens and acrylate monomers was added. The relative amount of added monomers (GMA:EMDA) and porogens (toluene:cyclohexanol) was systematically varied according to the experimental design (Table 1). The absolute volume of added monomers and porogens was 30 mL for each synthesis.

Table 1. Range of process factors level setting as used in the face-centered central composite experimental design (FCD).

Factor	Name	Low Setting (−1)	Center Point (0)	High Setting (+)
A	Monomer vol%	30	50	70
B	GMA vol%	20	50	80
C	Toluene vol%	0	50	100

To allow for complete swelling, the system was stirred at 200 rpm for another 24 h. 150 mL of a 23.3 $g{\cdot}L^{-1}$ PVA solution was added to the mixture as stabilizer. The reaction mixture was heated to 70 °C and stirred at 200 rpm for 24 h for polymerization. After polymerization the porous particles were filtered off and washed three times with ethanol and three times with water. The porous copolymer particles were then dried prior to analysis.

2.4. Experimental Design

A face-centered central composite experimental design (FCD) was set up, allowing the mathematical description of non-linear terms [34,35]. A total of 19 particle batches were synthesized with five center point (CP) replications to determine reproducibility and system variance.

The effects of three factors were investigated by systematic variation according to an FCD response surface design, with the low, intermediate and high factor level settings given in Table 1. As factors the ratio of monomer (methacrylates) to porogens (A: monomer:porogen vol%), the ratio of monomer with the functional group (GMA) to the crosslinker (EDMA) (B: GMA:EDMA vol%) and the ratio of the porogens toluene to cyclohexanol (C: toluene:cyclohexanol vol%) were varied.

The effects were analyzed using analysis of variance (ANOVA). The significance level was $\alpha = 0.05$, meaning that a model or model term was considered statistically significant if its p-value was $p \leq 0.05$.

For model validation four additional syntheses within the design space were conducted. The validation experiments Val1–Val4 were selected as a series with increasing GMA content moving through the experimental space along one factor axis, see (Table 2). This would correspond to a one-factor-at-a-time experiment. The run order is the randomized order in which the experiments were actually performed to compensate for systematic errors.

Table 2. Factor level settings and the corresponding particle properties specific pore volume, pore size, specific surface area, particle size and dispersity d_{90}/d_{10} listed according to Yates standard order (Std).

		Factor Level Settings			**Response Values**				
		A	**B**	**C**					
Std	**Run**	**Monomer:Porogen Ratio**	**GMA:EDMA Ratio**	**Toluene:Cyclohexanol Ratio**	**Pore Volume V_p**	**Pore Size Φ_{50}**	**Specific Surface Area S**	**ParticleSize**	**Dispersity d_{90}/d_{10}**
		/vol%	**/vol%**	**/vol%**	**/mL·g^{-1}**	**/Å**	**/m^2·g^{-1}**	**/µm**	**-**
*** 1**	**2**	30	20	0	0.52	166	126	7.41	1.15
2	**5**	70	20	0	0.06	37	71	8.15	1.11
*** 3**	**3**	30	80	0	0.44	631	28	7.42	1.08
4	**7**	70	80	0	**n.a.**	**n.a.**	**n.a.**	7.74	1.20
5	**4**	30	20	100	0.55	426	51	8.82	1.16
6	**8**	70	20	100	0.18	49	148	9.41	1.06
7	**10**	30	80	100	**n.a.**	**n.a.**	**n.a.**	**n.a.**	**n.a.**
8	**9**	70	80	100	0.25	715	14	9.22	1.13
9	**1**	50	50	50	0.3	217	56	8.31	1.14
10	**6**	50	50	50	0.3	237	50	8.09	1.11
11	**11**	50	50	50	0.26	197	53	8.83	1.11
12	**13**	30	50	50	0.49	438	45	8.56	1.05
13	**19**	70	50	50	0.09	126	28	9.1	1.06
14	**18**	50	20	50	0.3	83	146	9.07	1.04
15	**14**	50	80	50	0.26	538	20	8.81	1.07
16	**15**	50	50	0	0.17	88	77	8.39	1.06
17	**17**	50	50	100	0.5	332	60	9.38	1.04
18	**16**	50	50	50	0.29	177	66	8.92	1.05
19	**12**	50	50	50	0.28	193	58	8.37	1.07
Val1	**20**	50	20	73	0.41	124	132	8.41	1.09
Val2	**21**	50	40	73	0.56	141	159	7.81	1.15
Val3	**22**	50	60	73	0.37	370	40	7.87	1.15
Val4	**23**	50	80	73	0.36	744	20	7.19	1.19

* marks model outliers.

2.5. Pore Characterization Using Inverse Size Exclusion Chromatography (iSEC)

The particles were packed into stainless steel columns (4.6 × 250 mm) using the slurry method with ethanol/water (50:50 vol%:vol%). For characterization of the pore properties the columns were analyzed by iSEC. A set of 19 polystyrene (PS) standards from M_w = 162 Da–2.5 mDa with a molar-mass dispersity of < 1.1 were applied. 10 µL of each 2.5 g·L^{-1} PS in THF were separately injected (10 µL) three times. The lowest molecular weight standard was used as a t_0 marker. All standards were measured with THF as eluent and a flow rate of 0.25 mL·min^{-1}.

The pore parameters were analyzed in accordance to the method of Halász et al. (1978) [36]. The pore volume V_p is calculated using Equation (1):

$$V_p = V_0 - V_i \quad (1)$$

as the difference between the dead volume V_0 (=elution volume of t_0 marker) and V_i the interstitial volume (=elution volume of totally permeating volume).

The distribution coefficient K_{SEC} is dependent on the pore size of the particles. It can be derived from the experimentally determined elution volume V_e, the interstitial volume V_i and the elution volume of the totally permeating solute V_t, see Equations (2) and (3):

$$V_e = V_i + V_p \times K_{SEC} \quad (2)$$

$$K_{SEC} = \frac{V_e - V_i}{V_p} \quad (3)$$

According to Halász et al. the exclusion values (pore size) Φ in Å of linear PS in a good solvent can be calculated based on the molecular weights M_w (Da) of the PS standards as follows:

$$\Phi \cong 0.62\ {M_w}^{0.59} \quad (4)$$

The mean pore size Φ_{50} is determined from the lognormal distribution plot of K_{SEC} as function of log(Φ) the at K_{SEC} = 50%.

From the pore volume V_p (mL) and the mean pore size Φ_{50} (Å) the specific surface area S can be derived according to Equation (5):

$$\mathrm{S} = \frac{4000 \times V_p}{\Phi_{50}} \quad (5)$$

2.6. Scanning Electron Microscopy Images (SEM)

For the evaluation of morphology, particle size and dispersity SEM images were acquired using a Hitachi SU8030 (Hitachi High-Tech Europe GmbH, Krefeld, Germany). The size and dispersity were assessed semi-automatically from the SEM images using a self-written MATLAB script. 400–500 particles were measured (min. 374), except for Std7 were no sufficient number of intact particles could be evaluated. The median particle diameter is given as particle size in µm. The dispersity is given by the d_{90}/d_{10} value which indicates the width of the particle size distribution. Here d_{90} is the value below which 90% of the distribution lies, with d_{10} corresponding to 10% of the distribution. A d_{90}/d_{10} value smaller than 1.4 is considered as a monodisperse distribution.

3. Results and Discussion

For systematic evaluation of the synthesis factors which influence the particle size, pore volume, pore size, specific surface area and morphology of the porous particles, approach of RSM was applied. Compared to single-factor variation-based experiments, RSM not only offers a more time- and resource-efficient approach, but also allows the determination of non-linear effects and interactions of the parameters [37].

Factor level settings of the process factors A: monomer:porogen ratio, B: GMA:EDMA ratio and the porogen composition C: toluene:cyclohexanol were systematically varied according to the FCD design given in Table 2. All p(GMA-*co*-EDMA) particles Std1–19 (Table 2) were synthesized using a seeded swelling polymerization process. The employed seed PS particles were 1.95 µm in size and had a narrow size distribution of d_{90}/d_{10} = 1.09 (span: 0.09). They were all from the same batch. Std1 and Std3 were defined as outliers due to their untypically large residuals and increased lack of fit. These two experiments were excluded from further analysis.

3.1. Particle Size and Dispersity

The p(GMA-*co*-EDMA) particle sizes varied between 7.41–9.38 µm and particles of all batches showed a monodisperse distribution with a d_{90}/d_{10} range between 1.04 and 1.20 (CV% max. 15.8%), see Figure 1. No statistically significant effects of the factors on the dispersity were found. The median d_{90}/d_{10} is 1.08. This is in accordance with the finding that the dispersity of the seed particle is crucial for the dispersity of the product [38].

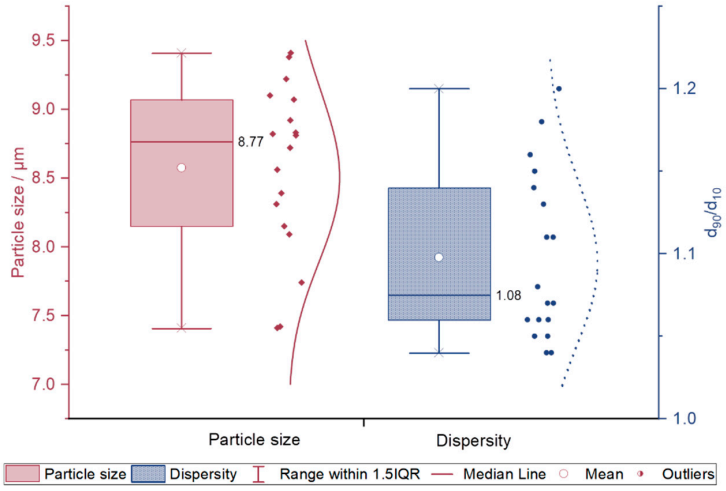


Figure 1. Box-Whisker-Plot with lognormal distribution curve of single values for particle sizes (left hand, red) and d_{90}/d_{10} (right hand, blue) of standard order 1–19. Box displays 1. and 3. quartile, whiskers display 1. and 3. quantile + 1.5·interquartile range. x = minimum and maximum values.

For the final particle size, a statistically significant effect ($p = 0.0004$) of the porogen composition is found. The model equation in terms of coded factors of the effect onto the particle size is given in Equation (6):

$$\text{Particle size}/\mu\text{m} = 8.69 + 0.5521\ \text{C} \quad (6)$$

The higher the ratio of toluene:cyclohexanol/vol% larger particles are obtained ($p = 0.0004$). The model quality parameters are $R^2 = 0.6070$ and $R^2_{\text{predicted}} = 0.4942$.

3.2. Morphology

A clear change in morphological characteristics is observed with the systematic variation factor level settings, (Figure 2). Increasing the monomer ratio of the organic phase, generates less porous particles. This effect is especially pronounced at high levels of GMA content of the monomers. The toluene:cyclohexanol ratio strongly affects the surface roughness. While a high content of toluene generates a smooth particle surface, high cyclohexanol content leads to a rough dimpled appearance. The roughness and surface irregularities are intensified with increasing GMA ratio in the monomer composition.

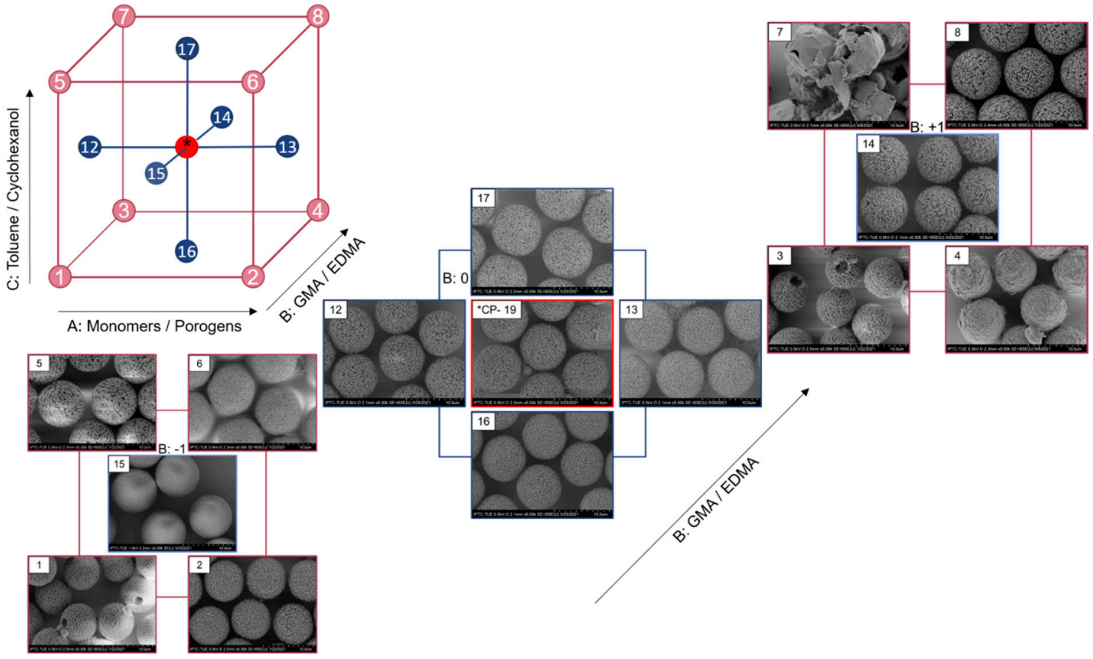


Figure 2. SEM images with 10,000 magnification of each particle batch numbered by standard order. The design cube is divided according to the level of factor B: GMA:EDMA ratio. Factorial points are numbered according to the standard order given in Table 2 and are displayed burgundy, central point is displayed red and axial points are displayed blue.

Interestingly, Std1 and Std3 show a hole at one side of the particle, which is approximately 2 µm in diameter. Both batches were synthesized with a high content of cyclohexanol as the porogen (70 vol% of organic phase). Similar behavior was found earlier when high amounts of cyclohexanol were used [19,39]. This finding can be related to the solubility of the seed particle PS in the overall composition of the organic phase. The suitability of solvents can be approximated using the relative energy difference (RED), which is the ratio of the distance in Hansen space R_a to the radius of the interaction sphere in the Hansen space R_0 (here for PS). Good solvents show RED values below 1, solvents around 1 are found to only partly dissolve the solute (or swell it), while RED values higher are non-solvents. [40] Cyclohexanol is the least suitable solvent for PS used in the experiments and shows a RED of 0.96 (GMA 0.82, toluene 0.65, DBP 0.59). While the seed particle is soluble in the organic phase still containing the monomers, with progressing polymerization the solubility decreases until the solubility limit is exceeded and the seed particle is reformed. Therefore, no polymerization of methacrylate takes place in this area, leaving a hole after the PS is detached during purification. In contrast to the syntheses shown here, the seed swelling polymerization of p(GMA-*co*-EDMA) using 1-hexanol as porogen results in polystyrene caps persisting on the particle surface instead of holes [41]. A dependence on the solubilities is assumed. This could also be the reason for the higher studentized residuals, for the analysis see Table 2.

With the reaction conditions Std7 with a high porogen content consisting of 100 vol% toluene and a high GMA ratio of monomers, no stable particles were obtained. From SEM pictures the particles look like empty shells or skins with a smooth outer layer (Figure 2). This phenomenon could result from low solubility of toluene in water, leading to a displacement of monomers at the interface with the continuous aqueous phase to minimize surface tension. Thus, a polymeric skin is formed during polymerization around the toluene which is present in and accumulated on the inside of the particle [20,42].

Particles obtained with factor settings according to Std4 exhibited no visible porosity, but rather outwardly curved dimple structures (Figure 2). This effect results from high monomer content with small ratio of GMA and the usage of pure cyclohexanol as porogen. Due to the lack in porosity no iSEC analysis could be performed with these particles.

3.3. Multivariate Calibration Model for Epoxy Functionalization

With the epoxy group as functional group the p(GMA-*co*-EDMA) particles can easily be converted to a desired functionalization. For multivariate calibration a PLSR model based on nine factors was calculated from the spectra of Std1–19 (Figure 3). To test the predictive power of the model, the GMA content of validation experiments Val1–4 was predicted (Table 3), based on the corresponding SNV pre-treated spectra (Figure 3c). The explained variance plot is given in Appendix B, Figure A1.

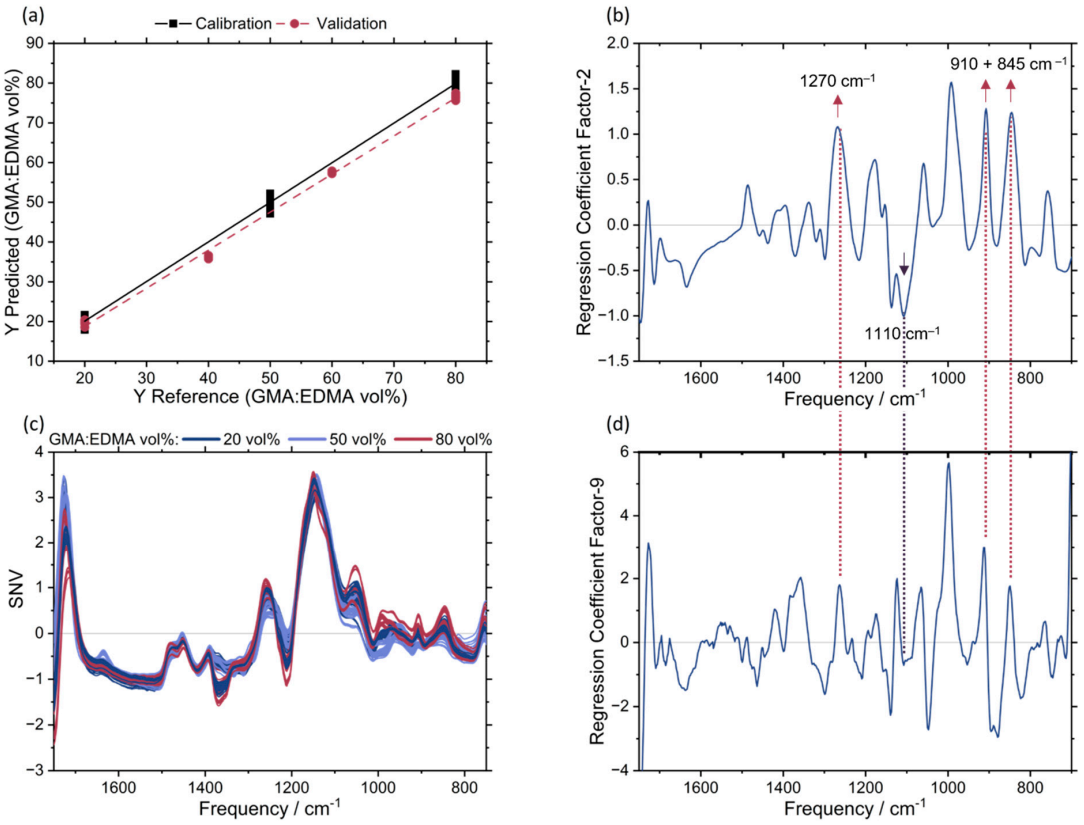


Figure 3. PLSR with nine factors for GMA:EDMA ratio based on FTIR spectra. (**a**) shows the predicted vs. reference of GMA:EDMA ratio for calibration (■) and validation (●). The SNV pre-treated spectra of GMA:EDMA ratio of 20 vol% (dark blue), 50 vol% (light blue) and 80 vol% (red) are displayed in (**c**). (**b**,**d**) show the regression coefficients for factor two (highest explained variance) and factor nine (model regression coefficient) and influential frequencies are highlighted.

With an $R^2_{calibration}$ = 0.99 and $R^2_{predicted}$ = 0.98 the model quality is very good (Figure 3a). The root-mean-square-error of calibration is 1.2 vol%, and that of prediction is 2.9 vol% GMA. The model allows an accurate determination of the GMA:EDMA monomer ratio (relative deviation predicted/actual < 5%) used in the synthesis (Table 3). The highest explained variances lie on factors 1 and 2 (88%, Figure 3b). However, due to the complex interplay between the process factors used in the system [33], nine regression coefficients are required to build a robust model with high predictive power. From the regression

coefficients, the relevant absorbance signals carrying the distinguishing information can be identified. The most important frequencies are indicated in Figure 3b.

Table 3. Actual versus predicted values of GMA:EDMA ratio/vol% and deviation.

Std	Actual GMA/vol% (GMA:EDMA)	Predicted GMA/vol% (GMA:EDMA)	Δ/vol%
Val1	20	19.8	−0.2
Val2	40	57.4	−2.6
Val3	60	76.6	−3.4
Val4	80	36.3	−3.7

For increasing EDMA ratio (and vice versa decreasing GMA content) the symmetric C-O-C stretching vibration at 1110 cm^{-1} [43] is increasing (Figure 3). The characteristic frequencies increasing with GMA ratio are mainly related to vibrations of the epoxide group, with the symmetric and asymmetric ring vibration of the epoxide ring at 845 cm^{-1} [43] and 910 cm^{-1} [43], respectively. The C-O stretching vibration of the epoxide ring at 1270 cm^{-1} [43] also responds to changes in GMA ratio. This shows that the monomers are converted proportional to the mixture components and epoxide groups are present in the respective amounts in the final product. Hence, the degree of functionalization can be controlled.

3.4. Pore Volume

The effects of the process factors on the pore volume were analyzed by ANOVA are given in Table 4.

Table 4. Analysis of variance (ANOVA) for the analysis of FCD design of pore volume.

Source	Sum of Squares	Df	Mean Square	F-Value	*p*-Value	
Model	0.2660	4	0.0665	77.64	<0.0001	significant
A-Monomer	0.1741	1	0.1741	203.24	<0.0001	
B-GMA	0.0026	1	0.0026	3.04	0.1118	
C-Toluene	0.0785	1	0.0785	91.59	<0.0001	
BC	0.0110	1	0.0110	12.88	0.0049	
Residual	0.0086	10	0.0009			
Lack of Fit	0.0074	6	0.0012	4.43	0.0856	not significant
Pure Error	0.0011	4	0.0003			
Cor Total	0.2746	14				

A statistically significant model ($p < 0.0001$) describing the pore volume in dependence of four effects was obtained. The effect of factors monomer:porogen ratio ($p < 0.0001$), toluene:cyclohexanol ratio ($p < 0.0001$) and the interaction effect between GMA:EDMA ratio and toluene:cyclohexanol ratio ($p = 0.0049$) are statistically significant. The linear term B (GMA:EDMA ratio) is only added to comply with model hierarchy [44]; since B is involved in an interaction effect it must be included in the model although by itself B was no statistically significant effect term. The lack of fit is non-significant with $p > 0.05$. The strengths of the effects are given as coded equation in Equation (7):

$$V_p/mL{\cdot}g^{-1} = 0.2903 - 0.1984\ A - 0.0249\ B + 0.1366\ C + 0.0749\ BC \quad (7)$$

Equation (7) shows a linear negative effect of A: monomer:porogen ratio on the pore volume and is also the strongest effect. As the amount of monomer increases or the amount of porogen on the organic phase decreases during swelling, the polymer network becomes denser, less space is occupied by inert porogen, and thus the pore volume is reduced [39,45].

However, Figure 3 and Equation (7) show that not only the monomer:porogen ratio influences the pore volume, but also the composition of the porogen mixture and its synergistic interaction with the GMA:EDMA ratio. The porogen composition was ex-

amined in a range of 0/100 v/v ratio of toluene:cyclohexanol to a ratio of 100/0 v/v of toluene:cyclohexanol.

Depending on the suitability of the solvent for the polymer either χ-induced or ν-induced syneresis takes place, corresponding to a phase separation before or after the gel point, respectively [42]. Good solvents lead to smaller pores, smaller pore volumes and larger surface areas through ν-induces syneresis. [42] Nonsolvent or even linear polymeric porogens, like the PS from the seed particle, lead to larger pores with higher pore volume but reduced specific surface area through χ-induced syneresis [4]. According to the Hildebrandt solubilities of the p(GMA-*co*-EDMA) polymer with 24.0 $Mpa^{1/2}$ [46], toluene with 18.2 $MPa^{1/2}$ [40] and cyclohexanol with 22.4 $MPa^{1/2}$ [40], cyclohexanol is a better suited solvent for the polymer and should therefore result in smaller pores and smaller pore volumes. Since the amount of PS seed is constant, its influence as linear polymeric porogen is assumed to be constant for all conducted syntheses.

The factor C: toluene vol% shows a generally positive effect on the pore volume. With increasing amount of toluene in the porogen composition, the pore volume increases as well. This is supported by the Hildebrand solubilities.

However, Figure 4a shows that this relationship is not linear, since the interaction term BC between GMA:EDMA ratio and porogen composition has a high significant (p = 0.0066). While particles which have a low GMA content, show similar pore volumes for high and low toluene ratio in the porogen mixture, a difference for particles with high GMA content is visible. With increasing GMA content lower pore volumes are obtained with low toluene ratio whereas high pore volumes are accessible with a high toluene ratio (Figure 4b). The interaction BC could therefore be caused by changing solubilities depending on the porogen and monomer mixture, indicating a better solubility of GMA in cyclohexanol. The relationships of the factors on the pore volume are very complex, due to the influence of the solubilities. Nevertheless, the model shows a very good correlation with R^2 = 0.9688 and $R^2_{predicted}$ = 0.9012.

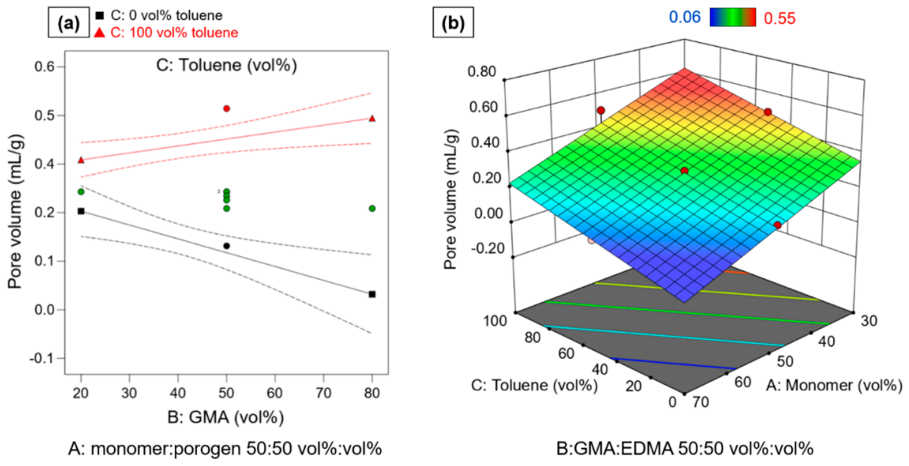


Figure 4. (**a**) Interaction plot of BC GMA:EDMA*toluene:cyclohexanol at medium level of factor A. Red triangles indicate measured pore volume at high toluene content. Black squares indicate measure particle volume at 0 vol% toluene (100 vol% cyclohexanol). Green circles indicate measured particle volume at medium toluene level. Dashed lines indicate 95% confidential intervals. (**b**) Shows response surface of pore volume in dependence of factors A and C. Blue areas correspond to low pore volumes, red areas correspond to high pore volume.

3.5. Pore Size

The effects of the variations in process factor levels on pore size were also found to be highly statistically significant (p < 0.0001). The pore size is dependent on factor A:

monomer:porogen ratio, factor B: GMA:EDMA ratio, and factor C: toluene:cyclohexanol ratio. However, the interrelationships between the factors are more complex, as can be seen from the fact that not only the non-linear effects terms A^2 and B^2 are required to describe the influences on the response, but there is also a synergistic interaction (second order interaction term, 2FIA) between the factors BC, the ratio of the monomers and the composition of the porogen mixture. This means the effect of neither the monomer nor the porogen composition can be adequately discussed without considering the other factor. The statistical parameters for the single model terms and the overall model are collected in Table 5.

Table 5. Analysis of variance (ANOVA) for the analysis of FCD design of pore size.

Source	Sum of Squares	Df	Mean Square	F-Value	*p*-Value	
Model	5.341×10^5	6	89,009.19	132.49	<0.0001	significant
A-Monomer	1.171×10^5	1	1.171×10^5	174.28	<0.0001	
B-GMA	1.563×10^5	1	1.563×10^5	232.68	<0.0001	
C-Toluene	54,489.80	1	54,489.80	81.11	<0.0001	
BC	21,969.58	1	21,969.58	32.70	0.0004	
A^2	24,163.44	1	24,163.44	35.97	0.0003	
B^2	40,191.80	1	40,191.80	59.82	<0.0001	
Residual	5374.59	8	671.82			
Lack of Fit	3217.79	4	804.45	1.49	0.3539	not significant
Pure Error	2156.80	4	539.20			
Cor Total	5.394×10^5	14				

The model shown provides a very good indication of the complex effects of the process factors on the response pore size. It allows a very good correlation with the data $R^2 = 0.9900$. Furthermore, a prediction of the pore size with an $R^2_{predicted} = 0.9452$ is possible.

The effect of the synthesis parameters in coded form is given in Equation (8):

$$\Phi_{50}/A = 200.92 - 167.93\,A + 215.35\,B + 127.15\,C + 109.11\,BC + 98.38\,A^2 + 126.88\,B^2 \quad (8)$$

The factor effect term B (GMA:EDMA) strongly influences the pore size of the particles, as both the linear and non-linear term show high positive values of factor effect coefficients. With an increase of GMA ratio the pore size increases, whereby the positive non-linear B^2 term indicates the even stronger influence the higher the GMA ratio is. As far as the chemical composition is concerned this finding can be explained through decreasing cross-linking degree in the polymer structure, since the EDMA cross-linker content diminishes.

However, due to the pronounced 2FIA of GMA:EDMA and toluene:cyclohexanol ratio, the effect of the GMA content cannot be understood without at the same time considering the composition of the porogen mixture. Yet, the synergistic effect is less pronounced and the second smallest with a coefficient of +109.11.

Figure 5a shows the interaction plot for the 2IA BC at a 50:50 vol% ratio for monomer:porogen. It can be seen that the higher the proportion of toluene in the porogen mixtures, the greater is the increase in pore size with increasing GMA content. This effect can be explained by the fact that with increasing GMA content toluene becomes less suitable as a solvent. As a result, phase separation starts earlier and earlier in relation to the gel point, which in turn leads to larger pores. A similar effect has already been shown for the pore volume.

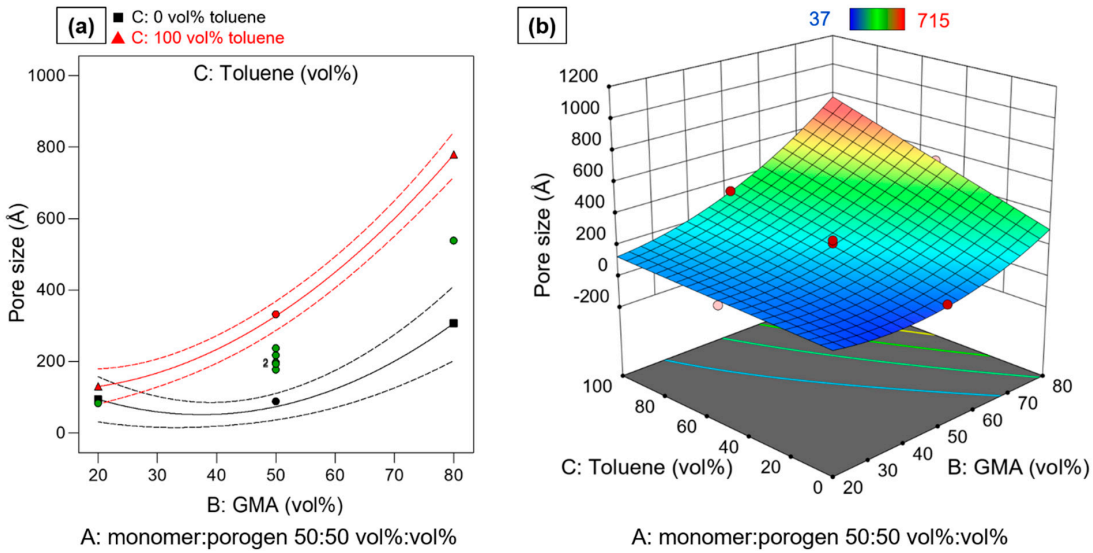


Figure 5. (**a**) Interaction plot of the synergistic interaction between GMA:EDMA*toluene:cyclohexanol at medium level of factor monomer:porogen ratio. Red triangles indicate measured pore size at high toluene content. Black squares indicate measure particle size at 0 vol% toluene (100 vol% cyclohexanol). Green circles indicate measured particle size at medium toluene level. Dashed lines indicate 95% confidential intervals. (**b**) Shows response surface of pore size in dependence of factors B and C at high level of A. Blue areas correspond to low pore sizes, red areas correspond to high pore sizes.

The only factor with a negative effect on the pore size is "A": an increasing ratio of monomer:porogen ratio results in smaller pore sizes. The positive effect of the non-linear term A^2 shows a diminishing effect strength for higher monomer ratios, i.e., at higher monomer ratios the depleting effect on "shrinking" pore sizes is less pronounced. Therefore, according to the model, the highest pore sizes should be achieved with a low monomer:porogen ratio, a high amount of GMA or a low amount of EDMA crosslinker, and a high toluene ratio in the porogen mixture (see Figure 5b). However, it should be noted that this very extreme setting (−/+/+) also corresponds to the synthesis und reaction conditions Std7 which did not lead to any stable particles (compare Figure 2). This area of the experimental space represents a critical combination of process factor levels.

The largest pore size with stable particles was achieved in the experiment with reaction conditions Std8 (+/+/+) at a high monomer content. Even higher pore sizes for stable particles are expected up to a range of about 40–70 vol% monomer at high toluene levels. If lower amounts of toluene are used in the porogen mixture, even lower monomer ratios can lead to stable particles (Std3 (−/+/−) 631 Å).

3.6. Specific Surface Area

The specific surface area is an important characteristic for many applications that depend on surface interactions. Therefore, the specific surface area was determined as the third response value and calculated according to Equation (5).

The specific surface area is a function of the two previously discussed properties pore volume and pore size. Data analysis was again performed via an ANOVA which is given in Table 6. Of the linear terms, only B, the GMA:EDMA ratio is statistically significant by itself. The other linear terms are A: monomer:porogen and C: toluene:cyclohexanol were added to preserve model hierarchy, since they are involved in the significant interaction term AC. However, the non-linear effects A^2 and B^2 are highly statistically significant. Although the specific surface area is deducted from the pore volume and the respective pore size, a different combination of factor effects is statistically significant and required for model

building. While the linear terms A and C were highly statistically significant for the other two parameters, these are only hierarchical in the model for the specific surface area. The interaction AC, on the other hand, was not relevant for any of the other responses. This shows that the relationship of the specific surface area and the process factors is highly complex and not predictable in a simple way. The relative impact of each process factor on the specific surface area can be seen in Equation (9) in terms of coded factors:

$$S/m^2 \cdot g^{-1} = 61.04 - 6.98\ A - 64.34\ B - 13.65\ C + 52.74\ AC - 28.16\ A^2 + 18.34\ B^2 \quad (9)$$

Table 6. Analysis of variance (ANOVA) for the analysis of FCD design of specific surface area.

Source	Sum of Squares	Df	Mean Square	F-Value	*p*-Value	
Model	20,322.72	6	3387.12	51.49	<0.0001	significant
A-Monomer	164.25	1	164.25	2.50	0.1527	
B-GMA	17,190.05	1	17,190.05	261.34	<0.0001	
C-Toluene	627.78	1	627.78	9.54	0.0149	
AC	5132.17	1	5132.17	78.02	<0.0001	
A^2	1980.56	1	1980.56	30.11	0.0006	
B^2	839.34	1	839.34	12.76	0.0073	
Residual	526.22	8	65.78			
Lack of Fit	379.02	4	94.75	2.57	0.1910	not significant
Pure Error	147.20	4	36.80			
Cor Total	20,848.93	14				

The strongest effect on the specific surface area results from the negative coefficient for the B: GMA:EDMA ratio.

With increasing amount of GMA, the specific surface area is reduced. This general trend has been reported in literature [21,23,45]. However, through application of RSM the non-linearity of this effect (B^2) was shown. The strength of the effect is leveled off with increasing GMA ratio as indicated by non-linear effect of B^2. The terms A, C, A^2 and C^2 are strongly interrelated through the 2FIA term AC, which is the second largest effect, i.e., the system is strongly dominated by the synergistic behavior of two non-linear effects.

The non-linear A^2 term shows a maximum for the specific surface area, but since the factor A: monomer:porogen ratio is involved in an 2FIA with factor C (toluene:cyclohexanol ratio of the porogen mixture). This interaction results in a shift in maximum for the specific surface area, the maximum being strongly dependent of the level for A and C. This behavior is clearly visible in the interaction plot given in Figure 6a. For low toluene content a maximum specific surface area can be seen at a monomer content of approximately 35 vol%. With further increase in monomer ratio, the specific surface decreases. For high toluene content the opposite effect is visible. With increasing monomer ratio, the specific surface area increases until a maximum at around 60 vol% is obtained and then decreases again slightly. This effect is not influenced by the GMA:EDMA ratio of the monomers (Figure 6b). Again, this behavior can be explained by the different solubilities of monomers, PS seed and polymer particle in the porogens. These opposing effects could lead to the shift of maximal specific surface as a function of process factors levels.

This rather complex behavior can also be described by the model equation in terms of coded factor effect terms (Equation (9)). The model describes the data very well with $R^2 = 0.9748$. It also shows a high predictive power with $R^2_{predicted} = 0.8678$.

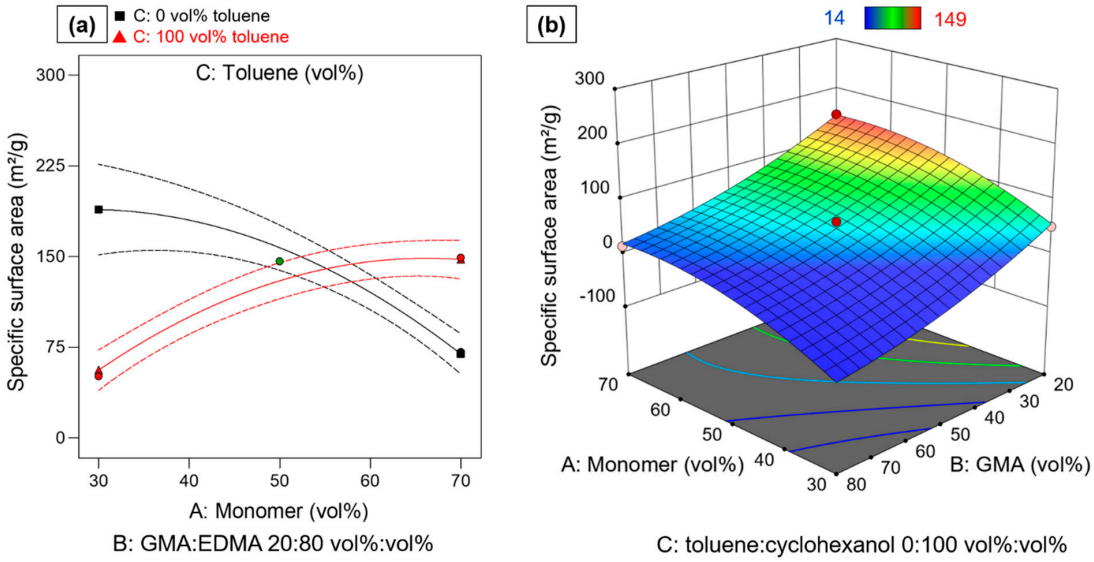


Figure 6. (**a**) Interaction plot of AC monomer:porogen×toluene:cyclohexanol at medium level of factor B for specific surface area. Red triangles indicate determined specific surface area at high toluene content. Black squares indicate determined specific surface area at 0 vol% toluene (100 vol% cyclohexanol). Green circles indicate determined specific surface area at medium toluene level. Dashed lines indicate 95% confidential intervals. (**b**) Shows response surface of specific surface area in dependence of factors A and B at low level of c. Blue areas correspond to low specific surface areas, red areas correspond to high specific surface areas.

3.7. Model Validation

For validating the models for pore volume, pore size and specific surface area, four validation experiments were performed and particles were synthesized under reaction conditions that were not used to build the model. The corresponding factor level settings for the experiments are given Table 2. Table 7 lists the values for the response values that were predicted by the model and the actual values, as well as the residuals (the deviations from the model) for all validation points regarding pore volume, pore size and specific surface area.

It can be seen from Table 7, that all values predicted by the models are in good agreement with the experiments, except for the value for pore size of validation experiment Val4. This combination of process factor level settings is in an extreme area of the design space where small changes in process factors cause large changes in the response (high model sensitivity). All values for all of the three pore parameters pore volume, pore size and specific surface area were correctly predicted within the 95% predictive interval (PI) and show only small deviations (residuals) from the predicted values. Therefore, the models were confirmed to be correct and show a high predictive power. It should be particularly noted that the validation points were synthesized using a PS from a different batch to test the transferability of the models to other seed batches. As a result, the findings are also transferable to the other seed particle batch, which shows high model robustness.

Table 7. Actual vs. predicted values (with low and high 95% prediction interval PI with alpha = 0.05) and corresponding residuals for the validation points Val1–4. Values exceeding the 95% PI range are written bold.

Std	Predicted/Actual/ Residual	Pore Volume/mL·g^{-1}	Pore Size/Å	Specific Surface Area/m^2·g
Val1	Predicted Value	0.34	121	137
	(±95% PI)	(0.27–0.42)	(48–194)	(115–160)
	Actual Value	0.41	124	132
	Residual	0.06	3	−5
Val2	Predicted Value	0.35	185	78
	(±95% PI)	(0.28–0.42)	(119–251)	(58–99)
	Actual Value	0.37	233	63
	Residual	0.02	48	−15
Val3	Predicted Value	0.36	362	35
	(±95% PI)	(0.29–0.43)	(297–427)	(15–56)
	Actual Value	0.37	370	40
	Residual	0.01	8	5
Val4	Predicted Value	0.36	652	9
	(±95% PI)	(0.29–0.44)	(576–728)	(0–33)
	Actual Value	0.36	**744**	20
	Residual	0.00	92	11

4. Conclusions

In this work, the effects of the synthesis parameters (factors) monomer:porogen, the ratios of functional and crosslinking monomer GMA:EDMA and the composition of the porogen mixture of toluene:cyclohexanol on the particle properties pore volume, pore size and specific surface area of monodisperse porous poly-(glycidyl methacrylate-*co*-ethyleneglycole dimethacrylate) particles were systematically studied by applying response surface methodology or Design of Experiment.

The multivariate regression analysis ($R^2_{predicted}$ = 0.98) based on FTIR data of the porous particles showed that the proportion of functional epoxy groups in the porous p(GMA-*co*-EDMA) particles depends directly on the proportion of the functional monomer. This allows the targeted adjustment of the degree of functional groups contained in the platform particles, which is required for application-specific re-functionalization.

The effects of the synthesis factors on the pore volume, pore size and specific surface area parameters could all be described by robust and predictive models ($R^2_{predicted}$ 0.9012, 0.9452 and 0.8678, respectively). Non-linear effects of factors and synergistic interaction effects among factors were identified and quantified and were found to affect all response variables. This highlights the underlying complexity of seed swelling polymerization for the generation of porous monodisperse polymer particles.

The complexity of the interrelationships in this system could only be demonstrated by simultaneously considering numerous factors simultaneously by the RSM approach. The method of isolated consideration of individual synthesis parameters (one-factor-at-a-time approach), which has prevailed in the literature up to now, has not provided any information about interactions so far and cannot be expected to do.

Despite this complexity of the system, it was successfully achieved to obtain validated, robust models that allow prediction and tuning of particle properties such as pore volume, pore size, specific surface area with a certain amount of epoxy groups.

It can be assumed that other systems based on seed swelling polymerization, e.g., other monomers or porogen mixtures, exhibit similarly complicated behavior and are also subject to complex solubility phenomena. The approach described in this work was demonstrated to be suitable for evaluating such a system quickly and to deliver reliable and comprehensive information for enabling tailored adjustment of pore characteristics. Thus, RSM is a powerful tool for enabling the rational design of porous polymer particles.

Author Contributions: Conceptualization, J.C.S., F.F., S.W., H.A.M. and A.K.; methodology, J.C.S. and A.K.; software, J.C.S.; validation, J.C.S. and F.F.; formal analysis, J.C.S.; investigation, J.C.S. and F.F.; resources, H.A.M. and A.K.; data curation, J.C.S., writing—original draft preparation, J.C.S.; writing—review and editing, F.F., A.W., M.B., H.A.M. and A.K.; visualization, J.C.S.; supervision, H.A.M. and A.K.; project administration, M.B., H.A.M. and A.K.; funding acquisition, H.A.M. and A.K. All authors have read and agreed to the published version of the manuscript.

Funding: This research was funded by Bundesministerium für Bildung und Forschung (BMBF), grant number 13FH647IX6. The article processing charge was funded by the "Ministerium für Wissenschaft, Forschung und Kunst Baden-Württemberg". The funders had no role in study design, data collection and analysis, decision to publish, or preparation of the manuscript.

Data Availability Statement: Data are available upon request from the authors.

Acknowledgments: The authors thank Natalia Behring, Katrin Markus, Patrick Wahrendorff and Mark Wolf for experimental support during particle synthesis. Furthermore, we would like to thank our cooperation partner Maisch GmbH for their support in preparing the iSEC columns. We thank Elke Nadler for contributing the SEM measurements.

Conflicts of Interest: The authors declare no conflict of interest.

Appendix A Synthesis of Polystyrene (PS) Seed Particles

PS seed particles were synthesized using dispersion polymerization in alcoholic media. 20 mL styrene (99%) and 80 mL ethanol (96%) were added in a three-necked round-bottom flask (250 mL). After the addition of 1.0 g PVP k30 as stabilizer and 0.5 g BPO as initiator the suspension was sonicated for 10 min. The suspension was stirred with 120 rpm with a magnetic stirrer at room temperature for 30 min while purging with Argon. Thereafter the temperature was elevated to 70 °C for 24 h under reflux. The PS seed particles were centrifugated for 2 min at 7500 rpm and were washed three times with ethanol and three times with deionized water to rmove the reaction solution. The particles were freeze-dried under vacuum for 72 h.

Appendix B Explained Variance of Multivariate Calibration Model for Epoxy Functionalization

Appendix B Figure A1 shows the explained variance plot for the PLSR model building for epoxy functionalization in the validation, an explained variance with >90% is obtained using nine PLSR factors.

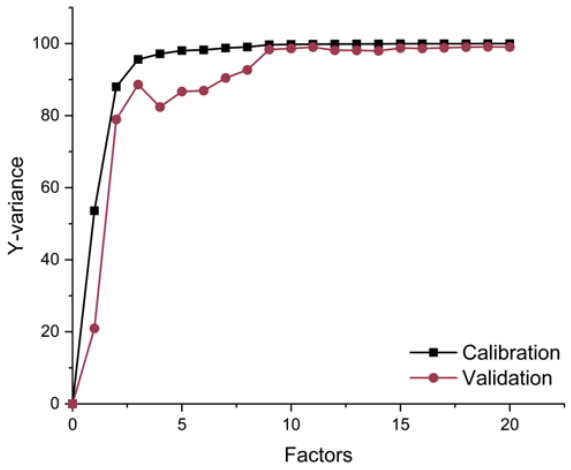


Figure A1. Plot of explained variance for the PLSR depending on the factors used to predict epoxy functionalization for calibration (■) and validation (●).

References

1. Reymond, F.; Vollet, C.; Plichta, Z.; Horák, D. Fabrication and characterization of tosyl-activated magnetic and nonmagnetic monodisperse microspheres for use in microfluic-based ferritin immunoassay. *Biotechnol. Progress* **2013**, *29*, 532–542. [CrossRef] [PubMed]
2. Miletić, N.; Vuković, Z.; Nastasović, A.; Loos, K. Macroporous poly(glycidyl methacrylate-co-ethylene glycol dimethacrylate) resins—Versatile immobilization supports for biocatalysts. *J. Mol. Catal. B Enzym.* **2009**, *56*, 196–201. [CrossRef]
3. Xu, S.; Wang, Y.; Tang, Y.; Ji, Y. A protein-based mixed selector chiral monolithic stationary phase in capillary electrochromatography. *New J. Chem.* **2018**, *42*, 13520–13528. [CrossRef]
4. Benes, M.J.; Horák, D.; Svec, F. Methacrylate-based chromatographic media. *J. Sep. Sci.* **2005**, *28*, 1855–1875. [CrossRef]
5. Gong, B.; Zhu, J.; Li, L.; Qiang, K.; Ren, L. Synthesis of non-porous poly(glycidylmethacrylate-co-ethylenedimethacrylate) beads and their application in separation of biopolymers. *Talanta* **2006**, *68*, 666–672. [CrossRef] [PubMed]
6. Roberts, M.W.H.; Ongkudon, C.M.; Forde, G.M.; Danquah, M.K. Versatility of polymethacrylate monoliths for chromatographic purification of biomolecules. *J. Sep. Sci.* **2009**, *32*, 2485–2494. [CrossRef]
7. Ding, M.-Y.; Zheng, R.; Peng, H. Preparation of Weak Cation Exchange Monolithic Capillary Column and Its Application for Protein Separation. *Chin. J. Anal. Chem.* **2009**, *37*, 395–398. [CrossRef]
8. Wang, X.; Liu, H.; Sun, Z.; Zhao, S.; Zhou, Y.; Li, J.; Cai, T.; Gong, B. Monodisperse restricted access material with molecularly imprinted surface for selective solid-phase extraction of 17β-estradiol from milk. *J. Sep. Sci.* **2020**, *43*, 3520–3533. [CrossRef]
9. Golub, D.; Krajnc, P. Emulsion templated hydrophilic polymethacrylates. Morphological features, water and dye absorption. *React. Funct. Polym.* **2020**, *149*, 104515. [CrossRef]
10. He, J.; Yang, C.; Xiong, X.; Jiang, B. Preparation and characterization of monodisperse porous silica microspheres with controllable morphology and structure. *J. Polym. Sci. A Polym. Chem.* **2012**, *50*, 2889–2897. [CrossRef]
11. Xia, H.; Wan, G.; Yang, F.; Wang, J.; Bai, Q. Preparation of monodisperse large-porous silica microspheres with polymer microspheres as the templates for protein separation. *Mater. Lett.* **2016**, *180*, 19–22. [CrossRef]
12. Liu, Y.; Goebl, J.; Yin, Y. Templated synthesis of nanostructured materials. *Chem. Soc. Rev.* **2013**, *42*, 2610–2653. [CrossRef]
13. Hérault, D.; Saluzzo, C.; Lemaire, M. Preparation of monodisperse enantiomerically pure glycidyl methacrylate–ethylene glycol dimethacrylate copolymers in dispersion copolymerization: Functionalization. *React. Funct. Polym.* **2006**, *66*, 567–577. [CrossRef]
14. Stefanović, I.S.; Ekmeščić, B.M.; Maksin, D.D.; Nastasović, A.B.; Miladinović, Z.P.; Vuković, Z.M.; Micić, D.M.; Pergal, M.V. Structure, Thermal, and Morphological Properties of Novel Macroporous Amino-Functionalized Glycidyl Methacrylate Based Copolymers. *Ind. Eng. Chem. Res.* **2015**, *54*, 6902–6911. [CrossRef]
15. Xiao, J.; Lu, Q.; Cong, H.; Shen, Y.; Yu, B. Microporous poly(glycidyl methacrylate-co-ethylene glycol dimethyl acrylate) microspheres: Synthesis, functionalization and applications. *Polym. Chem.* **2021**, *12*, 6050–6070. [CrossRef]
16. Srisopa, A. Preparation of monodisperse porous poly(glycidylmethacrylate-co-ethylenedimethacrylate) microspheres and their application as stationary phase for superheated water HPLC. *Talanta* **2016**, *147*, 358–363. [CrossRef]
17. Flores-Rojas, G.G.; Pino-Ramos, V.H.; López-Saucedo, F.; Concheiro, A.; Alvarez-Lorenzo, C.; Bucio, E. Improved covalent immobilization of lysozyme on silicone rubber-films grafted with poly(ethylene glycol dimethacrylate-co-glycidylmethacrylate). *Eur. Polym. J.* **2017**, *95*, 27–40. [CrossRef]
18. Ugelstad, J.; Söderberg, L.; Berge, A.; Bergström, J. Monodisperse polymer particles—A step forward for chromatography. *Nature* **1983**, *303*, 95–96. [CrossRef]
19. Šmigol, V.; Švec, F. Synthesis and properties of uniform beads based on macroporous copolymer glycidyl methacrylate–ethylene dimethacrylate: A way to improve separation media for HPLC. *J. Appl. Polym. Sci.* **1992**, *46*, 1439–1448. [CrossRef]
20. Dubinsky, S.; Park, J.I.; Gourevich, I.; Chan, C.; Deetz, M.; Kumacheva, E. Toward Controlling the Surface Morphology of Macroporous Copolymer Particles. *Macromolecules* **2009**, *42*, 1990–1994. [CrossRef]
21. Pączkowski, P.; Gawdzik, B. Studies on Preparation, Characterization and Application of Porous Functionalized Glycidyl Methacrylate-Based Microspheres. *Materials* **2021**, *14*, 1438. [CrossRef]
22. Hosoya, K.; Fréchet, J.M.J. Influence of the seed polymer on the chromatographic properties of size monodisperse polymeric separation media prepared by a multi-step swelling and polymerization method. *J. Polym. Sci. A Polym. Chem.* **1993**, *31*, 2129–2141. [CrossRef]
23. Costa, L.C.; Monteiro, R.C.; Castro, H.M.A.; Ribeiro, T.S.; Oliveira, M.A.; Torquato, E.C.C.; Arcanjo, M.E.; Marques, M.R.C. Glycidyl Methacrylate-ethylene Glycol Dimethacrylate Copolymers with Varied Pore Structures Prepared with Different Reaction Parameters. *Mat. Res.* **2020**, 23. [CrossRef]
24. Yu, B.; Xue, T.; Pang, L.; Zhang, X.; Shen, Y.; Cong, H. The Effect of Different Porogens on Porous PMMA Microspheres by Seed Swelling Polymerization and Its Application in High-Performance Liquid Chromatography. *Materials* **2018**, *11*, 705. [CrossRef] [PubMed]
25. Yu, S.; Ng, F.L.; Ma, K.C.C.; Mon, A.A.; Ng, F.L.; Ng, Y.Y. Effect of porogenic solvent on the porous properties of polymer monoliths. *J. Appl. Polym. Sci.* **2013**, *127*, 2641–2647. [CrossRef]
26. Ferreira, A.; Bigan, M.; Blondeau, D. Optimization of a polymeric HPLC phase: Poly(glycidyl methacrylate–co-ethylene dimethacrylate). *React. Funct. Polym.* **2003**, *56*, 123–136. [CrossRef]

27. Smigol, V.; Svec, F. Preparation and properties of uniform beads based on macroporous glycidyl methacrylate–ethylene dimethacrylate copolymer: Use of chain transfer agent for control of pore-size distribution. *J. Appl. Polym. Sci.* **1993**, *48*, 2033–2039. [CrossRef]
28. Pączkowski, P.; Grochowicz, M.; Chabros, A.; Gawdzik, B.; Ryczkowski, J. Infrared photoacoustic spectroscopy as an alternative tool for the analysis of surface-modified glycidyl-based polymeric microspheres. *Polym. Test.* **2019**, *76*, 173–180. [CrossRef]
29. Myers, R.H.; Montgomery, D.C.; Anderson-Cook, C.M. *Response Surface Methodology: Process and Product Optimization Using Designed Experiments*, 4th ed.; Wiley: Hoboken, NJ, USA, 2016; ISBN 9781118916025.
30. Box, G.E.P.; Hunter, J.S.; Hunter, W.G. *Statistics for Experimenters: Design, Innovation, and Discovery*, 2nd ed.; Wiley-Interscience: Hoboken, NJ, USA, 2005; ISBN 0471718130.
31. Ryan, T.P. *Modern Experimental Design*; Wiley-Interscience: Hoboken, NJ, USA, 2007; ISBN 978-0-471-21077-1.
32. Kessler, W. *Multivariate Datenanalyse für die Pharma-, Bio- und Prozessanalytik: Ein Lehrbuch*; Ein Lehrbuch, 1. Aufl., 1. Nachdr; Wiley-VCH: Weinheim, Germany, 2008; ISBN 978-3-527-31262-7.
33. Esbensen, K.H.; Swarbrick, B.; Westad, F.; Whitcombe, P.; Andersen, M. *Multivariate Data Analysis: An Introduction to Multivariate Analysis, Process Analytical Technology and Quality by Design*, 6th ed.; CAMO: Magnolia, TX, USA, 2018; ISBN 978-82-691104-0-1.
34. Ulitzsch, S.; Bäuerle, T.; Chassé, T.; Lorenz, G.; Kandelbauer, A. Optimizing the Process Efficiency of Reactive Extrusion in the Synthesis of Vinyltrimethoxysilane-Grafted Ethylene-Octene-Copolymer (EOC-g-VTMS) by Response Surface Methodology. *Polymers* **2020**, *12*, 2798. [CrossRef]
35. Bäuerle, T.; Ulitzsch, S.; Lorenz, A.; Rebner, K.; Chassé, T.; Kandelbauer, A.; Lorenz, G. Effects of process parameters on silane grafting of liquid ethylene-propylene copolymer by reactive extrusion as quantified by response surface methodology. *Polymer* **2020**, *202*, 122601. [CrossRef]
36. Halász, I.; Martin, K. Pore Sizes of Solids. *Angew. Chem. Int. Ed. Engl.* **1978**, *17*, 901–908. [CrossRef]
37. Seidl, R.; Weiss, S.; Zikulnig-Rusch, E.M.; Kandelbauer, A. Response surface optimization for improving the processing behavior of melamine formaldehyde impregnation resins. *J. Appl. Polym. Sci.* **2021**, *138*, 50181. [CrossRef]
38. Kim, J.-W.; Suh, K.-D. Monodisperse polymer particles synthesized by seeded polymerization techniques. *J. Ind. Eng. Chem.* **2008**, *14*, 71–76. [CrossRef]
39. Xu, M.; Peterson, D.S.; Rohr, T.; Svec, F.; Fréchet, J.M.J. Polar polymeric stationary phases for normal-phase HPLC based on monodisperse macroporous poly(2,3-dihydroxypropyl methacrylate-co-ethylene dimethacrylate) beads. *Anal. Chem.* **2003**, *75*, 1011–1021. [CrossRef]
40. Hansen, C.M. *Hansen Solubility Parameters: A User's Handbook*, 2nd ed.; CRC Press: Boca Raton, FL, USA, 2007.
41. Wagner, A.; Wagner, S.; Bredfeldt, J.-E.; Steinbach, J.C.; Mukherjee, A.; Kronenberger, S.; Braun, K.; Kandelbauer, A.; Mayer, H.A.; Brecht, M. Chemical Imaging of Single Anisotropic Polystyrene/Poly (Methacrylate) Microspheres with Complex Hierarchical Architecture. *Polymers* **2021**, *13*, 1438. [CrossRef]
42. Gokmen, M.T.; Du Prez, F.E. Porous polymer particles—A comprehensive guide to synthesis, characterization, functionalization and applications. *Prog. Polym. Sci.* **2012**, *37*, 365–405. [CrossRef]
43. Socrates, G. *Infrared and Raman Characteristic Group Frequencies: Tables and Charts*, 3rd ed.; repr. as Paperback; Wiley: Chichester, UK, 2010; ISBN 9780470093078.
44. Wahrendorff, P.; Stefanakis, M.; Steinbach, J.C.; Allnoch, D.; Zuber, R.; Kapfhammer, R.; Brecht, M.; Kandelbauer, A.; Rebner, K. Simultaneous Determination of Droplet Size, pH Value and Concentration to Evaluate the Aging Behavior of Metalworking Fluids. *Sensors* **2021**, *21*, 8299. [CrossRef]
45. Rahman, M.A.; Mutalib, M.A.; Li, K.; Othman, M. Pore Size Measurements and Distribution for Ceramic Membranes. In *Membrane Characterization*; Elsevier: Amsterdam, The Netherlands, 2017; pp. 183–198.
46. Dubinsky, S.; Zhang, H.; Nie, Z.; Gourevich, I.; Voicu, D.; Deetz, M.; Kumacheva, E. Microfluidic Synthesis of Macroporous Copolymer Particles. *Macromolecules* **2008**, *41*, 3555–3561. [CrossRef]

8 Publikation III

Journal of Chromatography A 1705 (2023) 464190

Contents lists available at ScienceDirect

Journal of Chromatography A

journal homepage: www.elsevier.com/locate/chroma



Incorporation of silica nanoparticles into porous templates to fabricate mesoporous silica microspheres for high performance liquid chromatography applications

Fabio Fait[a,b], Julia C. Steinbach[a,b], Andreas Kandelbauer[b,c], Hermann A. Mayer[a,*]

[a] Institute of Inorganic Chemistry, University of Tübingen, Auf der Morgenstelle 18, Tübingen 72076, Germany
[b] Process Analysis and Technology (PA&T), Reutlingen Research Institute, Reutlingen University, Alteburgstrasse 150, Reutlingen 72762, Germany
[c] Institute of Wood Technology and Renewable Materials, Department of Material Sciences and Process Engineering (MAP), University of Natural Resources and Life Sciences, Gregor-Mendel-Straße 33, Vienna 1180, Austria

ARTICLE INFO

Article history:
Received 20 February 2023
Revised 28 June 2023
Accepted 30 June 2023
Available online 1 July 2023

Keywords:
Polymer template method
Siloxane functionalized polymer
Mesoporous silica microspheres
^{29}Si solid state NMR
High performance liquid chromatography (HPLC)

ABSTRACT

High-performance liquid chromatography is one of the most important analytical tools for the identification and separation of substances. The efficiency of this method is largely determined by the stationary phase of the columns. Although monodisperse mesoporous silica microspheres (MPSM) represent a commonly used material as stationary phase their tailored preparation remains challenging. Here we report on the synthesis of four MPSMs via the hard template method. Silica nanoparticles (SNPs) which form the silica network of the final MPSMs were generated *in situ* from tetraethyl orthosilicate (TEOS) in the presence of (3-aminopropyl) triethoxysilane (APTES) functionalized *p*(GMA-*co*-EDMA) as hard template. Methanol, ethanol, 2-propanol, and 1-butanol were applied as solvents to control the size of the SNPs in the hybrid beads (HB). After calcination, MPSMs with different sizes, morphology and pore properties were obtained and characterized by scanning electron microscopy, nitrogen adsorption and desorption measurements, thermogravimetric analysis, solid state NMR and DRIFT IR spectroscopy. Interestingly, the ^{29}Si NMR spectra of the HBs show T and Q group species which suggests that there is no covalent linkage between the SNPs and the template. The MPSMs were functionalized with trimethoxy (octadecyl) silane and used as stationary phases in reversed-phase chromatography to separate a mixture of eleven different amino acids. The separation characteristics of the MPSMs strongly depend on their morphology and pore properties which are controlled by the solvent during the preparation of the MPSMs. Overall, the separation behavior of the best phases is comparable with those of commercially available columns. The phases even achieve faster separation of the amino acids without loss of quality.

© 2023 Published by Elsevier B.V.

1. Introduction

Porous silica particles are widely applied as catalysts and drug carriers, and are used as adsorbents or in separation processes [1–5]. In high-performance liquid chromatography (HPLC), totally porous silica particles in the micrometer range with narrow size distributions are of high interest, because they provide high specific surfaces and thus allow best interactions of the analytes between stationary and mobile phases [6].

Industrially, silica particles are produced by emulsion processes or spray drying [7–9]. The desired particle diameter is adjusted by the size of the droplet during emulsification or spraying. Unfortunately, these methods generate broad particle size distributions and require classification of the resulting silica particle batches [10,11]. Therefore sieving, air classification or sedimentation have to be applied to separate the silica particles into fractions with narrow size distributions. This is time-consuming and costly and is also of low productivity, due to waste batches.

Stoeber developed a simple method to prepare colloidal nonporous spherical silica particles in a wide range from 10 to 500 nm by ammonia catalyzed hydrolysis and condensation of alkoxy silanes [12]. The size of the silica particles increases up to 800 nm, if in this process the hydrolysis rate of the alkoxy silanes and the siloxane network formation are controlled accordingly. This can be adjusted by critical parameters such as type of alkoxide, NH_3 and H_2O concentration as well as temperature [12–17]. Moreover, with increasing chain length of the alcoholic solvent larger silica particles are obtained [18,19]. Seeded growth, semi-batch and the addition of electrolytes are improved techniques which provide access

* Corresponding author.
E-mail address: hermann.mayer@uni-tuebingen.de (H.A. Mayer).

https://doi.org/10.1016/j.chroma.2023.464190
0021-9673/© 2023 Published by Elsevier B.V.

to silica particles in the micrometer range but the particles remain nonporous [20–23].

The synthesis of mesoporous and macroporous silica particles requires templates [24–26]. Soft template methods are based on molecular interaction of silica precursors with non-covalently binding of organic reagents such as cetyltrimethylammonium bromide or triblock copolymers such as Pluronic P123. The size of the silica particles is either in the nanometer range or polydisperse particles in the micrometer range are obtained [25,27–29].

Functionalized poly(glycidyl methacrylate-*co*-ethylene dimethacrylate) (*p*(GMA-*co*-EDMA)) particles have been successfully applied as hard templates in a sol-gel process with tetraethyl orthosilicate (TEOS) to produce porous silica particles in the micrometer range [30–33]. Amines such as ethylenediamine, trimethylamine, or tetraethylenepentamine have proven to be useful as functionalization agents, as they provide positive charges on the template surface under the sol-gel conditions. Positively charged amino functions attract the negatively charged silica species, which fill the pores of the template and construct the silica network [30,34].

(3-aminopropyl) triethoxysilane (APTES) is a popular reagent to functionalize silica surfaces [35,36]. The molecule is covalently linked to silica species via the condensation of the triethoxysilane function with surface silanol groups leaving the amino group for further functionalization. In contrast to this, Grama et al. treated *p*(GMA-*co*-EDMA) particles with APTES to bind the molecule via the amino group in an addition reaction with the epoxide to the polymer surface [37]. Here, the triethoxysilane groups enable silica to be deposited in the pores by condensation with silica species generated by a sol-gel process. This was exploited by Chen et al. in the preparation of micron sized porous silica particles. However, compared to those particles which were prepared with the TMA functionalized *p*(GMA-*co*-EDMA) polymer, the yield was poor [38].

Mainly, amino functionalized *p*(GMA-*co*-EDMA) templates with different porosity have been investigated for the preparation of MPSMs with comparable settings of the sol-gel process [33,34,38]. In previous studies it was shown, that the concentration of ammonia and the molar ratio of H_2O to TEOS have a strong impact on the pore size distribution, the size of the silica particle and the morphology of their surfaces. This is because the conditions of the sol-gel process control the size of the silica nanoparticles (SNPs) which are incorporated into the template [39]. However, the sol-gel process provides multiple other parameters to produce different pore properties and morphologies of the porous silica particles.

The present study aims to demonstrate the control of pore parameters and morphology of mesoporous silica microspheres (MPSMs) prepared via the hard template method using different solvents in the sol-gel process. For this purpose, a base-catalyzed sol-gel process is carried out in the presence of the APTES functionalized *p*(GMA-*co*-EDMA) particles P@APTES in methanol, ethanol, 2-propanol, and 1-butanol, respectively (Fig. 1). The relevant synthesis steps are analyzed for pore size, pore volume and specific surface area and characterized by NMR and IR spectroscopy. The separation behavior of the silica particles is demonstrated by analyzing amino acids in high performance liquid chromatography.

2. Materials and methods

2.1. Chemicals

Tetraethyl orthosilicate (TEOS) and trimethoxy (octadecyl) silane (ODTMS) were obtained from abcr GmbH (Germany). Acetonitrile (ACN), 1-butanol, tetrahydrofuran, and water (all HPLC grade) were purchased from fisher scientific and ammonia (28-30% aqueous solution) from Alfa Aesar (Germany). The D,L – amino acids, (3-aminopropyl) triethoxysilane, ethanol), hydrochloric acid, methanol (MeOH), 2-propanol, and triethylamine were bought from Sigma-Aldrich (Germany). Toluene and deionized water were cleaned through a solvent purification system. *ortho*-phthalaldehyde (OPA) reagent for pre-column derivatization of the amino acids was provided by Dr. Maisch HPLC (Germany).

2.2. Characterization

Scanning electron microscopy images were taken with a Hitachi SU8030 to determine size, dispersity, and morphology of the particles. The size and dispersity of the particles were obtained by measuring at least 400 particles from scanning electron microscopy images. The mean particle diameter is expressed as particle size in µm. The dispersity is given as d_{90}/d_{10} value.

Solid state CP/MAS ^{13}C and ^{29}Si NMR spectra were recorded on a Bruker AVIIIHD-300WB NMR spectrometer at rotation speeds of 8 kHz (^{13}C) and 5 kHz (^{29}Si), respectively. The measurement frequencies were 75.47 MHz (^{13}C) and 59.63 MHz (^{29}Si) and the spectra were referenced to adamantane (^{13}C) and octakis(trimethylsiloxy)silsesquioxane (Q_8M_8) (^{29}Si) as external standards. The contact times of the cross-polarization magic angle spinning (CP/MAS) recordings are 2000 µsec (^{13}C) and 5000 µsec (^{29}Si) and the relaxation delays are 4 sec (^{13}C) and 2 sec (^{29}Si), respectively. High pulse decoupling (HPDEC) NMR measurements of ^{29}Si has contact times of 9000 µsec and relaxation delays of 30 sec. IR spectra were recorded on a Bruker Vertex 70 FT-IR spectrometer. Particles were pulverized in KBr (20 w%) and measured using the DRIFT method. Spectra analysis was performed using TopSpin (NMR) and OPUS (IR) software (Bruker).

For the determination of specific surface area, pore size and pore volume the BELSORP MiniX (Microtrac Retsch GmbH) was used. Polymer and hybrid particles were outgassed at 30°C for 24 h and silica samples at 300°C for 3 h up to a final vacuum of about $2 \bullet 10^{-2}$ mbar, to eliminate possible physisorbed substances and achieve a reproducible intermediate state [40]. The samples were evacuated using the BELSORP VACII (Microtrac Retsch GmbH). The N_2 adsorption and desorption measurements were performed at 77 K. The analysis of adsorption and desorption isotherms was performed using the BELMaster 7 software. Specific surface area was

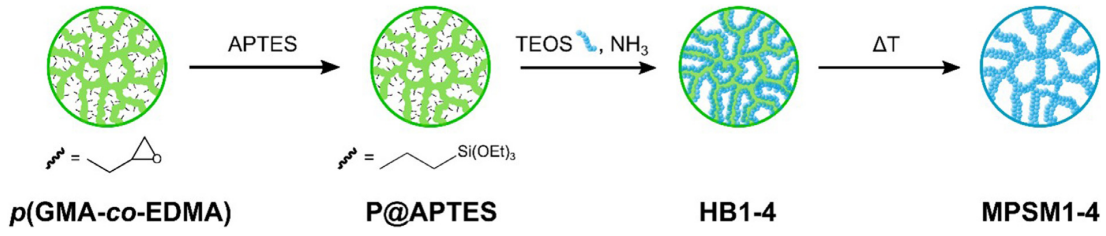


Fig. 1. Fabrication of mesoporous silica microspheres using (3-aminopropyl) triethoxysilane functionalized particles as hard template.

Table 1
Particle properties.

	particle size [µm]	dispersity d_{90}/d_{10}	median pore size [nm]	pore volume [$cm^3\ g^{-1}$]	specific surface area [$m^2\ g^{-1}$]
p(GMA-*co*-EDMA)	7.6	1.22	16.2	0.20	121
P@APTES	-	-	15.9	0.17	94
HB1	8.2	1.09	20.3	0.08	42
HB2	8.4	1.06	27.3	0.03	15
HB3	8.3	1.07	29.3	0.04	13
HB4	8.4	1.08	29.8	0.01	5
MPSM1	5.8	1.22	4.7	0.73	573
MPSM2	7.4	1.14	20.3	0.46	309
MPSM3	7.1	1.21	20.3	0.48	317
MPSM4	7.7	1.10	23.5	0.49	247

analyzed according to the Brunauer-Emmet-Teller method (BET) [41]. The pore size distributions were determined by using the Barrett-Joyner-Halenda (BJH) method to the desorption isotherms [42]. As previously observed, forced closure of the hysteresis of the desorption isotherm can occur for the organic templates, resulting in a putative pore size distribution at ∼ 4 nm [33,43]. This phenomen is also observed for the hybrid beads. Since the BJH method is designed for the desorption isotherm and the median pore size is less affected by this, the pore size distributions of the desorption isotherms were nevertheless shown in this work (Figure S4, S.I.). Therefore, the data of the median pore sizes of the polymer and hybrid materials in Table 1 are only approximate. The pore volume was obtained from a single point adsorption at p/p_0 of 0.95.

Thermogravimetric analysis was performed using the TGA/DSC I from Mettler Toledo. The samples were weight into a 900 µl alumina crucible and were measured under synthetic air (50 mL min^{-1}) with a heating rate of 5 K min^{-1}. The relative mass of the remaining residue correlates to the amount of SiO_2.

Analytical high performance liquid chromatography of amino acids was performed on an Agilent 1100 series system from Agilent Technologies equipped with a quaternary pump with degasser, an auto sampling system, column oven and a fluorescent detector (330 nm extinction, 450 nm emission). Instrument control, data acquisition and automated data analysis was performed by the OpenLab CDS software (Rev. C.01.07 SR3, Agilent Technologies). A sodium phosphate buffer (25 mM, pH = 7.2) was used as eluent buffer. A running gradient from eluent A consisting of buffer and 0.75 v.% THF to eluent B consisting of methanol, acetonitrile, and buffer (35/15/50 v.%) within 50 minutes was used for the separation of the amino acids.

2.3. Synthesis

p(GMA-*co*-EDMA) particles were prepared by a modified procedure which was reported earlier (for details see S.I.) [31,32,37,38,44].

2.3.1. Preparation of (3-aminopropyl) triethoxysilane functionalized particles P@APTES

5 g of *p*(GMA-*co*-EDMA) particles were dispersed in 150 ml of methanol, 52.5 ml of APTES was added and the mixture was stirred at 60°C (130 rpm) for 24 h. The particles were separated from the solution, washed three times with H_2O and EtOH, each and dried at 65°C for 16 h.

2.3.2. Preparation of particles HB1–4 and MPSM1–4

5 g of APTES functionalized particles (P@APTES) were dispersed in 270 mL of methanol (HB1), ethanol (HB2), 2-propanol (HB3) and 1-butanol (HB4), respectively, and 30 mL of H_2O. Then 12.5 mL of TEOS and 1.25 mL of an ammonia solution were added and stirred at room temperature (130 rpm) for 24 h. The particles were separated from the solution, washed three times with H_2O and EtOH, each and dried at 65°C for 16 h to generate HB1–4 (Figure S3, S.I.). After calcination at 600°C for 10 h mesoporous silica microspheres MPSM1–4 remained.

2.3.3. Octadecyl functionalization of MPSM1–4 for chromatographic measurements

5 g of silica particles MPSM1–4 were dispersed in 600 mL of hydrochloric acid (3.7%) and stirred for 3 h at 100°C (130 rpm). The particles were separated from the solution, washed with EtOH and H_2O until neutral and dried at 65°C for 16 h. The particles were then dispersed in 75 mL of toluene, 25 mL of trimethoxy (octadecyl) silane and 0.5 mL of triethylamine were added, and the mixture was stirred at 100°C (130 rpm) for 6 h. The particles were separated from the solution, washed three times with toluene, three times with EtOH and twice with MeOH and dried at 65°C for 16 h.

2 g of functionalized particles were packed with 25 mL of acetone as slurry and MeOH / H_2O (85 v.% / 15 v.%) as pressure medium.

For the analysis of amino acids by reversed phase chromatography, derivatization of the samples is necessary for detection. In this case, a pre-column derivatization with a mixture of *ortho*-phthalaldehyde and 3-mercaptopropionic acid was used for the primary amines. The derivatized samples were excited with a fluorescence detector at 330 nm and detected at 450 nm. A gradient of 100% eluent A to 100% eluent B was run within 50 minutes. A 25 mM sodium phosphate buffer (pH 7.2) containing 0.75% THF was used as eluent A and a mixture of methanol, acetonitrile, and sodium phosphate buffer (35/15/50 v.%) was used as eluent B. Peaks were assigned by retention times based on single measurements of amino acids in the measurement system.

3. Results and discussion

Mesoporous micron sized silica particles MPSM1–4 were prepared from *p*(GMA-*co*-EDMA) polymer as starting material in three steps (Fig. 1) [34,38]. Monodisperse *p*(GMA-*co*-EDMA) polymer microspheres with a size of 7.6 µm are obtained by a seeded swelling polymerization [31,33,44]. The pore properties of the organic polymer are characterized by a median pore size of 16.2 nm, a pore volume of 0.20 mL g^{-1} and a specific surface area of 121 $m^2\ g^{-1}$ (Table 1). Functionalization of *p*(GMA-*co*-EDMA) with APTES to give P@APTES was achieved via nucleophilic attack of the amino group at the epoxide of the polymer, which results in ring opening to form an amino alcohol (Fig. 1). Connecting APTES to the polymer did not change the template in size, dispersity, and morphology. From thermogravimetric and elemental analysis of P@APTES a silica content of 6.6 % (Fig. 3) and a nitrogen content of 1.6 % were estimated which confirmed the successful functionalization of the *p*(GMA-*co*-EDMA) particles with APTES [37]. TEOS as precursor was hydrolyzed and condensed to silica nanoparticles (SNPs) in a base-catalyzed sol-gel process in methanol,

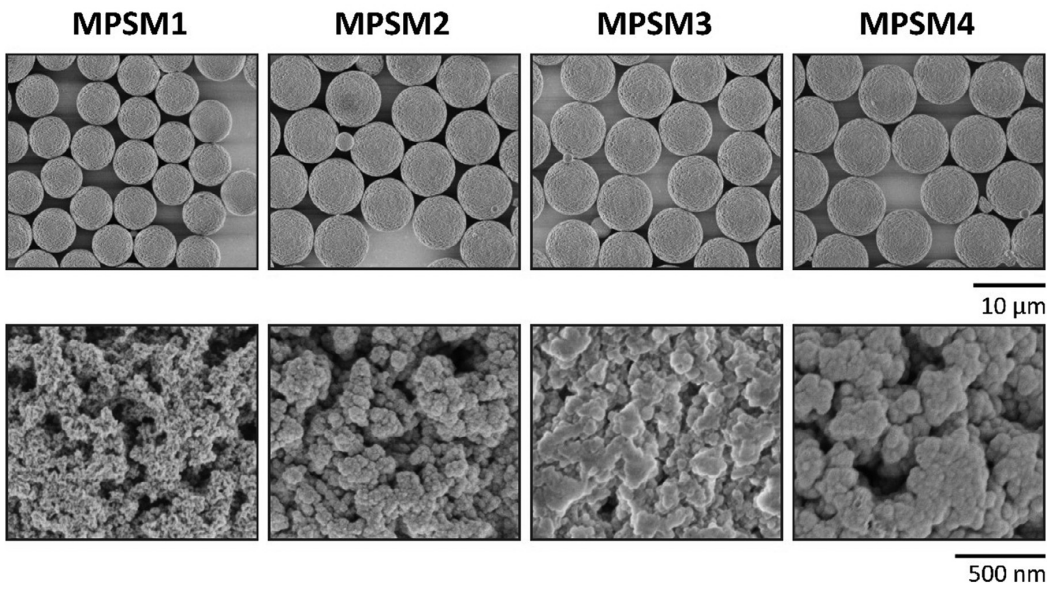


Fig. 2. Scanning electron microscopy images (top row: 2,000x, bottom row: 50,000x magnification) from silica particles MPSM1–4 after calcination at 600°C for 10 h.

ethanol, 2-propanol, and 1-butanol, respectively, as solvents. In the presence of P@APTES the *in situ* formed SNPs diffuse into the template where they aggregate and built the polymer/silica hybrid beads HB1–4 which consist of interpenetrating organic/inorganic networks (Fig. 1, Table 1 and Figure S3, S.I.). The polymer template was removed by calcination leaving the mesoporous silica microspheres MPSM1–4 (Table 1, Fig. 2).

The size of the hybrid beads HB1–4 increases by 600 to 800 nm compared to that of the *p*(GMA-*co*-EDMA) template, while the size distributions of the hybrid particles remained highly monodisperse (Table 1). When methanol was applied as solvent an edged morphology was obtained (Figure S3, S.I.). In ethanol and 2-propanol the silica network consisted of nanometer-sized SNPs which enter the pores of the template and agglomerate. As a result, a particulate morphology is obtained. Larger SNPs were formed in 1-butanol which result in a cauliflower-like morphology of the hybrid beads HB4 (Figure S3, S.I.). To conclude, with increasing chain length of the alcoholic solvent larger nanometer-sized SNPs are formed which construct the silica network in the P@APTES template.

After the polymer was removed by calcination the silica networks of all particles shrank. Compared to the size of the template the size of the silica particle MPSM1 is reduced to 5.8 µm while those of the silica particles MPSM2–4 showed only minor changes and remained comparable to the size of the template (Table 1). The original morphologies of the hybrid particles were transferred to the final mesoporous silica microspheres (Fig. 2). Thus, in methanol an edged, in ethanol and 2-propanol a particular and in 1-butanol a cauliflower-like surface was obtained (Fig. 2).

The thermogravimetric curves of the hybrid beads HB1–4 are composed of the thermal degradation behavior of silica and P@APTES (Fig. 3). Roughly three regions of degradation can be identified. The loss of surface water which is mainly due to the silica is observed between 30 and 150°C. Depolymerization and isomerization processes of the polymer template between 200 and 400°C as well as degradation of the polymer backbone between 400 and 600°C lead to the complete decomposition of the template P@APTES [45–47]. Moreover, thermogravimetric analysis of the hybrid beads HB1–4 reveal that different amounts of silica were deposited in the pores of P@APTES (Fig. 3). The smallest quantity of

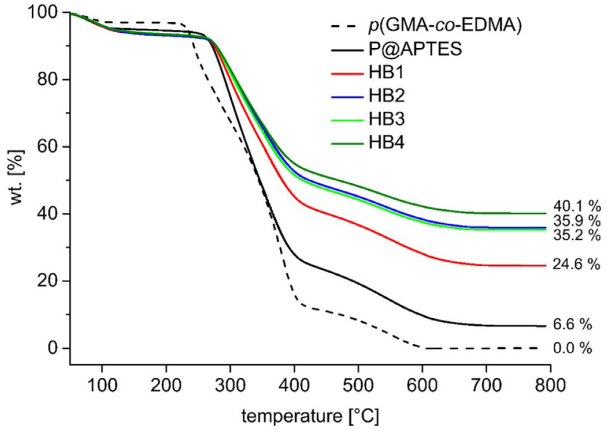


Fig. 3. Thermogravimetric curves of the thermal degradation of *p*(GMA-co-EDMA), P@APTES and HB1-4 particles.

silica was found in the particles HB1 (24.6% silica). Hybrid beads HB2, HB3 and HB4 contain higher amounts of silica (35.9%, 35.2% and 40.1%, respectively). Interestingly, these results indicate that the extent of silica which is incorporated into the polymer network depends on the size of the SNPs that form the silica network [39].

The silica network that penetrates the polymer template P@APTES leads to a decrease of the pore volumes as well as the specific surface areas in the hybrid beads HB1–4 (Table 1, Figure S4, S.I.). Thus, in the hybrid particles HB1 which contain the least silica remain the highest pore volume (0.08 mL g^{-1}) and specific surface areas of 42 m^2 g^{-1} of all hybrid beads. The pore volumes and the specific surface area of HB2 and HB3 decreased more (0.03 mL g^{-1} and 0.04 mL g^{-1}, as well as 15 m^2 g^{-1} and 13 m^2 g^{-1}). The largest SNPs were formed in 1-butanol, which resulted in the smallest pore volume (0.01 mL g^{-1}) and specific surface area (5 m^2 g^{-1}) for HB4. The median pore sizes increase steadily from HB1 to HB4 (Table 1, Figure S4, S.I.). This is a consequence of the size of the SNPs which are responsible for the pore properties.

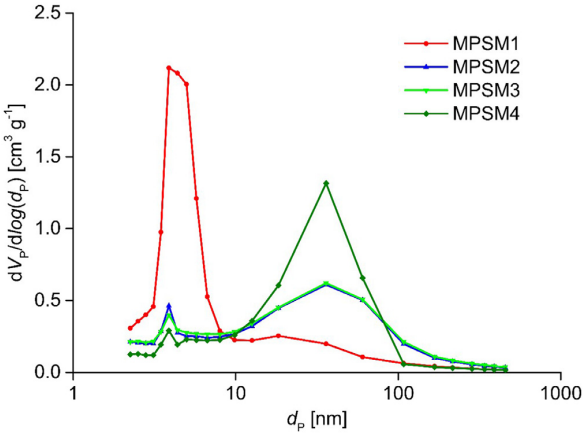


Fig. 4. Pore size distributions of silica particles MPSM1–4.

Larger SNPs lead to a lower specific surface area and higher median pore diameters [39]. With higher chain length of the alcoholic solvent the pore volume of the hybrid beads reduces.

Removing the organic polymer from the hybrid particles by calcination leaves more space in the final MPSMs. Thus, compared to the hybrid materials, the MPSMs possess considerably larger pore parameters in terms of pore volume and specific surface area (Table 1, Fig. 4). During calcination of HB1 the resulting MPSM1 shrank and the number of pores with a diameter of about 20.3 nm is strongly reduced, while the pores with a size of 4.7 nm remain (Figure 4). As a consequence of the small pores and the high pore volume (0.73 mL g^{-1}), the highest specific surface area of the present experimental series of 573 m^2 g^{-1} is obtained. The pore parameters of the particles MPSM2 and MPSM3 are very similar. Both MPSMs have a pore volume of ~ 0.5 mL g^{-1}, a specific surface area of 305 – 320 m^2 g^{-1} and a median pore size of 20.3 nm. The median pore diameter of MPSM4 is 23.5 nm. Due to larger pores, a lower specific surface area of 247 m^2 g^{-1} results.

The ^{13}C CP/MAS NMR and DRIFT-IR spectra of the *p*(GMA-*co*-EDMA) particles show the corresponding signals and bands of the copolymer (Figure S5 and S6, S.I.) [30,31,48]. Successful functionalization with (3-aminopropyl) triethoxysilane was confirmed by additional characteristic resonances in the ^{13}C NMR spectrum and absorption bands in the DRIFT IR spectrum of P@APTES (Figure S5 and S7, S.I.) [49]. The ^{13}C NMR spectrum of the hybrid particles do not change compared to the previous stage. The resulting characteristic bands of the siloxane network and the silanol groups are also visible in the IR spectra of the polymer/silica hybrid particles (Figure S8, S.I.).

In the ^{29}Si CP/MAS NMR spectrum of P@APTES four resonances are observed between -40 and -80 ppm which are assigned to non-hydrolyzed (T^0), partially condensed (T^1, T^2) and fully condensed (T^3) alkoxy silane species (Fig. 5a) [50]. Obviously the trialkoxy silane functions hydrolyze and condense to some extent during the functionalization of the templates. In the ^{29}Si CP/MAS NMR spectrum of the hybrid beads, the resonances of the Q^2, Q^3 and Q^4 groups between -90 and -110 ppm, respectively, confirm the successful incorporation of silica into the template (Fig. 5b) [50]. Interestingly, the signal pattern of the T groups in ^{29}Si CP/MAS NMR spectrum of the hybrids hardly changed compared to that in the spectrum of P@APTES (Figure 5a,b). This indicates that the *in situ* formed SNPs do not condense with the T groups bound to the template, but rather fill the pores. ^{29}Si HPDEC NMR spectra of the hybrid materials and MPSMs show, that the silica network mainly consists of fully condensed Q^4 groups (Fig. 5b). While after calcination the T groups are completely converted to Q groups (Fig. 5c), the conversion of Q^2 and Q^3 to fully condensed Q^4 groups require higher temperatures [51].

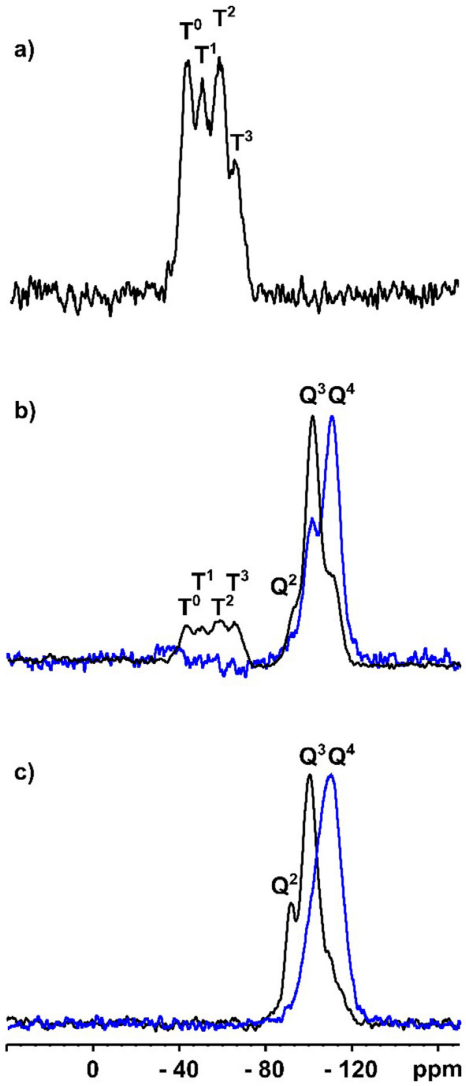


Fig. 5. ^{29}Si CP/MAS NMR spectra (black) and ^{29}Si HPDEC NMR (blue dashed) of functionalized template P@APTES (a), hybrid beads HB (b) and mesoporous silica microspehres MPSM (c).

The morphology and pore properties of the particles MPSM1-4 are determined by the size of the nonporous SNPs which comprise the silica network (Fig. 2). The SNPs are generated via a sol-gel process *in situ* and diffuse into the pores of the P@APTES template. The size of the SNPs is controlled by the parameters of the sol-gel process and the diffusion rate of the SNPs into the template [39]. Here, under otherwise identical reaction conditions the choice of the solvent controls the *in situ* SNP growth and thus the properties of the final MPSM. Based on the low hydrolysis and condensation rate of TEOS in methanol a low yield of silica is incorporated into the template (HB1), which results in smaller MPSM1 particles after calcination. The small SNPs condense and the silica network shrinks when the size-forming template is decomposed. The large mesopores, distributed in the template, also disappear, leaving only mesopores of a size of 4.7 nm. In ethanol, 2-propanol, and butanol

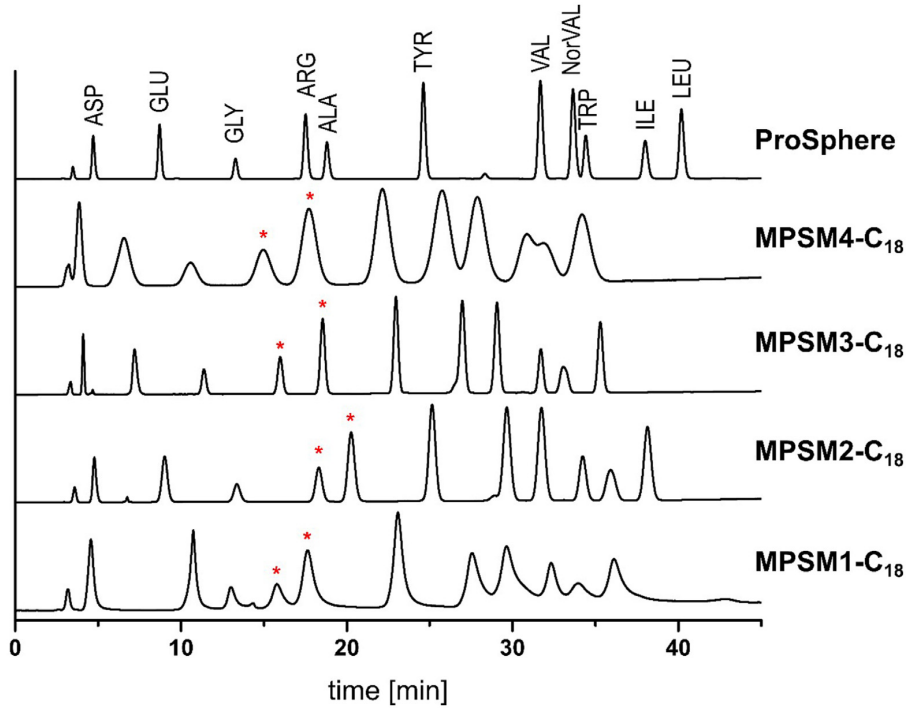


Fig. 6. Separation of eleven amino acids on MPSM1–4-C_{18}. Chromatographic settings: column dimension: 250 × 4.6 mm; mobile phase A: sodium phosphate buffer (25 mM, pH = 7.2) with 0.75 v.% THF, mobile phase B: MeOH/ACN/buffer (35/15/50 v.%); gradient from 0 % B to 100 % B within 50 minutes; injection volume: 20 µl (2.1 µmol μL^{-1} each amino acid); column temperature: 30°C; fluorescence detection: 330 nm extinction, 450 nm emission. The order of elution of arginine and alanine (asterisks) is reversed for all MPSMs compared to that of the ProSphere column.

the SNPs become larger and construct a silica network with larger pores. Due to the introduction of larger amounts of silica into the pores of the template and their larger SNPs, MPSM2–4 map the template and the void space remains intact after calcination. Consequently, the median pore sizes of the particles MPSM2–4 hardly decrease.

Porous silica particles are commonly used as C_{18} functionalized materials in reversed phase chromatography [52,53]. To determine the separation behavior of the MPSMs as stationary phases, the particles MPSM1–4 were functionalized with trimethoxy (octadecyl) silane and packed into a 250 × 4.6 mm stainless steel column with acetone as slurry and MeOH / H_2O (85 v.% / 15 v.%) as pressure medium. A linear gradient from 100% eluent A to 100% eluent B in 50 minutes was applied to separate the amino acids. The primary amines were derivatized with a mixture of *ortho*-phthalaldehyde and 3-mercaptopropionic acid. Therefore, the analytes were treated with the pre-column derivatization reagent for 90 seconds and then injected. All injections were performed with freshly prepared samples to avoid degradation of the derivatization agent. The derivatized samples were excited with a fluorescence detector at 330 nm and detected at 450 nm. The separation behavior of the four new stationary phases was compared with the commercially available column ProSphere C18 (300 Å, 10 µm, 250 × 4.6 mm).

Fig. 6 shows the separation of a mixture of 11 different amino acids consisting of aspartic acid, glutamic acid, glycine, arginine, alanine, tyrosine, valine, norvaline, tryptophan, isoleucine, and leucine. The retention times of each amino acid and the corresponding capacity factors are listed in Table S1.

As a result of the high specific surface area of MPSM1, the analytes interact longer with the stationary phase, which leads to an incomplete separation. Thus, on MPSM1-C_{18} just ten of the amino acids can be detected and in addition, the last five amino acids elute into each other. For MPSM4-C_{18} a few amino acids overlap, so that no complete separation of the components is obtained. This could result from the agglomerated morphology of MPSM4, which inhibits the accessibility of pores and thus impedes the diffusion of the analytes into the pores. In contrast to this baseline separations of all amino acids were achieved with the stationary phases MPSM2-C_{18} and MPSM3-C_{18}. Since the particle size and pore parameters of MPSM2 and MPSM3 are very similar their chromatographic properties are comparable (Fig. 6 and Table 2). The peak resolution of the separation of arginine and alanine is increased for MPSM3-C_{18} and all amino acids elute earlier compared to MPSM3-

Table 2
Column performance for the separation of several amino acids of the MPSM-C_{18} and a commercially available column.

	$R_{ASP-GLU}$	$R_{GLU-GLY}$	$R_{GLY-ARG}$	$R_{ARG-ALA}$	$R_{ALA-TYR}$	$R_{TYR-VAL}$	$R_{VAL-NorVAL}$	$R_{NorVAL-TRP}$	$R_{TRP-ILE}$	$R_{ILE-LEU}$
MPSM1-C_{18}	10.07	3.20	2.81	1.55	4.86	3.68	1.35	1.88	0.95	1.16
MPSM2-C_{18}	8.06	6.24	6.53	2.49	6.25	5.63	2.51	3.04	1.76	2.27
MPSM3-C_{18}	8.55	8.37	8.73	4.64	8.25	7.14	3.55	4.68	1.84	2.95
MPSM4-C_{18}	2.56	2.71	2.75	1.62	2.63	2.00	1.12	1.55	0.53	1.29
ProSphere	11.32	11.33	9.36	2.75	12.29	14.04	3.72	1.48	6.54	3.87

C_{18} and ProSphere C18. Overall, the separation on both synthesized phases is comparable to the commercially available column. In addition, the phases achieve faster separation of amino acids without loss of quality (Table 2). Interestingly, the order of elution (asterisk) of arginine and alanine is reversed for all MPSMs compared to that of the ProSphere column (Fig. 6). Provided that the derivatization reagents are freshly prepared, the retention behavior of each amino acid is reproducible over several runs. We also used the particles discussed in this manuscript to perform the separation of various proteins as in reference [33]. Preliminary results are shown in Figure S10.

4. Conclusion

APTES functionalized *p*(GMA-*co*-EDMA) particles provide a good platform to prepare MPSMs and are thus an alternative to amino functionalized *p*(GMA-*co*-EDMA) templates. The particle size, morphology, and pore parameters of MPSMs depend on the settings of the sol-gel process and are thus adjusted at the stage of the hybrid bead syntheses. If the amount of silica deposited in the template and the size of the SNPs are properly tuned the template is mapped accurately. Moreover, larger SNPs also ensure the preservation of the pore structure and the morphology of the MPSMs after calcination.

Interestingly, ^{29}Si NMR spectroscopy of the hybrid beads and MPSMs indicate that the SNPs do not covalently bind to the APTES functions. This agrees with observations made earlier, that TEOS is hydrolyzed and condensed in the alcoholic solvent to SNPs before they diffuse into the template [39]. As the SNP growth depends on the solvent, morphology and pore properties of the final MPSM can be adjusted simply by the right choice of the solvent. The successful separation of eleven amino acids was achieved with selected MPSMs as stationary phases. The separation behavior strongly depends on the pore properties of the MPSMs. This opens the opportunity preparing tailored stationary phases for HPLC applications.

Declaration of Competing Interest

The authors declare the following financial interests/personal relationships which may be considered as potential competing interests:

Hermann A. Mayer reports equipment, drugs, or supplies was provided by Dr. Maisch GmbH.

CRediT authorship contribution statement

Fabio Fait: Investigation, Methodology, Resources, Formal analysis, Writing – original draft, Writing – review & editing. **Julia C. Steinbach:** Investigation, Resources, Formal analysis, Writing – original draft, Writing – review & editing. **Andreas Kandelbauer:** Project administration, Funding acquisition, Supervision, Writing – original draft, Writing – review & editing. **Hermann A. Mayer:** Project administration, Funding acquisition, Supervision, Writing – original draft, Writing – review & editing.

Data availability

Data will be made available on request.

Acknowledgments

This research was funded the by Bundesministerium für Bildung und Forschung (BMBF, grant number 13FH647IX6) and the Bundesministerium für Wirtschaft und Energie (AiF/ZIM, grant number ZF4019203SL8). Furthermore, we would like to thank our cooperation partner Dr. Maisch GmbH for their support in preparing the columns. We thank Elke Nadler for contributing the SEM measurements.

Supplementary materials

Supplementary material associated with this article can be found, in the online version, at doi:10.1016/j.chroma.2023.464190.

References

[1] A. Dohare, S. Sudhakar, B. Brodbeck, A. Mukherjee, M. Brecht, A. Kandelbauer, E. Schäffer, H.A. Mayer, Anisotropic and amphiphilic mesoporous core–shell silica microparticles provide chemically selective environments for simultaneous delivery of curcumin and quercetin, Langmuir 37 (2021) 13460–13470, doi:10.1021/acs.langmuir.1c02210.
[2] C.M. Crudden, M. Sateesh, R. Lewis, Mercaptopropyl-modified mesoporous silica: a remarkable support for the preparation of a reusable, heterogeneous palladium catalyst for coupling reactions, J. Am. Chem. Soc. 127 (2005) 10045–10050, doi:10.1021/ja0430954.
[3] F. Ditzinger, D.J. Price, A.R. Ilie, N.J. Köhl, S. Jankovic, G. Tsakiridou, S. Aleandri, L. Kalantzi, R. Holm, A. Nair, C. Saal, B. Griffin, M. Kuentz, Lipophilicity and hydrophobicity considerations in bio-enabling oral formulations approaches – a PEARRL review, J.Pharm. Pharmacol. 71 (2019) 464–482, doi:10.1111/jphp.12984.
[4] Q. He, J. Shi, F. Chen, M. Zhu, L. Zhang, An anticancer drug delivery system based on surfactant-templated mesoporous silica nanoparticles, Biomaterials 31 (2010) 3335–3346, doi:10.1016/j.biomaterials.2010.01.015.
[5] K.W. Gallis, J.T. Araujo, K.J. Duff, J.G. Moore, C.C. Landry, The use of mesoporous silica in liquid chromatography, Adv. Mater. 11 (1999) 1452–1455, doi:10.1002/(SICI)1521-4095(199912)11:17⟨1452::AID-ADMA1452⟩3.0.CO;2-R.
[6] J.J. Kirkland, C.H. Dilks, J.J. DeStefano, Normal-phase high-performance liquid chromatography with highly purified porous silica microspheres, J. Chromatogr. A 635 (1993) 19–30, doi:10.1016/0021-9673(93)83111-5.
[7] W. Liu, C. Selomulya, W. Wu, X.D. Chen, A single step assembly of uniform microparticles for controlled release applications, Soft Matter 7 (2011) 3323–3330, doi:10.1039/c0sm01371d.
[8] R. Arshady, Beaded polymer supports and gels: i. manufacturing techniques, J. Chromatogr. A 586 (1991) 181–197, doi:10.1016/0021-9673(91)85124-X.
[9] E.D.E.R. Hyde, A. Seyfaee, F. Neville, R. Moreno-Atanasio, Colloidal silica particle synthesis and future industrial manufacturing pathways: a review, Ind. Eng. Chem. Res. 55 (2016) 8891–8913, doi:10.1021/acs.iecr.6b01839.
[10] K. Waldron, Z. Wu, W.D. Wu, W. Liu, D. Zhao, X.D. Chen, C. Selomulya, Formation of uniform large SBA-15 microspheres via spray drying, J. Mater. Chem. A. 2 (2014) 19500–19508, doi:10.1039/C4TA05002A.
[11] I.V. Melnyk, B. Alonso, Y.L. Zub, E. Véron, D. Massiot, T. Cacciaguerra, Spray-dried mesoporous silica microspheres with adjustable textures and pore surfaces homogenously covered by accessible thiol functions, J. Mater. Chem. 18 (2008) 1368–1382, doi:10.1039/b717133a.
[12] W. Stöber, A. Fink, E. Bohn, Controlled growth of monodisperse silica spheres in the micron size range, J. Colloid Interface Sci. 26 (1968) 62–69, doi:10.1016/0021-9797(68)90272-5.
[13] C.G. Tan, B.D. Bowen, N. Epstein, Production of monodisperse colloidal silica spheres: Effect of temperature, J. Colloid Interface Sci. 118 (1987) 290–293, doi:10.1016/0021-9797(87)90458-9.
[14] M.T. Harris, R.R. Brunson, C.H. Byers, The base-catalyzed hydrolysis and condensation reactions of dilute and concentrated TEOS solutions, J. Non Cryst. Solids 121 (1990) 397–403, doi:10.1016/0022-3093(90)90165-I.
[15] A. Van Blaaderen, J. Van Geest, A. Vrij, Monodisperse colloidal silica spheres from tetraalkoxysilanes: Particle formation and growth mechanism, J. Colloid Interface Sci. 154 (1992) 481–501, doi:10.1016/0021-9797(92)90163-G.
[16] N. Plumeré, A. Ruff, B. Speiser, V. Feldmann, H.A. Mayer, Stöber silica particles as basis for redox modifications: particle shape, size, polydispersity, and porosity, J. Colloid Interface Sci. 368 (2012) 208–219, doi:10.1016/j.jcis.2011.10.070.
[17] L.P. Singh, S.K. Bhattacharyya, R. Kumar, G. Mishra, U. Sharma, G. Singh, S. Ahalawat, Sol-gel processing of silica nanoparticles and their applications, Adv. Colloid Interface Sci. 214 (2014) 17–37, doi:10.1016/j.cis.2014.10.007.
[18] S. Sadasivan, A.K. Dubey, Y. Li, D.H. Rasmussen, Alcoholic solvent effect on silica synthesis—NMR and DLS investigation, J. Sol-Gel Sci. Technol. 12 (1998) 5–14, doi:10.1023/A:1008659708390.
[19] O. Malay, I. Yilgor, Y.Z. Menceloglu, Effects of solvent on TEOS hydrolysis kinetics and silica particle size under basic conditions, J. Sol Gel Sci. Technol. 67 (2013) 351–361, doi:10.1007/s10971-013-3088-4.
[20] S.L. Chen, P. Dong, G.H. Yang, J.J. Yang, Characteristic aspects of formation of new particles during the growth of monosize silica seeds, J. Colloid Interface Sci. 180 (1996) 237–241, doi:10.1006/jcis.1996.0295.
[21] J.H. Zhang, P. Zhan, Z.L. Wang, W.Y. Zhang, N.B. Ming, Preparation of monodisperse silica particles with controllable size and shape, J. Mater. Res. 18 (2003) 649–653, doi:10.1557/JMR.2003.0085.
[22] K. Nozawa, H. Gailhanou, L. Raison, P. Panizza, H. Ushiki, E. Sellier, J.P. Delville, M.H. Delville, Smart control of monodisperse stöber silica particles: effect of reactant addition rate on growth process, Langmuir 21 (2005) 1516–1523, doi:10.1021/la048569r.

[23] H. Nakabayashi, A. Yamada, M. Noba, Y. Kobayashi, M. Konno, D. Nagao, Electrolyte-added one-pot synthesis for producing monodisperse, micrometer-sized silica particles up to 7 μm, Langmuir 26 (2010) 7512–7515, doi:10.1021/la904316f.
[24] C.T. Kresge, M.E. Leonowicz, W.J. Roth, J.C. Vartuli, J.S. Beck, Ordered mesoporous molecular sieves synthesized by a liquid-crystal template mechanism, Nature 359 (1992) 710–712, doi:10.1038/359710a0.
[25] N.K. Raman, M.T. Anderson, C.J. Brinker, Template-based approaches to the preparation of amorphous, nanoporous silicas, Chem. Mater. 8 (1996) 1682–1701, doi:10.1021/cm960138+.
[26] L. Zhang, L. Jin, B. Liu, J. He, Templated growth of crystalline mesoporous materials: from soft/hard templates to colloidal templates, Front. Chem. 7 (2019) 22, doi:10.3389/fchem.2019.00022.
[27] M. Mesa, L. Sierra, B. López, A. Ramirez, J.L. Guth, Preparation of micron-sized spherical particles of mesoporous silica from a triblock copolymer surfactant, usable as a stationary phase for liquid chromatography, Solid State Sci. 5 (2003) 1303–1308, doi:10.1016/S1293-2558(03)00185-7.
[28] J.P. Hanrahan, A. Donovan, M.A. Morris, J.D. Holmes, Synthesis and swelling of large pore diameter mesoporous silica spheres, J. Mater. Chem. 17 (2007) 3881–3887, doi:10.1039/b705023b.
[29] A. Ahmed, R. Clowes, E. Willneff, H. Ritchie, P. Myers, H. Zhang, Synthesis of uniform porous silica microspheres with hydrophilic polymer as stabilizing agent, Ind. Eng. Chem. Res. 49 (2010) 602–608, doi:10.1021/ie901213v.
[30] J. He, C. Yang, X. Xiong, B. Jiang, Preparation and characterization of monodisperse porous silica microspheres with controllable morphology and structure, J. Polym. Sci. A Polym. Chem. 50 (2012) 2889–2897, doi:10.1002/pola.26066.
[31] H. Xia, G. Wan, J. Zhao, J. Liu, Q. Bai, Preparation and characterization of monodisperse large-porous silica microspheres as the matrix for protein separation, J. Chromatogr. A 1471 (2016) 138–144, doi:10.1016/j.chroma.2016.10.025.
[32] H. Xia, Q. Bai, G. Wan, F. Yang, J. Wang, Preparation of monodisperse large-porous silica microspheres with polymer microspheres as the templates for protein separation, Mater. Lett. 180 (2016) 19–22, doi:10.1016/j.matlet.2016.05.044.
[33] F. Fait, J.C. Steinbach, A. Kandelbauer, H.A. Mayer, Impact of porosity and surface functionalization of hard templates on the preparation of mesoporous silica microspheres, Microporous Mesoporous Mater. (2023) 112482, doi:10.1016/j.micromeso.2023.112482.
[34] J. Bai, Q. Zhu, C. Tang, J. Liu, Y. Yi, Q. Bai, Synthesis and application of 5 μm monodisperse porous silica microspheres with controllable pore size using polymeric microspheres as templates for the separation of small solutes and proteins by high-performance liquid chromatography, J. Chromatogr. A 1675 (2022) 463165, doi:10.1016/j.chroma.2022.463165.
[35] N. Gartmann, C. Schütze, H. Ritter, D. Brühwiler, The effect of water on the functionalization of mesoporous silica with 3-aminopropyltriethoxysilane, J. Phys. Chem. Lett. 1 (2010) 379–382, doi:10.1021/jz9002795.
[36] H.W. Lee, H.J. Cho, J.H. Yim, J.M. Kim, J.K. Jeon, J.M. Sohn, K.S. Yoo, S.S. Kim, Y.K. Park, Removal of Cu(II)-ion over amine-functionalized mesoporous silica materials, J. Ind. Eng. Chem. 17 (2011) 504–509, doi:10.1016/j.jiec.2010.09.022.
[37] S. Grama, Z. Plichta, M. Trchová, J. Kovářová, M. Beneš, D. Horák, Monodisperse macroporous poly(glycidyl methacrylate) microspheres coated with silica: Design, preparation and characterization, React. Funct. Polym. 77 (2014) 11–17, doi:10.1016/j.reactfunctpolym.2014.01.010.
[38] J. Chen, L. Zhu, L. Ren, C. Teng, Y. Wang, B. Jiang, J. He, Fabrication of monodisperse porous silica microspheres with a tunable particle size and pore size for protein separation, ACS Appl. Bio Mater. 1 (2018) 604–612, doi:10.1021/acsabm.8b00088.
[39] J.C. Steinbach, F. Fait, H.A. Mayer, A. Kandelbauer, Monodisperse porous silica/polymer nanocomposite microspheres with tunable silica loading, morphology and porosity, IJMS 23 (2022) 14977, doi:10.3390/ijms232314977.
[40] F. Rouquerol, J. Rouquerol, K.S.W. Sing, P.L. Llewellyn, G. Maurin, Adsorption by Powders and Porous Solids: Principles, Methodology and Applications, 2nd ed., Elsevier/AP, Amsterdam, 2014.
[41] S. Lowell, J.E. Shields, M.A. Thomas, M. Thommes, Characterization of Porous Solids and Powders: Surface Area, Pore Size and Density, Springer, Netherlands, Dordrecht, 2004, doi:10.1007/978-1-4020-2303-3.
[42] M. Thommes, K. Kaneko, A.V. Neimark, J.P. Olivier, F. Rodriguez-Reinoso, J. Rouquerol, K.S.W. Sing, Physisorption of gases, with special reference to the evaluation of surface area and pore size distribution (IUPAC Technical Report), Pure Appl. Chem. 87 (2015) 1051–1069, doi:10.1515/pac-2014-1117.
[43] J.C. Groen, L.A.A. Peffer, J. Pérez-Ramírez, Pore size determination in modified micro- and mesoporous materials. Pitfalls and limitations in gas adsorption data analysis, Microporous Mesoporous Mater. 60 (2003) 1–17, doi:10.1016/S1387-1811(03)00339-1.
[44] J.C. Steinbach, F. Fait, S. Wagner, A. Wagner, M. Brecht, H.A. Mayer, A. Kandelbauer, Rational design of pore parameters in monodisperse porous Poly(glycidyl methacrylate-co-ethylene glycol dimethacrylate) particles based on response surface methodology, Polymers 14 (2022) 382, doi:10.3390/polym14030382.
[45] J. Macan, I. Brnardić, S. Orlić, H. Ivanković, M. Ivanković, Thermal degradation of epoxy–silica organic–inorganic hybrid materials, Polym. Degrad. Stab. 91 (2006) 122–127, doi:10.1016/j.polymdegradstab.2005.04.024.
[46] C. Acquah, M.K. Danquah, C.K.S. Moy, M. Anwar, C.M. Ongkudon, Thermogravimetric characterization of ex situ polymethacrylate (EDMA-co-GMA) monoliths, Can. J. Chem. Eng. 95 (2017) 1345–1351, doi:10.1002/cjce.22781.
[47] M. Grochowicz, P. Pączkowski, B. Gawdzik, Investigation of the thermal properties of glycidyl methacrylate–ethylene glycol dimethacrylate copolymeric microspheres modified by Diels–Alder reaction, J. Therm. Anal. Calorim. 133 (2018) 499–508, doi:10.1007/s10973-017-6785-3.
[48] I.S. Stefanović, M.V. Pergal, B.M. Ekmeščić, D.D. Maksin, A.B. Nastasović, Z.P. Miladinović, Z.M. Vuković, D.M. Micić, Structure, Thermal, and Morphological Properties of Novel Macroporous Amino-Functionalized Glycidyl Methacrylate Based Copolymers, Ind. Eng. Chem. Res. 54 (2015) 6902–6911, doi:10.1021/acs.iecr.5b01285.
[49] G.S. Caravajal, D.E. Leyden, G.R. Quinting, G.E. Maciel, Structural characterization of (3-aminopropyl)triethoxysilane-modified silicas by silicon-29 and carbon-13 nuclear magnetic resonance, Anal. Chem. 60 (1988) 1776–1786, doi:10.1021/ac00168a027.
[50] E. Lippmaa, M. Maegi, A. Samoson, G. Engelhardt, A.R. Grimmer, Structural studies of silicates by solid-state high-resolution silicon-29 NMR, J. Am. Chem. Soc. 102 (1980) 4889–4893, doi:10.1021/ja00535a008.
[51] L.T. Zhuravlev, The surface chemistry of amorphous silica. Zhuravlev model, Colloids Surf. A 173 (2000) 1–38, doi:10.1016/S0927-7757(00)00556-2.
[52] H. Claessens, M. Vanstraten, Review on the chemical and thermal stability of stationary phases for reversed-phase liquid chromatography, J. Chromatogr. A 1060 (2004) 23–41, doi:10.1016/S0021-9673(04)01438-4.
[53] R. Hayes, A. Ahmed, T. Edge, H. Zhang, Core–shell particles: Preparation, fundamentals and applications in high performance liquid chromatography, J. Chromatogr. A 1357 (2014) 36–52, doi:10.1016/j.chroma.2014.05.010.

Supporting Information

Incorporation of silica nanoparticles into porous templates to fabricate mesoporous silica microspheres for high performance liquid chromatography applications

Fabio Fait[1,2], Julia C. Steinbach[1,2], Andreas Kandelbauer[2,3] and Hermann A. Mayer*[1]

[1]Institute of Inorganic Chemistry, University of Tübingen, Auf der Morgenstelle 18, 72076 Tübingen, Germany

[2]Process Analysis and Technology (PA&T), Reutlingen Research Institute, Reutlingen University, Alteburgstrasse 150, 72762 Reutlingen, Germany

[3]Institute of Wood Technology and Renewable Materials, Department of Material Sciences and Process Engineering (MAP), University of Natural Resources and Life Sciences, Gregor-Mendel-Straße 33, 1180 Vienna, Austria

*Correspondence: hermann.mayer@uni-tuebingen.de

Chemicals

Polyvinyl alcohol (PVA, 87-89% hydrolyzed, mean average 88000 – 97000 g mol^{-1}) and polyvinylpyrrolidone K_{30} (PVP, mean average 40000 g mol^{-1}) were acquired from abcr GmbH (Germany). Ethyleneglycol dimethacrylate (EDMA) was bought from Acros Organics (Germany). Cyclohexanol and sodium dodecyl sulfate (SDS) were purchased from Carl Roth (Germany). Styrene was obtained by Fisher Chemicals (Germany). Dibenzoyl peroxide (BPO), dibutyl phthalate (DBP), glycidyl methacrylate (GMA) and the protein test mixture H2899 (ribonuclease A, cytochrome C, holo-transferrin and apomyoglobin) were purchased from Sigma-Aldrich (Germany).

Synthesis of polystyrene

Monodisperse polystyrene particles with diameters of 1.9 ± 0.1 µm were prepared as reported earlier [1] (**Figure S1**).

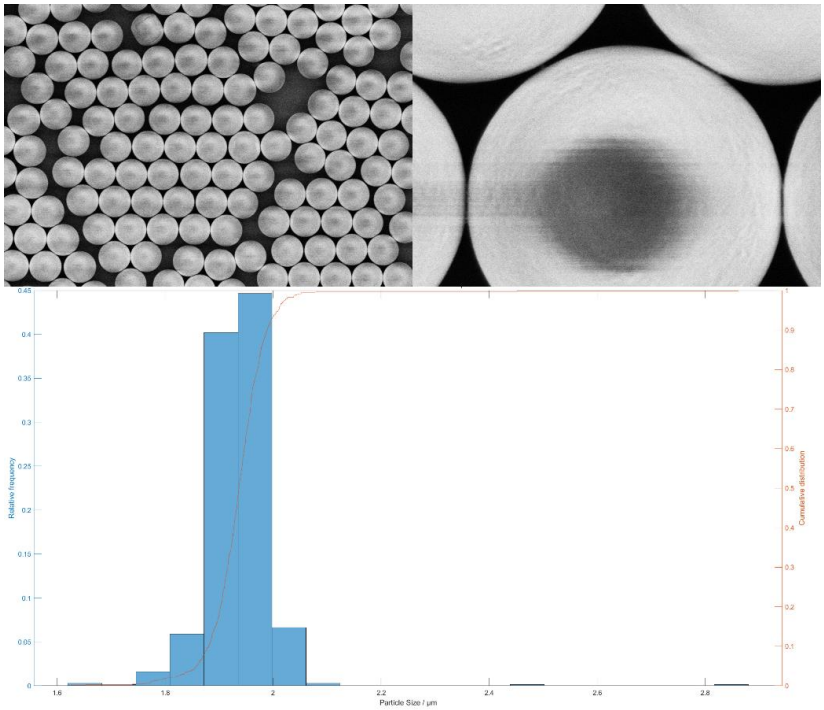


Figure S1. SEM images of applied polystyrene particles (top) and their particle size distribution (bottom).

Synthesis of *p*(GMA-*co*-EDMA)

0.3 g of polystyrene particles and 5 mL of an aqueous SDS solution (0.25 wt.%) were dispersed in a 250 mL flask. 2 mL DBP were emulsified in 150 mL aqueous SDS solution (0.25 wt.%) with a homogenizer at 4500 rpm for 15 min and then added to the polystyrene suspension. The mixture was stirred for 24 h at 200 rpm. 6 mL GMA, 9 mL EDMA, 4 mL cyclohexanol, 11 mL toluene, 0.4 g BPO and 150 mL aqueous SDS solution (0.25 wt.%) were emulsified with a homogenizer at 4500 rpm for 15 min. This emulsion, a 150 mL aqueous PVA solution (2.3 wt.%) and the activated polystyrene particles were transferred to a 500 mL three-necked flask and stirred for 24 h at 200 rpm. Argon was passed into the reaction mixture for 30 minutes and then heated to 70 °C for 24 hours. The particles were separated from the solution, washed three times with EtOH and three times with H_2O and dried at 65 °C for 16 h. The average particle size of the *p*(GMA-*co*-EDMA) particles is 7.6 ± 0.7 µm (**Figure S2**).

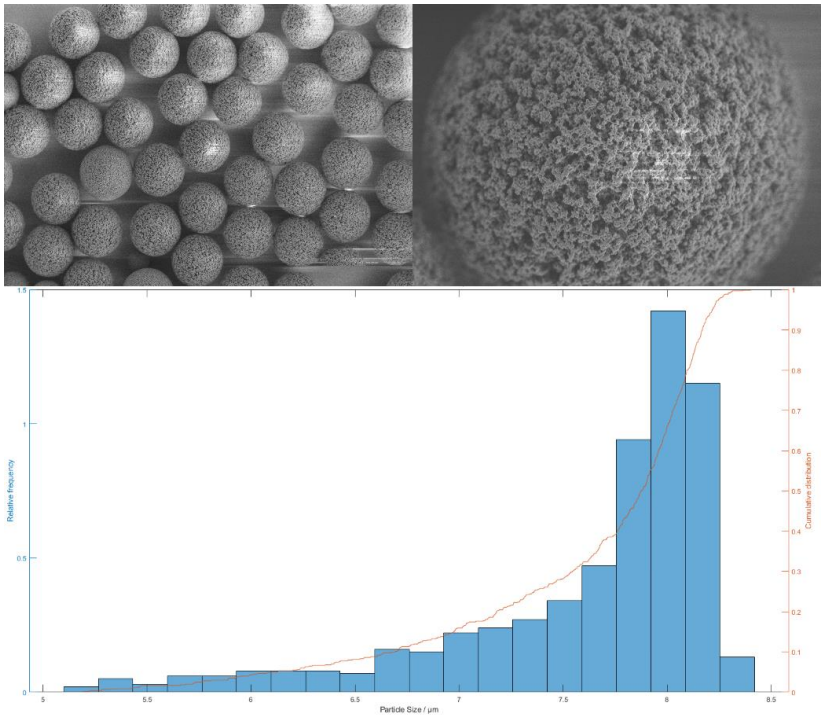


Figure S2. SEM images of the polymer templates ***p*(GMA-*co*-EDMA)** (7.6 ± 0.7 µm) (top) and the corresponding particle size distribution (bottom).

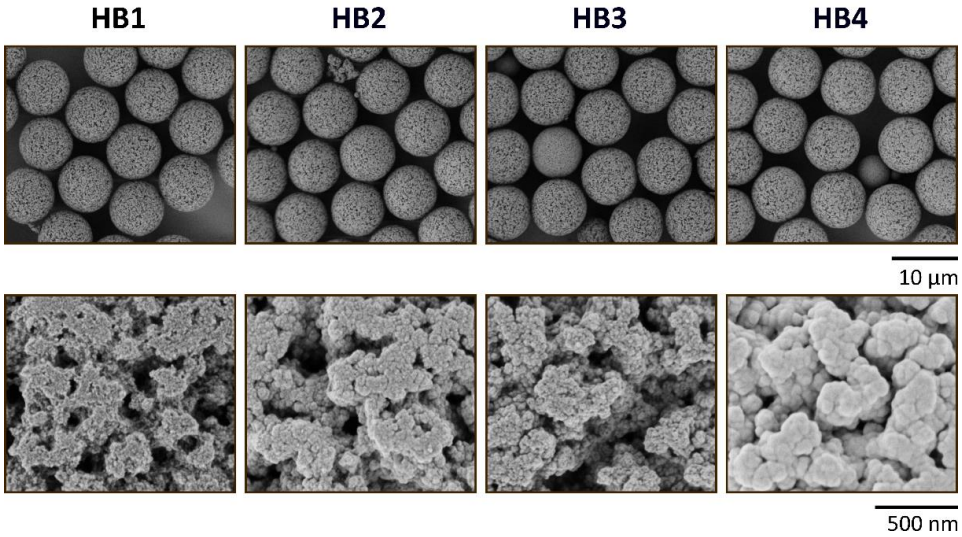


Figure S3. SEM images (top row: 2,000x, bottom row: 50,000x magnification) from hybrid beads after sol-gel process in methanol (**HB1**), ethanol (**HB2**), 2-propanol (**HB3**) and 1-butanol (**HB4**).

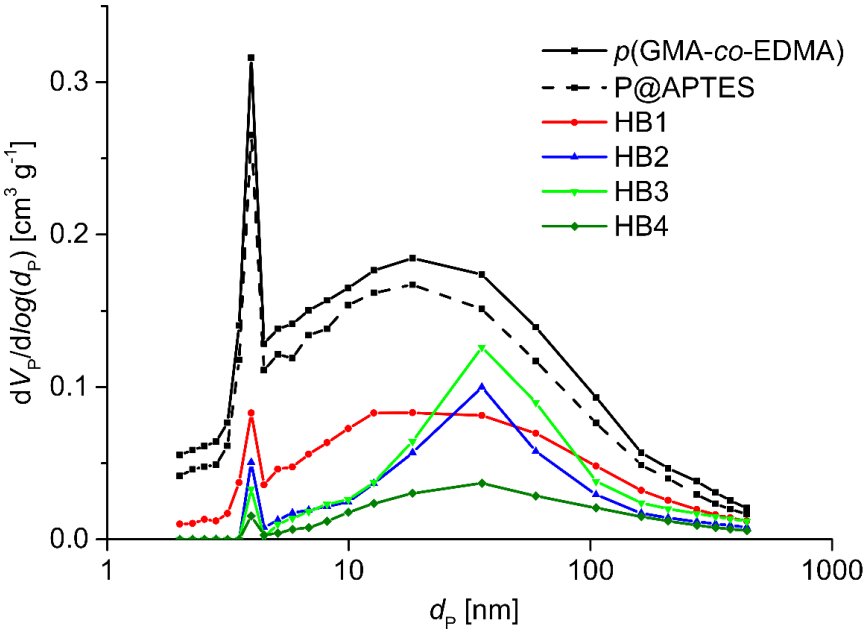


Figure S4. Pore size distributions of porous ***p*(GMA-*co*-EDMA)**, functionalized **P@APTES** template and hybrid beads **HB1**–**4**.

^{13}C CP/MAS solid state NMR spectroscopy of *p*(GMA-*co*-EDMA) and P@APTES

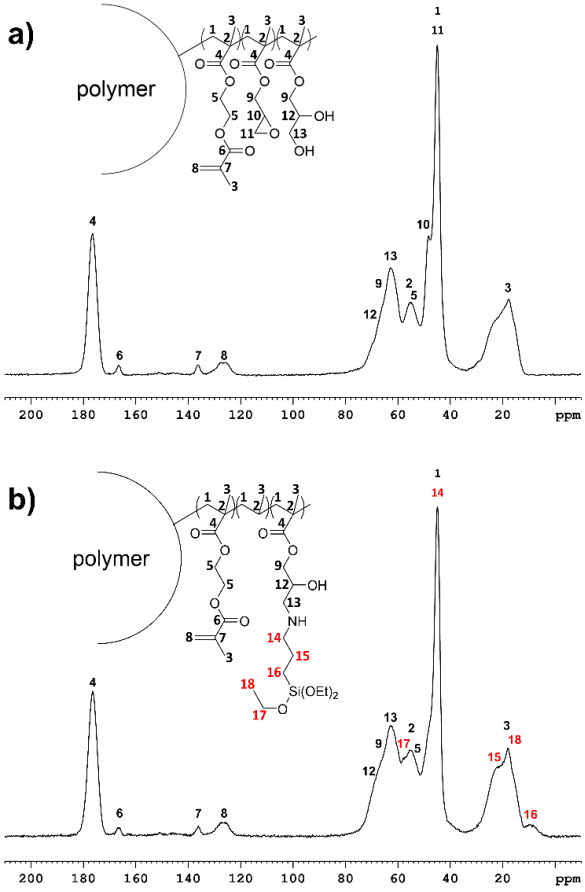


Figure S5. ^{13}C CP/MAS NMR spectra of (**a**) ***p*(GMA-co-EDMA)** and (**b**) **P@APTES** particles.

DRIFT IR spectroscopy of *p*(GMA-*co*-EDMA), P@APTES, HBs and MPSMs

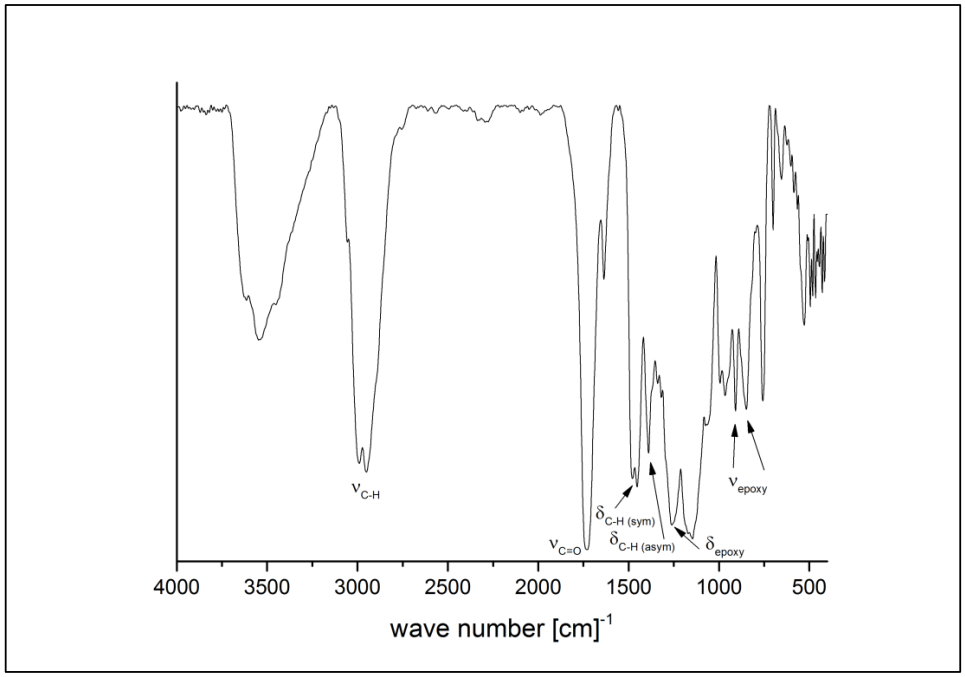


Figure S6. DRIFT IR spectra of ***p*(GMA-*co*-EDMA)** copolymer particles.

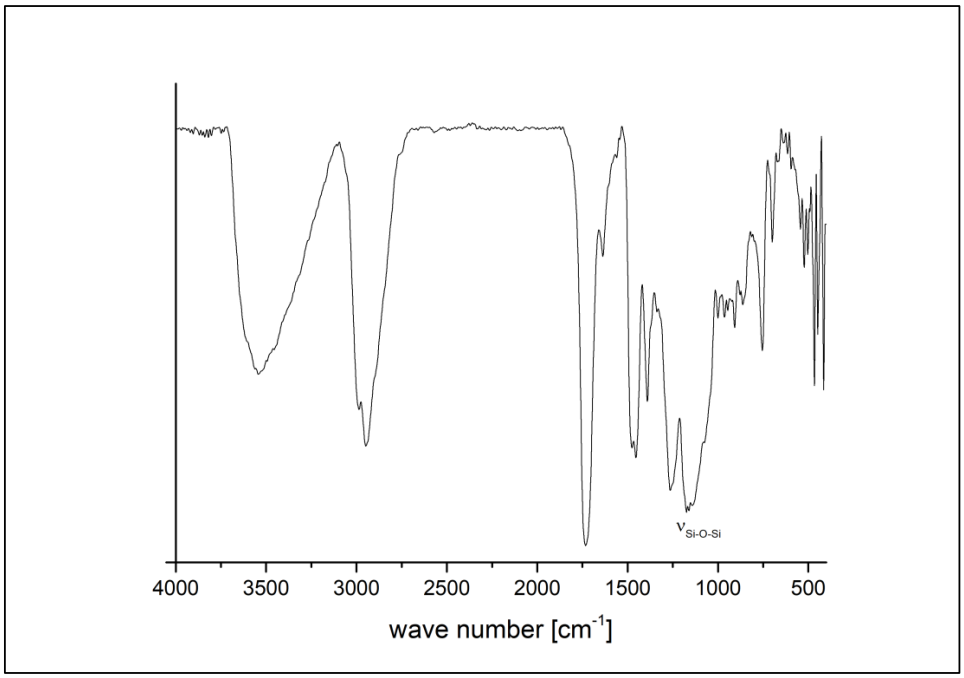


Figure S7. DRIFT IR spectra of functionalized **P@APTES** particles.

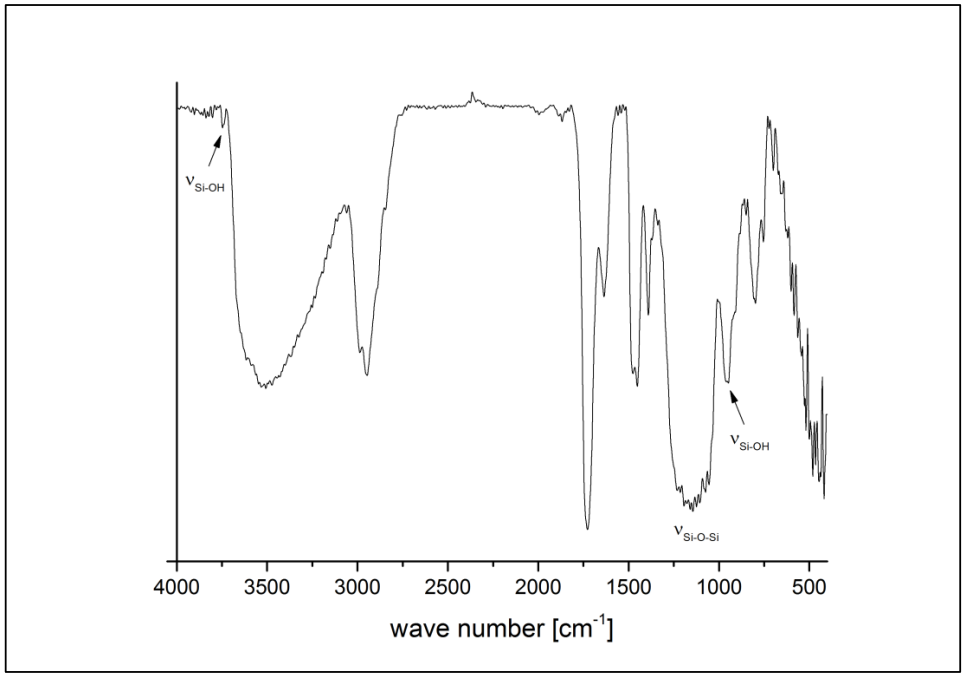


Figure S8. DRIFT IR spectra of **HB2** exemplary for hybrid particles.

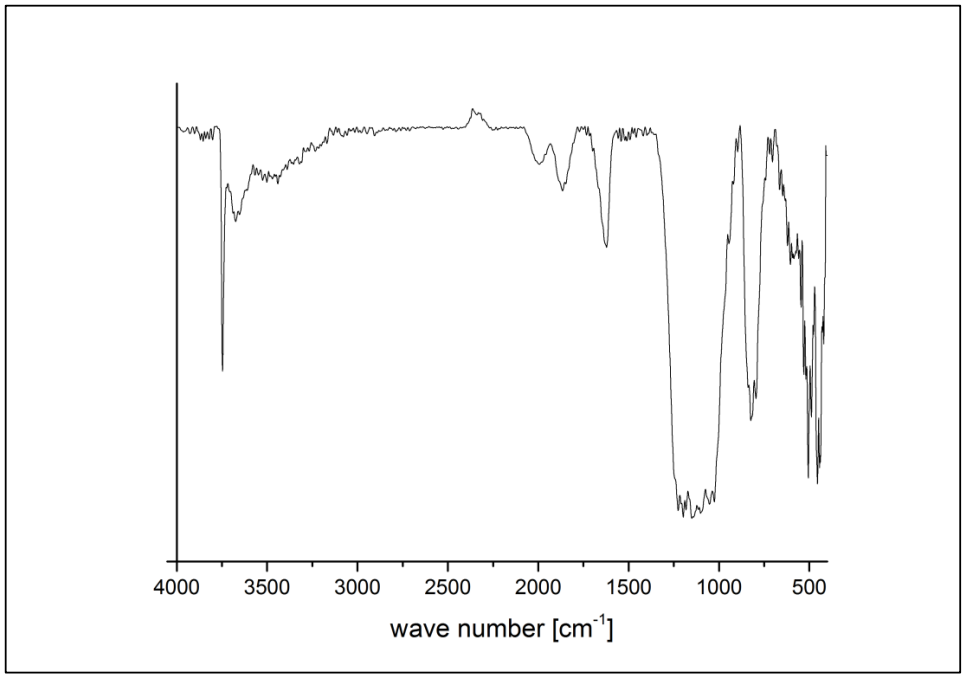


Figure S9. DRIFT IR spectra of **MPSM2** exemplary for silica particles.

Table S1. Retention times (t_r) and capacity factors (k') of the different amino acids on the corresponding stationary phases.

	MPSM1-C_{18}		**MPSM2-C_{18}**		**MPSM3-C_{18}**		**MPSM4-C_{18}**		**ProSphere**	
	t_r	k'	t_r	k'	t_r	k'	t_r	k'	t_r	k'
ASP	4.73	0.75	4.60	0.84	4.10	0.65	3.86	0.55	4.70	0.89
GLU	9.91	2.68	8.61	2.45	7.20	1.89	6.62	1.66	8.71	2.49
GLY	12.04	3.47	13.03	4.23	11.38	3.57	10.60	3.25	13.29	4.33
ARG	17.25	5.41	17.96	6.20	15.98	5.41	14.98	5.01	17.51	6.02
ALA	18.59	5.90	19.28	6.73	18.54	6.44	17.71	6.11	18.80	6.54
TYR	24.11	7.95	24.50	8.83	22.96	8.21	22.17	7.89	24.61	8.87
VAL	29.34	9.90	29.12	10.68	26.97	9.82	25.77	9.34	31.67	11.70
NorVAL	31.28	10.61	31.13	11.49	29.06	10.66	27.89	10.19	33.64	12.50
TRP	33.57	11.47	33.34	12.37	31.70	11.72	30.90	11.39	34.41	12.80
ILE	35.62	12.23	35.09	13.07	33.06	12.26	31.89	11.79	38.00	14.24
LEU	37.56	12.95	37.19	13.92	35.29	13.16	34.21	12.72	40.18	15.12

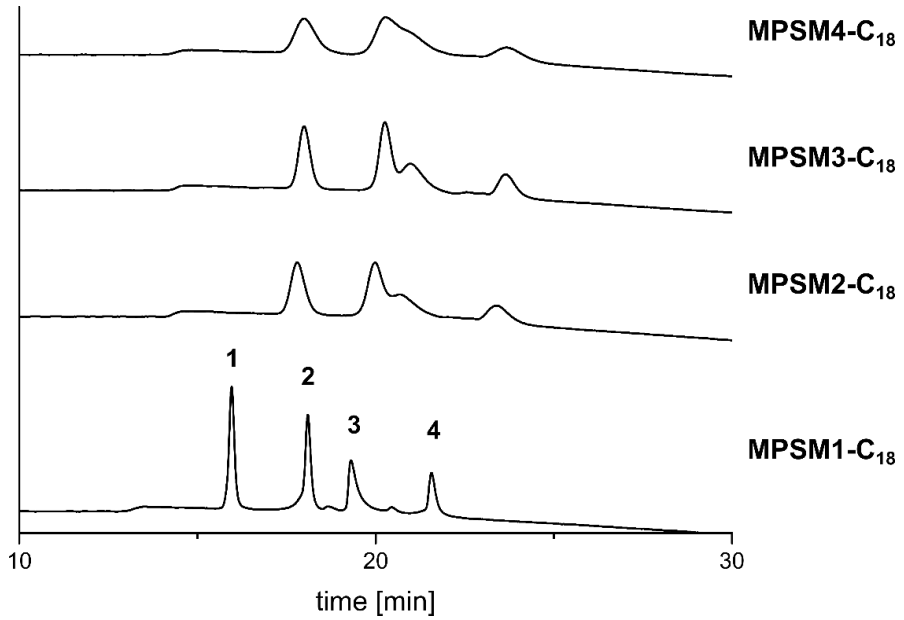


Figure S10. Chromatograms of protein mixture H2899 separation with the prepared C_{18} functionalized stationary phases. Chromatographic settings: column dimension: 250 × 4.6 mm; mobile phase A: H_2O with 0.1% TFA, mobile phase B: ACN with 0.08% TFA; gradient from 20% B to 85% B within 25 min; test mixture: 4 mg mL^{-1} (each 1 mg mL^{-1}) with 5 µL injection volume, **1** – ribonuclease A, **2** – cytochrome C, **3** – holo-transferrin, **4** – apomyoglobin; column temperature: 30 °C; detection wavelength: 215 nm.

References

[1] H. Xia, G. Wan, J. Zhao, J. Liu, Q. Bai, Preparation and characterization of monodisperse large-porous silica microspheres as the matrix for protein separation, J. Chrom. A. 1471 (2016) 138–144.

9 Publikation IV

International Journal of
Molecular Sciences

MDPI

Article

Tailoring the Morphology of Monodisperse Mesoporous Silica Particles Using Different Alkoxysilanes as Silica Precursors

Fabio Fait [1,2], Stefanie Wagner [1], Julia C. Steinbach [1,2], Andreas Kandelbauer [2,3] and Hermann A. Mayer [1,*]

[1] Institute of Inorganic Chemistry, University of Tübingen, Auf der Morgenstelle 18, 72076 Tübingen, Germany; fabio.fait@reutlingen-university.de (F.F.); stefaniewagnersb@googlemail.com (S.W.); julia.steinbach@reutlingen-university.de (J.C.S.)
[2] Process Analysis and Technology (PA&T), Reutlingen Research Institute, Reutlingen University, Alteburgstrasse 150, 72762 Reutlingen, Germany; andreas.kandelbauer@reutlingen-university.de
[3] Institute of Wood Technology and Renewable Materials, Department of Material Sciences and Process Engineering (MAP), University of Natural Resources and Life Sciences, Gregor-Mendel-Strasse 33, 1180 Vienna, Austria
* Correspondence: hermann.mayer@uni-tuebingen.de

Abstract: The hard template method for the preparation of monodisperse mesoporous silica microspheres (MPSMs) has been established in recent years. In this process, in situ-generated silica nanoparticles (SNPs) enter the porous organic template and control the size and pore parameters of the final MPSMs. Here, the sizes of the deposited SNPs are determined by the hydrolysis and condensation rates of different alkoxysilanes in a base catalyzed sol–gel process. Thus, tetramethyl orthosilicate (TMOS), tetraethyl orthosilicate (TEOS), tetrapropyl orthosilicate (TPOS) and tetrabutyl orthosilicate (TBOS) were sol–gel processed in the presence of amino-functionalized *poly* (glycidyl methacrylate-*co*-ethylene glycol dimethacrylate) (*p*(GMA-*co*-EDMA)) templates. The size of the final MPSMs covers a broad range of 0.5–7.3 µm and a median pore size distribution from 4.0 to 24.9 nm. Moreover, the specific surface area can be adjusted between 271 and 637 m^2 g^{-1}. Also, the properties and morphology of the MPSMs differ according to the SNPs. Furthermore, the combination of different alkoxysilanes allows the individual design of the morphology and pore parameters of the silica particles. Selected MPSMs were packed into columns and successfully applied as stationary phases in high-performance liquid chromatography (HPLC) in the separation of various water-soluble vitamins.

Keywords: mesoporous silica microspheres (MPSMs); hard template method; high-performance liquid chromatography (HPLC)

check for updates

Citation: Fait, F.; Wagner, S.; Steinbach, J.C.; Kandelbauer, A.; Mayer, H.A. Tailoring the Morphology of Monodisperse Mesoporous Silica Particles Using Different Alkoxysilanes as Silica Precursors. *Int. J. Mol. Sci.* **2023**, *24*, 11729. https://doi.org/10.3390/ijms241411729

Academic Editor: Marina G. Shelyapina

Received: 13 June 2023
Revised: 17 July 2023
Accepted: 19 July 2023
Published: 21 July 2023

Copyright: © 2023 by the authors. Licensee MDPI, Basel, Switzerland. This article is an open access article distributed under the terms and conditions of the Creative Commons Attribution (CC BY) license (https://creativecommons.org/licenses/by/4.0/).

1. Introduction

The introduction of high-performance liquid chromatography (HPLC) has enabled a rapid chemical analysis and separation process for substances and end products. The wide range of applications extends from small molecules [1–3] to pharmaceuticals [4,5], food and environmental analysis [6–8], long-chain polymers [9,10] and biomolecules [11–13]. The most common material in HPLC columns are spherical silica particles because of their mechanical robustness. Moreover, silica particles possess reactive groups on their surface, by which a variety of functionalizations allow a fine tuning of the particle features [14–16]. Characteristics such as particle size, dispersity, pore structure and surface functionalization influence their chromatographic properties such as selectivity, analysis time, plate number and back pressure. Due to their high specific surface area, fully porous silica particles in the µm range have proven successful in HPLC [17–19].

Probably the best-known representation of spherical silica networks is the silica material obtained from the Stoeber process [20]. Non-porous spherical silica particles in the

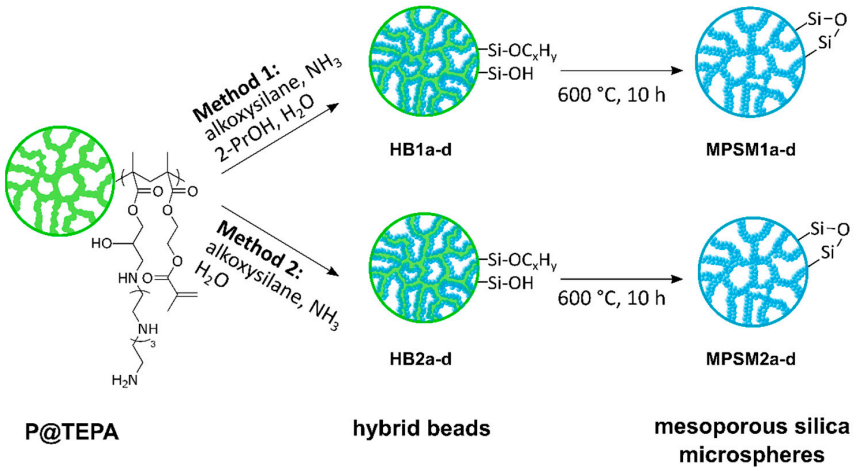
range of 10 to 500 nm can be formed by ammonia-catalyzed hydrolysis and the condensation of molecular alkoxysilanes. With semi-batch processes and the addition of electrolytes, the particle size can be increased into the µm range [21–24].

The hydrolysis rates of the alkoxysilanes are crucial for the size of the siloxane network. The hydrolysis rates are controlled by different parameters like the temperature; the chain length and branching of the alkoxysilane; NH_3 and H_2O concentrations; and the chain length and branching of the alcohol, which is used as a solvent [20,25–29]. Under basic conditions, an increase in the chain length of the alkyl groups of the alkoxysilane leads to a decrease in the rate of hydrolysis. The increasing steric hindrance and inductive effects of the alkyl groups increase the electron density at the silicon atom and make a nucleophilic attack more difficult. In addition, the decreasing polarity of the alkoxysilanes can lead to phase separation, depending on the solvent applied [29–32]. The NH_3 and H_2O concentrations influence the equilibrium reactions of hydrolysis and condensation. While under basic conditions the condensation of hydrolyzed alkoxysilanes is extremely fast, higher concentrations of H_2O affect the hydrolysis positively but the condensation negatively [28,29,31,33,34]. Overall, the Stoeber process provides non-porous silica nanoparticles with narrow size distributions. However, the preparation of monodisperse silica particles in the micrometer range is challenging, and the obtained particles remain nonporous.

The preparation of mesoporous silica microspheres (MPSMs) with narrow size distributions remains challenging [35–40]. Recently, for the synthesis of MPSMs, a promising protocol has been developed that employs functionalized porous *poly* (glycidyl methacrylate-*co*-ethylene glycol dimethacrylate) polymer particles (*p*(GMA-*co*-EDMA)) as hard templates in the presence of the basic hydrolysis and condensation of TEOS [35]. *p*(GMA-*co*-EDMA) functionalized with trimethylamine, (3-amino propyl) triethoxysilane or tetra ethylene pentamine (TEPA) provides excellent environments to deposit silica nanoparticles (SNPs) in the pores of the template, where they form a silica network [36–38]. The best matches of the templates are achieved if the rate of the growth of the SNPs and their rate of diffusion into the template pores are well balanced. Moreover, the particle and pore properties correlate with the size of the SNPs, which depends on the sol–gel conditions (see above) and the template [39,40].

In this study, we focus on the sol–gel conditions during the formation of MPSMs via the hard template method. Therefore, we investigated the influence of alkoxysilane precursors, which differ in their rates of hydrolysis on the particle and pore properties of MPSMs. For this, the sol–gel process of the precursors is carried out under basic conditions in the presence of the tetraethylenepentaamine-functionalized *p*(GMA-*co*-EDMA) template P@TEPA (Scheme 1). The size of the silica nanoparticles that accumulate in and on the template depends on the hydrolysis rate of the precursors. The *p*(GMA-*co*-EDMA)/SiO_2 hybrid beads (HB) and the MPSMs are characterized for their particles and pore properties by scanning electron microscopy, thermogravimetric analysis, and nitrogen adsorption/desorption measurements. Finally, selected MPSMs are functionalized with trimethoxy (octadecyl) silane and applied as stationary phases in the separation of different water-soluble vitamins.

Int. J. Mol. Sci. **2023**, *24*, 11729



Scheme 1. Synthesis of mesoporous silica microspheres **MPSM1a-d** and **MPSM2a-d** (TMOS = **a**, TEOS = **b**, TPOS = **c** and TBOS = **d**).

2. Results and Discussion

2.1. Preparation and Characterization of MPSM1a-d and MPSM2a-d

Monodisperse tetraethylenepentamine (TEPA)-functionalized *p*(GMA-*co*-EDMA) served as the template in the preparation of all MPSMs discussed here. The characteristic features of this P@TEPA template are a diameter of 6.0 ± 0.5 µm, a median pore diameter of 14.4 nm and a pore volume of 0.24 mL g^{-1} (Figures S2 and S3, Supporting Information).

In the presence of the P@TEPA template, a basic sol–gel process was performed with the four different alkoxysilanes, TMOS (**a**), TEOS (**b**), TPOS (**c**) and TBOS (**d**), in 2-propanol and H_2O as solvents (Methods 1 and 2, Scheme 1). In Method 1, all reactants except the template are soluble in 2-propanol. Under these conditions silica nanoparticles (SNP) are formed in the continuous phase, which diffuse into the template and accumulate in the pores and on the surface [37–40]. The size of the SNPs depends on the hydrolysis and condensation rates of the precursors. With the fastest rate of hydrolysis, TMOS forms the largest SNPs, which accumulate in the pores (Figure S4, **HB1a**). Moreover, the hydrolysis and condensation rates of TMOS are so high that some of the SNPs become too large (~60 nm) to enter the template network. These secondary particles remain in the continuous phase and are mostly removed from the reaction mixture during the purification process, while some of them are left at the template surface (Figure S4, **HB1a**). With TEOS as the precursor, particle formation is already four times slower than for TMOS [32], resulting in smaller SNPs that easily penetrate the porous network of the template and form **HB1b** (Figure S4). The longer alkoxy chains of the TPOS and TBOS alkoxides decrease their hydrolysis rates further. Thus, less silica species are available for condensation to build SNPs. The accumulation of SNPs in the template is now difficult, and SNPs are hardly observed on the surface of the hybrid particles (Figure S4, **HB1c** and **HB1d**). Overall, the size of the SNPs decreases with the rates of hydrolysis in the TMOS > TEOS > TPOS > TBOS series (Figure S4), and the incorporation of silica into the pores of the template is best achieved for TEOS.

In Method 2, the sol–gel process is carried out in H_2O, which reduces the differences of the kinetic effects of the hydrolysis and condensation of the four different alkoxysilanes (Method 2, Scheme 1). This should have an impact on the SNP formation and the incorporation of silica into the pores of the template. Ammonia as catalyst is added after 24 h of stirring to enable the nonpolar precursors to diffuse into the template network. Condensation does not start until NH_3 is added. After another 24 h, the hybrid particles **HB2a-d** are obtained (Figure S5 and Table 1). As a consequence of the reduced rate of the hydrolysis of TMOS, no secondary particles are observed. The particles **HB2a** grow

Int. J. Mol. Sci. **2023**, *24*, 11729

by 0.7 µm and **HB2b** by 0.3 µm and are thus larger than **HB1a-d**. In contrast to particles prepared by Method 1, a more edgy morphology of the hybrid materials is achieved. For TPOS (**HB2c**) and TBOS (**HB2d**) as precursors, there are no changes in size and morphology compared to the template.

Table 1. Particle properties of hybrid beads and corresponding mesoporous silica microspheres.

	Particle Size	SiO_2 Content		Particle Size	Median Pore Size	Pore Volume	Specific Surface Area
	(µm)	(%)		(µm)	(nm)	(mL g^{-1})	(m^2 g^{-1})
HB1a	6.3	37.8	MPSM1a	6.0	23.6	0.50	271
HB1b	6.3	29.9	MPSM1b	5.5	11.3	0.84	389
HB1c	6.3	17.7	MPSM1c	3.6	8.8	0.62	339
HB1d	6.3	6.6	MPSM1d	2.2	4.0	0.68	637
HB2a	6.7	32.7	MPSM2a	5.9	15.7	0.87	390
HB2b	6.2	35.8	MPSM2b	6.0	24.9	0.69	346
HB2c	6.0	0.01	MPSM2c	0.8	[1]	[1]	[1]
HB2d	6.0	0.01	MPSM2d	0.5	[1]	[1]	[1]
HB1e	7.1	43.0	MPSM1e	7.3	16.6	0.79	247
HB1f	8.6	33.8	MPSM1f	6.6	15.6	1.06	311

[1] The poor yield did not allow us to record adsorption/desorption measurements.

The thermal degradation behavior of the hybrid beads **HB1a-d** and **HB2a-d** compares well with that reported earlier (Figure 1) [41]. After the loss of surface water, the degradation processes of the polymer backbone led to a complete decomposition of the template and allowed the determination of the silica content of the hybrid beats. Here the hybrid particles **HB1a** contain the highest quantity of silica (37.8 %). The amounts of silica of **HB1b** (29.9%), **HB1c** (17.7%) and **HB1d** (6.6%) correlate with their decreasing hydrolysis rates. The amounts of SiO_2 in **HB2a** and **HB2b** (32.7% and 35.8%, respectively) differ little (Figure 1). Due to the suppressed hydrolysis in H_2O, the hydrolysis rates of TMOS and TEOS are comparable. Thus, similar amounts of SiO_2 are deposited. The percentage of incorporated silica in the hybrid particles correlates well with the particle size of the resulting MPSMs (Table 1). Thermogravimetric analyses of **HB2c** and **HB2d** result in only very small amounts of SiO_2. This is traced back to the poor miscibility of the alkoxysilanes TPOS and TBOS with water. Thus, only small amounts of SNPs are generated during the reaction.

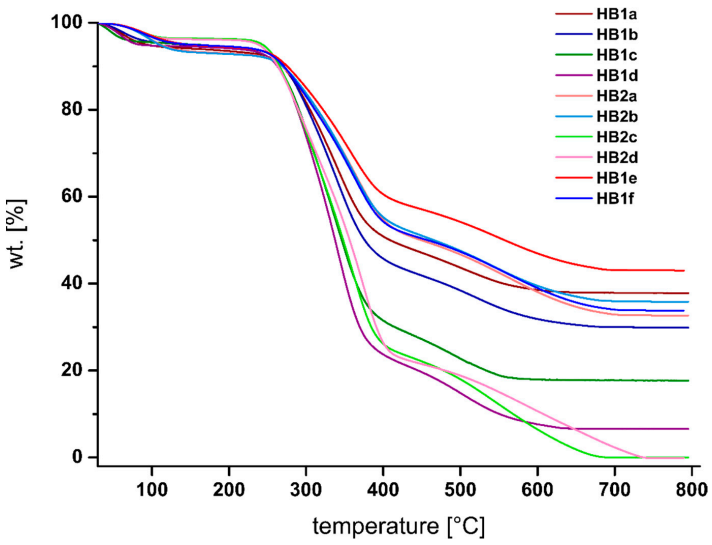


Figure 1. TGA measurements of hybrid beads **HB1a-f** and **HB2a-d**.

Int. J. Mol. Sci. **2023**, *24*, 11729

The calcination of the hybrid beads **HB1a-d** and **HB2a-d** for 10 h at 600 °C removed the organic polymer template and released the monodisperse mesoporous silica microspheres **MPSM1a-d** (Figure 2) and **MPSM2a-d** (Figure 3). The nanoparticulate morphology of the MPSMs is comparable to that of their corresponding hybrid beads. The particle size of the MPSMs decreases with the decreasing hydrolysis rate of the precursors. Thus, while **MPSM1a** (6.0 µm) and **MPSM1b** (5.5 µm) represent the size of the template quite well, the sizes of **MPSM1c** (3.6 µm) and **MPSM1d** (2.2 µm) are strongly reduced. Consequently, only TMOS and TEOS map the template to 100% and 92%, respectively, while, for TPOS and TBOS, the template is mapped to only 60% and 37%, respectively. The particle sizes of **MPSM2a** and **MPSM2b** are 5.9 µm and 6.0 µm, respectively, and completely replicate the template. For **MPSM2c** and **MPSM2d**, 800 nm and 500 nm polydisperse porous silica particles are generated.

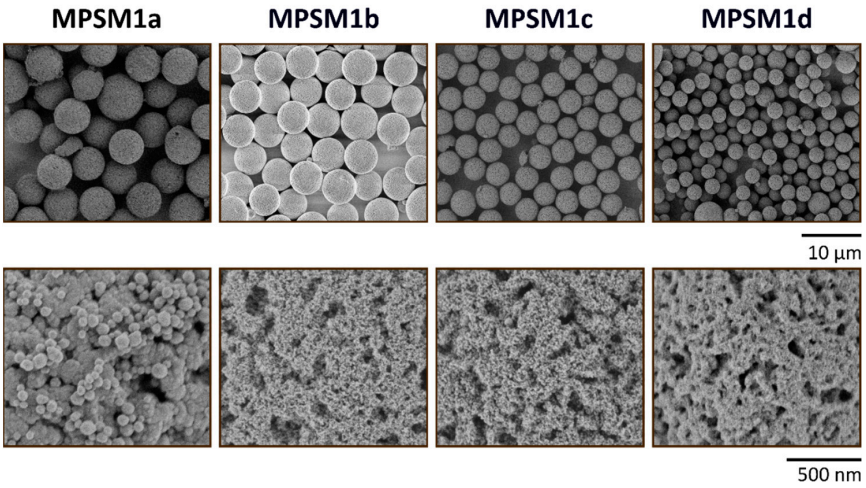


Figure 2. SEM images of mesoporous silica microspheres **MPSM1a-d** with 2000× magnification (**top row**) and 50,000× magnification (**bottom row**).

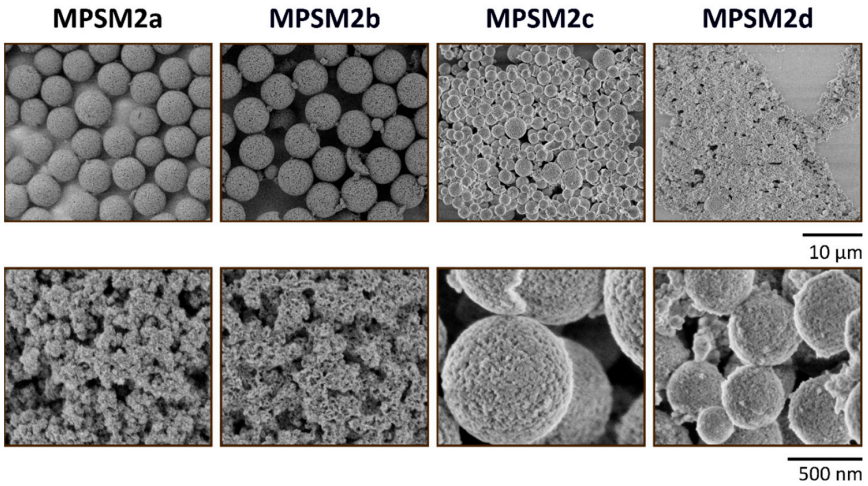


Figure 3. SEM images of mesoporous silica microspheres **MPSM2a-d** with 2000× magnification (**top row**) and 50,000× magnification (**bottom row**).

The pore properties of the MPSMs were determined via nitrogen adsorption/desorption measurements and are listed in Table 1. The corresponding pore size distributions are shown in Figure 4. Here, the median pore size of the MPSMs decreases and the specific

surface area increases with the decreasing hydrolysis rates of the precursors. This result is consistent with the size of the SNPs that form the silica network. Large SNPs generate large pores of the MPSMs, while small SNPs result in smaller pores [38,40]. Therefore, the median pore size becomes smaller in the order of **MPSM1a** (23.6 nm), **MPSM1b** (11.3 nm), **MPSM1c** (8.8 nm), and **MPSM1d** (4.0 nm). As smaller pores form larger specific surface areas, the highest specific surface area is obtained for **MPSM1d**, and the lowest specific surface area is obtained for **MPSM1a**. The sol–gel process according to Method 2 leads to an edgier morphology for **MPSM2a** and **MPSM2b**, resulting in larger surface areas compared to **MPSM1a** and **MPSM1b**. The pore volume of the MPSMs differs between 0.5 mL g^{-1} and 0.9 mL g^{-1}.

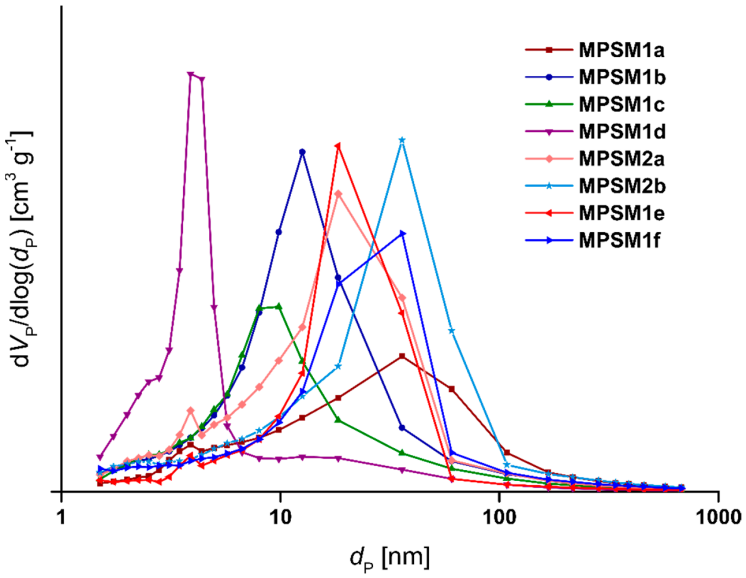


Figure 4. Pore size distributions of MPSM1a-f and MPSM2a-b.

2.2. Preparation and Characterization of MPSM1e and MPSM1f

The properties of the MPSMs are controlled by the hydrolysis rate of the precursors and the solvent medium. TMOS produces non-porous secondary particles while TPOS does not fully map the size of the template if the sol–gel process is carried out in 2-propanol and H_2O. To avoid this unwanted behavior, the two precursor combinations of TMOS with TEOS (**MPSM1e**) and TPOS with TEOS (**MPSM1f**) were applied in a sol–gel process in the presence of a P@TEPA template with a diameter of 7.2 µm. The new HBs and MPSMs are shown in Figure 5. Interestingly, no secondary particles are observed for **HB1e** and **MPSM1e**. The **HB1e** particles have the highest silica content of all hybrid particles, and the corresponding silica microspheres have a nanoparticulate surface and exhibit a size of 7.3 µm (Table 1). Thus, they completely map the template without the negative effects of the high hydrolysis rate of TMOS. With a median pore size of 16.6 nm, this is in between that of **MPSM1a** and **MPSM1b**. This results in SNPs in the continuous phase that are smaller than those of **MPSM1a** and larger than those of **MPSM1b**. The combination of TEOS and TPOS leads to the particles **HB1f** and **MPSM1f**. The resulting silica materials have a size of 6.6 µm, representing 92% of the template. Interestingly, the median pore size of 15.6 nm and the pore volume of 1.06 mL g^{-1} are larger than the pore properties of **MPSM1b**, for which only TEOS was used. Compared with **MPSM1c**, the template is better replicated in **MPSM1f**.

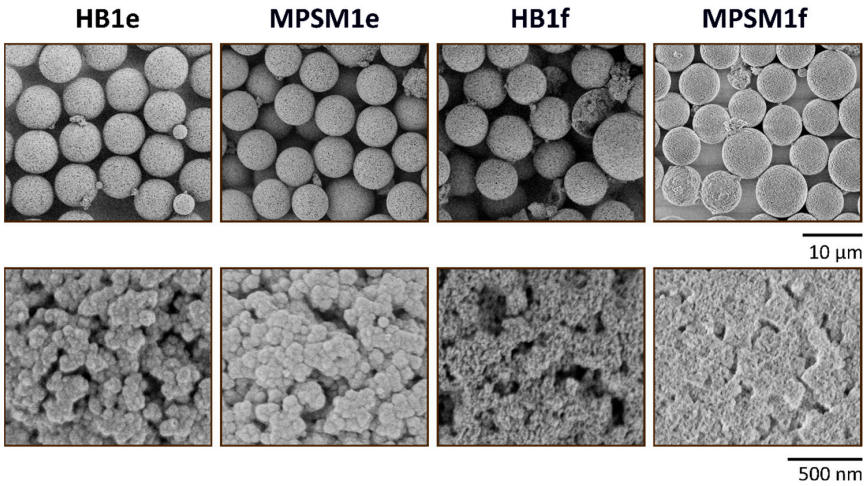


Figure 5. SEM images of hybrid beads **HB1e** and **HB1f** and corresponding **MPSM1e** and **MPSM1f** with 2000× magnification (**top row**) and 50,000× magnification (**bottom row**).

2.3. Chromatographic Measurements of MPSM1b

For the use of MPSMs as a stationary phase in high-performance liquid chromatography, high monodispersity is required to achieve efficient separation. **MPSM1b** particles were chosen based on their particle size and monodispersity to investigate their suitability as a stationary phase in HPLC. Therefore, **MPSM1b** particles were functionalized with trimethoxy (octadecyl) silane and packed in a 250 mm × 4.6 mm stainless steel column with acetone as the slurry and methanol/water (85 v.%/15 v.%) as the pressure medium.

The reproducibility of the synthesis of **MPSM1b** in its chromatographic properties is shown in Figure 6. The particles of three different batches with the same reaction conditions were packed in 250 mm × 4.6 mm stainless steel columns and examined for their chromatographic properties. As can be seen in Figure 6, the particles of all three batches show the same retention behavior of the test mixture. Moreover, even after one hundred injections, the retention times of toluene and uracil did not change (Supporting Information Table S1). This indicates the good stability of the stationary phase **MPSM1b-C_{18}**.

The successful separation of five water-soluble vitamins is shown in Figure 7. A gradient from eluent A, consisting of water containing 0.025% TFA, to eluent B, consisting of acetonitrile (ACN), was used for the separation. An initial isocratic step for five minutes with eluent A is followed by an increase from eluent B to eluent A to 25/75 (v.%/v.%) in six minutes, as proposed by Heudi et al. [42]. This is followed by a second gradient on eluent B to eluent A 40/60 (v.%/v.%) in eight minutes, holding this for an additional minute. Then, the initial conditions are restored in one minute and equilibrated for four minutes. The vitamins were baseline separated and assigned based on single measurements of the analytes. The elution order is vitamin $B_1 < B_3 < B_5 < B_9 < B_{12}$ as detected at 210 nm.

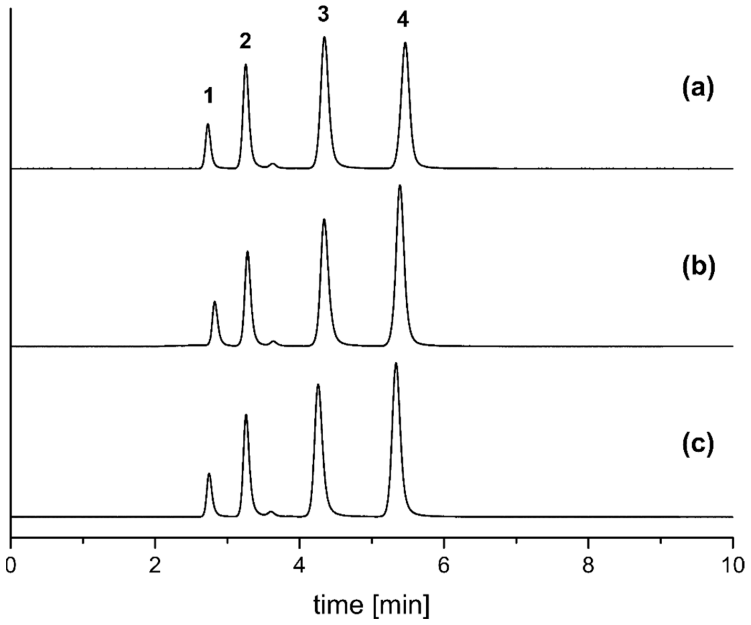


Figure 6. Reproducibility of chromatographic properties from three different batches (**a**–**c**) of **MPSM1b-C_{18}** synthesized according to Method 1. Chromatographic settings: column dimension: 250 × 4.6 mm; mobile phase: MeOH/H_2O (85 v.%/15 v.%); analytes: uracil (**1**), phenol (**2**), *N*,*N*-diethyl-*m*-toluamide (**3**) and toluene (**4**); flow: 1 mL min^{-1}; injection volume: 5 µL; UV detection: 254 nm.

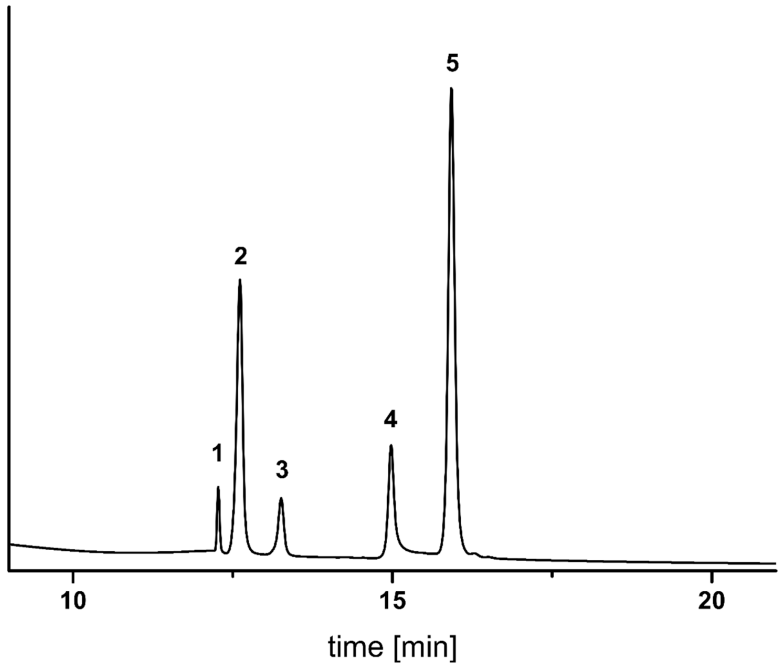


Figure 7. Separation of five water-soluble vitamins B_1 (**1**), B_3 (**2**), B_5 (**3**), B_9 (**4**) and B_{12} (**5**). Chromatographic settings: column dimension: 250 × 4.6 mm; eluent A: H_2O with 0.025 v.% TFA; eluent phase B: ACN; gradient (A/B): 5 min (100/0), 11 min (75/25), 19 min (60/40), 20 min (60/40), 21 min (100/0) and 25 min (100/0); flow: 0.8 mL · min^{-1}; injection volume: 20 µL; column temperature: 30 °C; UV detection: 210 nm.

3. Materials and Methods

3.1. Chemicals

Tetraethyl orthosilicate (TEOS), tetramethyl orthosilicate (TMOS) and trimethoxy (octadecyl) silane (ODTMS) were obtained from abcr GmbH (Karlsruhe, Germany). Ammonia (28–30% aqueous solution), tetrapropyl orthosilicate (TPOS) and tetrabutyl orthosilicate (TBOS) were purchased from Alfa Aesar (Schwerte, Germany). Ethanol, hydrochloric acid, 2-propanol, triethylamine and the water-soluble vitamins (B_1, B_3, B_5, B_9 and B_{12}) were bought from Sigma-Aldrich (Taufkirchen, Germany). Acetonitrile (ACN), trifluoro acetic acid (TFA) and water (all HPLC grade) were purchased from Fisher Scientific (Schwerte, Germany). Toluene and deionized water were cleaned using a solvent purification system. The test mixture (uracil, phenol, *N*,*N*-diethyl-*m*-toluamide and toluene) for column characterization was provided by Dr. Maisch HPLC, (Ammerbuch, Germany).

3.2. Characterization

For the evaluation of the morphology, particle size and dispersity, SEM images were acquired using a Hitachi SU8030 (Krefeld, Germany). The mean particle diameter was obtained by calculating at least 400 particles from SEM images and is expressed in µm. The pore parameters of the materials are determined by nitrogen adsorption on a BELSORP MiniX from Microtrac Retsch GmbH (Haan, Germany). The sample preparation was carried out on a BELSORP VACII (Microtrac Retsch GmbH, Haan, Germany). For that, the silica materials were heated for 3 h at 300 °C, and a vacuum of 2×10^{-2} mbar was used to remove possible physisorbed residues and to achieve a reproducible equilibrium [43]. Adsorption and desorption isotherms were performed at 77 K. For the determination of the specific surface area, the adsorption isotherms were evaluated by the Brunauer–Emmet–Teller (BET) method, and for the pore volume (single point measurement at $p/p_0 = 0.95$) and pore size distributions, the desorption isotherms were evaluated by the Barrett–Joyner–Halenda (BJH) method using BELMaster 7 software [44,45]. The amount of SiO_2 was determined after thermogravimetric measurements on a Mettler Toledo TGA/DSC. Samples were weighed in an aluminum vessel and measured at a heating rate of 5 K min^{-1} and synthetic air (50 mL min^{-1}).

Analytical high-performance liquid chromatography of water-soluble vitamins was performed on an Agilent 1100 series system from Agilent Technologies (Waldbronn, Germany), which consisted of a quaternary pump with degasser, an autosampling system, a column oven and a diode array detector. Instrument control, data acquisition and automated data analysis was performed by the OpenLAB CDS (Rev. C.01.07 SR3 software, Agilent Technologies, Walbronn, Germany). A running gradient of eluent A consisting of water and 0.025 v.% TFA to eluent B consisting of acetonitrile was used according to Heudi et al. [42] The vitamins B_1, B_5 and B_{12} (1 mg mL^{-1}), B_3 (0.5 mg mL^{-1}) and B_9 (2 mg mL^{-1}) were dissolved in water.

3.3. Syntheses

Monodisperse porous *p*(GMA-*co*-EDMA) particles were prepared by a seed suspension polymerization of glycidyl methacrylate and ethylene glycol dimethacrylate in the presence of monodisperse polystyrene particles (1.5 ± 0.1 µm, Figure S1, Supporting Information) [35,36,46]. Then, the *p*(GMA-*co*-EDMA) particles were functionalized with TEPA according to previous reports (for details, see Supporting Information, Figures S1–S3 [36,38,39]) to generate P@TEPA template particles. A nitrogen content of 2.4% and spectroscopic analysis indicate successful functionalization.

3.3.1. Preparation of Monodisperse Porous Hybrid Beads (HB1a-f and HB2a-d) and Mesoporous Silica Microspheres (MPSM1a-f and MPSM2a-d)

Method 1: An amount of 1 g of P@TEPA particles was dispersed in a mixture of 60 mL of 2-propanol and 7.5 mL of H_2O. Then, 2.4 mL of TMOS (**a**), TEOS (**b**), TPOS (**c**) and TBOS

(**d**) and 0.2 mL of an aqueous ammonia solution (28–30%) was added, and the mixture was stirred at 200 rpm for 24 h to produce hybrid beads **HB1a-d** (Table 1).

The hybrids **HB1e-f** were produced after 2.4 mL of TEOS and 1.5 mL of TMOS (**e**) or TPOS (**f**) and 0.2 mL of an aqueous ammonia solution (28–30%) were added to a dispersion of 1 g P@TEPA particles in 60 mL of 2-propanol and 7.5 mL of H_2O. The mixture was stirred at 200 rpm for 24 h (Table 1).

Method 2: An amount of 1 g of P@TEPA particles was dispersed in 67.5 mL of H_2O. Then, 2.4 mL of the corresponding alkoxysilane was added, and the mixture was stirred at 200 rpm. After 24 h, 0.2 mL of an aqueous ammonia solution (28–30%) was added, and the reaction was stirred for further 24 h at 200 rpm to produce hybrid beads **HB2a-d** (Table 1).

All hybrid beads were separated from their solutions, washed three times with EtOH and three times with H_2O, and dried at 65 °C for 16 h. The resulting hybrid beads were calcinated at 600 °C for 10 h to provide the corresponding mesoporous silica microspheres **MPSMs** (Table 1).

3.3.2. Octadecyl Functionalization of Mesoporous Silica Microspheres for Chromatographic Measurements

An amount of 5 g of silica particles **MPSM1b** was dispersed in 600 mL of hydrochloric acid (3.7%) and stirred for 3 h at 100 °C (200 rpm). The particles were separated from the solution, washed with EtOH and H_2O until neutral and dried at 65 °C for 16 h. The particles were then dispersed in 75 mL of toluene; 25 mL of ODTMS and 0.5 mL of triethylamine were added; and the mixture was stirred at 100 °C (200 rpm) for 6 h. The particles were separated from the solution; washed three times with toluene, three times with EtOH and twice with MeOH; and dried at 65 °C for 16 h.

The functionalized particles were packed with acetone as slurry and MeOH/H_2O (85 v.%/15 v.%) as pressure medium.

4. Conclusions

Monodisperse mesoporous silica microspheres (MPSM) can be tailored in their sizes and pore parameters via the hard template method. This is achieved if, at the stage of the hybrid bead syntheses, the sol–gel parameters are adjusted properly. This has been successfully demonstrated here by applying a basic sol–gel process with four different alkoxysilanes in the presence of functionalized *p*(GMA-*co*-EDMA) as the template. The SNPs grow at various rates and are thus incorporated into the template pores in non-uniform sizes, which is a consequence of the different hydrolysis and condensation rates of the alkoxysilane precursors. Thus, different amounts of silica are incorporated into the template, which has an impact on the final size of the MPSM. With TMOS and TEOS as precursors, the size of the template is reproduced, while TPOS and TBOS as precursors lead to much smaller MPSMs. Moreover, the various sizes of the incorporated SNPs generate different pore parameters. The larger the SNP, the larger the pores of the MPSM, which is important for HPLC applications. The silica particles synthesized with TEOS according to Method 1 were functionalized with trimethoxy (octadecyl) silane and used as the stationary phase in HPLC. The complete baseline separation of five water-soluble vitamins was achieved with these microspheres. The robustness of the synthesis of MPSMs in their chromatographic properties was demonstrated via HPLC using three different batches with a reversed phase test mixture.

Supplementary Materials: The following supporting information can be downloaded at https://www.mdpi.com/article/10.3390/ijms241411729/s1.

Author Contributions: Conceptualization, A.K. and H.A.M.; methodology, F.F. and S.W.; software, J.C.S.; validation, F.F., S.W. and J.C.S.; formal analysis, F.F., S.W. and J.C.S.; investigation, F.F., S.W. and J.C.S.; resources, A.K. and H.A.M.; data curation, F.F., S.W. and J.C.S.; writing—original draft preparation, F.F.; writing—review and editing, A.K., H.A.M., J.C.S., and S.W.; visualization, F.F. and J.C.S.; supervision, A.K. and H.A.M.; project administration, A.K. and H.A.M.; funding acquisition, A.K. and H.A.M. All authors have read and agreed to the published version of the manuscript.

Funding: This research was funded by the Bundesministerium für Bildung und Forschung (BMBF, grant number 13FH647IX6) and the Bundesministerium für Wirtschaft und Energie (AiF/ZIM, grant number ZF4019203SL8). We acknowledge support from the Open Access Publication Fund of the University of Tübingen.

Institutional Review Board Statement: Not applicable.

Informed Consent Statement: Not applicable.

Data Availability Statement: Data will be made available on request.

Acknowledgments: We would like to thank our cooperation partner Dr. Maisch GmbH for their support in preparing the columns. We thank Elke Nadler for contributing the SEM measurements.

Conflicts of Interest: The authors declare no conflict of interest.

References

1. Wang, Q.C.; Fréchet, J.M.J.; Švec, F. Reversed-phase chromatography of small molecules and peptides on a continuous rod of macroporous poly (styrene-co-divinylbenzene). *J. Chromatogr. A* **1994**, *669*, 230–235. [CrossRef] [PubMed]
2. DeStefano, J.J.; Langlois, T.J.; Kirkland, J.J. Characteristics of Superficially-Porous Silica Particles for Fast HPLC: Some Performance Comparisons with Sub-2-µm Particles. *J. Chromatogr. Sci.* **2008**, *46*, 7. [CrossRef] [PubMed]
3. DeStefano, J.J.; Boyes, B.E.; Schuster, S.A.; Miles, W.L.; Kirkland, J.J. Are sub-2 µm particles best for separating small molecules? An alternative. *J. Chromatogr. A* **2014**, *1368*, 163–172. [CrossRef] [PubMed]
4. Peysson, W.; Vulliet, E. Determination of 136 pharmaceuticals and hormones in sewage sludge using quick, easy, cheap, effective, rugged and safe extraction followed by analysis with liquid chromatography–time-of-flight-mass spectrometry. *J. Chromatogr. A* **2013**, *1290*, 46–61. [CrossRef]
5. Bayen, S.; Yi, X.; Segovia, E.; Zhou, Z.; Kelly, B.C. Analysis of selected antibiotics in surface freshwater and seawater using direct injection in liquid chromatography electrospray ionization tandem mass spectrometry. *J. Chromatogr. A* **2014**, *1338*, 38–43. [CrossRef]
6. Lu, Y.; Shen, Q.; Dai, Z.; Zhang, H. Multi-walled carbon nanotubes as solid-phase extraction adsorbent for the ultra-fast determination of chloramphenicol in egg, honey, and milk by fused-core C18-based high-performance liquid chromatography–tandem mass spectrometry. *Anal. Bioanal. Chem.* **2010**, *398*, 1819–1826. [CrossRef]
7. Tölgyesi, Á.; Sharma, V.K.; Fekete, J. Development and validation of a method for determination of corticosteroids in pig fat using liquid chromatography–tandem mass spectrometry. *J. Chromatogr. B* **2011**, *879*, 403–410. [CrossRef]
8. Šatínský, D.; Jägerová, K.; Havlíková, L.; Solich, P. A New and Fast HPLC Method for Determination of Rutin, Troxerutin, Diosmin and Hesperidin in Food Supplements Using Fused-Core Column Technology. *Food Anal. Methods* **2013**, *6*, 1353–1360. [CrossRef]
9. Gaborieau, M.; Castignolles, P. Size-exclusion chromatography (SEC) of branched polymers and polysaccharides. *Anal. Bioanal. Chem.* **2011**, *399*, 1413–1423. [CrossRef]
10. Schoenmakers, P.; Aarnoutse, P. Multi-Dimensional Separations of Polymers. *Anal. Chem.* **2014**, *86*, 6172–6179. [CrossRef]
11. Kirkland, J.J.; Schuster, S.A.; Johnson, W.L.; Boyes, B.E. Fused-core particle technology in high-performance liquid chromatography: An overview. *J. Pharm. Anal.* **2013**, *3*, 303–312. [CrossRef]
12. Staub, A.; Zurlino, D.; Rudaz, S.; Veuthey, J.-L.; Guillarme, D. Analysis of peptides and proteins using sub-2µm fully porous and sub 3-µm shell particles. *J. Chromatogr. A* **2011**, *1218*, 8903–8914. [CrossRef]
13. Wagner, B.M.; Schuster, S.A.; Boyes, B.E.; Kirkland, J.J. Superficially porous silica particles with wide pores for biomacromolecular separations. *J. Chromatogr. A* **2012**, *1264*, 22–30. [CrossRef]
14. Badley, R.D.; Ford, W.T.; McEnroe, F.J.; Assink, R.A. Surface modification of colloidal silica. *Langmuir* **1990**, *6*, 792–801. [CrossRef]
15. Albert, K.; Brindle, R.; Martin, P.; Wilson, I.D. Characterisation of C18-bonded silicas for solid-phase extraction by solid-state NMR spectroscopy. *J. Chromatogr. A* **1994**, *665*, 253–258. [CrossRef]
16. Vrancken, K.C.; Possemiers, K.; Van Der Voort, P.; Vansant, E.F. Surface modification of silica gels with aminoorganosilanes. *Colloids Surfaces A Physicochem. Eng. Asp.* **1995**, *98*, 235–241. [CrossRef]
17. Gritti, F.; Guiochon, G. Comparative study of the performance of columns packed with several new fine silica particles. *J. Chromatogr. A* **2007**, *1166*, 30–46. [CrossRef]
18. Baker, J.S.; Vinci, J.C.; Moore, A.D.; Colón, L.A. Physical characterization and evaluation of HPLC columns packed with superficially porous particles. *J. Sep. Sci.* **2010**, *33*, 2547–2557. [CrossRef]
19. Cabooter, D.; Fanigliulo, A.; Bellazzi, G.; Allieri, B.; Rottigni, A.; Desmet, G. Relationship between the particle size distribution of commercial fully porous and superficially porous high-performance liquid chromatography column packings and their chromatographic performance. *J. Chromatogr. A* **2010**, *1217*, 7074–7081. [CrossRef]
20. Stöber, W.; Fink, A.; Bohn, E. Controlled growth of monodisperse silica spheres in the micron size range. *J. Colloid Interface Sci.* **1968**, *26*, 62–69. [CrossRef]

21. Chen, S.-L.; Dong, P.; Yang, G.-H.; Yang, J.-J. Characteristic Aspects of Formation of New Particles during the Growth of Monosize Silica Seeds. *J. Colloid Interface Sci.* **1996**, *180*, 237–241. [CrossRef]
22. Zhang, J.H.; Zhan, P.; Wang, Z.L.; Zhang, W.Y.; Ming, N.B. Preparation of monodisperse silica particles with controllable size and shape. *J. Mater. Res.* **2003**, *18*, 649–653. [CrossRef]
23. Nozawa, K.; Gailhanou, H.; Raison, L.; Panizza, P.; Ushiki, H.; Sellier, E.; Delville, J.P.; Delville, M.H. Smart Control of Monodisperse Stöber Silica Particles: Effect of Reactant Addition Rate on Growth Process. *Langmuir* **2005**, *21*, 1516–1523. [CrossRef]
24. Nakabayashi, H.; Yamada, A.; Noba, M.; Kobayashi, Y.; Konno, M.; Nagao, D. Electrolyte-Added One-Pot Synthesis for Producing Monodisperse, Micrometer-Sized Silica Particles up to 7 µm. *Langmuir* **2010**, *26*, 7512–7515. [CrossRef]
25. Harris, M.T.; Brunson, R.R.; Byers, C.H. The base-catalyzed hydrolysis and condensation reactions of dilute and concentrated TEOS solutions. *J. Non-Cryst. Solids* **1990**, *121*, 397–403. [CrossRef]
26. Sadasivan, S.; Dubey, A.K.; Li, Y.; Rasmussen, D.H. Alcoholic Solvent Effect on Silica Synthesis—NMR and DLS Investigation. *J. Sol-Gel. Sci. Technol.* **1998**, *12*, 5–14. [CrossRef]
27. Malay, O.; Yilgor, I.; Menceloglu, Y.Z. Effects of solvent on TEOS hydrolysis kinetics and silica particle size under basic conditions. *J. Sol-Gel. Sci. Technol.* **2013**, *67*, 351–361. [CrossRef]
28. Van Blaaderen, A.; Van Geest, J.; Vrij, A. Monodisperse colloidal silica spheres from tetraalkoxysilanes: Particle formation and growth mechanism. *J. Colloid Interface Sci.* **1992**, *154*, 481–501. [CrossRef]
29. Van Helden, A.K.; Jansen, J.W.; Vrij, A. Preparation and characterization of spherical monodisperse silica dispersions in nonaqueous solvents. *J. Colloid Interface Sci.* **1981**, *81*, 354–368. [CrossRef]
30. Bogush, G.H.; Tracy, M.A.; Zukoski, C.F. Preparation of monodisperse silica particles: Control of size and mass fraction. *J. Non-Cryst. Solids* **1988**, *104*, 95–106. [CrossRef]
31. Giesche, H. Synthesis of monodispersed silica powders I. Particle properties and reaction kinetics. *J. Eur. Ceram. Soc.* **1994**, *14*, 189–204. [CrossRef]
32. Chen, K.C.; Tsuchiya, T.; Mackenzie, J.D. Sol-Gel Processing of Silica I. The role of the starting compounds. *J. Non-Cryst. Solids* **1986**, *86*, 227–237. [CrossRef]
33. Matsoukas, T.; Gulari, E. Dynamics of growth of silica particles from ammonia-catalyzed hydrolysis of tetra-ethyl-orthosilicate. *J. Colloid Interface Sci.* **1988**, *124*, 252–261. [CrossRef]
34. Han, Y.; Lu, Z.; Teng, Z.; Liang, J.; Guo, Z.; Wang, D.; Han, M.-Y.; Yang, W. Unraveling the Growth Mechanism of Silica Particles in the Stöber Method: In Situ Seeded Growth Model. *Langmuir* **2017**, *33*, 5879–5890. [CrossRef]
35. He, J.; Yang, C.; Xiong, X.; Jiang, B. Preparation and characterization of monodisperse porous silica microspheres with controllable morphology and structure. *J. Polym. Sci. A Polym. Chem.* **2012**, *50*, 2889–2897. [CrossRef]
36. Xia, H.; Wan, G.; Zhao, J.; Liu, J.; Bai, Q. Preparation and characterization of monodisperse large-porous silica microspheres as the matrix for protein separation. *J. Chromatogr. A* **2016**, *1471*, 138–144. [CrossRef]
37. Chen, J.; Zhu, L.; Ren, L.; Teng, C.; Wang, Y.; Jiang, B.; He, J. Fabrication of Monodisperse Porous Silica Microspheres with a Tunable Particle Size and Pore Size for Protein Separation. *ACS Appl. Bio Mater.* **2018**, *1*, 604–612. [CrossRef]
38. Bai, J.; Zhu, Q.; Tang, C.; Liu, J.; Yi, Y.; Bai, Q. Synthesis and application of 5 µm monodisperse porous silica microspheres with controllable pore size using polymeric microspheres as templates for the separation of small solutes and proteins by high-performance liquid chromatography. *J. Chromatogr. A* **2022**, *1675*, 463165. [CrossRef]
39. Steinbach, J.C.; Fait, F.; Mayer, H.A.; Kandelbauer, A. Monodisperse Porous Silica/Polymer Nanocomposite Microspheres with Tunable Silica Loading, Morphology and Porosity. *Int. J. Mol. Sci.* **2022**, *23*, 14977. [CrossRef]
40. Fait, F.; Steinbach, J.C.; Kandelbauer, A.; Mayer, H.A. Impact of porosity and surface functionalization of hard templates on the preparation of mesoporous silica microspheres. *Micropor. Mesopor. Mat.* **2023**, *351*, 112482. [CrossRef]
41. Göpferich, A. Mechanisms of polymer degradation and erosion. *Biomaterials* **1996**, *17*, 103–114. [CrossRef]
42. Heudi, O.; Kilinç, T.; Fontannaz, P. Separation of water-soluble vitamins by reversed-phase high performance liquid chromatography with ultra-violet detection: Application to polyvitaminated premixes. *J. Chromatogr. A* **2005**, *1070*, 49–56. [CrossRef]
43. Rouquerol, F.; Rouquerol, J.; Sing, K.S.W.; Llewellyn, P.L.; Maurin, G. *Adsorption by Powders and Porous Solids: Principles, Methodology and Applications*, 2nd ed.; Elsevier: Amsterdam, The Netherlands, 2014.
44. Lowell, S.; Shields, J.E.; Thomas, M.A.; Thommes, M. *Characterization of Porous Solids and Powders: Surface Area, Pore Size and Density*; Springer: Dordrecht, The Netherlands, 2004. [CrossRef]
45. Thommes, M.; Kaneko, K.; Neimark, A.V.; Olivier, J.P.; Rodriguez-Reinoso, F.; Rouquerol, J.; Sing, K.S.W. Physisorption of gases, with special reference to the evaluation of surface area and pore size distribution (IUPAC Technical Report). *Pure Appl. Chem.* **2015**, *87*, 1051–1069. [CrossRef]
46. Steinbach, J.C.; Fait, F.; Wagner, S.; Wagner, A.; Brecht, M.; Mayer, H.A.; Kandelbauer, A. Rational Design of Pore Parameters in Monodisperse Porous Poly(glycidyl methacrylate-co-ethylene glycol dimethacrylate) Particles Based on Response Surface Methodology. *Polymers* **2022**, *14*, 382. [CrossRef]

Disclaimer/Publisher's Note: The statements, opinions and data contained in all publications are solely those of the individual author(s) and contributor(s) and not of MDPI and/or the editor(s). MDPI and/or the editor(s) disclaim responsibility for any injury to people or property resulting from any ideas, methods, instructions or products referred to in the content.

Supporting Information

Modification of the morphology of monodisperse mesoporous silica particles using different alkoxysilanes.

Fabio Fait [1,2], Stefanie Wagner [1], Julia C. Steinbach [1,2], Andreas Kandelbauer [2,3] and Hermann A. Mayer [1,*]

[1] Institute of Inorganic Chemistry, University of Tübingen, Auf der Morgenstelle 18, 72076 Tübingen, Germany; fabio.fait@reutlingen-university.de (F.F.); stefaniewagnersb@googlemail.com (S.W.); julia.steinbach@reutlingen-university.de (J.C.S.)
[2] Process Analysis and Technology (PA&T), Reutlingen Research Institute, Reutlingen University,
Alteburgstrasse 150, 72762 Reutlingen, Germany; andreas.kandelbauer@reutlingen-university.de
[3] Institute of Wood Technology and Renewable Materials, Department of Material Sciences and Process
Engineering (MAP), University of Natural Resources and Life Sciences, Gregor-Mendel-Strasse 33,
1180 Vienna, Austria
* Correspondence: hermann.mayer@uni-tuebingen.de

Chemicals

Polyvinyl alcohol (PVA, 87-89% hydrolyzed, mean average 88000 – 97000 g mol^{-1}), polyvinylpyrrolidone K_{30} (PVP, mean average 40000 g mol^{-1}) and K_{90} (mean average 360000 g mol^{-1}) from abcr GmbH. Ethyleneglycol dimethacrylate (EDMA) was bought from Acros Organics. Cyclohexanol and sodium dodecyl sulfate (SDS) were purchased from Carl Roth. Styrene was obtained by Fisher Chemicals. Dibenzoyl peroxide (BPO), dibutyl phthalate (DBP), glycidyl methacrylate (GMA) and tetraethylene pentamine (TEPA) were purchased from Sigma-Aldrich.

Synthesis of polystyrene

Monodisperse polystyrene particles with diameters of 1.5 ± 0.1 were prepared as reported earlier (**Figure S1**)

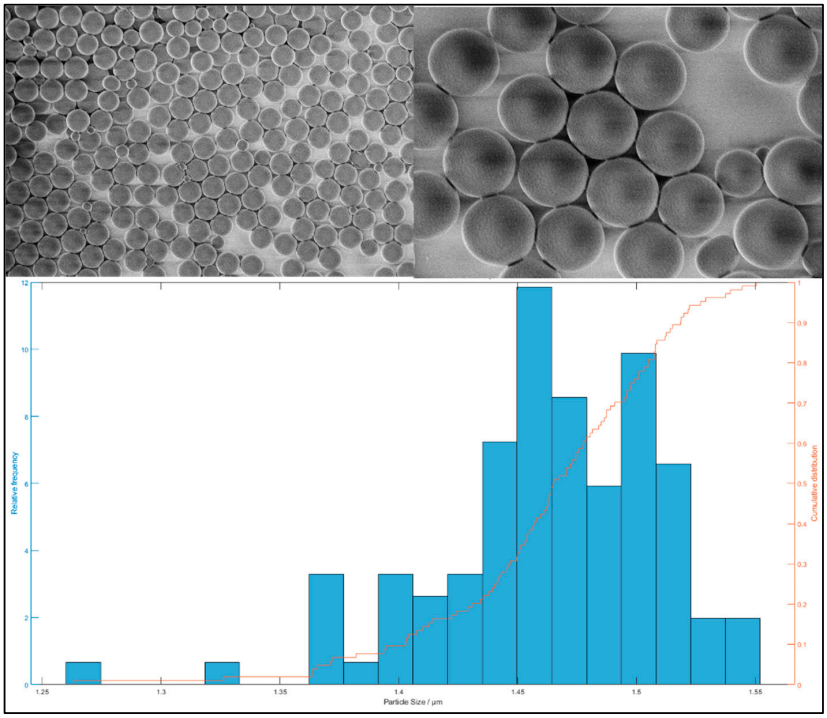


Figure S1. SEM images of applied polystyrene particles (top) and their particle size distribution (bottom).

Synthesis of P@TEPA

0.3 g of polystyrene particles and 5 mL of an aqueous SDS solution (0.25 wt.%) were dispersed in a 250 mL flask. 2 mL DBP were emulsified in 150 mL aqueous SDS solution (0.25 wt.%) with a homogenizer at 4500 rpm for 15 min and then added to the polystyrene suspension. The mixture was stirred for 24 h at 200 rpm. 6 mL GMA, 9 mL EDMA, 6 mL cyclohexanol, 16.5 mL toluene, 0.4 g BPO and 150 mL aqueous SDS solution (0.25 wt.%) were emulsified with a homogenizer at 4500 rpm for 15 min. This emulsion, a 150 mL aqueous PVA solution (2.3 wt.%) and the activated polystyrene particles were transferred to a 500 mL three-necked flask and stirred for 24 h at 200 rpm. Argon was passed into the reaction mixture for 30 minutes and then heated to 70 °C for 24 hours. The particles were separated from the solution, washed three times with EtOH and three times with H_2O and dried at 65 °C for 16 h. The average particle size of the *p*(GMA-*co*-EDMA) particles were 6.0 ± 0.5 µm (**Figure S2**).

5 g of *p*(GMA-*co*-EDMA) particles and 200 mL of H_2O were dispersed in a 500 mL flask. 7.5 of mL TEPA were added while stirring the suspension at 200 rpm. The reaction mixture was

heated to 80 °C for 24 h. The particles were separated from the solution, washed three times with EtOH and three times with H_2O and dried at 65 °C for 16 h.

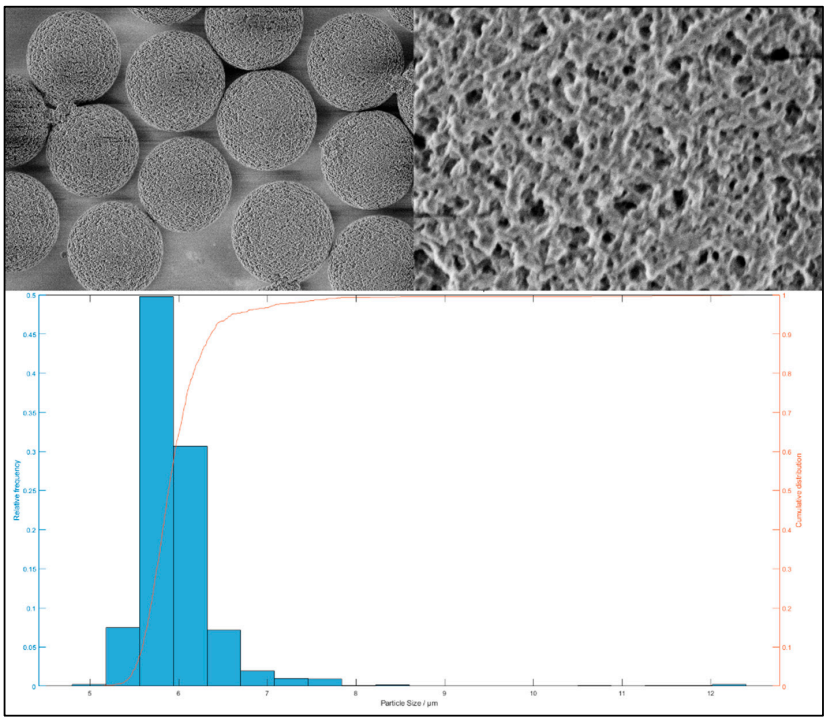


Figure S2. SEM images of the polymer templates *p*(GMA-*co*-EDMA) (top) and corresponding particle size distribution (bottom).

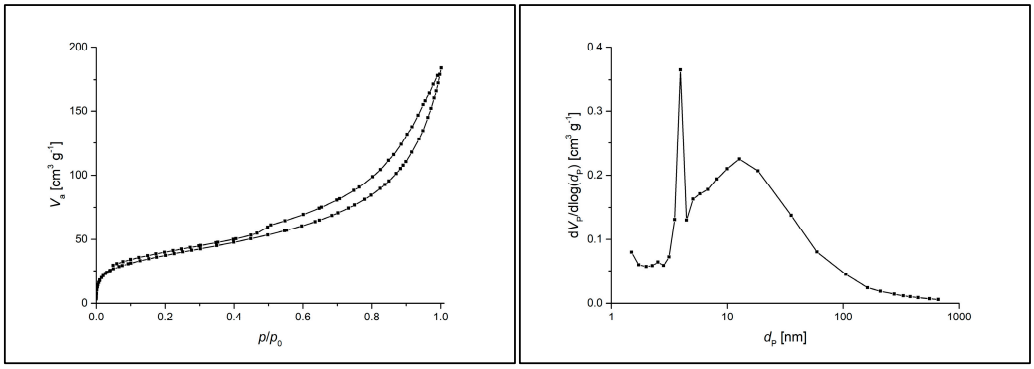


Figure S3. Isotherms (left) and pore size distribution (right) of *p*(GMA-*co*-EDMA).

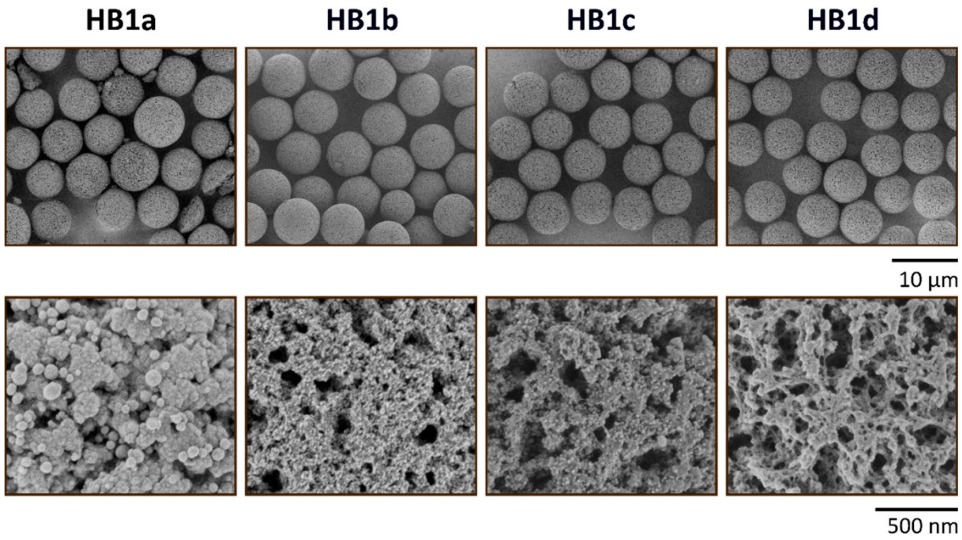


Figure S4. SEM images of hybrid beads **HB1a-d** with 2,000x magnification (top row) and 50,000x magnification (bottom row).

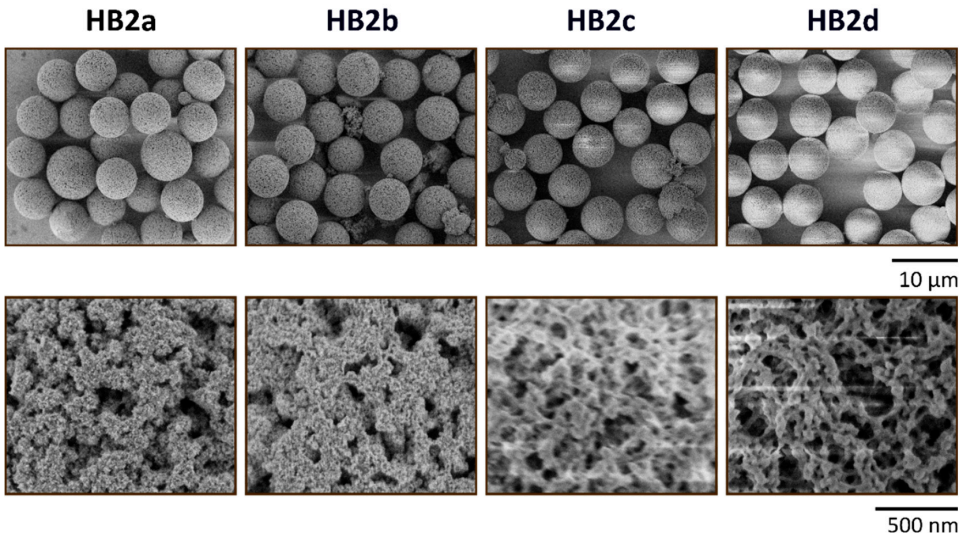


Figure S5. SEM images of hybrid beads **HB2a-d** with 2,000x magnification (top row) and 50,000x magnification (bottom row).

Table S1. Retention times of uracil and toluene after 1, 25, 50,75 and 100 runs in [min]

	1st run	25th run	50th run	75th run	100th run
t_r (Uracil)	3.31	3.31	3.33	3.31	3.28
t_r (Toluene)	4.03	4.03	4.05	4.01	3.98

10 Publikation V

International Journal of
Molecular Sciences

MDPI

Article

Monodisperse Porous Silica/Polymer Nanocomposite Microspheres with Tunable Silica Loading, Morphology and Porosity

Julia C. Steinbach [1,2], Fabio Fait [1,2], Hermann A. Mayer [2] and Andreas Kandelbauer [1,3,*]

[1] Process Analysis & Technology, Reutlingen Research Institute, Reutlingen University, Alteburgstraße 150, 72762 Reutlingen, Germany
[2] Institute of Inorganic Chemistry, University of Tübingen, Auf der Morgenstelle 18, 72076 Tübingen, Germany
[3] Institute of Wood Technology and Renewable Materials, Department of Material Sciences and Process Engineering (MAP), University of Natural Resources and Life Sciences, Gregor-Mendel-Straße 33, 1180 Vienna, Austria
* Correspondence: andreas.kandelbauer@reutlingen-university.de; Tel.: +49-(0)7121-271-2009

Abstract: Hybrid organic/inorganic nanocomposites combine the distinct properties of the organic polymer and the inorganic filler, resulting in overall improved system properties. Monodisperse porous hybrid beads consisting of tetraethylene pentamine functionalized *poly*(glycidyl methacrylate-*co*-ethylene glycol dimethacrylate) particles and silica nanoparticles (SNPs) were synthesized under Stoeber sol-gel process conditions. A wide range of hybrid organic/silica nanocomposite materials with different material properties was generated. The effects of n(H_2O)/n(TEOS) and c(NH_3) on the hybrid bead properties particle size, SiO_2 content, median pore size, specific surface area, pore volume and size of the SNPs were studied. Quantitative models with a high robustness and predictive power were established using a statistical and systematic approach based on response surface methodology. It was shown that the material properties depend in a complex way on the process factor settings and exhibit non-linear behaviors as well as partly synergistic interactions between the process factors. Thus, the silica content, median pore size, specific surface area, pore volume and size of the SNPs are non-linearly dependent on the water-to-precursor ratio. This is attributed to the effect of the water-to-precursor ratio on the hydrolysis and condensation rates of TEOS. A possible mechanism of SNP incorporation into the porous polymer network is discussed.

Keywords: nanocomposites; porous microspheres; design of experiment; response surface methodology; rational design; sol-gel processing

check for updates

Citation: Steinbach, J.C.; Fait, F.; Mayer, H.A.; Kandelbauer, A. Monodisperse Porous Silica/Polymer Nanocomposite Microspheres with Tunable Silica Loading, Morphology and Porosity. *Int. J. Mol. Sci.* **2022**, *23*, 14977. https://doi.org/10.3390/ijms232314977

Academic Editors: József Kalmár and Petra Herman

Received: 13 October 2022
Accepted: 24 November 2022
Published: 29 November 2022

Publisher's Note: MDPI stays neutral with regard to jurisdictional claims in published maps and institutional affiliations.

Copyright: © 2022 by the authors. Licensee MDPI, Basel, Switzerland. This article is an open access article distributed under the terms and conditions of the Creative Commons Attribution (CC BY) license (https://creativecommons.org/licenses/by/4.0/).

1. Introduction

The combination of organic and inorganic materials provides composites exhibiting different properties than the inorganic and organic components alone and is, therefore, of great interest in material sciences [1–4]. The incorporation of inorganic components, such as silica nanoparticles (SNPs), into organic networks allows for the design of material properties which affect their thermal and/or mechanical stability [5,6] and electronic behavior [7] and enhance biocompatibility [8]. Thus, hybrid materials are applied in catalysis [9] and separation technologies [10] and as drug delivery systems [8,11]. Moreover the organic component can function as a sacrificial template to generate defined porous inorganic structures [12–15].

For many applications, defined specific surface areas are favorable, which are achieved by introducing porous networks into the material. A good effective accessibility of the porous material for diffusion controlled processes, such as separation processes or catalysis, is achieved by mesopores and/or macropores [16]. The properties of porous *poly*(glycidyl methacrylate-*co*-ethylene glycol dimethacrylate) (*p*(GMA-*co*-EDMA)) particles in the micron

scale are specifically adjustable [17–20], which makes them an adaptable polymer matrix with a broad pore size distribution.

Nanocomposites are multiphase materials with at least one component in the nanometer range [21]. The preparation of hybrid organic/silica nanocomposites can be achieved by (1) the blending of dispersed polymer and silica nanoparticles, (2) the in situ polymerization of monomers in the presence of silica and (3) performing the sol-gel process from precursors in the presence of a polymer matrix [22]. The sol-gel process allows for the preparation of tailored silica materials with, e.g., defined nanoparticle sizes and dispersion under mild process conditions and is therefore particularly suitable for preparing tailored organic/silica composites [23].

Discrete SNPs with narrow size distributions are readily synthesized under basic reaction conditions by the Stoeber method. The sizes of silica nanoparticles obtained with this method vary between 0.05 µm and 2.0 µm [24]. The Stoeber method exploits the basic hydrolysis and condensation reactions of alkoxysilanes in alcoholic media [24]. The hydrolysis of the precursor (Equation (1)), e.g., tetraethyl orthosilicate (TEOS), proceeds under the formation of silanol groups (n = 1–4). The condensation with the formation of siloxane bonds and entire silica networks occurs either between silanol groups as water condensation (Equation (2)) or between silanol and ethoxy groups as alcohol condensation (Equation (3)).

$$\text{Hydrolysis:} \quad Si(OC_2H_5)_4 + n\ H_2O \rightleftharpoons Si(OC_2H_5)_{4\text{-}n}(OH)_n + n\ C_2H_5OH \tag{1}$$

$$\text{Water condensation:} \quad \equiv Si(OH) + (HO)Si\equiv \rightleftharpoons \equiv Si\text{-}O\text{-}Si\equiv + H_2O \tag{2}$$

$$\text{Alcohol condensation:} \quad \equiv Si(OC_2H_5) + (HO)Si\equiv \rightleftharpoons \equiv Si\text{-}O\text{-}Si\equiv + C_2H_5OH \tag{3}$$

Immediately after the addition of TEOS to an ammonia solution, progressing hydrolysis and condensation of the precursor starts. After reaching a critical supersaturation concentration, neighboring silanol monomers condense under the formation of clusters, which collapse to form primary particles [25–27]. There are two prevailing models to describe the further growth mechanism of silica particles: the monomer addition model [28], which depicts the growth as the addition of the monomer to already-formed primary particles, and the aggregation-only model [29], which explains particle growth through the aggregation of primary particles and the subsequent addition of oligomers. Small silica particles are not stable and aggregate, while stable large silica particles grow by the addition of monomers [30]. The size of the resulting SNPs depends on the relative rates of the hydrolysis and condensation reactions of the precursor. These are controlled by the relative concentrations of ammonia, TEOS and water as well as the reaction temperature and the alcohol chosen as the solvent [31].

As the sol-gel process is very susceptible to changes in the process conditions, a univariate study focusing on the effects of single factors only cannot depict the system complexity. The one-factor-at-a-time approach does not allow for the covering of a multidimensional experimental space and therefore for the identification of the synergistic interplay between two factors. The observation of the influence of single-factor variations cannot straightforwardly be transferred to other systems settings, since even small changes have a strong impact on the results. This is reflected by the sometimes even contradicting conclusions when the experimental findings of different studies are compared with one another, although they are self-consistent by themselves. Especially for the sol-gel process, where the relative rates of hydrolysis and condensation are affected by many parameters [25,26,30], a study where at least two process factors are simultaneously varied is required to understand the impacts and possible interaction effects between experimental variables. Response surface methodology (RSM) provides a statistical and systematic approach for the observation and quantification of not only linear but also non-linear behavior. Moreover, possible synergistic interactions between process factors are identified and provide detailed causal models for multiple process factors [17,32–34]. This approach

has been used to study a wide range of chemical processes [35–38] and has also been successfully applied for the preparation of SNPs [39–43].

In this study, micron-sized monodisperse porous hybrid organic/silica hybrid beads (HBs) are generated by performing a sol-gel process under Stoeber reaction conditions in the presence of porous amino-functionalized *p*(GMA-*co*-EDMA) particles (p@TEPA) as hard templates. The hybrid beads consist of two interpenetrating networks: the organic network of the template, which remains unchanged due to the mild reaction conditions, and the new silica network, which is composed of aggregated silica nanoparticles of different sizes [12,14].

The aim is to achieve a range of such hybrid materials with different and defined properties such as SiO_2 content, median pore size, specific surface area and pore volume. Thus, the two critical process factors for the sol-gel process, the water-to-precursor ratio ($n(H_2O)/n(TEOS)$) and the ammonia concentration ($c(NH_3)$) were investigated in the presence of a porous polymeric template. These were systematically changed according to a face-centered-central composite design (FCD) to establish response surface models describing the process factor effects on the morphological characteristics. Moreover, a possible mechanism of silica nanoparticle incorporation into the porous polymer matrix is proposed and discussed.

2. Results

The preparation of micron-sized porous hybrid beads (HBs) with a tunable ratio of organic components to silica and morphological properties was systematically investigated using response surface methodology (RSM) (Figure 1). The organic porous *p*(GMA-*co*-EDMA) template was prepared by seeded swelling polymerization (see Appendix A) [17]. Tetra ethylene pentamine (TEPA) was covalently bound to the porous polymer surface via ring opening reactions of the prevalent epoxy groups [44,45]. The TEPA functionalization of polymer particles (p@TEPA) has been shown to provide a well-suited surface modification for depositing silica into the polymer network [12,46]. The prepared p@TEPA template had a median particle size of 8.3 µm and was highly monodisperse, with a d_{90}/d_{10} value of 1.04. The median pore diameter (Φ_{50}) of the p@TEPA was 13.0 nm in combination with a specific surface area (SSA) of 63.79 $m^2 \cdot g^{-1}$ and a pore volume (V_p) of 0.12 $cm^3 \cdot g^{-1}$.

The hybrid beads HB1-HB16 consisting of p@TEPA/SiO_2 were prepared by varying the sol-gel process conditions according to Table 1 in the presence of the p@TEPA template. With RSM, linear and non-linear effects of the process factors $n(H_2O)/n(TEOS)$ and $c(NH_3)$, as well as their possible synergistic interactions, on the material properties SiO_2 content, Φ_{50}, V_p, SSA and size of the SNPs were analyzed using a face-centered-central composite design (FCD). Figure 1a schematically shows the experimental space covered by the FCD. Selected HBs which result from different process factor settings according to the RSM are shown in Figure 1.

Table 1 summarizes the factor-level settings of $n(H_2O)/n(TEOS)$ and $c(NH_3)$ and the resulting values of the measured response properties. The samples are listed in the Yates standard order. In addition to the HB samples, the material properties of the template (p@TEPA) are given for comparison. One of the axial design points, HB9, was identified as an outlier based on the extremely high values of its residuals for the pore volume and silica content. Thus, it was not used for model building. Model quality likewise improved for the models of all other targeted responses as well upon the omission of HB9.

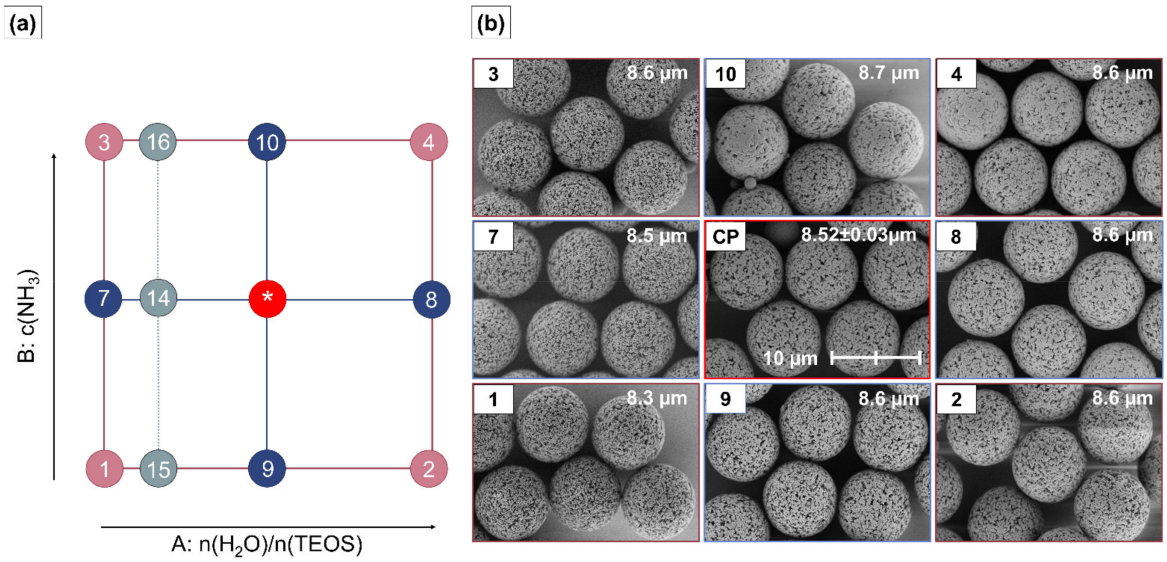


Figure 1. (**a**) Illustration of the face-centered-central composite design including the additional points HB14–16 (**b**) Systematic overview over SEM images at 5000× magnification of HBs. The median size of each sample is indicated in the respective image corner. For the CPs, the average particle size and its standard deviation over all five samples is given. The SEM image of HB13 is shown as a representative example for the CPs. Factorial design points (HB1–4) are displayed in dark red, center points (CPs) are displayed in red (HB5–6, HB11–13), axial design points (HB7–10) are displayed in blue and additional design points are shown in grey (HB14–16). SEM images of the additional design points HB14–16 are shown separately in Appendix B Figure A1. * indicates the center point experiments at intermediate factor level settings.

Table 1. Factor-level settings and their corresponding particle properties particle size, dispersity, specific surface area, pore diameter, pore volume (at $p/p_0 = 0.95$), SiO_2 content and size of the SNPs. The experiments are listed according to Yates standard order (Std). * Outlier-HB9 is marked in italics and was not included in the model building. † No SNPs visible or not measurable (below image resolution of SEM).

	Factor-Level Settings			Response Values					
	A $n(H_2O)/n(TEOS)$	B $n(NH_3)$ /mmol·L^{-1}	Particle Size /µm	d_{90}/d_{10}	SSA /m^2·g^{-1}	Pore Diameter Φ_{50} /nm	Pore Volume V_p /cm^3·g^{-1}	SiO_2 Content /wt%	SNP Size /nm
p@TEPA	-	-	8.3	1.04	63.79	13.0	0.12	0	-
HB1	4	17.1	8.3	1.11	73.87	12.9	0.13	0.1	0 †
HB2	74	17.1	8.6	1.14	35.11	12.6	0.03	19.7	20
HB3	4	74.1	8.6	1.06	55.86	12.7	0.10	2.7	0
HB4	74	74.1	8.6	1.07	8.75	18.1	0.02	31.2	66
HB5	39	45.6	8.5	1.09	20.87	16.1	0.04	22.6	27
HB6	39	45.6	8.5	1.08	12.92	17.8	0.03	26.9	35
HB7	4	45.6	8.5	1.06	62.72	13.8	0.12	0.4	0 †
HB8	74	45.6	8.6	1.06	9.63	16.5	0.02	30.1	47
HB9 *	*39*	*17.1*	*8.6*	*1.05*	*47.38*	*17.5*	* *0.09*	* *13.0*	*24*
HB10	39	74.1	8.7	1.07	12.02	17.1	0.03	28.6	58
HB11	39	45.6	8.6	1.06	13.51	16.3	0.03	26.7	35
HB12	39	45.6	8.5	1.07	17.10	15.5	0.05	25.9	43
HB13	39	45.6	8.5	1.08	14.32	17.0	0.03	25.9	40
HB14	8	45.6	8.5	1.07	50.76	15.5	0.10	2.7	0 †
HB15	8	17.1	8.5	1.06	64.03	14.2	0.12	0.2	0 †
HB16	8	74.1	8.3	1.15	47.03	14.9	0.09	7.9	18

2.1. Size and Dispersity

The particle sizes of the produced HB1–HB16 vary in a narrow range from 8.3 to 8.6 µm (8.5 ± 0.1 µm) and are monodisperse, with a particle size distribution with d_{90}/d_{10} values between 1.05 and 1.15 (1.08 ± 0.08). SEM images of the particles obtained at each design point are given in Figure 1b. Thus, the polymeric hard template is mainly determining the size of the HBs within the examined design space, and the narrow dispersity of the template particles is very well reproduced by the HBs. However, a small positive effect of the ratio $n(H_2O)/n(TEOS)$ on the particle size was found to be statistically significant (see Table 2). This indicates that an increase in $n(H_2O)/n(TEOS)$ leads to a minor increase in the HB particle size. The rather poor values for the model quality parameters $R^2 = 0.3642$ and $R^2_{pred} = 0.1684$ indicate that an effect can be detected; however, it is too weak to be quantitatively modeled sufficiently well within the range of the examined design space.

Table 2. Excerpt from the analysis of variance (ANOVA) tables with *p*-values for the response surface models of the target response variables particle size, SiO_2 content, median pore diameter (Φ_{50}), specific surface area (SSA), pore volume (V_p) and size of the SNPs, as well as their fit statistics. Complete ANOVA tables for each model are given in Appendix C Tables A1–A6.

	***p*-Values**					
Response	**Particle Size**	**SiO_2**	**Φ_{50}**	**SSA**	**V_p (p/p_0 = 0.95)**	**SNP Size**
	/µm	**/wt%**	**/nm**	**/$m^2 \cdot g^{-1}$**	**/$cm^3 \cdot g^{-1}$**	**/nm**
Model	0.0172	<0.0001	0.0007	<0.0001	<0.0001	<0.0001
A–$n(H_2O)/n(TEOS)$	0.0172	<0.0001	0.0099	<0.0001	0.0007	<0.0001
B–$c(NH_3)$	n.s.	0.0011	0.0051	<0.0001	<0.0001	<0.0001
AB	n.s.	n.s.	0.0074	n.s.	n.s.	0.0026
A^2	n.s.	<0.0001	0.0050	<0.0001	<0.0001	0.0009
B^2	n.s.	n.s.	n.s.	0.0146	n.s.	n.s.
Lack of fit	0.0163	0.2204 (n.s.)	0.4990 (n.s.)	0.4397 (n.s.)	0.9670 (n.s.)	0.6132 (n.s.)
R^2	0.3624	0.9780	0.8299	0.9840	0.9800	0.9545
R^2_{adj}	0.3152	0.9720	0.7618	0.9776	0.9745	0.9364
R^2_{pred}	0.1684	0.9459	0.5529	0.9535	0.9635	0.8874

n.s. = not statistically significant.

2.2. SiO_2 Content

The amount of silica, which is deposited in the pores of the template, was determined thermogravimetrically (see Section 4.5). The SiO_2 content in the hybrid materials is described by a statistically highly significant model ($p < 0.0001$) with a high robustness $R^2_{pred} = 0.9459$ and, hence, a good predictive power (Table 2).

The model effect terms A–$n(H_2O)/n(TEOS)$ and A^2, as well as B–$c(NH_3)$, are statistically highly significant at an α-value of 0.05. The effect strengths in terms of coded factors are given in Equation (4):

$$SiO_2 = 25.49 + 13.34\ A + 3.55\ B - 11.80\ A^2 \quad (4)$$

The stoichiometric water-to-precursor ratio shows by far the strongest effect and a non-linear behavior. The positive effect leads to an increase in the amount of deposited silica in the polymer with an increasing molar ratio. The negative A^2 effect term describes the non-linear behavior of the increase in silica deposition with an increasing $n(H_2O)/n(TEOS)$ ratio. At a stoichiometric water-to-precursor ratio of ~60:1, the silica deposition reaches a maximum (Figure 2a–c).

Int. J. Mol. Sci. **2022**, *23*, 14977

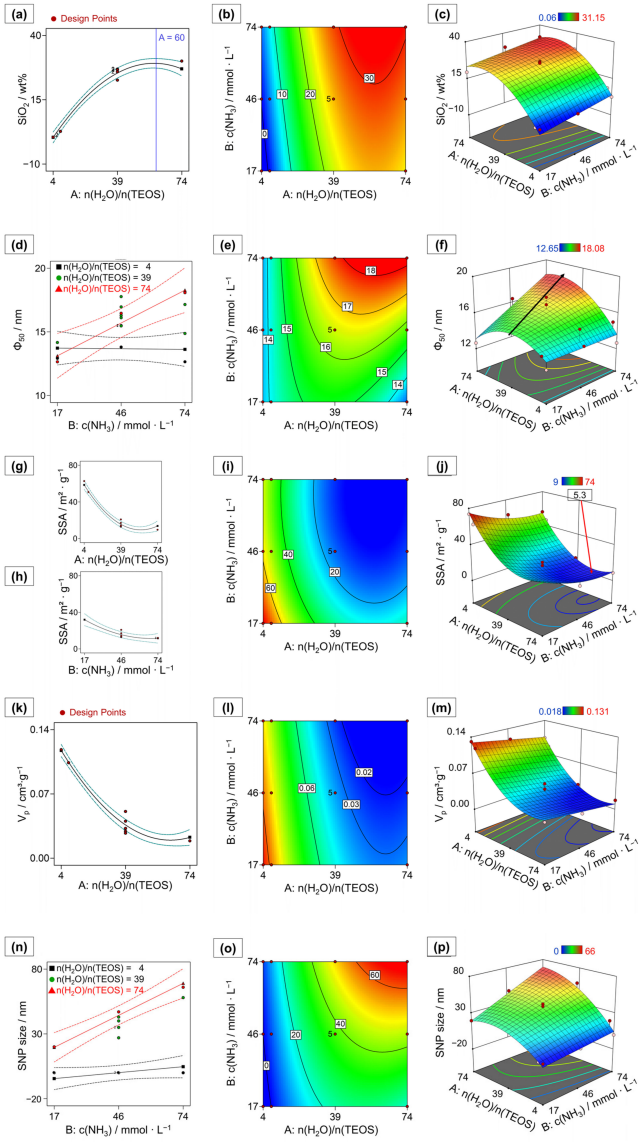


Figure 2. Overview over all relevant model graphs–one factor effect plots, depicting the effect of a single factor on the response at a medium level of the other studied process factor (**a**,**g**,**h**,**k**); interaction plots showing the dependence of the response on the settings of the two synergistically interacting factors (. = low setting, . = medium setting, . = high setting) and visualizing the strengths of the synergistic interactions (**d**,**n**); contour plots displaying a heatmap for each response variable dependent on both process factors (**b**,**e**,**i**,**l**,**o**); response surface plots showing the values for the responses predicted by the response surface model across the design space for each combination of process factor settings (**c**,**f**,**j**,**m**,**p**). Note that, in the 3D-plots (**j**,**m**), the axes of n(H_2O)/n(TEOS) are given in opposite direction to (**c**,**f**,**p**) for better visibility. Dashed lines indicate 95% confidence intervals for one factor and interaction plots. Red areas correspond to high and blue areas correspond to low response values in the response surface models. The responses are as follows: (**a**–**c**) SiO_2 content, blue line indicates maximum SiO_2 deposition; (**d**–**f**) median pore size (ϕ_{50}), the black arrow indicates a shift in maximal ϕ_{50} across the design space; (**g**–**j**) specific surface area (SSA) with the minimal SSA within the experimental space indicated by a flag; (**k**–**m**) pore volume (V_p); (**n**–**p**) SNP size.

2.3. Pore Size

Pore characteristics were determined by nitrogen adsorption measurements at 77 K. The pore size was calculated according to the Barrett–Joyner–Halenda (BJH) method from the desorption curve. For response surface modeling, the median of the pore size was used. The pore size distributions of all HBs, after the incorporation of in situ-prepared SNPs into the porous template network, and the template are shown in Figure 3, and the median pore size values are listed in Table 1.

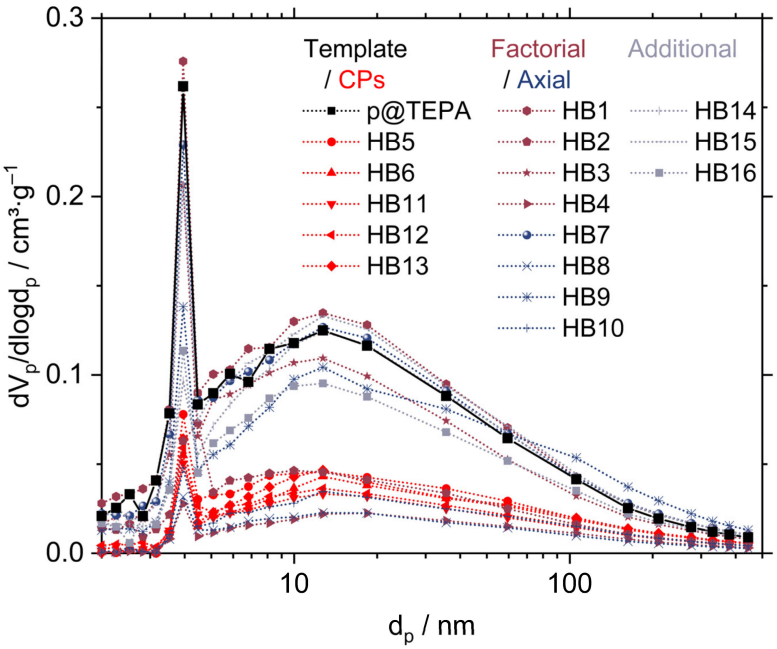


Figure 3. Pore size distribution of the porous p@TEPA template (solid line) and porous HBs (dotted lines). The template is shown in black, factorial design points are shown in dark red, center points (CPs) are shown in red, axial design points are shown in blue and additional design points are shown in grey.

The pore size distribution of the HBs is mainly determined by the pore size distribution already present in the p@TEPA template. It displays a very wide distribution from the meso- to macroporous range. Compared to the template, the median of the pore sizes is shifted to larger pores in the hybrid materials (see Table 1).

With a correlation coefficient of $R^2 = 0.8299$ and a regression coefficient of prediction of $R^2_{pred} = 0.5529$, the model ($p < 0.001$) can describe the pore size median well. The median of the pore sizes is statistically significantly affected by the effect terms A–n(H_2O)/n(TEOS) and B–c(NH_3), the synergistic interaction effect term AB between the water-to-precursor ratio and ammonia concentration and the non-linear effect term A^2. The relative importance of the factors is evident from Equation (5), the model equation in terms of coded factors:

$$\Phi_{50} = 16.49 + 1.01\ A + 1.26\ B + 1.31\ AB - 1.80\ A^2 \quad (5)$$

The synergistic interaction effect term AB quantifies the interdependence between the two factors. Consequently, restricting the discussion to only one of the factors is not meaningful, since the behavior of one factor depends on the factor-level setting of the other and changes while dependent on the second factor involved in the interaction. Figure 2d shows the two-factor interaction (2FIA) plot for the median pore size, with the ammonia concentration depicted on the abscissa. For small ratios A–n(H_2O)/n(TEOS), the ammonia concentration has very little or no effect on the median pore size, while for large

n(H_2O)/n(TEOS) ratios, the median pores size distinctly increases with an increasing B–c(NH_3). Increasing the ratio n(H_2O)/n(TEOS) amplifies the effect of the NH_3 concentration. Comparing HB1 (−/−) and HB3 (−/+), the median pore size is almost constant (12.9 nm and 12.6 nm, respectively), while for a high water-to-precursor ratio, the median pore size increases strongly from HB2 (+/−) at 12.7 nm to HB4 (+/+) at 18.1 nm with an increasing ammonia concentration.

The non-linear A^2 term shows that the increase in the median pore size towards higher values with increasing n(H_2O)/n(TEOS) becomes less pronounced at higher levels of n(H_2O)/n(TEOS). It also indicates that there is a maximum mean pore size, the location of which depends on the corresponding level of ammonia concentration used. This is especially visible in the trajectory of the contour plot (Figure 2e) and in the curvature of the response surface (Figure 2f) at high ammonia concentrations. The shift in the maximum pore size median is indicated by an arrow.

The combination of the non-linear A^2 term with the synergistic interaction term AB results in a twisted response surface with a steep ascent and a shifting maximum which shows a high sensitivity towards small changes in the factor-level settings of both the n(H_2O)/n(TEOS) ratio and the ammonia concentration. This sensitivity is also reflected by the relatively large statistical variance of the pore sizes observed within the replicated CP experiments.

2.4. Specific Surface Area

For many applications, the specific surface area (SSA) is of great importance, since it is crucial for the surface available for, e.g., the amount of functionalization or adsorption. The SSA was determined by nitrogen adsorption measurements under the application of the Brunauer–Emmet–Teller (BET) theory [47]. All samples showed values for the C parameter from the BET equation, referring to the surface interaction energy, between 48.7 (HB3) and 133.7 (HB2). This indicates a sufficiently well discriminated knee in the adsorption isotherm to determine the theoretical formation of the molecular monolayer [47]. The SSAs of the prepared HBs are modeled with a high predictive power and robustness (R^2 = 0.9840 and R^2_{pred} = 0.9535, respectively). The model is highly statistically significant ($p < 0.0001$) and includes the statistically significant factor effect terms A–n(H_2O)/n(TEOS) and B–c(NH_3), as well as both non-linear factor effect terms A^2 and B^2. No synergistic interactions between the two factors were found. The coded equation describing the relative effect strengths is given in Equation (6):

$$SSA = 15.59 - 22.38\ A - 10.17\ B + 20.57\ A^2 + 6.22\ B^2 \quad (6)$$

The SSAs of the HBs are mainly determined by the ratio n(H_2O)/n(TEOS), which has a strong negative effect. The SSAs decrease with an increasing water ratio. This effect is attenuated by the positive A^2 effect term accounting for the minimum which is observed at high n(H_2O)/n(TEOS) ratios (Figure 2g).

A similar behavior is seen for increasing ammonia concentrations. The negative linear effect term B combined with the positive non-linear effect term B^2 indicate a decrease in the SSAs with increasing ammonia concentrations, which, again, levels off at higher concentrations (Figure 2h,i). A minimum in SSA of approximately 5.3 $m^2 \cdot g^{-1}$ is found in the experimental space at A = 58 and B = 68 $mmol \cdot L^{-1}$, which is highlighted in the response surface plot of Figure 2j.

2.5. Pore Volume

The pore volumes V_p of the HB samples which were determined at p/p_0 = 0.95 are expressed by a highly statistically significant RSM ($p < 0.0001$) as a function of the process factor effect terms A–n(H_2O)/n(TEOS) and B–c(NH_3) and the non-linear factor effect term

A^2. The dependence of V_p on the process factors is given in terms of coded factor effect terms in Equation (7):

$$V_p = 0.0362 - 0.0473\ A - 0.0122\ B + 0.0388\ A^2 \quad (7)$$

The factor effect term A has the strongest influence determining the pore volume. The pore volume of the HBs decreases with an increasing water-to-precursor ratio. However, this decrease is attenuated at higher ratios by the positive nonlinear A^2 term (see Figure 2k).

In addition, increasing ammonia concentrations also lead to a decrease in pore volume, but this effect is much less pronounced and is only about one-fourth of the magnitude of the effect of factor A. This results in the highest pore volumes found at low factor-level settings for both factors A and B (Figure 2l,m). The model quality parameters $R^2 = 0.9800$ and $R^2_{pred} = 0.9635$ indicate an excellent predictive power and model robustness.

2.6. Morphology and Silica Nanoparticle Size

The morphology of the HBs is structured by the morphological properties of the template (Figures 4 and A1). Textural changes result from the sol-gel process to varying degrees, dependent on the factor-level combinations. They are especially pronounced at high factor-level settings and are not visible below a certain threshold. Distinct differences in surface appearance are observed for the first time for the factor-level combinations of particle HB16 ($n(H_2O)/n(TEOS) = 8$, c(NH3) = 74.1 mmol) (Appendix B Figure A2b). Instead of the smooth surfaces between the pore structures, small SNPs deposited in and onto the p@TEPA lead to an apparently rough surface texture. At medium and higher levels of the $n(H_2O)/n(TEOS)$ ratio, all produced HB particles exhibit a nanoparticulate surface texture (Figure 4). However, with higher ammonia concentrations, the discrimination between the SNPs from each other becomes less distinct. For HB4 and HB8, nonporous secondary particles were observed in the filtrate (Appendix B Figure A3). For HB4, these secondary particles were stable enough to be isolated. They showed a median size of ~300 nm and a d_{90}/d_{10} value of 1.88. For HB8, agglomeration occurred during the evaporation of the solvent. Secondary particles were obtained with a median size of ~240 nm and a $d_{90/d10}$ value of 2.05. However, since agglomeration occurred, this indicates that at least a portion of the secondary particles' original size was below 50 nm [26].

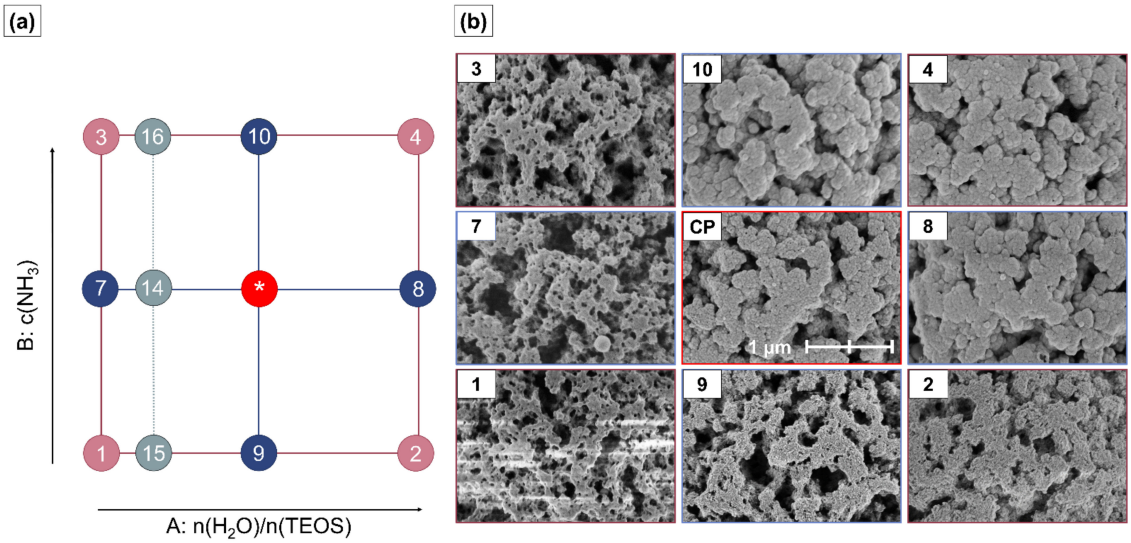


Figure 4. (**a**) Schematic representation of the design space covered by the factor-level combinations used in the face-centered-central composite design including the additional design points HB14–16. (**b**) Systematic overview over SEM images at 50,000× magnification of each sample obtained at the various factor-level combinations. A representative example of the center point (CP) combinations, HB13, is shown. Factorial design points (HB1–4) are displayed in dark red, center points are displayed in red (HB5–6, HB11–13), axial design points (HB7–10) are displayed in blue, and additional design points are shown in grey (HB14–16). Numbers reflect the Yates standard order. SEM images of the additional design points HB14–16 are shown separately in Appendix B Figure A2. * indicates the center point experiments at intermediate factor level settings.

The sizes of the SNPs are statistically significantly affected by the process factor A–n(H_2O)/n(TEOS) in combination with the non-linear factor effect A^2, the linear effect B–c(NH_3) and the synergistic interaction AB. The statistically significant model ($p < 0.0001$) shows a good data fit ($R^2 = 0.9545$) and allows for the prediction of new observations ($R^2_{pred} = 0.8874$). The relative importance of the factor effects is again evident from the coefficients in Equation (8) in coded terms:

$$\text{SNP size} = 37.24 + 22.11\ A + 14.65\ B + 10.06\ AB - 15.02\ A^2 \quad (8)$$

The positive direction of the synergistic interaction AB (Figure 2n) results in a pronounced increase in the SNP size that is dependent on increasing ammonia concentrations at the higher levels of n(H_2O)/n(TEOS) ratios. The non-linear A^2 term is negative and reduces the increase in the size of the SNPs for higher n(H_2O)/n(TEOS) levels, and the SNP size approaches a limiting value (at a factor-level setting of $A \approx 60$).

3. Discussion

The response surfaces of the five response variables SiO_2 content, ϕ_{50}, SSA, V_p and the sizes of the SNPs show similarities with respect to the factor effect directions and indicate similar interdependencies (Figure 2). To illustrate how the various target responses depend on each other, all variables were plotted in pairs against each other in scatterplots. Figure 5 summarizes the resulting correlation matrix for each combination of response variables with Pearson r and R^2_{adj} correlation coefficients. Pearson r is a measure of linear correlation with an indication of direct or indirect proportionality, and R^2_{adj} is a measure for correlation adjusted by the number of model terms relative to the number of experiments to avoid overfitting.

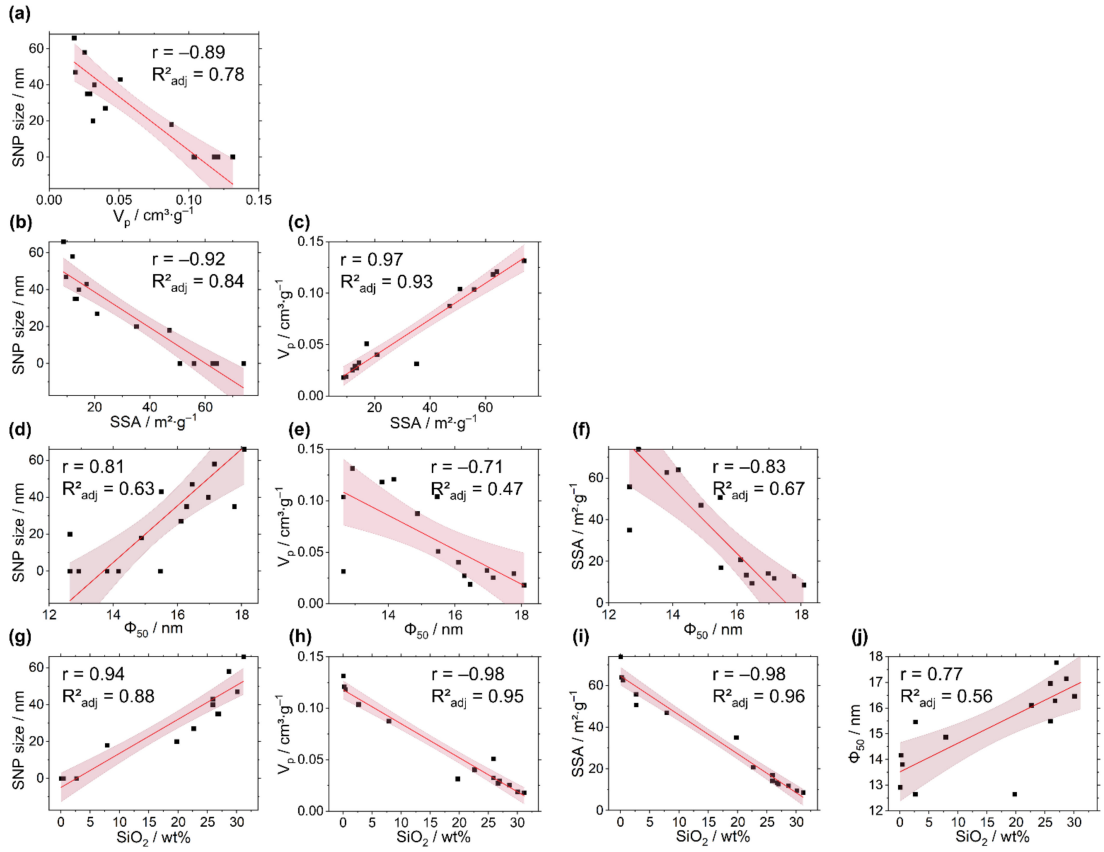


Figure 5. (**a**–**j**) Multiple scatterplots illustrating the correlations between response variables with Pearson correlation coefficients r and R^2_{adj} fit parameters. Red lines indicate linear fits. 95% confidence intervals are given by shaded areas.

All linear correlations are statistically significant at an α-level of 0.05. Here, the correlations with SiO_2 content are generally the best (Figure 5g–j), while the median pore size shows a rather poor but still statistically significant correlation (Figure 5d–f). With an increase in SiO_2 deposition, the V_p and SSA decrease, while the size of the SNPs at the HB surfaces increases (Figure 5g–i). Furthermore, the median of the pore size increases as well, which results in a decrease in the number of smaller pores. The positive correlation between the median pore size and SNP size shows that the median pore sizes of the HBs increase with the increasing size of SNPs (Figure 5d).

Figure 6 compares the relative changes in pore volume as a function of the pore diameter of the HBs and the template. From these data, it is deduced how the process factor settings influence the deposition of silica as a function of the pore size.

The most prominent difference in the relative V_p change compared to the porous template p@TEPA occurs at pore sizes < 5 nm. Samples that exhibit an increase in V_p are HB1 (−/−), HB7 (−/0) and, to some extent, HB14 (8/0) and HB15 (8/−). Apart from HB1, which shows an increase in the pore volume across the entire pore size range, the relative pore volume for pore sizes < 10 nm decreases for HB7, HB14 and HB15 as a result of silica deposition in small pores. Starting from pore sizes > 10 nm, the relative pore volume also increases compared to the template. These samples were prepared with low water-to-TEOS ratios and low ammonia concentrations. This group of particles is found in the lower left corner of the experimental design space (Figure 4a). Here, very small mass depositions of SiO_2 were observed, with values of <1 wt% (except for H14 2.67 wt%). In this region of the experimental design space, the deposition of silica is almost negligible. In

contrast, the pores of these HB particles are observed to be enlarged. Lacking protective silica deposits on the pore walls, in these HBs, the pores are still accessible to the solvent. This can lead to mechanical washing-out effects and the dissolution of non-crosslinked small polymer residues into the continuous phase of the sol-gel process, which consists of isopropyl alcohol. This external influence superimposes the effects of the controlled process factor variations. For all other samples, where the silica deposition prevents solubility and mechanical washing-out effects, this external influence on the relative pore volume changes does not play a role. Here, the change in pore volume can be fully explained by the following controlled process factors: water-to-precursor ratio and ammonia concentration.

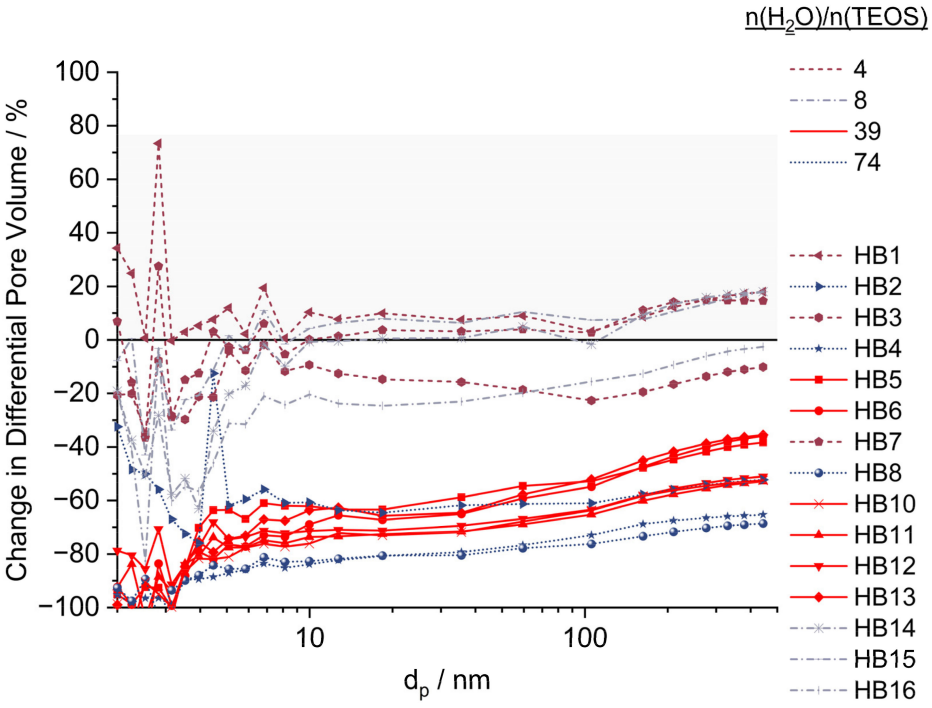


Figure 6. Relative change in pore volume distribution dependent on the pore size compared to the template particle. Line colors and types are grouped according to n(H_2O)/n(TEOS) level setting: n(H_2O)/n(TEOS) = 4 as burgundy dashed line, n/n = 8 as grey dashed-dotted line, n/n = 39 as solid red line and n/n = 74 as dotted blue line.

The decrease in pore volume is most pronounced for small pores, which are simply closed by silica deposition. Syntheses, which were carried out at low ratios of n(H_2O)/n(TEOS), display the lowest silica deposition and the smallest loss of pore volume at pore diameters of <10 nm. Syntheses with medium (CPs, in red) or high water/precursor ratios lead to an almost total closure of small pores < 5 nm (–80 to –100 %). Above around 5 nm, the decrease is then very uniform, with a slight increase in preserved pore volume for larger pores. This indicates the formation of a uniformly thick silica layer on the pore walls. These findings suggest an adsorptive deposition of silica onto the p@TEPA pore walls.

Although the response variables correlate well with each other linearly (Figure 5), they are each affected by the varied process factors in different ways and strengths. Table 3 shows the relative factor effect strengths, with the factors normalized to factor A–n(H_2O)/n(TEOS). This allows for a comparison of the relative strengths of the effects for the factor B–c(NH_3), the synergistic interaction effect AB and the nonlinear effect terms A^2 and B^2 between the models for the respective response variable.

Table 3. Relative effect strength normalized to A = ±1.00 in terms of coded factors for particle size, SiO_2 content, median pore diameter, specific surface area, pore volume and SNP size.

	SiO_2	Φ_{50}	SSA	V_p	SNP Size
	/wt%	/nm	/$m^2 \cdot g^{-1}$	/$cm^3 \cdot g^{-1}$	/nm
A–n(H_2O)/n(TEOS)	+1.00	+1.00	−1.00	−1.00	+1.00
B–c(NH_3),	+0.27	+1.25	−0.45	−0.26	+0.66
AB		+1.30			+0.45
$\mathbf{A^2}$	−0.88	−1.78	+0.92	+0.71	−0.68
$\mathbf{B^2}$			+0.28		

The effect of c(NH_3) always has the same algebraic sign as the effect term of factor A in all models and therefore always acts in the same direction as the ratio n(H_2O)/n(TEOS). However, the effect of the ammonia concentration is always smaller than the effect of the stoichiometric ratio of water to TEOS, except for the model of the median pore size. The SiO_2 content and V_p not only show a strong negative correlation (Figure 2b,l) but are also very similar in terms of relative effect strengths, but with opposing effect directions. With normalized factor strengths for the ammonia concentration of B = + 0.27 and B = –0.26 and an A^2 = –0.88 and A^2 = +0.71 for SiO_2 content and V_p, respectively, the V_p declines gradually with SNP deposition inside the porous template. The deposition of SNPs thus takes place inside the porous network of the template within the observed experimental space, except for HB4 and HB8, where non-porous secondary particles were formed. Here, a critical factor-level combination of A = 60 and B = 45.6 mmol·L^{-1} was exceeded.

In contrast to the V_p, the SSA shows a non-linear dependence on the ammonia concentration. The effect strength of ammonia is nearly twice as strong, but the decline in SSA with an increasing ammonia concentration levels off. This results from the deposition of SNPs at the outer surface of the template, which leads to a rougher surface texture of the HBs and an increase in the available particle surface (Figures 3g and 4b). This counterbalances the steep decline in SSA due to the closure of pores, which prevents the accessibility of the inner pore walls, even for small molecules such as nitrogen.

For all models, the linear A term is coupled to a non-linear A^2 in an opposing effect direction. This means that the ratio of n(H_2O)/n(TEOS) always has a non-linear component which leads to the diminishing of the overall influence with increasing water-to-precursor ratios n(H_2O)/n(TEOS). The non-linear behavior of the water-to-TEOS ratio has already been discussed regarding the size of the SNPs by other groups and was summarized by Bourebab et al. [48], who report a maximum size of the SNPs occurring between 10 and 35 wt% water. In the present study, the maximum size of the SNP was at an approximate water content of 20 wt%, which corresponds to an n(H_2O)/n(TEOS) ratio of 60. When this critical level was exceeded, a comparatively smaller increase in SNP size with increasing water content was found, which is reflected by the statistically significant A^2 term. Here, with the factor-level combination used as the starting conditions in the synthesis of HB4 and HB8 (Figures 4b and A3), the formation of secondary particles in the continuous phase was observed. As the hydrolysis and condensation rates increase with the increase in n(H_2O)/n(TEOS), along with simultaneously elevated levels of ammonia, the fast-growing SNPs become too large to penetrate into the pores of the template.

Since all HB particles which result from the combinations of factor-level settings according to the FCD were prepared at a pH between 10.5 and 11.0, the amino groups of the TEPA functionalization are still partly protonated, and, thus, the template carries a positive surface charge [46]. At the same time, the surface near silanol groups of the SNPs, which are produced in the continuous phase, are deprotonated and form negatively charged –Si-O^- functions. Small SNPs have a higher surface-to-volume ratio than larger ones and, thus, a higher silanol concentration [4]. This results in a high negative charge-to-volume ratio coupled with an increased mobility for small SNPs [49]. As a consequence of the strong electrostatic attraction of the negatively charged SNPs to the positively charged amino-

functionalized polymer surface, SNPs are readily incorporated into the porous network of the p@TEPA template. The p@TEPA template acts like a filter which removes small SNPs permanently from the reaction medium, withdraws them from reaction equilibria and thus prevents further growth. Therefore, as long as the rate of the diffusion of SNPs into the porous template exceeds the rate of particle growth, they cannot grow beyond a certain size on the outside, despite a sufficient monomer being available. This is the case at low n(H_2O)/n(TEOS) ratios. On the other hand, monomers and other hydrolyzed silanol species do not diffuse into the template as they rapidly undergo hydrolysis and condensation reactions in the continuous phase. Inside the porous network of the template, the small silica particles adsorb onto the positively charged pore walls, agglomerate and form uniform layers on the pore walls.

By the systematic variation in the critical process factors within our experimental design space, HBs with different morphological characteristics were produced, the formation of which can be assigned to three reaction regimes depending on the sol-gel starting conditions (Figure 7).

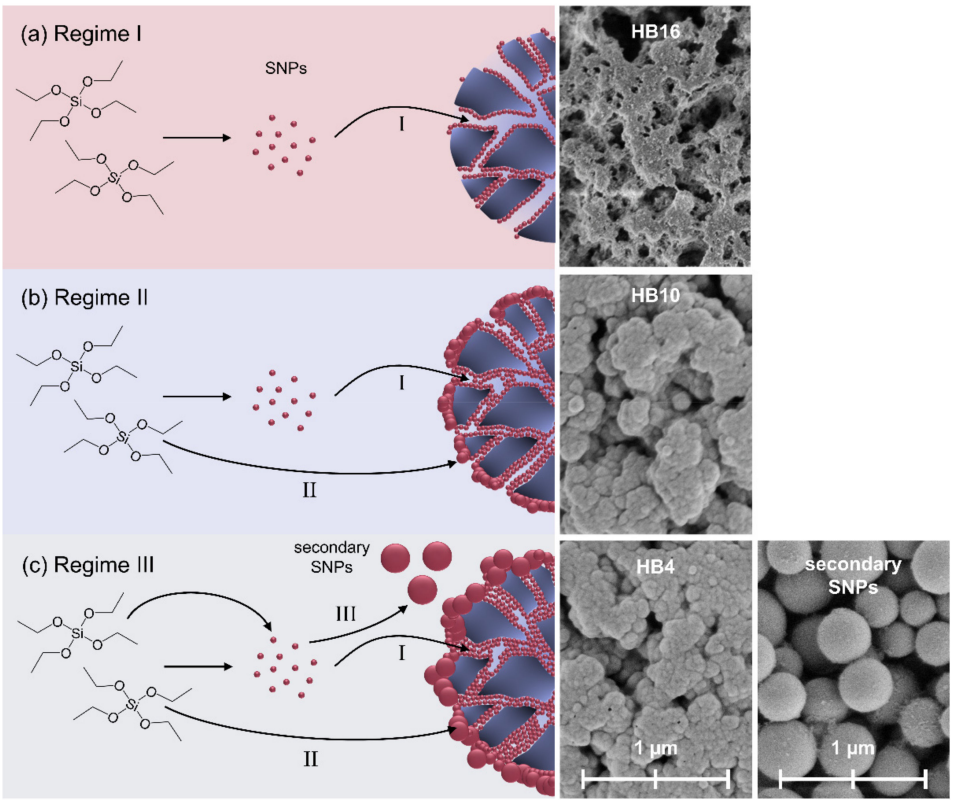


Figure 7. (**a**) Regime I corresponds to relatively low water values, (**b**) Regime II corresponds to medium values and (**c**) Regime III corresponds to high water-to-precursor ratios. Exemplarily, the regions are derived from the particles HB16, HB10 and HB4, respectively. It shows the diffusion of SNPs, after exceeding the supersaturation concentration, into the template. There, they aggregate in the absence of monomer (I). The hydrolysis is accelerated (Regime II), which deposits in the pores (I) and on the HB surface, where they undergo both the aggregation of SNPs and monomer addition, as they are in contact with the reaction medium (II). In Regime III, with highest hydrolysis/condensation rate, SNPs additionally undergo monomer addition (III) in the continuous phase, forming secondary particles, which are not attached to the HB.

At low water-to-TEOS ratios, hydrolysis is slow. The small SNPs formed are readily attracted by the template and are completely deposited inside the pores of p@TEPA. Thus, few silica particles are formed that attach to the pore walls on the inside of the template (HB1, 3, 7, 14–16) (Regime I, Figure 7b). If the water ratio is increased (HBs 2, 9, 10 and CPs) and the rate of hydrolysis is accelerated [28], the amount of silica deposition is increased. Those particles that are deposited on the outer surface of the template are still in contact with the reaction medium and continue to grow by monomer addition (Region II, Figure 7c).

The particle growth is further promoted by increasing the ammonia concentration [30]. This behavior affects the size of the SNP on the outer surface of the HBs and the HB pore size median (Figure 2d–f,n–p). Furthermore, more SNPs are deposited in the pores on the inside of the HBs, resulting in thicker silica layers covering the pore walls.

If hydrolysis and condensation rates are increased to an extent at which they exceed the diffusion of the SNPs into the p@TEPA pores, the SNPs remain in the reaction medium. There, they undergo further growth and form nonporous secondary particles (Region III Figure 7c). This is the case for $n(H_2O)/n(TEOS) \geq 60$ combined with a $c(NH_3)$ of 45.6 mmol·L^{-1} or higher (HB4 and 8; see Appendix B Figure A3).

4. Materials and Methods

4.1. Chemicals

Ammonia solution (28–30%), benzoyl peroxide (BPO, 75%), dibutyl phthalate (DBP, 99%), glycidyl methacrylate (GMA $\geq$ 97%), tetraethyl orthosilicate (TEOS) and toluene (anhydrous 99.8%) were purchased from Sigma-Aldrich Chemie GmbH (Traufkirchen Germany). Polyvinyl alcohol (PVA, hydrolyzed 86–89%) was supplied from abcr GmbH (Karlsruhe, Germany). Cyclohexanol (99%), ethylene glycole dimethacrylate (EDMA, 98%), HPLC grade water and tetraethylene pentamine (TEPA) were purchased from Fisher Scientific GmbH (Schwerte, Germany). Sodium dodecyl sulfate (SDS $\geq$ 99%) and 2-propanol (HPLC grade > 99.8 %) were purchased from Carl Roth GmbH + Co. KG (Karlsruhe, Germany). All chemicals were used as received.

4.2. Preparation of HBs

The hybrid microspheres were synthesized using a polymeric hard template. The porous *p*(GMA-*co*-EDMA) particles were synthesized according to the procedure described previously [17], with a scale-up. Further information is given in Appendix A.

The HBs were synthesized under basic hydrolysis-condensation conditions. The ammonia concentration and the molar ratio of $n(H_2O)/n(TEOS)$ were systematically changed according to a face-centered-central composite design (FCD) to assess the synthesis parameter effects on HB particle morphology, the surface and pore characteristics as well as the silica deposition behavior. The range of process factor levels is given in Table 4.

Table 4. Range of process factor-level settings as used in the face-centered-central composite experimental design (FCD).

Factor	Name	Low Setting (−)	Center Point (0)	High Setting (+)
A	$n(H_2O)/n(TEOS)$	4	39	74
B	$c(NH_3)$/mmol	2.39	6.38	10.37

The absolute amount of TEOS was the same for all particle syntheses. Depending on the molar ratio of $n(H_2O)/n(TEOS)$, the amount of additional water was calculated and varied accordingly. The water content of the NH_4OH solution was included in these calculations. A total volume of 140 mL was used, and the volume of the reaction mixtures was adjusted using 2-propanol. The changes in 2-propanol volume were <8%. Generally, 2 g of the p@TEPA particles were dispersed in a 2-propanol/H_2O mixture and sonicated for 5 min. Then, the NH_4OH solution was added as the basic catalyst under stirring, followed by the addition of 21.5 mmol TEOS. The mixture was stirred with 550 rpm for 24 h at room

temperature. The HBs were filtered off and washed three times with ethanol and water. The particles were then dried at room temperature prior to analysis.

4.3. Nitrogen Adsorption Measurements

For the determination of the specific surface area, pore size and pore volume, the BELSORP MiniX (Microtrac Retsch GmbH, Haan, Germany) was used for nitrogen adsorption measurements. The sample mass was ~ 150 mg (145 ± 14 mg), except for samples with a very small surface area, which were measured with an increased sample amount of ~300 mg (HB4 with 291 mg and HB8 with 290 mg). All samples were degassed at 30 °C for 24 h up to a final vacuum of about $2{\cdot}10^{-2}$ mbar to eliminate possible physisorbed substances and to achieve a reproducible intermediate state [50]. The samples were evacuated using the BELSORP VACII (Microtrac Retsch GmbH, Haan, Germany). The N_2-adsorption and desorption measurements were performed at 77 K. The analysis of adsorption and desorption isotherms was performed using the BELMaster 7 software (7.3.2.0, Microtrac Retsch GmbH, Haan, Germany). The specific surface area was analyzed according to the Brunauer–Emmet–Teller method (BET) [51,52]. For this, the relative pressure range of p/p_0 0.05–0.3 was used [47]. The pore size distribution was determined using the Barrett–Joyner–Halenda (BJH) method from the desorption branch and the Harkins–Jura standard isotherm. The pore size diameters were analyzed in the range from 2 to 500 nm. The pore volume was determined from a single adsorption point at p/p_0 of 0.95.

4.4. Scanning Electron Microscopy Images (SEM)

SEM images were acquired using a Hitachi SU8030 (Hitachi High-Tech Europe GmbH, Krefeld, Germany) to assess surface morphology, particle size and dispersity. A self-written MATLAB script was used to semi-automatically measure the size and dispersity from the SEM images. At least 120 particles were measured. The dispersity is given by the d_{90}/d_{10} value which indicates the width of the particle size distribution. Here, d_{90} is the value below which 90% of the measured values of the particle sizes lie. d_{10} is the value below which 10% of the measured particle sizes lie. A d_{90}/d_{10} value smaller than 1.4 was considered as a monodisperse distribution.

4.5. Thermogravimetric (TGA) Determination of SiO_2 Content

The amount of deposited SiO_2 content was determined using thermogravimetric analysis (TGA) using the TGA/DSC I from Mettler Toledo. Portions of a 119.9–121.4 mg (125.8 ± 3.1 mg) sample were weighed into a 900 µL alumina crucible, and thermal analysis was performed under synthetic air (50 mL/min). A heating rate of 5 K/min in a temperature range from 30 to 800 °C was performed. The relative mass of the remaining residue is the proportion of SiO_2 to the mass of the hybrid material.

4.6. Experimental Design

The mathematical description of linear, non-linear and interaction effect terms [36,53] was carried out by systematic analysis based on an FCD. Then, 16 HB particle batches were synthesized with five center point (CP) replications to determine reproducibility and system variance. Three additional syntheses were conducted with $n(H_2O)/n(TEOS) = 8$ to support model stability in the critical model region with low molar ratios. The effects of two factors and their possible synergistic interactions, $c(NH_3)$ and $n(H_2O)/n(TEOS)$, were investigated by systematic variations in the factor-level settings according to the FCD response surface design. The factor levels for low, intermediate and high settings are given in Table 4. The model effect terms were analyzed using analysis of variance (ANOVA). A model or model term was considered statistically significant when its p-value was $p \leq 0.05$. For model conceptualization and analysis, the Design Expert DX12 (Version 12.0.12.0, Stat-Ease Inc., Minneapolis, MN, USA) software package was used.

5. Conclusions

The process factors n(H_2O)/n(TEOS) and c(NH_3) specifically control the silica deposition on the inside and the outside of the p@TEPA template. Three discrete process regimes were identified. At low water conditions, only pores < 5 nm are filled with deposited silica to some extent. At medium to high water-to-precursor ratios, pores < 5 nm are almost completely filled with silica, and the pore volume of pores > 5 nm decreases uniformly. This suggests the formation of a uniform silica layer inside the porous template network through primary particle adsorption at the pore walls and aggregation within the porous network of the template. The present work demonstrates under which conditions the pores are closed and in which way and presents a mechanistic proposal for the construction of a silica network in a porous organic template.

This allows for access to new tailor-made hybrid materials with different properties. Specific hybrid materials can be created in which the organic template is coated with a thin silica layer, e.g., to protect the organic matter. These silica layers covering the pore walls can be further built up until the pores are filled with silica.

Furthermore, by extending the presented experimental space towards even higher ammonia and water concentrations and thus higher rates of hydrolysis and condensation, the formation of large SNPs exceeds the rate of diffusion, which hinders the incorporation of SNPs into the porous network of the template. This leads to the formation of particles with a porous organic core protected by a silica shell.

Author Contributions: Conceptualization, A.K. and H.A.M.; methodology, J.C.S., F.F., H.A.M. and A.K.; validation, J.C.S. and F.F.; formal analysis, J.C.S.; investigation, J.C.S. and F.F.; resources, H.A.M. and A.K.; data curation, J.C.S.; writing—original draft preparation, J.C.S.; writing—review and editing, F.F., H.A.M. and A.K.; visualization, J.C.S.; supervision, H.A.M. and A.K.; project administration, H.A.M. and A.K.; funding acquisition, A.K. All authors have read and agreed to the published version of the manuscript.

Funding: This research was funded by Bundesministerium für Bildung und Forschung (BMBF), grant number 13FH647IX6. The article processing charge was funded by the Baden-Württemberg Ministry of Science, Research and Arts and by Reutlingen University in the funding program Open Access Publishing.

Institutional Review Board Statement: Not applicable.

Informed Consent Statement: Not applicable.

Data Availability Statement: The data presented in this study are available within this article or are available from the authors upon request.

Acknowledgments: We thank Elke Nadler for contributing the SEM measurements. We also thank Leon Rösch for the experimental support.

Conflicts of Interest: The authors declare no conflict of interest. The funders had no role in the design of the study; in the collection, analyses or interpretation of the data; in the writing of the manuscript; or in the decision to publish the results.

Appendix A. Preparation of Amino-Functionalized Porous Polymer Template

First, 0.9 g monodisperse polystyrene seeds (1.95 µm, of d_{90}/d_{10} = 1.09) were sonicated for 10 min in 15 mL of a 2.0 g·L^{-1} SDS solution. An emulsion of 6.0 mL DBP and 450 mL of a 2.53 g·L^{-1} SDS solution (10 min at 5000 rpm) were added to the seed particle suspension. The suspension was stirred for 24 h at 200 rpm at room temperature. Then, 450 mL of SDS (3.33 g·L^{-1}), the initiator BPO (1.2 g), 22.5 mL of each cyclohexanol, EDMA, GMA and toluene were homogenized for 10 min at 5000 rpm. The emulsion was added, and the system was stirred at 200 rpm for another 24 h. Then, 450 mL of a PVA solution (23.3 g·L^{-1}) was added to the mixture as a stabilizer. The reaction mixture was stirred at 200 rpm for 24 h at 70 °C for polymerization. Thereafter, the porous *p*(GMA-*co*-EDMA) particles were washed three times with ethanol and three times with water.

For amino functionalization, 35 g of dried *p*(GMA-*co*-EDMA) particles were suspended in 1400 mL of deionized water and sonicated for 15 min. Then, 0.256 mol of TEPA were added dropwise under stirring (200 rpm). After the addition, the mixture was heated to 80 °C for 24 h. The functionalized particles were filtered off and washed three times with ethanol and water. The particles will be further referred to as p@TEPA.

Appendix B. Supplementary SEM Images

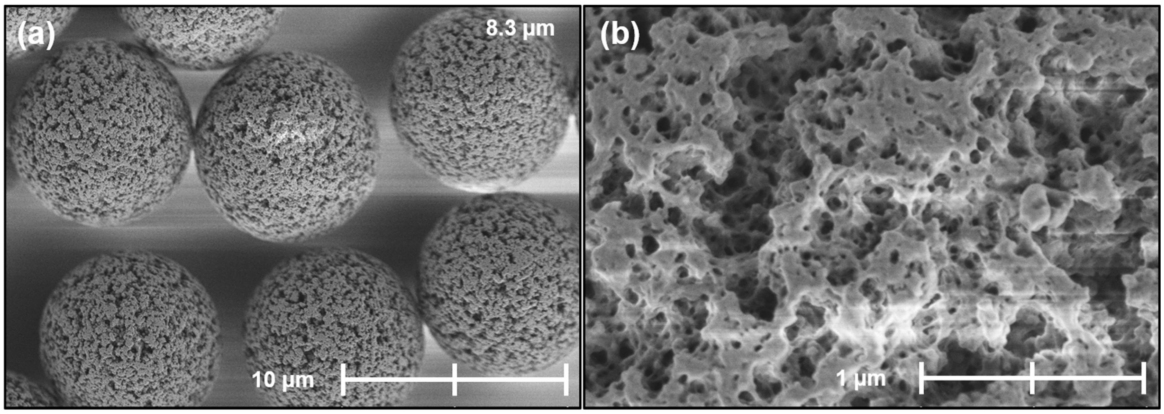


Figure A1. SEM image of *p*(GMA-*co*-EDMA) template batch at (**a**) 5000× and (**b**) 50,000× magnification. Particle size: 8.3 µm, d_{90}/d_{10}: 1.04, SSA: 63.79 $m^2 \cdot g^{-1}$, V_p: 0.12 $cm^3 \cdot g^{-1}$, ϕ_{50}: 14.47 nm.

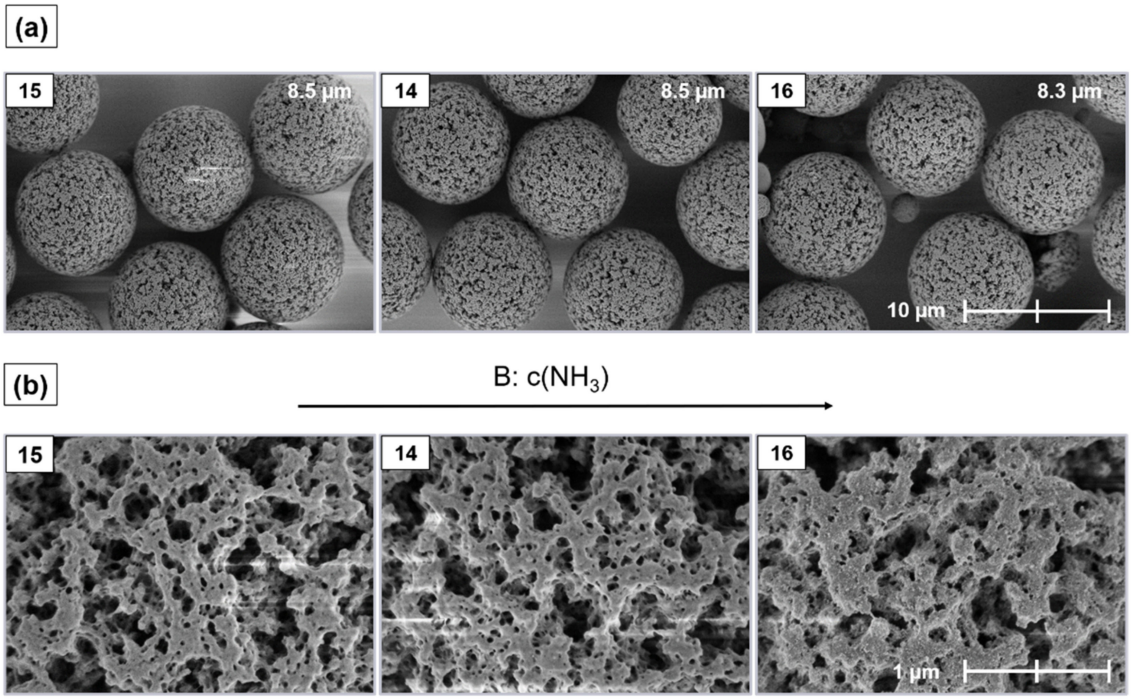


Figure A2. SEM image of the additional samples HB14–16 with $n(H_2O)/n(TEOS)$ = 8 sorted by increasing $c(NH_3)$ (l.t.r.) at (**a**) 5000× and (**b**) 50,000× magnification.

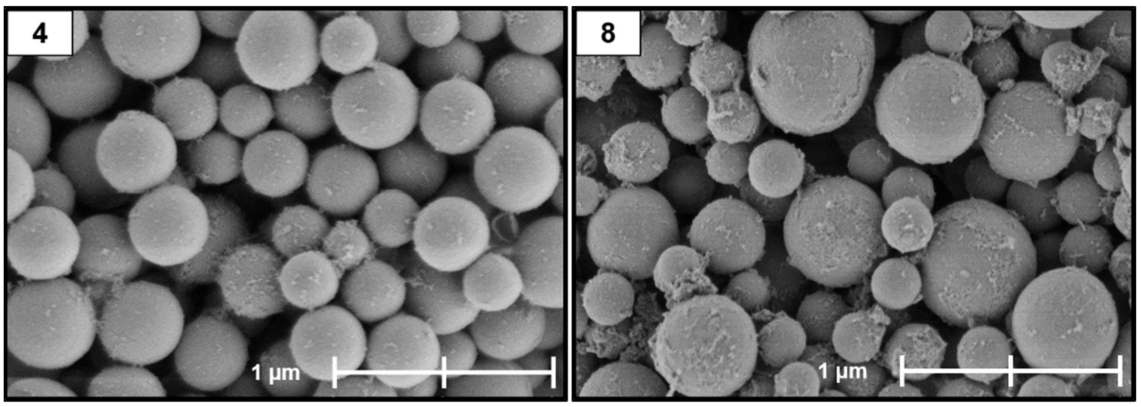


Figure A3. SEM image of filtrates with secondary particles of HB4 and HB8 at 50,000× magnification.

Appendix C. ANOVA Tables for the RSMs

Table A1. Analysis of variance (ANOVA) for the analysis of the FCD design of the median particle size.

Source	Sum of Squares	df	Mean Square	F-Value	*p*-Value	
Model	0.0561	1	0.0561	7.45	0.0172	significant
A-n(H_2O)/n(TEOS)	0.0561	1	0.0561	7.45	0.0172	
Residual	0.0980	13	0.0075			
Lack of Fit	0.0943	9	0.0105	11.26	0.0163	significant
Pure Error	0.0037	4	0.0009			
Cor Total	0.1541	14				

Table A2. Analysis of variance (ANOVA) for the analysis of the FCD design of SiO_2 content.

Source	Sum of Squares	df	Mean Square	F-Value	*p*-Value	
Model	2187.31	3	729.10	162.91	<0.0001	significant
A-n(H_2O)/n(TEOS)	1381.35	1	1381.35	308.65	<0.0001	
B-c(NH3)	86.00	1	86.00	19.21	0.0011	
A^2	432.20	1	432.20	96.57	<0.0001	
Residual	49.23	11	4.48			
Lack of Fit	39.41	7	5.63	2.29	0.2204	not significant
Pure Error	9.82	4	2.45			
Cor Total	2236.54	14				

Table A3. Analysis of variance (ANOVA) for the analysis of the FCD design of the median pore size ϕ_{50}.

Source	Sum of Squares	df	Mean Square	F-Value	*p*-Value	
Model	38.43	4	9.61	12.20	0.0007	significant
A-n(H_2O)/n(TEOS)	7.93	1	7.93	10.07	0.0099	
B-c(NH3)	10.03	1	10.03	12.74	0.0051	
AB	8.81	1	8.81	11.19	0.0074	
A^2	10.08	1	10.08	12.79	0.0050	
Residual	7.88	10	0.7879			
Lack of Fit	4.84	6	0.8074	1.06	0.4990	not significant
Pure Error	3.03	4	0.7586			
Cor Total	46.31	14				

Table A4. Analysis of variance (ANOVA) for the analysis of the FCD design of the SSA.

Source	Sum of Squares	df	Mean Square	F-Value	*p*-Value	
Model	7539.12	4	1884.78	153.80	<0.0001	significant
A-n(H_2O)/n(TEOS)	3882.36	1	3882.36	316.80	<0.0001	
B-c(NH3)	681.83	1	681.83	55.64	<0.0001	
A^2	989.61	1	989.61	80.75	<0.0001	
B^2	106.41	1	106.41	8.68	0.0146	
Residual	122.55	10	12.25			
Lack of Fit	79.47	6	13.25	1.23	0.4397	not significant
Pure Error	43.08	4	10.77			
Cor Total	7661.67	14				

Table A5. Analysis of variance (ANOVA) for the analysis of the FCD design of the V_p.

Source	Sum of Squares	df	Mean Square	F-Value	*p*-Value	
Model	0.0249	3	0.0083	179.66	<0.0001	significant
A-n(H_2O)/n(TEOS)	0.0174	1	0.0174	375.80	<0.0001	
B-c(NH3)	0.0010	1	0.0010	21.98	0.0007	
A^2	0.0036	1	0.0036	76.88	<0.0001	
Residual	0.0005	11	0.0000			
Lack of Fit	0.0001	7	0.0000	0.2028	0.9670	not significant
Pure Error	0.0004	4	0.0001			
Cor Total	0.0254	14				

Table A6. Analysis of variance (ANOVA) for the analysis of the FCD design of the SNP size.

Source	Sum of Squares	df	Mean Square	F-Value	*p*-Value	
Model	6865.92	4	1716.48	52.49	<0.0001	significant
A-n(H2O)/n(TEOS)	3797.04	1	3797.04	116.11	<0.0001	
B-c(NH3)	1346.92	1	1346.92	41.19	<0.0001	
AB	517.00	1	517.00	15.81	0.0026	
A^2	699.79	1	699.79	21.40	0.0009	
Residual	327.01	10	32.70			
Lack of Fit	179.01	6	29.84	0.8064	0.6132	not significant
Pure Error	148.00	4	37.00			
Cor Total	7192.93	14				

References

1. Lee, K.; Sathyagal, A.N.; McCormick, A.V. A closer look at an aggregation model of the Stöber process. *Colloids Surf. A Physicochem. Eng. Asp.* **1998**, *144*, 115–125. [CrossRef]
2. Meer, S.; Kausar, A.; Iqbal, T. Attributes of Polymer and Silica Nanoparticle Composites: A Review. *Polym. Plast. Technol. Eng.* **2016**, *55*, 826–861. [CrossRef]
3. Krasucka, P.; Stefaniak, W.; Kierys, A.; Goworek, J. Polymer–silica composites and silicas produced by high-temperature degradation of organic component. *Thermochim. Acta* **2015**, *615*, 43–50. [CrossRef]
4. Rahman, I.A.; Padavettan, V. Synthesis of Silica Nanoparticles by Sol-Gel: Size-Dependent Properties, Surface Modification, and Applications in Silica-Polymer Nanocomposites—A Review. *J. Nanomater.* **2012**, *2012*, 8. [CrossRef]
5. Kwon, S.; Adachi, T.; Araki, W.; Yamaji, A. Thermo-viscoelastic properties of silica particulate-reinforced epoxy composites: Considered in terms of the particle packing model. *Acta Mater.* **2006**, *54*, 3369–3374. [CrossRef]
6. Li, Q.; Li, X.; Cho, U.R. Mechanical Properties of Styrene-Butadiene Rubber Reinforced with Silica by in situ Tetraethoxysilane Hydrolysis over Acid Catalyst. *Elastomers Compos.* **2018**, *53*, 57–66. [CrossRef]
7. Kelly, T.L.; Che, S.P.Y.; Yamada, Y.; Yano, K.; Wolf, M.O. Influence of surface morphology on the colloidal and electronic behavior of conjugated polymer-silica microspheres. *Langmuir* **2008**, *24*, 9809–9815. [CrossRef]
8. McInnes, S.J.P.; Voelcker, N.H. Silicon-polymer hybrid materials for drug delivery. *Future Med. Chem.* **2009**, *1*, 1051–1074. [CrossRef]
9. Kiasat, A.R.; Nazari, S.; Davarpanah, J. Facile synthesis of an organic–inorganic nanocomposite, PEG–silica, by sol–gel method; its characterization and application as an efficient catalyst in regioselective nucleophilic ring opening of epoxides: Preparation of β-azido alcohols and β-cyanohydrins. *C. R. Chim.* **2014**, *17*, 124–130. [CrossRef]
10. Tumnantong, D.; Rempel, G.L.; Prasassarakich, P. Preparation of poly(methyl methacrylate)-Silica nanoparticles via differential microemulsion polymerization and physical properties of NR/PMMA-SiO 2 hybrid membranes. *Polym. Eng. Sci.* **2018**, *58*, 759–766. [CrossRef]
11. Guo, J.; Mattos, B.D.; Tardy, B.L.; Moody, V.M.; Xiao, G.; Ejima, H.; Cui, J.; Liang, K.; Richardson, J.J. Porous Inorganic and Hybrid Systems for Drug Delivery: Future Promise in Combatting Drug Resistance and Translation to Botanical Applications. *Curr. Med. Chem.* **2019**, *26*, 6107–6131. [CrossRef] [PubMed]
12. Xia, H.; Wan, G.; Yang, F.; Wang, J.; Bai, Q. Preparation of monodisperse large-porous silica microspheres with polymer microspheres as the templates for protein separation. *Mater. Lett.* **2016**, *180*, 19–22. [CrossRef]
13. Chen, J.; Zhu, L.; Ren, L.; Teng, C.; Wang, Y.; Jiang, B.; He, J. Fabrication of Monodisperse Porous Silica Microspheres with a Tunable Particle Size and Pore Size for Protein Separation. *ACS Appl. Bio Mater.* **2018**, *1*, 604–612. [CrossRef]
14. He, J.; Yang, C.; Xiong, X.; Jiang, B. Preparation and characterization of monodisperse porous silica microspheres with controllable morphology and structure. *J. Polym. Sci. A Polym. Chem.* **2012**, *50*, 2889–2897. [CrossRef]
15. Grama, S.; Horák, D. Preparation of monodisperse porous silica particles using poly(glycidyl methacrylate) microspheres as a template. *Physiol. Res.* **2015**, *64*, S11–S17. [CrossRef]
16. Yuan, Z.-Y.; Su, B.-L. Insights into hierarchically meso–macroporous structured materials. *J. Mater. Chem. UR* **2006**, *16*, 663–677. [CrossRef]
17. Steinbach, J.C.; Fait, F.; Wagner, S.; Wagner, A.; Brecht, M.; Mayer, H.A.; Kandelbauer, A. Rational Design of Pore Parameters in Monodisperse Porous Poly(glycidyl methacrylate-co-ethylene glycol dimethacrylate) Particles Based on Response Surface Methodology. *Polymers* **2022**, *14*, 382. [CrossRef] [PubMed]
18. Dubinsky, S.; Park, J.I.; Gourevich, I.; Chan, C.; Deetz, M.; Kumacheva, E. Toward Controlling the Surface Morphology of Macroporous Copolymer Particles. *Macromolecules* **2009**, *42*, 1990–1994. [CrossRef]
19. Gokmen, M.T.; Du Prez, F.E. Porous polymer particles—A comprehensive guide to synthesis, characterization, functionalization and applications. *Prog. Polym. Sci.* **2012**, *37*, 365–405. [CrossRef]
20. Costa, L.C.; Monteiro, R.C.; Castro, H.M.A.; Ribeiro, T.S.; Oliveira, M.A.; Torquato, E.C.C.; Arcanjo, M.E.; Marques, M.R.C. Glycidyl Methacrylate-ethylene Glycol Dimethacrylate Copolymers with Varied Pore Structures Prepared with Different Reaction Parameters. *Mater. Res.* **2020**, *23*, e20190550. [CrossRef]
21. Roy, R. Nanocomposites: Retrospecr and Prospect. *MRS Online Proc. Libr.* **1992**, *286*, 241–250. [CrossRef]
22. Zou, H.; Wu, S.; Shen, J. Polymer/silica nanocomposites: Preparation, characterization, properties, and applications. *Chem. Rev.* **2008**, *108*, 3893–3957. [CrossRef] [PubMed]
23. Ciriminna, R.; Fidalgo, A.; Pandarus, V.; Béland, F.; Ilharco, L.M.; Pagliaro, M. The sol-gel route to advanced silica-based materials and recent applications. *Chem. Rev.* **2013**, *113*, 6592–6620. [CrossRef]
24. Stöber, W.; Fink, A.; Bohn, E. Controlled growth of monodisperse silica spheres in the micron size range. *J. Colloid Interface Sci.* **1968**, *26*, 62–69. [CrossRef]
25. Park, S.K.; Kim, K.D.; Kim, H.T. Preparation of silica nanoparticles: Determination of the optimal synthesis conditions for small and uniform particles. *Colloids Surf. A Physicochem. Eng. Asp.* **2002**, *197*, 7–17. [CrossRef]
26. Plumeré, N.; Ruff, A.; Speiser, B.; Feldmann, V.; Mayer, H.A. Stöber silica particles as basis for redox modifications: Particle shape, size, polydispersity, and porosity. *J. Colloid Interface Sci.* **2012**, *368*, 208–219. [CrossRef] [PubMed]
27. LaMer, V.K.; Dinegar, R.H. Theory, Production and Mechanism of Formation of Monodispersed Hydrosols. *J. Am. Chem. Soc.* **1950**, *72*, 4847–4854. [CrossRef]

28. Matsoukas, T.; Gulari, E. Dynamics of growth of silica particles from ammonia-catalyzed hydrolysis of tetra-ethyl-orthosilicate. *J. Colloid Interface Sci.* **1988**, *124*, 252–261. [CrossRef]
29. Bogush, G.; Zukoski, C. Studies of the kinetics of the precipitation of uniform silica particles through the hydrolysis and condensation of silicon alkoxides. *J. Colloid Interface Sci.* **1991**, *142*, 1–18. [CrossRef]
30. Particles in the Stöber Method: In Situ Seeded Growth Model. *Langmuir* **2017**, *33*, 5879–5890. [CrossRef]
31. Sadasivan, S.; Dubey, A.K.; Li, Y.; Rasmussen, D.H. Alcoholic Solvent Effect on Silica Synthesis—NMR and DLS Investigation. *J. Solgel. Sci. Technol.* **1998**, *12*, 5–14. [CrossRef]
32. Myers, R.H.; Montgomery, D.C.; Anderson-Cook, C.M. *Response Surface Methodology: Process and Product Optimization Using Designed Experiments*, 2nd ed.; Wiley: Hoboken, NJ, USA, 2016; ISBN 9781118916025.
33. Box, G.E.P.; Hunter, J.S.; Hunter, W.G. *Statistics for Experimenters: Design, Innovation, and Discovery*, 2nd ed.; Wiley-Interscience: Hoboken, NJ, USA, 2005; ISBN 0471718130.
34. Ryan, T.P. *Modern Experimental Design*; Wiley-Interscience: Hoboken, NJ, USA, 2007; ISBN 978-0-471-21077-1.
35. Seidl, R.; Weiss, S.; Zikulnig-Rusch, E.M.; Kandelbauer, A. Response surface optimization for improving the processing behavior of melamine formaldehyde impregnation resins. *J. Appl. Polym. Sci.* **2021**, *138*, 50181. [CrossRef]
36. Ulitzsch, S.; Bäuerle, T.; Chassé, T.; Lorenz, G.; Kandelbauer, A. Optimizing the Process Efficiency of Reactive Extrusion in the Synthesis of Vinyltrimethoxysilane-Grafted Ethylene-Octene-Copolymer (EOC-g-VTMS) by Response Surface Methodology. *Polymers* **2020**, *12*, 2798. [CrossRef]
37. Wahrendorff, P.; Stefanakis, M.; Steinbach, J.C.; Allnoch, D.; Zuber, R.; Kapfhammer, R.; Brecht, M.; Kandelbauer, A.; Rebner, K. Simultaneous Determination of Droplet Size, pH Value and Concentration to Evaluate the Aging Behavior of Metalworking Fluids. *Sensors* **2021**, *21*, 8299. [CrossRef]
38. Thébault, M.; Kutuzova, L.; Jury, S.; Eicher, I.; Zikulnig-Rusch, E.-M.; Kandelbauer, A. Effect of Phenolation, Lignin-Type and Degree of Substitution on the Properties of Lignin-Modified Phenol-Formaldehyde Impregnation Resins: Molecular Weight Distribution, Wetting Behavior, Rheological Properties and Thermal Curing Profiles. *J. Renew. Mater.: JRM* **2020**, *8*, 603–630. [CrossRef]
39. Arantes, T.M.; Pinto, A.H.; Leite, E.R.; Longo, E.; Camargo, E.R. Synthesis and optimization of colloidal silica nanoparticles and their functionalization with methacrylic acid. *Colloids Surf. A Physicochem. Eng. Asp.* **2012**, *415*, 209–217. [CrossRef]
40. Chiang, Y.-D.; Lian, H.-Y.; Leo, S.-Y.; Wang, S.-G.; Yamauchi, Y.; Wu, K.C.-W. Controlling Particle Size and Structural Properties of Mesoporous Silica Nanoparticles Using the Taguchi Method. *J. Phys. Chem. C* **2011**, *115*, 13158–13165. [CrossRef]
41. Davies, G.-L.; Barry, A.; Gun'ko, Y.K. Preparation and size optimisation of silica nanoparticles using statistical analyses. *Chem. Phys. Lett.* **2009**, *468*, 239–244. [CrossRef]
42. González-Álvarez, R.J.; Naranjo-Rodríguez, I.; Hernández-Artiga, M.P.; Palacios-Santander, J.M.; Cubillana-Aguilera, L.; Bellido-Milla, D. Experimental design applied to optimisation of silica nanoparticles size obtained by sonosynthesis. *J. Sol-Gel Sci. Technol.* **2016**, *80*, 378–388. [CrossRef]
43. Wang, H.-C.; Wu, C.-Y.; Chung, C.-C.; Lai, M.-H.; Chung, T.-W. Analysis of Parameters and Interaction between Parameters in Preparation of Uniform Silicon Dioxide Nanoparticles Using Response Surface Methodology. *Ind. Eng. Chem. Res.* **2006**, *45*, 8043–8048. [CrossRef]
44. Grama, S.; Plichta, Z.; Trchová, M.; Kovářová, J.; Beneš, M.; Horák, D. Monodisperse macroporous poly(glycidyl methacrylate) microspheres coated with silica: Design, preparation and characterization. *React. Funct. Polym.* **2014**, *77*, 11–17. [CrossRef]
45. Muzammil, E.M.; Khan, A.; Stuparu, M.C. Post-polymerization modification reactions of poly(glycidyl methacrylate)s. *RSC Adv.* **2017**, *7*, 55874–55884. [CrossRef]
46. Bai, J.; Zhu, Q.; Tang, C.; Liu, J.; Yi, Y.; Bai, Q. Synthesis and application of 5 μm monodisperse porous silica microspheres with controllable pore size using polymeric microspheres as templates for the separation of small solutes and proteins by high-performance liquid chromatography. *J. Chromatogr. A* **2022**, *1675*, 463165. [CrossRef]
47. Thommes, M.; Kaneko, K.; Neimark, A.V.; Olivier, J.P.; Rodriguez-Reinoso, F.; Rouquerol, J.; Sing, K.S. Physisorption of gases, with special reference to the evaluation of surface area and pore size distribution (IUPAC Technical Report). *Pure Appl. Chem.* **2015**, *87*, 1051–1069. [CrossRef]
48. Bourebrab, M.A.; Oben, D.T.; Durand, G.G.; Taylor, P.G.; Bruce, J.I.; Bassindale, A.R.; Taylor, A. Influence of the initial chemical conditions on the rational design of silica particles. *J. Solgel. Sci. Technol.* **2018**, *88*, 430–441. [CrossRef]
49. Xu, P.; Wang, H.; Tong, R.; Du, Q.; Zhong, W. Preparation and morphology of SiO2/PMMA nanohybrids by microemulsion polymerization. *Colloid Polym. Sci.* **2006**, *284*, 755–762. [CrossRef]
50. Rouquerol, F.; Rouquerol, J.; Sing, K.S.W.; Llewellyn, P.L.; Maurin, G. *Adsorption by Powders and Porous Solids: Principles, Methodology and Applications*, 2nd ed.; Elsevier/AP: Amsterdam, The Netherlands, 2014.
51. Brunauer, S.; Emmett, P.H.; Teller, E. Adsorption of Gases in Multimolecular Layers. *J. Am. Chem. Soc.* **1938**, *60*, 309–319. [CrossRef]
52. Lowell, S.; Shields, J.E.; Thomas, M.A.; Thommes, M. (Eds.) *Characterization of Porous Solids and Powders: Surface Area, Pore Size and Density*; Springer: Dordrecht, The Netherlands, 2004; ISBN 978-1-4020-2303-3.
53. Bäuerle, T.; Ulitzsch, S.; Lorenz, A.; Rebner, K.; Chassé, T.; Kandelbauer, A.; Lorenz, G. Effects of process parameters on silane grafting of liquid ethylene-propylene copolymer by reactive extrusion as quantified by response surface methodology. *Polymer* **2020**, *202*, 122601. [CrossRef]

11 Publikation VI

ACS OMEGA

http://pubs.acs.org/journal/acsodf

Article

Sol–Gel-Controlled Size and Morphology of Mesoporous Silica Microspheres Using Hard Templates

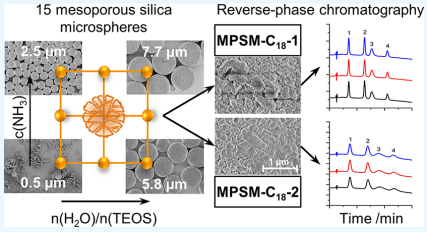
Julia C. Steinbach, Fabio Fait, Hermann A. Mayer, and Andreas Kandelbauer*

Cite This: *ACS Omega* 2023, 8, 30273–30284

Read Online

ACCESS | Metrics & More | Article Recommendations | Supporting Information

ABSTRACT: Mesoporous silica microspheres (MPSMs) represent a promising material as a stationary phase for HPLC separations. The use of hard templates provides a preparation strategy for producing such monodisperse silica microspheres. Here, 15 MPSMs were systematically synthesized by varying the sol–gel reaction parameters of water-to-precursor ratio and ammonia concentration in the presence of a porous *p*(GMA-*co*-EDMA) polymeric hard template. Changing the sol–gel process factors resulted in a wide range of MPSMs with varying particle sizes from smaller than one to several micrometers. The application of response surface methodology allowed to derive quantitative predictive models based on the process factor effects on particle size, pore size, pore volume, and specific surface area of the MPSMs. A narrow size distribution of the silica particles was maintained over the entire experimental space. Two larger-scale batches of MPSMs were prepared, and the particles were functionalized with trimethoxy(octadecyl) silane for the application as stationary phase in reversed-phases liquid chromatography. The separation of proteins and amino acids was successfully accomplished, and the effect of the pore properties of the silica particles on separation was demonstrated.



Downloaded via 78.43.40.99 on September 4, 2023 at 18:44:39 (UTC).
See https://pubs.acs.org/sharingguidelines for options on how to legitimately share published articles.

INTRODUCTION

Porous silica particles are relevant in catalysis,[1] in biosensors,[2,3] as drug carriers,[4−6] and as column material in purification and separation via chromatography.[7−9] To fit the requirements of a particular application, the control of particle size, size distribution, morphology, specific surface area, and pore parameters of these silica particles is of great importance. For instance, in drug delivery, silica particles as drug carriers require a size of <5 μm to be able to penetrate through the skin and release the drug in the tissue. Larger particles remain on the surface of the skin, where they may form a protective layer, as known from, e.g., sunscreen.[10] For high-performance liquid chromatography (HPLC) applications, silica-based packing materials are very common. The properties of the stationary phase dictate to a large extent the separation efficiency for various separation operations. The specific surface area is important for the column performance in many separation processes and chromatographic applications, as it affects the number of contact events available for interaction between the analyte and stationary phase and, thus, retention time. As smaller particles have a higher surface to volume ratio, particles with small average diameters are preferably used as column packing materials to increase the available interaction surface.[11] However, smaller particles also result in higher backpressures within the system and thus higher requirements are imposed on the equipment in terms of pressure resistance, and some analytes cannot be measured nondestructively under such conditions.[11−13] One way to increase the surface area without decreasing the particle size is the incorporation of pores into the particles. The introduction of meso-/macropores allows a good effective accessibility of the porous material for diffusion-controlled processes.[14] Templating methods have been widely applied to prepare porous silica materials with tunable size and pore characteristics.[15−18] While soft templates are successfully used to prepare nanometer-sized silica particles,[15,17,19] hard templates are the choice to synthesize micrometer-sized mesoporous silica spheres (MPSMs).[9,20] This is because hard templates such as poly(glycidyl methacrylate-*co*-ethylene glycol dimethacrylate) particles (*p*(GMA-*co*-EDMA))[9,20−24] are usually formative, i.e., determining the three-dimensional morphology.[15,17,25] Template-assisted methods for the preparation of MPSMs consist usually of three sequential steps:[26−28] (a) synthesis of the formative template,[23,24] (b) synthesis and/or incorporation of silica into the template,[23,29] and (c) subsequent removal of the template[30,31] (Figure 1).

The sol–gel process is particularly suitable because of its mild reaction conditions. Here, in the presence of the template, *in situ* generated silica nanoparticles (SNPs) diffuse into the pores of the template and build up the silica network. Thus, tailored MPSMs with narrow size distributions and defined

Received: May 5, 2023
Accepted: July 28, 2023
Published: August 9, 2023



ACS Publications

© 2023 The Authors. Published by American Chemical Society

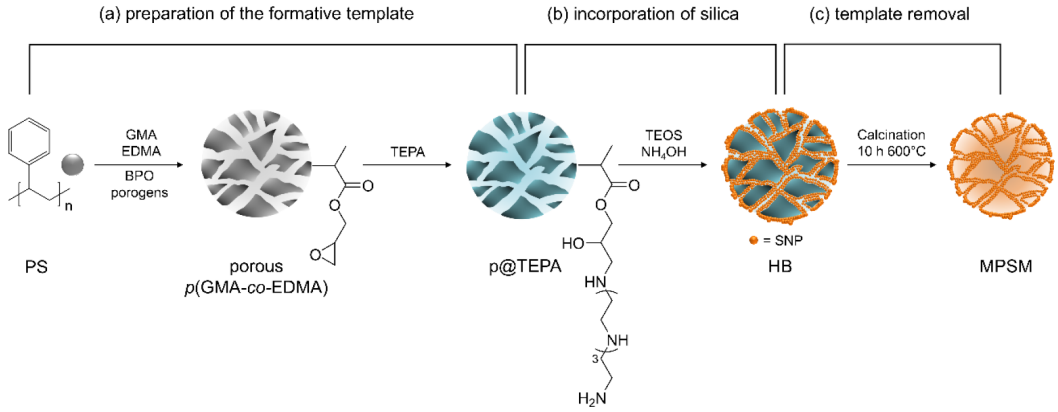


Figure 1. Reaction scheme for the preparation of mesoporous silica microspheres (MPSMs) by a hard-template method used in this study. The polymer template is removed during calcination by thermal degradation. A typical TGA trace of the calcination of the hybrid beads (HB) is given in Figure S2; PS: polystyrene seed particles, *p*(GMA-*co*-EDMA): poly(glycidyl methacrylate-*co*-ethylene glycol dimethacrylat), p@TEPA: tetraethylene pentaamine-functionalized polymer template, HB: hybrid bead consisting of polymer template/silica; SNP: silica nanoparticle.

particle sizes are formed after removal of the sacrificial porous polymer template by calcination.[32,33] The main advantage of this approach is that the template determines the shape of the resulting MPSM, which allows the generation of spherical particles with narrow size distribution. Earlier work suggests[9,15,20,34] that the way silica is deposited in the pores of the template has a large impact on the characteristics of the final MPSMs.

Our previous study[29] determined how the sol–gel process factors the water-to-precursor ratio (here: tetraethyl ortho silicate, TEOS) and the ammonia concentration affects the silica deposition within the porous network of polymeric hard-templates.[24] By systematically varying the sol–gel process conditions according to response surface methodology, three reaction regimes were identified.[29] These regimes result from changes in the relative reaction rates of hydrolysis and condensation depending on the sol–gel process factors, as well as the diffusion rate of *in situ*-generated SNPs into the polymer pore network. The polymer templates are either just coated with a thin silica layer (regime I); the pores of the polymer template are almost completely filled with silica (regime II); or the formation of silica nanoparticles exceeds the diffusion rate of SNPs into the polymer pores and thus results in the additional formation of secondary nonporous SNPs in the continuous phase outside of the template.[29] The prepared hybrid materials are the intermediate step of the preparation of porous silica particles before template removal (Figure 1b).

The present study focuses on the removal of the sacrificial organic polymer template via calcination, which is the third step of the template-assisted approach (Figure 1c). The effects of the sol–gel process factors $n(H_2O)/n(TEOS)$ and $c(NH_3)$ and their potential synergistic interaction effects on particle size, size distribution, morphology, and porosity were systematically examined using the approach of response surface methodology.[35−38] By this, quantitative models are established that allow the correlation and prediction of the effects of the sol–gel process factors on the material properties of MPSMs prepared using the hard-template-assisted preparation method. Furthermore, two larger-scale batches of MPSMs were prepared, functionalized with trimethoxy(octadecyl) silane and were used as reversed-phased column packing material for the separation of proteins and amino acids.

MATERIALS AND METHODS

Chemicals. Polyvinyl alcohol (PVA, hydrolyzed 86−89%) and trimethoxy(octadecyl)silane were purchased from abcr GmbH (Karlsruhe, Germany). Sodium dodecyl sulfate (SDS ≥ 99%) and 2-propanol (HPLC grade > 99.8%) were obtained from Carl Roth GmbH + Co. KG (Karlsruhe, Germany). Ammonia solution (28−30%), benzoyl peroxide (BPO, 75%), dibutyl phthalate (DBP, 99%), ethanol, glycidyl methacrylate (GMA ≥ 97%), hydrochloric acid (37%), methanol, tetraethyl orthosilicate (TEOS), toluene (anhydrous 99.8%), triethylamine (pure), and the protein test mixture H2899 were bought from Sigma-Aldrich Chemie GmbH (Traufkirchen Germany). Acetonitrile (ACN, HPLC grade), cyclohexanol (99%), ethylene glycole dimethacrylate (EDMA, 98%), HPLC grade water and tetraethylene pentamine (TEPA) were purchased from Fisher Scientific GmbH (Schwerte, Germany). All chemicals were used as received. *Ortho*-phthalaldehyde (OPA) reagent for precolumn derivatization of the amino acids was provided by Dr. Maisch HPLC, Germany.

Preparation of MPSM. The MPSMs were prepared using a hard-templating method with a multistep synthesis sequence schematically shown in Figure 1. A porous *p*(GMA-*co*-EDMA) template was prepared by a seed swelling-polymerization with self-prepared polystyrene particles (see Supporting Information, SI, Figure S1) as seeds[24] and subsequently amino-functionalized with TEPA (see SI).

The method for preparation of organic/silica hybrid beads (HBs) **HB1−15** has been extensively reported on earlier[29] and is therefore only briefly summarized here. The sol–gel process was conducted under basic conditions with varying water to precursor ratios ($n(H_2O)/n(TEOS)$) and ammonia concentrations ($c(NH_3)$) in the presence of the p@TEPA particles as template to generate the hybrid beads **HB1−15**. The overall TEOS molarity with respect to the total solvent content was kept constant for all experiments (21.5 mmol). Furthermore, the overall solvent amount was also kept constant. Variations in water content were compensated by complementary changes in the 2-propanol content. For detailed information, see reference 29.

The ammonia concentration and the molar ratio of $n(H_2O)/n(TEOS)$ were systematically changed according to

https://doi.org/10.1021/acsomega.3c03098
ACS Omega 2023, 8, 30273−30284

a face-centered central composite design (FCD) (Figure 2). Table 1 provides the range of variation for the levels of the

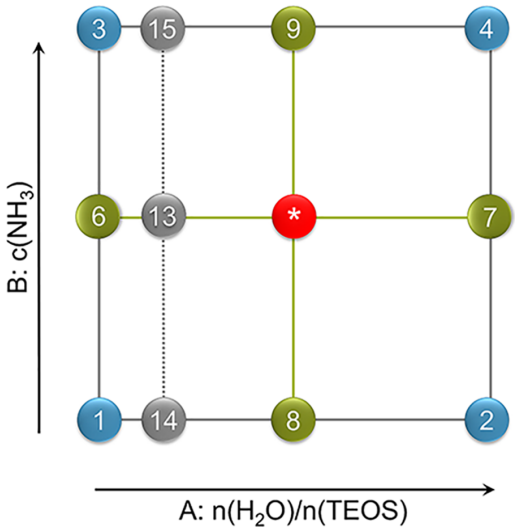


Figure 2. Illustration of the face centered central composite design. The numbers correspond to the sample numbers given in Table 2. Factorial points are displayed in blue, axial points in green, additional points in gray, and the CPs in red.

Table 1. Range of Process Factors Level Settings Used in the Face-Centered Central Composite Experimental Design (FCD)

factor	name	low setting (−)	center point (0)	high setting (+)
A	$n(H_2O)/n(TEOS)$	4	39	74
B	$c(NH_3)$/mmol·L^{-1}	2.39	6.38	10.37

process factors. All experiments were performed in random order. The pH values were determined after 24 h of stirring for each synthesis (Table S1, SI).

The sacrificial polymer templates of the HBs were removed by calcination under synthetic air flow (50 mL·min^{-1}) at 600 °C for 10 h (heating rate 200 K·h^{-1}) to give the **MPSM1−15** (Table 2).

Preparation of Reversed Phase HPLC Column Materials. For the preparation of trimethoxy(octadecyl)silane (C_{18})-functionalized MPSMs as HPLC column packing material, an additional batch of porous polymer template was prepared and TEPA functionalized. Two different sol−gel process factor level combinations within the FCD design space were used to generate two types of HB particles with significantly different pore parameters. The synthesis was scaled up by a factor of 3.75. The prepared HB materials were calcinated at 600 °C for 10 h under synthetic air flow to yield the MPSMs (heating rate of 200 K·h^{-1}).

A total of 3 g of **MPSM** was rehydroxylated with 360 mL 3.7% HCl at 100 °C for 3 h under continuous stirring (mechanic stirrer, 300 rpm). After cooling to room temperature, the rehydroxylated MPSM were thoroughly washed three times with water and three times with ethanol. After drying the rehydroxylated MPSMs at 70 °C overnight, they were C_{18}-functionalized with trimethoxy(octadecyl)silane.

A total of 3 g of rehydroxylated **MPSM** was dispersed in 45 mL of toluene and 15 mL of trimethoxy(octadecyl)silane. The trimethoxy(octadecyl)silane was added in excess to provide complete functionalization of the available functional groups on the particle surface. As a catalyst, 0.3 mL of triethylamine was added. The mixture was stirred at 100 °C for 6 h (300 rpm, magnetic stirrer) and washed three times with toluene, ethanol, and methanol after cooling to room temperature. The **MPSM-C_{18}** was then dried at 70 °C overnight.

To test the **MPSM-C_{18}** for their applicability as the reversed HPLC phase, the particles were packed with acetone as slurry and MeOH/H_2O (85/15 vol %/vol %) as a pressure medium into 4.0 × 250 mm stainless steel columns.

Nitrogen Sorption Measurements. BELSORP MiniX (Microtrac Retsch GmbH, Haan, Germany) for nitrogen sorption measurements was used for the determination of specific surface area, pore size, and pore volume. The sample mass was 50 mg of the MPSMs. To eliminate possible physisorbed substances and to achieve a reproducible intermediate state, all particles were vacuum degassed at 300 °C for 3 h under a final vacuum of about 2 × 10^{-2} mbar.[39] The samples were pretreated using the BELSOPR VACII (Microtrac Retsch GmbH, Haan, Germany). The N_2 adsorption and desorption measurements were performed at 77 K. The BELMaster 7 software (7.3.2.0, Microtrac Retsch GmbH, Haan, Germany) was applied to perform the analysis of adsorption and desorption isotherms. Specific surface area was analyzed according to the Brunauer−Emmet−Teller method (BET)[40,41] in a relative pressure range of p/p_0 0.05−0.30.[42] Using the Barret−Joyner−Helenda method (BJH), the pore size distribution was determined from the desorption branch using the silica-BEL standard isotherm. The pore volume was determined from a single point adsorption at a p/p_0 of 0.95.

Scanning Electron Microscopy Images (SEM). To assess the surface morphology, particle size, and dispersity, SEM images were acquired using a Hitachi SU8030 (Hitachi High-Tech Europe GmbH, Germany). The size and dispersity from the SEM images were analyzed using a self-written MATLAB script. A minimum of 248 particles were measured. The d_{90}/d_{10} value indicates the width of the particle size distribution. A monodisperse distribution is reflected by a d_{90}/d_{10} value of ≤1.4.[43]

Experimental Design. The mathematical description of linear, nonlinear, and interaction effect terms[44,45] was enabled through systematic analysis using a face-centered central composite experimental design (FCD). A total of 15 MPSMs were synthesized. The center point (CP) experiment was replicated four times to determine reproducibility and system variance. To support model stability in the critical region of low molar ratios, three of the syntheses were conducted with $n(H_2O)/n(TEOS) = 8$. The systematic variation of the factor level setting allows the investigation of the effects of two factors and their possible synergistic interactions, $c(NH_3)$ and $n(H_2O)/n(TEOS)$. The factor levels for the low, intermediate, and high settings are given in Table 1. The model effect terms were analyzed using analysis of variance (ANOVA). A model or model term was considered statistically significant if its p-value was $p \leq 0.05$.

HPLC Analyses. The high-performance liquid chromatography (HPLC) was performed on an Agilent 1100 series system (Agilent Technologies, Waldbronn, Germany). The setup included a degasser, quaternary pump, autosampler, column oven, diode array detector, and a fluorescence

https://doi.org/10.1021/acsomega.3c03098
ACS Omega 2023, 8, 30273−30284

Table 2. Factor Level Settings and Their Corresponding Particle Properties Particle Size, Dispersity, Specific Surface Area, Pore Diameter, and Pore Volume (at $p/p_0 = 0.95$), as well as the Silica Content in the HBs Determined by TGA (See SI Figure S3)

	factor level settings		response variables					material property
	A $n(H_2O)/n(TEOS)$	B $n(NH_3)$	particle size		SSA	pore diameter PD	Pore volume V_p	SiO_2 in HB
	$mmol \cdot L^{-1}$	$mmol \cdot L^{-1}$	μm	$\frac{d_{90}}{d_{10}}$	$m^2 \cdot g^{-1}$	nm	$cm^3 \cdot g^{-1}$	%
p@TEPA			8.3	1.04	63.8	8.6	0.12	
MPSM1	4	17.1	0.5	1.31	[a]	[a]	[a]	0.1
MPSM2	74	17.1	5.8	1.18	443.7	8.3	0.92	19.7
MPSM3	4	74.1	2.5	1.32	771.6	3.2	0.63	2.7
MPSM4	74	74.1	7.7	1.14	163.8	14.8	0.35	31.2
MPSM5	39	45.6	7.0	1.09	291.6	9.3	0.51	23.0
MPSM6	4	45.6	1.3	1.32	[a]	[a]	[a]	0.4
MPSM7	74	45.6	7.4	1.13	170.9	12.1	0.32	30.1
MPSM8	39	17.1	4.8	1.18	568.6	4.8	0.73	13.0
MPSM9	39	74.1	7.8	1.14	167.8	14.4	0.35	28.6
MPSM10	39	45.6	7.8	1.13	209.3	9.9	0.36	26.7
MPSM11	39	45.6	6.9	1.25	222.9	9.6	0.39	25.9
MPSM12	39	45.6	7.4	1.15	233.8	9.9	0.41	25.9
MPSM13	8	45.6	2.4	1.37	674.7	3.7	0.68	2.7
MPSM14	8	17.1	1.3	1.22	[a]	[a]	[a]	0.2
MPSM15	8	74.1	4.2	1.19	559.8	5.4	0.84	7.9
p@TEPA-2			8.9	1.06	75.7	13.6	0.16	
MPSM-C_{18}-1	74	17.1	7.5	1.11	246.3	16.6	0.57	26.5
MPSM-C_{18}-2	39	45.6	7.9	1.10	186.4	20.8	0.44	28.2

[a]For the particles **MPSM1**, **MPSM6**, and **MPSM14**, no nitrogen adsorption analysis could be performed as the obtained amounts of MPSMs (<10 mg) were too poor. These samples were therefore only included in the model for particle size.

detector. The detector was chosen according to the separation application. The OpenLAB CDS (Rev. C.01.07 SR3, Agilent Technologies, Waldbronn, Germany) was used for instrument control, data acquisition, and automated data analysis.

For the protein separation, the protein mixture H2899 (ribonuclease A, cytochrome c, holo-transferrin and apomyoglobin) was dissolved in 90:10 eluent A (H_2O, 0.1% TFA) and eluent B (acetonitrile, 0.08% TFA). A total of 5 μL of the sample (1 $mg \cdot L^{-1}$ of each protein) was injected and measured at 30 °C. A gradient elution was performed with 25% B to 70% B within 40 min with a flow of 1.0 $mL \cdot min^{-1}$. The detection wavelength was 215 nm.

The separation of 11 D/L-amino acids (asparagine, glutamic acid, glycine, arginine, alanine, tyrosine, valine, norvaline, tryptophan, iso-leucine, and leucine) was performed by a linear gradient elution of phosphate buffer (25 mM, pH 7.2) with 0.75 vol % THF as eluent A and a mixture of methanol:acetonitrile:phosphate buffer (35/15/50 vol %) as eluent B. The gradient was 0% B to 100% B in 50 min with a flowrate of 1.0 $mL \cdot min^{-1}$. A total of 20 μL of sample (2.1 $\mu mol \cdot \mu L^{-1}$ of each amino acid) was injected and measured at 30 °C. Detection of the amino acids was performed through precolumn derivatization (90 s performed with the injector program) with OPA reagent with $\lambda_{excitation}$ = 330 nm and $\lambda_{emission}$ = 450 nm.

RESULTS AND DISCUSSION

The set of **HB1−15** particles, which was prepared by variation of the sol−gel process conditions according to a statistical experimental design (design of experiment) in the presence of a p@TEPA template, forms the basis for the investigations discussed here (Table 2, Figure 1b).[24] The sacrificial template was removed by calcination, and the final **MPSM1−15** was characterized by SEM and nitrogen adsorption measurements to determine their particle size, dispersity, specific surface area, pore diameter, and pore volume (Table 2).

Particle Size and Morphology. After calcination, the particle diameters of **MPSM1−15** varied widely within the range from 0.5 to 7.8 μm (Figure S4, SI). This is in contrast to the HBs, from which the MPSMs were derived. The size of the HBs remained constant when the sol−gel conditions were varied.[29] Interestingly, for each factor level setting, a narrow size distribution with d_{90}/d_{10} values below 1.4 is observed (Figure 3, Table 2, and Figure S4, SI).

The effect of the two process factors on the size distribution of the **MPSM1−15** can be accurately described by a statistically highly significant model ($p < 0.0001$) (Table 3).

The high predictive power ($R^2_{predicted}$ = 0.9470) of the model allows prediction of the expected particle size as a function of the statistically significant factor effects of the $n(H_2O)/n(TEOS)$ ratio, its nonlinear effect term, and the comparatively lower effect of $c(NH_3)$ (Figure 4). Model eq 1 gives the relation between the statistically significant effect and interaction effect terms on the particle size in terms of the coded equation:

$$\text{particle size}/\mu m = 6.96 + 2.69A + 1.21B - 2.71A^2 \quad (1)$$

When the ratio of water to TEOS is increased, the resulting MPSMs undergo less shrinkage and thus stay large after calcination. However, larger amounts of water attenuate this effect within the examined experimental design space. This leveling behavior is described by the negative A^2 effect term. This is a result of the hydrolysis and condensation rates, which exceed the rate of SNP incorporation into the porous template.

https://doi.org/10.1021/acsomega.3c03098
ACS Omega 2023, 8, 30273−30284

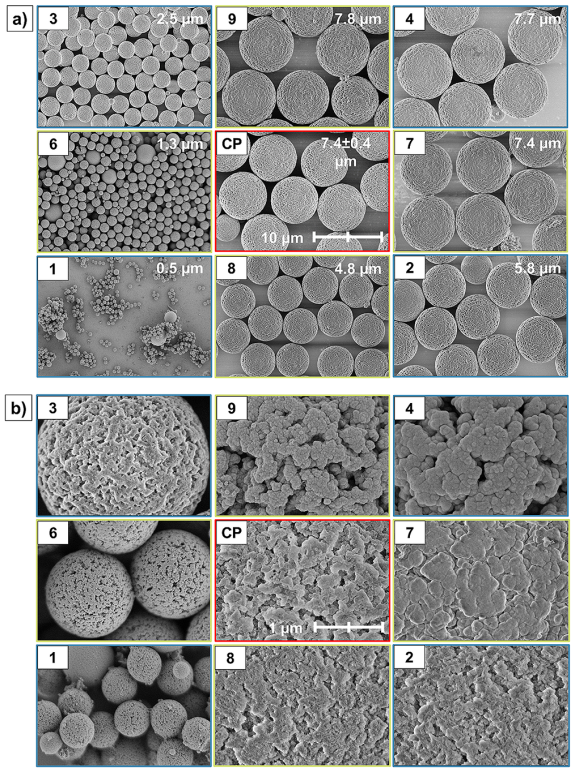


Figure 3. SEM images of the MPSMs according to the face-centered central-composite design. (a) MPSMs in 5000× magnification with the particle size median given. For the center points, the size ± standard deviation is indicated. The scale bar is the same for all SEM images in (a) and marks 10 μm. (b) MPSMs in 50,000× magnification. For CPs, **MPSM5** is shown. Factorial points are highlighted in blue, axial points in green, and CPs in red. The scale bar is the same for all SEM images in (b) and marks 1 μm.

Consequently, the silica nanoparticles become too large to diffuse into the pores and thus remain in the continuous phase where they form nonporous secondary particles in the continuous phase (see SI Figure S5) and do not enter the porous template. They are removed by filtration upon isolating the hybrid beads. Thus, less silica is incorporated into the templates, which leads to smaller silica particles.[29]

For the ammonia concentration, a clear trend of size increase can be observed. When the initial ammonia concentration is increased at the start of the synthesis, larger MPSMs result after calcination. On the other hand, at low initial ammonia concentration, the SNP production is inefficient. This results in the incorporation of small amounts of SNPs into the polymer beads. After calcination, the remaining MPSMs are much smaller than the applied templates. This behavior can be seen clearly in Figure 4a. For the same molar ratio of water-to-TEOS, the MPSM size increases when the ammonia concentration is increased. This increase varies between 2 and 3 μm. By applying a low initial ammonia concentration at a low level of $n(H_2O)/n(TEOS)$, MPSMs as small as 0.5 μm (**MPSM1**) can be prepared, whereas at a high ammonia concentration, the particle size increases to 2.5 μm (**MPSM3**) at the same $n(H_2O)/n(TEOS)$ ratio. The slope of the MPSM size increases with increasing ammonia concentration within the investigated design space and is on average + 0.04 $\mu m/mmol \cdot L^{-1}$.

Table 3. Excerpt from the Analysis of Variance (ANOVA) Tables with p-Values for the Response Surface Models of the Target Responses Particle Size, Pore Diameter (PD), Specific Surface Area (SSA), and Pore Volume (V_p) and Shrinkage Compared to the HB, as well as Their Fit Statistics[a]

response	particle size	PD	SSA	V_p
	μm	nm	$m^2 \cdot g^{-1}$	$cm^3 \cdot g^{-1}$
model	<0.0001	<0.0001	<0.0001	0.0068
$A = n(H_2O)/n(TEOS)$	<0.0001	<0.0001	<0.0001	0.0072
$B = c(NH_3)$	<0.0001	<0.0001	0.0001	0.0029
AB	n.s.	0.0018	n.s.	n.s.
A^2	<0.0001	<0.0001	0.0002	0.0420
B^2	n.s.	n.s.	0.0041	0.0181
A^2B		0.0001		
lack of fit	0.3067 (n.s.)	0.5145 (n.s.)	0.2588 (n.s.)	0.1459 (n.s.)
R^2	0.9727	0.9968	0.9697	0.8373
$R^2_{adjusted}$	0.9652	0.9941	0.9523	0.7443
$R^2_{predicted}$	0.9470	n.a.	0.8991	0.3806

[a]Complete ANOVA Tables for each model are given in Tables S2–S5, SI.

The final size of the MPSMs is determined by the size and number of incorporated SNPs. Smaller SNPs have a higher volume-to-surface ratio, which results in OH-bonding sites between particles.[46,47] Under the elevated temperature during template removal (600 °C), these silanol groups undergo condensation and form Si–O–Si bonds, which results in shrinkage.[48] This reduces the total surface and thus the total free energy.[49] The typical necking was observed (see Figure S6, SI). As the calcination conditions were similar for all samples, here, the scaling law applies. The larger SNPs require more time at the same temperature to reach a similar sintering degree as samples consisting of smaller SNPs.[50,51] Hence, the larger the SNPs in the HB are, the smaller is the effect of interparticle condensation and thus shrinkage. Moreover, in this polymer/silica system, the size of the SNPs and the amount of incorporated silica correlates linearly and in dependence on the sol–gel process conditions.[29] The smaller the SNPs, the less silica is incorporated. This results in even more pronounced shrinkage and explains the strong decrease in MPSM size in the lower region of the design space, where the factor level settings are low for both factors. Under these conditions, sub-2 μm particles were obtained (**MPSM1, 6, 14**).

Figure 3a,b displays the morphology of the prepared **MPSM1–12**. The SEM images of the morphology of the particles **MPSM13–15** are given in Figure S7 (SI). All MPSMs are formed by interconnected SNPs, which generate pores in the silica network. During template removal via calcination, the interconnected SNPs underwent grain growth,[51] which is especially pronounced for the settings with less silica incorporation and small SNPs (<50 nm,[29,52] e.g., **MPSM3** Figure 3b). However, surface appearance changes when different regions in the design space are explored. When both the stoichiometric ratio of water and the ammonia concentration are increased, the larger (≥50 nm) and more spherical SNPs are obtained. With increasing ammonia

https://doi.org/10.1021/acsomega.3c03098
ACS Omega 2023, 8, 30273–30284

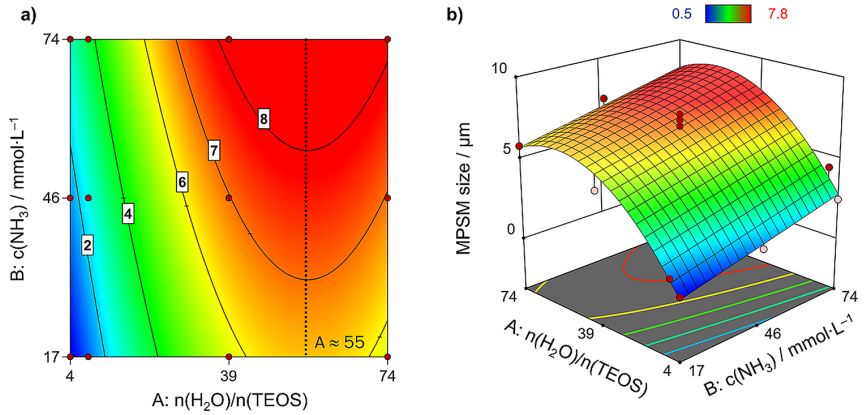


Figure 4. (a) Contour plot with contour lines for different particle sizes in dependence of the process factor levels and (b) 3D response surface plot of the augmented FCD model regarding the MPSM size. Red areas indicate large particles. Blue areas indicate small particles.

concentration, the interconnection of SNPs is less pronounced and single nanoparticulate structures are visible (**MPSM4, MPSM9** Figure 3b). The size of the SNPs formed during the sol–gel process increases with an increase in $n(H_2O)/n(TEOS)$ and $c(NH_3)$ via aggregation within the pores of the polymer template and aggregation and monomer addition growth of the SNPs at the outer surface of the template.[29]

Effect of Incorporated Silica Content on MPSMs Pore Volume. As after calcination only the silica part of the HB remains (see Figure 1), the silica content in the HBs is seen as a critical parameter affecting the properties of the final MPSMs. The pore size, specific surface area, and the pore volume of the MPSMs were determined by nitrogen adsorption measurements at 77 K (Table 2). The pore volumes of the prepared MPSMs were all within the range from 0.32 to 0.92 $cm^3 \cdot g^{-1}$. The smallest pore volumes were observed, when the highest amounts of silica were incorporated into the preceding HB. The statistically significant effects of the process conditions on the pore volume V_p of the MPSMs were identified and were used to derive a statistically significant response surface model. With R^2 = 0.8373 and $R^2_{adjusted}$ = 0.7443 this model describes the data well. However, the predictive power of the model is comparatively low with $R^2_{predicted}$ = 0.3806, which can be attributed to the different types of pores, which are formed during calcination in dependence on the amount of incorporated silica (Figure 5).

The pore volume of the MPSMs in dependence on the determined silica content of the preceding HBs, from which the MPSMs were derived by calcination, is given in Figure 5 and can be fitted by a second order polynomial function with $R^2_{adjusted}$ = 0.7251. For high silica contents in the HBs, the pore volume of the MPSMs was found to be the lowest and to increase rapidly with decreasing silica contents. For silica contents lower than approximately 11 wt %, the pore volume decreases again (Figure 5).

Depending on the amount and the size of the SNPs incorporated into the sacrificial template, the morphology of the resulting MPSMs also changes.

In Figure 6a, the pore formation in the MPSM after calcination for reaction regime III is displayed. Reaction regime III is characterized by high rates of hydrolysis and condensation. This results in an effective incorporation of silica into the template pores and a complete closure of the

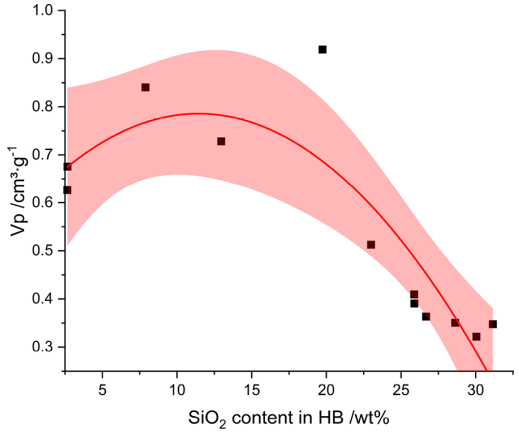


Figure 5. Second order polynomial fit of V_p of the MPSMs and the silica content of the hybrid material. Shaded areas indicate 95% confidence interval. $R^2_{adjusted}$ = 0.7251.

template pores. In this reaction regime, the largest SNPs are incorporated into the template pores and deposited on the surface of the template. When the template is removed by thermal degradation during calcination, a negative imprint of the template pores forms from this. The former polymer walls are now pores of the MPSM, and the new silica pore walls are formed from the original pores of the polymer template filled with silica (Figure 6a).

At lower hydrolysis and condensation rates (reaction regime II), less SiO_2 is incorporated into the template pores (Figure 6b). Thus, the polymer walls are only covered with a thin silica layer consisting of smaller SNPs and the template pores are not completely filled with silica. Compared to the thickness of the walls of the porous polymer matrix, the silica layers are quite thin, only a few nanometers thick, as the SNPs which diffused into the polymer matrix are small (~10–20 nm). During calcination, not only is the template removed but condensation of neighboring SNPs also occurs. However, because only thin silica layers are formed, these layers are too far apart from each other to condense into a closed plug and cannot completely fill the former template pores (Figure 6b). Thus, in addition to the pores formed by removing the polymer walls, also pores

https://doi.org/10.1021/acsomega.3c03098
ACS Omega 2023, 8, 30273–30284

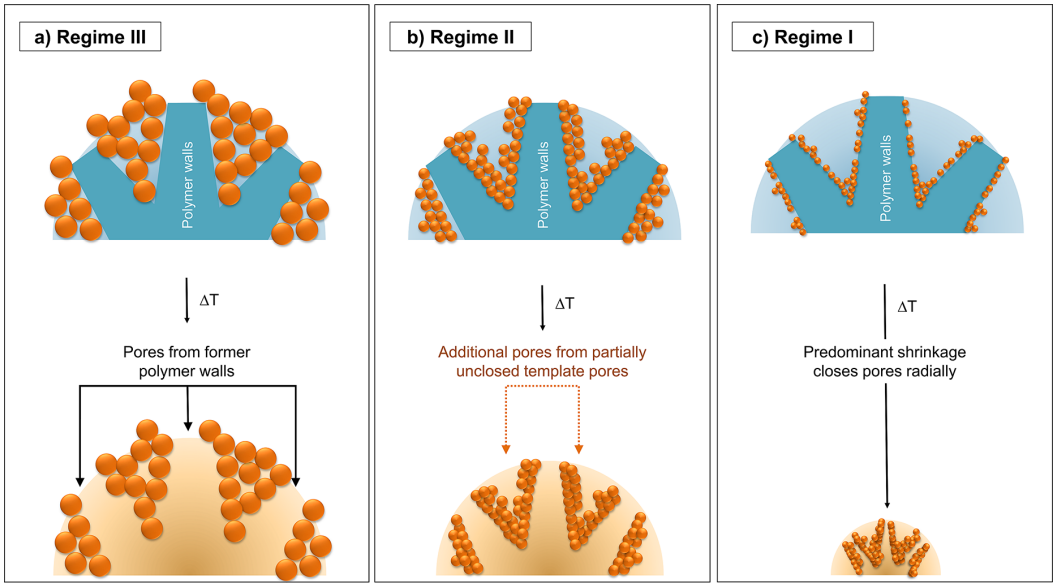


Figure 6. Scheme of pore formation after template removal by calcination for three degrees of silica deposition in the hybrid material according to the defined reaction regimes.[29]

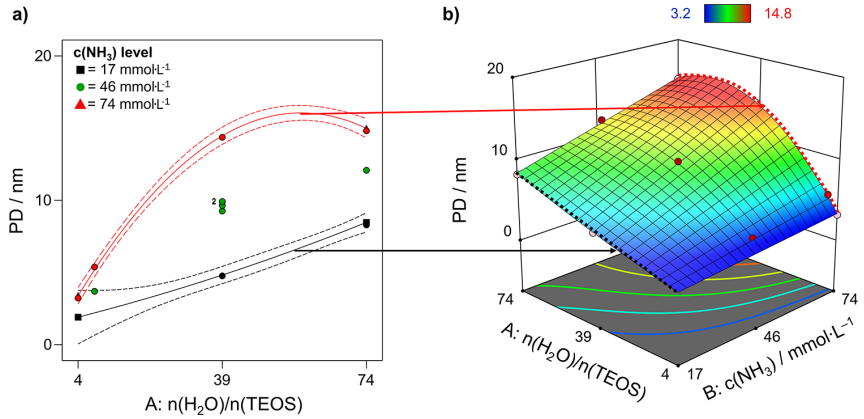


Figure 7. (a) Interaction plot: the black line indicates the effect of higher water levels at low ammonia concentrations, while the red line displays the effect of the water-to-TEOS ratio at high levels of ammonia. Dashed lines indicate the 95% confidence intervals. (b) 3D response surface plot: red areas correspond to large pore diameters, whereas blue areas indicate small pores. The dashed black and red lines highlight projected the surface edges represented in the interaction plot (a).

already present in the polymer template are present in the calcinated MPSM. This increases the total porosity and thus the overall pore volume of the MPSM in reaction regime II (Figures 5 and 6b). In the case of samples with a rather low silica content and very small SNPs incorporated into the polymer template (Figure 6c, corresponding to reaction regime I with the lowest hydrolysis and condensation rates), on the other hand, shrinkage by condensation during calcination is very pronounced. This leads to correspondingly small MPSMs with partial closure of the MPSM pores due to the sintering of neighboring SNPs during calcination (Figure 6c). Therefore, a reduction of the pore volume at silica contents below 11 wt % is observed (Figure 5). This process progresses while some porosity is retained, which is clearly visible for e.g. **MPSM1** in Figure 3b. However, as the small SNPs are sintered to a greater extent than larger SNPs, the grain growth progresses further,[50] leading to closure of pores. Therefore, for samples with low silica content in the HBs, the pore volume is comparatively smaller (Figure 6c). This change in mechanism of pore formation during calcination in dependence on the silica content in the preceding HBs restricts the predictive power of the pore volume model. The response surface methodology assumes that the system behavior follows the same underlying mechanism throughout the complete studied design space.

Pore Size. The pore sizes of **MPSM2**−**5**, **7**−**13**, and **15** varied between 3.2 and 14.8 nm and show mostly broad pore size distributions (see Figure S8, SI). The distribution is narrower for MPSMs with pores below 8.3 nm in the median (**MPSM2**, **3**, **8**, **13**, and **15**). These particles show a bimodal pore size distribution at lower pore sizes, with an increasing

https://doi.org/10.1021/acsomega.3c03098
ACS Omega 2023, 8, 30273−30284

amount of micropores with decreasing mean pore size. **MPSM2**, **3**, **8**, **13**, and **15** also are the smallest MPSMs in this design space and underwent the most shrinkage (>30% decrease in diameter compared to HB). From the FCD, a clear dependence of the mean pore size on the effect of both process factors $n(H_2O)/n(TEOS)$ and $c(NH_3)$ was observed. However, the effect of the $n(H_2O)/n(TEOS)$ is nonlinear and the factor effects are synergistic as the two-factor interaction effect term AB and the higher-order interaction effect term A^2B are both statistically significant. This means that each of the process factors strongly depends on the factor level setting of the other factor, and neither of the two can be separately and independently be discussed. As there is one sample (**MPSM13**) with a leverage value of one, the $R^2_{predicted}$ value cannot be calculated. This sample is located in the lower area of the design space. Moreover, the silica deposition for three samples in this region (**MPSM1**, **MPSM14**, and **MPSM6**) was too low to characterize them by means of nitrogen adsorption after calcination. The position of **MPSM13** in the design space is quite isolated, meaning that this factor level combination strongly influences the model.[35] However, as the $R^2_{adjusted} = 0.9941$ indicates that an adequate number of terms was used in the mathematical model (meaning that the data were not overfitted), the unusual and hard to physically interpret factor effect term A^2B was included in the model. Moreover, exclusion of the A^2B term leads to a prediction of negative pores size values, which does not make sense and illustrates that the A^2B term is actually real and required for an adequate model. With the A^2B factor interaction term, the predicted pore size of **MPSM1** $n(H_2O)/n(TEOS)$ and $c(NH_3)$ at the low factor setting is 1.9 nm, which is a reasonable prediction, since the porous nature of the particles is clearly visible in Figure 3b. The relative importance of the factors is evident from eq 2, which is the model equation in terms of coded factors:

$$PD/nm = 9.64 + 4.54A + 4.82B + 1.26AB - 2.46A^2 - 2.83A^2B \quad (2)$$

The corresponding interaction plot (Figure 7a) illustrates the relation between the process factor effects $n(H_2O)/n(TEOS)$ and $c(NH_3)$ and the pore size. With increase in ammonia concentration, the pore sizes generally become larger (Figure 7b), but the steepness of the increase is dependent on the $n(H_2O)/n(TEOS)$ level.

Under basic reaction conditions, the hydrolysis rate is slower than the condensation rate and thus, it is the rate determining reaction. However, the reaction rates are also dependent on the water-to-TEOS ratio. The addition of water promotes the formation of silanol groups favoring the hydrolysis.[53] At low ammonia concentrations, the reaction pH for **MPSM1**, **2**, **8**, and **14** lies at 10.5 ± 0.0. Here, the effect of $n(H_2O)/n(TEOS)$ is linear and the pore size increases linearly with an increase in the water-to-TEOS ratio. If the ammonia concentration is increased, the effect of the water-to-TEOS ratio changes gradually from linear to nonlinear. For high ammonia concentrations the pH value is 10.9 ± 0.1 (**MPSM3**, **4**, **9**, **15**, Table S1, SI). At high water-to-TEOS ratios and higher ammonia concentrations, the dependence of the pore size on the $n(H_2O)/n(TEOS)$ ratio turns nonlinear. In this case, the pore size first increases with increasing water quantity, but from a certain point on, a further increase in pore size becomes the smaller the higher the water quantity is (Figure 7a, red line). A similar dependence on the process factor settings was observed for the SNP size, which increases in size with increasing ammonia concentration and also exhibit a nonlinear behavior with increasing water-to-TEOS ratios.[29,54,55] A clearly linear relation between the size of SNPs incorporated in the porous polymeric template, forming the HBs, and the resulting pore size of the corresponding MPSMs after calcination was observed (see Figure S9, SI).

Thus, the pore size of the MPSM is not only dependent on the pore size of the template[23] but also on the size of the SNPs incorporated into the porous network of the polymeric template. As a result, the pore size of the MPSMs can be varied by adjusting the sol−gel process conditions using the process factors $n(H_2O)/n(TEOS)$ and $c(NH_3)$.

Specific Surface Area (SSA). The specific surface area is an important material characteristic when it comes to separation processes dependent on surface interactions between the analyte and stationary phase. The prepared MPSMs showed a range of specific surface area from 164 to 772 $m^2 \cdot g^{-1}$, where the lowest SSA occurred at the highest factor level settings for both process factors (the high | high factorial experiment **MPSM4**) and the highest SSA was obtained at the lowest water to precursor ratio and ammonia concentration (the low | low factorial experiment **MPSM3**).

The SSAs of the prepared MPSMs are statistically significantly affected by both process factors $n(H_2O)/n(TEOS)$ ratio and $c(NH_3)$, each in a nonlinear manner (significant effect terms A^2 and B^2). The relative process factor strengths are given in model eq 3 in coded terms:

$$SSA/m^2 \cdot g^{-1} = 237.67 - 291.18A - 172.77B + 229.98A^2 + 126.28B^2 \quad (3)$$

Both factors affect the SSA in a similar direction. The factor effect strength of A on the SSA is by far stronger than the factor effect strength B, as can be seen by the model term coefficients in eq 3. When the factor level of either factor is increased, the SSA decreases (Figure 8). However, the degree of decrease levels off with a further increase in factor level settings. This leveling effect, represented by the second order

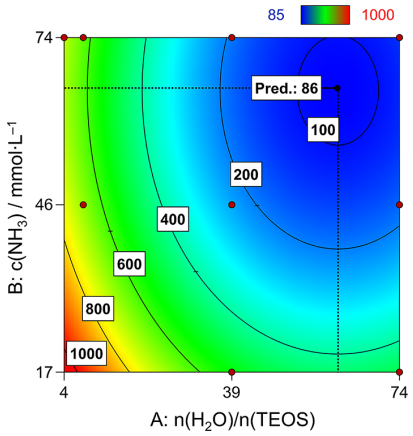


Figure 8. Contour plot for SSA in dependence of $c(NH_3)$ and $n(H_2O)/n(TEOS)$. Contour lines for multiple SSAs are given. Large SSAs are displayed in red. Small SSAs are displayed in blue. Dashed lines indicate the position of predicted minimum of the SSA.

https://doi.org/10.1021/acsomega.3c03098
ACS Omega 2023, 8, 30273−30284

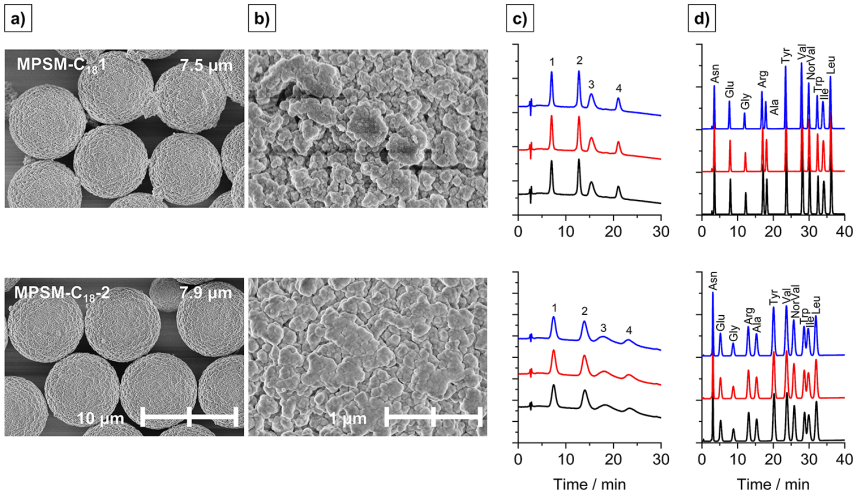


Figure 9. SEM images of MPSMs as packing materials prior to rehydroxylation and C_{18}-functionalization with (a) 5000× magnification and (b) 50,000× magnification. (c) Chromatograms for the separation of the protein mixture and (d) chromatograms for the amino acid separations for both columns.

effect terms (eq 3), is more pronounced upon changing $n(H_2O)/n(TEOS)$ (Figure 8). The nonlinear behavior for both factors leads to the formation of a region in which a global minimum of SSA is observed within the investigated experimental design space at $n(H_2O)/n(TEOS) \approx 61$ and at $c(NH_3) \approx 65$ mmol·L^{-1}. On the other hand, large SSAs were achieved when the starting conditions of the sol–gel process were selected in the low factor level regions of the design space. With $R^2_{predicted} = 0.8991$, the dependence of SSA on the stoichiometric ratio of water-to-precursor and the ammonia concentration can be predicted with good accuracy.

HPLC Separations of Biomolecules. In order to yield enough MPSM material to pack an HPLC column, a new batch of polymeric template was prepared and TEPA functionalized. This template exhibited a slightly higher pore volume, larger specific surface area, and larger pore sizes than the template used in the statistical design (see Table 2). This reflects the low extent of common cause variability of the hard template preparation procedure due to scaling up the process. From this, two batches of MPSMs were prepared (see **MPSM-C_{18}-1** Figure 9a and **MPSM-C_{18}-2** Figure 9b) with process factor level settings corresponding to **MPSM2** and the **CP**s, respectively. Thus, although the sol–gel parameters were the same for **MPSM-C_{18}-1** as **MPSM2** and for **MPSM-C_{18}-2** as the **CP**s the materials differ slightly. This is a result from changes in the template characteristics and scale up.[23] Interestingly, the template with the higher pore volume, larger pores, and higher SSA resulted in MPSMs with lower pore volumes and lower SSA but enlarged pore sizes. The properties of **MPSM-C_{18}-1** and **MPSM-C_{18}-2** were also determined by inverse size exclusion chromatography, which exhibited similar trends as the nitrogen sorption characteristics (see Table S6, SI). **MPSM-C_{18}-1** exhibited smaller pores but a higher SSA than **MPSM-C_{18}-2.** This trend fits well with the observations made in the statistical evaluation of the process factor effects $n(H_2O)/n(TEOS)$ and $c(NH_3)$. This offers more space within the template pores for aggregation of *in situ* formed highly reactive small silica species und consequently larger SNPs.[23] In combination with the higher template pore volume, more and larger SNPs were incorporated into the template. The sizes of the incorporated SNPs were slightly larger with 25 (**MPSM-C_{18}-1**, **MPSM2**: 20 nm) and 48 nm (**MPSM-C_{18}-2**, **CPs**: 43 nm).

The columns **MPSM-C_{18}-1** and **MPSM-C_{18}-2** were tested for their separation capability for proteins and amino acids, and the corresponding chromatograms are shown in Figure 9c,d. Both C_{18}-functionalized column materials allowed the separation of all four proteins. The retention times were thereby ribonuclease-A < cytochrome c < holo-transferrin < apomyoglobin. This was consistent for both columns, and the reproducibility of the measurement was high (Figure 9c). However, **MPSM-C_{18}-1** exhibited sharper peaks than **MPSM-C_{18}-2**; the elution of the last peak was earlier, and overall, the resolution was better. All peaks were baseline separated using column **MPSM-C_{18}-1** ($R \geq 2.0$), while the resolution between cytochrome c and holo-transferrin was $R_{2-3} = 1.92$. For **MPSM-C_{18}-2**, the resolutions were reduced with $R \geq 1.25$ due to peak broadening. This can be a result of the larger particle size and increased diffusion pathways with larger pores.

The separation of amino acids was successful using both columns. Both columns exhibited a good separation performance. Also, here the peaks of **MPSM-C_{18}-2** were generally broader and less intense (Figure 9d). Interestingly, the elution of the last amino acid leucin was earlier for **MPSM-C_{18}-2** than **MPSM-C_{18}-1**, which can be attributed to the reduced surface area and thus less retention of the amino acids. The available surface area corresponds directly to the degree of functionalization (see SI Figure S9) and thus a better retention. However, the separation of arginine and alanine was better using **MPSM-C_{18}-2** than **MPSM-C_{18}-1**. Column **MPSM-C_{18}-1** was able to separate all amino acids in the mixture with a resolution of $R \geq 2.0$ ($R_{ARG-ALA} = 2.0$). Using **MPSM-C_{18}-2** all peaks were separated with a good resolution (>1.5) except for the pair of TRP and ILE ($R = 1.0$). For **MPSM-C_{18}-2**, the analysis time was reduced by 11% compared to **MPSM-C_{18}-1**; however, the separation efficiency was decreased. This is a result of the smaller surface area compared to **MPSM-C_{18}-1**.

https://doi.org/10.1021/acsomega.3c03098
ACS Omega 2023, 8, 30273−30284

While for the separation of proteins the separation time was increased when using column **MPSM-C_{18}-2**, the time required for the separation of the amino acids was less when using column **MPSM-C_{18}-2.** This can be attributed to the different types of separation. The separation of the proteins is mainly determined by size exclusion. Here, the larger pores allow better mass transfer and increase the retention of proteins with a higher radius of gyration. For the separation of the amino acids, the smaller surface area of **MPSM-C_{18}-2** reduces the retention times but also the separation efficiency of the materials. Here, **MPSM-C_{18}-1** shows superior separation efficiency allowing a baseline separation of all 11 amino acids.

CONCLUSIONS

In this study, it was shown that the hard-template approach can be used as a platform for fabricating a wide range of fully porous monodisperse silica particles. The silica content of the preceding HBs is a critical parameter for the final properties of the silica particles. Thus, the particle size, pore volume, pore size distribution, and morphology of the silica particles are determined by the size and number of incorporated SNPs. The installation of the SNPs into the template network is the result of the interaction of the template and the sol−gel process. In this design space, the same template was applied. As a result, properties of the MPSMs can be varied by adjusting the sol−gel process conditions using the process factors $n(H_2O)/n(TEOS)$ and $c(NH_3)$.

The tailoring of the property profile was demonstrated with MPSMs. These were successfully applied as column materials for the separation of amino acids and proteins by HPLC.

ASSOCIATED CONTENT

Data Availability Statement

Data will be made available on request.

Supporting Information

The Supporting Information is available free of charge at https://pubs.acs.org/doi/10.1021/acsomega.3c03098.

Materials and methods for the preparation of polystyrene seeds and hybrid beads; ANOVA tables for the statistical analysis of the face centered design of experiments data for the various investigated response variables particle size, specific surface area (SSA), pore diameter (PD), and pore volume (V_p); SEM images of polystyrene seed particles and additional MPSMs particles **13**−**15**; graphs displaying the particle size distribution of various particle types prepared in the study including secondary particles removed from the filtrate; thermogravimetric data for the characterization of the particles subjected to calcination procedure and template removal of template polymer; figure displaying the neck formation between two silica nanoparticles after calcination; linear regression of pore size distribution and the size of SNPs incorporated into the polymeric template; inverse size exclusion chromatography characterization of columns MPSM-C18-1 and MPSM-C18-2 (PDF)

AUTHOR INFORMATION

Corresponding Author

Andreas Kandelbauer − *Process Analysis & Technology, Reutlingen Research Institute, Reutlingen University, Reutlingen 72762, Germany; Institute of Wood Technology and Renewable Materials, Department of Material Sciences and Process Engineering (MAP), University of Natural Resources and Life Sciences, Vienna 1180, Austria;* orcid.org/0000-0001-9786-964X; Phone: +49-(0)7121-271-2009; Email: andreas.kandelbauer@reutlingen-university.de

Authors

Julia C. Steinbach − *Process Analysis & Technology, Reutlingen Research Institute, Reutlingen University, Reutlingen 72762, Germany; Institute of Inorganic Chemistry, University of Tübingen, Tübingen 72076, Germany;* orcid.org/0000-0001-5833-460X

Fabio Fait − *Process Analysis & Technology, Reutlingen Research Institute, Reutlingen University, Reutlingen 72762, Germany; Institute of Inorganic Chemistry, University of Tübingen, Tübingen 72076, Germany*

Hermann A. Mayer − *Institute of Inorganic Chemistry, University of Tübingen, Tübingen 72076, Germany;* orcid.org/0000-0002-8263-4255

Complete contact information is available at: https://pubs.acs.org/10.1021/acsomega.3c03098

Author Contributions

Conceptualization was done by A.K. and H.A.M.; methodology was developed by J.C.S., F.F., H.A.M., and A.K.; formal analysis was done by J.C.S.; investigation was conducted by J.C.S. and F.F.; resource gathering was performed by H.A.M. and A.K.; data curation was done by J.C.S.; writing—original draft preparation was done by J.C.S.; writing—review and editing was done by F.F., H.A.M., and A.K.; visualization was carried out by J.C.S.; supervision was done by H.A.M. and A.K.; project administration was done by H.A.M. and A.K.; funding acquisition was done by A.K. All authors have read and agreed to the published version of the manuscript.

Notes

The authors declare no competing financial interest.

ACKNOWLEDGMENTS

This research was funded the by Bundesministerium für Bildung und Forschung (BMBF, grant number 13FH647IX6). The article processing charge was funded by the Baden-Württemberg Ministry of Science, Research and Arts and by Reutlingen University in the funding program Open Access Publishing. Furthermore, we would like to thank our cooperation partner Dr. Maisch GmbH for their support in packing the columns. We thank Elke Nadler for contributing the SEM measurements.

REFERENCES

(1) Giraldo, L. F.; López, B. L.; Pérez, L.; Urrego, S.; Sierra, L.; Mesa, M. Mesoporous Silica Applications. *Macromol. Symp.* **2007**, *258*, 129−141.

(2) Hartmann, M. Ordered Mesoporous Materials for Bioadsorption and Biocatalysis. *Chem. Mater.* **2005**, *17*, 4577−4593.

(3) Slowing, I. I.; Trewyn, B. G.; Giri, S.; Lin, V. S.-Y. Mesoporous Silica Nanoparticles for Drug Delivery and Biosensing Applications. *Adv. Funct. Mater.* **2007**, *17*, 1225−1236.

(4) Manzano, M.; Vallet-Regí, M. Mesoporous Silica Nanoparticles for Drug Delivery. *Adv. Funct. Mater.* **2020**, *30*, 1902634.

(5) Siavashani, A. Z.; Nazarpak, M. H.; Bakhsh, F. F.; Toliyat, T.; Solati-Hashjin, M. Preparation of Mesoporous Silica Nanoparticles for Insulin Drug Delivery. *Adv. Mater. Res.* **2013**, *829*, 251−257.

(6) Dohare, A.; Sudhakar, S.; Brodbeck, B.; Mukherjee, A.; Brecht, M.; Kandelbauer, A.; Schäffer, E.; Mayer, H. A. Anisotropic and Amphiphilic Mesoporous Core-Shell Silica Microparticles Provide Chemically Selective Environments for Simultaneous Delivery of Curcumin and Quercetin. *Langmuir* **2021**, *37*, 13460−13470.
(7) Cheong, W. J. Porous Silica Particles As Chromatographic Separation Media: A Review. *Bull. Korean Chem. Soc.* **2014**, *35*, 3465−3474.
(8) Unsal, E.; Elmas, B.; Çamlı, S. T.; Tuncel, M.; Şenel, S.; Tuncel, A. Monodisperse-porous poly(styrene-co-divinylbenzene) beads providing high column efficiency in reversed phase HPLC. *J. Appl. Polym. Sci.* **2005**, *95*, 1430−1438.
(9) Chen, J.; Zhu, L.; Ren, L.; Teng, C.; Wang, Y.; Jiang, B.; He, J. Fabrication of Monodisperse Porous Silica Microspheres with a Tunable Particle Size and Pore Size for Protein Separation. *ACS Appl. Bio Mater.* **2018**, *1*, 604−612.
(10) Galarneau, A.; Iapichella, J.; Bonhomme, K.; Di Renzo, F.; Kooyman, P.; Terasaki, O.; Fajula, F. Controlling the Morphology of Mesostructured Silicas by Pseudomorphic Transformation: a Route Towards Applications. *Adv. Funct. Mater.* **2006**, *16*, 1657−1667.
(11) Hayes, R.; Ahmed, A.; Edge, T.; Zhang, H. Core−shell particles: Preparation, fundamentals and applications in high performance liquid chromatography. *J. Chromatogr. A* **2014**, *1357*, 36−52.
(12) Unger, K. K.; Skudas, R.; Schulte, M. M. Particle packed columns and monolithic columns in high-performance liquid chromatography-comparison and critical appraisal. *J. Chromatogr. A* **2008**, *1184*, 393−415.
(13) Makarov, A.; LoBrutto, R.; Karpinski, P. Effect of pressure on secondary structure of proteins under ultra high pressure liquid chromatographic conditions. *J. Chromatogr. A* **2013**, *1318*, 112−121.
(14) Yuan, Z.-Y.; Su, B.-L. Insights into hierarchically meso−macroporous structured materials. *J. Mater. Chem.* **2006**, *16*, 663−677.
(15) Bao, Y.; Shi, C.; Wang, T.; Li, X.; Ma, J. Recent progress in hollow silica: Template synthesis, morphologies and applications. *Microporous Mesoporous Mater.* **2016**, *227*, 121−136.
(16) Deng, Y.; Wei, J.; Sun, Z.; Zhao, D. Large-pore ordered mesoporous materials templated from non-Pluronic amphiphilic block copolymers. *Chem. Soc. Rev.* **2013**, *42*, 4054−4070.
(17) Singh, L. P.; Bhattacharyya, S. K.; Kumar, R.; Mishra, G.; Sharma, U.; Singh, G.; Ahalawat, S. Sol-Gel processing of silica nanoparticles and their applications. *Adv. Colloid Interface Sci.* **2014**, *214*, 17−37.
(18) Galabova, B. B. Mesoporous silica nanoparticles: Synthesis, functionalization, drug loading and release - A review. *Trop. J. Pharm. Res.* **2022**, *20*, 1091−1100.
(19) Shiba, K.; Shimura, N.; Ogawa, M. Mesoporous silica spherical particles. *J. Nanosci. Nanotechnol.* **2013**, *13*, 2483−2494.
(20) He, J.; Yang, C.; Xiong, X.; Jiang, B. Preparation and characterization of monodisperse porous silica microspheres with controllable morphology and structure. *J. Polym. Sci., Part A: Polym. Chem.* **2012**, *50*, 2889−2897.
(21) Xia, H.; Wan, G.; Yang, F.; Wang, J.; Bai, Q. Preparation of monodisperse large-porous silica microspheres with polymer microspheres as the templates for protein separation. *Mater. Lett.* **2016**, *180*, 19−22.
(22) Bai, J.; Zhu, Q.; Tang, C.; Liu, J.; Yi, Y.; Bai, Q. Synthesis and application of 5 μm monodisperse porous silica microspheres with controllable pore size using polymeric microspheres as templates for the separation of small solutes and proteins by high-performance liquid chromatography. *J. Chromatogr. A* **2022**, *1675*, No. 463165.
(23) Fait, F.; Steinbach, J. C.; Kandelbauer, A.; Mayer, H. A. Impact of porosity and surface functionalization of hard templates on the preparation of mesoporous silica microspheres. *Microporous. Mesoporous. Mater.* **2023**, *351*, No. 112482.
(24) Steinbach, J. C.; Fait, F.; Wagner, S.; Wagner, A.; Brecht, M.; Mayer, H. A.; Kandelbauer, A. Rational Design of Pore Parameters in Monodisperse Porous Poly(glycidyl methacrylate-co-ethylene glycol dimethacrylate) Particles Based on Response Surface Methodology. *Polymer* **2022**, *14*, 382.
(25) Wu, S.-H.; Mou, C.-Y.; Lin, H.-P. Synthesis of mesoporous silica nanoparticles. *Chem. Soc. Rev.* **2013**, *42*, 3862−3875.
(26) Yiding, L.; James, G.; Yadong, Y. Templated synthesis of nanostructured materials. *Chem. Soc. Rev.* **2013**, *42*, 2610−2653.
(27) Caruso, R. A. Nanocasting and Nanocoating. In *Colloid Chemistry I*; Springer, Berlin, Heidelberg, 2003; pp. 91−118, DOI: 10.1007/3-540-36408-0_4.
(28) Petkovich, N. D.; Stein, A. Controlling macro- and mesostructures with hierarchical porosity through combined hard and soft templating. *Chem. Soc. Rev.* **2013**, *42*, 3721−3739.
(29) Steinbach, J. C.; Fait, F.; Mayer, H. A.; Kandelbauer, A. Monodisperse Porous Silica/Polymer Nanocomposite Microspheres with Tunable Silica Loading, Morphology and Porosity. *Int. J. Mol. Sci.* **2022**, *23*, 1−22.
(30) Basso, A. M.; Nicola, B. P.; Bernardo-Gusmão, K.; Pergher, S. B. C. Tunable Effect of the Calcination of the Silanol Groups of KIT-6 and SBA-15 Mesoporous Materials. *Appl. Sci.* **2020**, *10*, 970.
(31) Kleitz, F.; Schmidt, W.; Schüth, F. Evolution of mesoporous materials during the calcination process: structural and chemical behavior. *Microporous. Mesoporous. Mater.* **2001**, *44-45*, 95−109.
(32) Ciriminna, R.; Fidalgo, A.; Pandarus, V.; Béland, F.; Ilharco, L. M.; Pagliaro, M. The sol-gel route to advanced silica-based materials and recent applications. *Chem. Rev.* **2013**, *113*, 6592−6620.
(33) Stöber, W.; Fink, A.; Bohn, E. Controlled growth of monodisperse silica spheres in the micron size range. *J. Colloid Interface Sci.* **1968**, *26*, 62−69.
(34) Xia, H.; Wan, G.; Zhao, J.; Liu, J.; Bai, Q. Preparation and characterization of monodisperse large-porous silica microspheres as the matrix for protein separation. *J. Chromatogr. A* **2016**, *1471*, 138−144.
(35) Myers, R. H.; Montgomery, D. C.; Anderson-Cook, C. M. *Response surface methodology:Process and product optimization using designed experiments*, Fourth edition; Wiley Series in Probability and Statistics Ser: Wiley, 2016.
(36) Box, G. E. P.; Hunter, J. S.; Hunter, W. G. *Statistics for experimenters:Design, innovation, and discovery*, 2. ed.; Wiley series in probability and statistics: Wiley-Interscience, 2005.
(37) Ryan, T. P. *Modern experimental design; Wiley series in probability and statistics*; Wiley-Interscience, 2007.
(38) Seidl, R.; Weiss, S.; Zikulnig-Rusch, E. M.; Kandelbauer, A. Response surface optimization for improving the processing behavior of melamine formaldehyde impregnation resins. *J. Appl. Polym. Sci.* **2021**, *138*, 50181.
(39) Rouquerol, F.; Rouquerol, J.; Sing, K. S. W.; Llewellyn, P. L.; Maurin, G. *Adsorption by powders and porous solids:Principles, methodology and applications*, Second edition; Elsevier/AP, 2014.
(40) Brunauer, S.; Emmett, P. H.; Teller, E. Adsorption of Gases in Multimolecular Layers. *J. Am. Chem. Soc.* **1938**, *60*, 309−319.
(41) Lowell, S.; Shields, J. E.; Thomas, M. A.; Thommes, M., Eds. *Characterization of porous solids and powders: surface area, pore size and density*; Particle Technology Series, Vol. *16*; Springer, 2004, DOI: 10.1007/978-1-4020-2303-3.
(42) Thommes, M.; Kaneko, K.; Neimark, A. V.; Olivier, J. P.; Rodriguez-Reinoso, F.; Rouquerol, J.; Sing, K. S. W. Physisorption of gases, with special reference to the evaluation of surface area and pore size distribution (IUPAC Technical Report). *Pure Appl. Chem.* **2015**, *87*, 1051−1069.
(43) Dewaele, C.; Verzele, M. Influence of the particle size distribution of the packing material in reversed-phase high-performance liquid chromatography. *J. Chromatogr. A* **1983**, *260*, 13−21.
(44) Ulitzsch, S.; Bäuerle, T.; Chassé, T.; Lorenz, G.; Kandelbauer, A. Optimizing the Process Efficiency of Reactive Extrusion in the Synthesis of Vinyltrimethoxysilane-Grafted Ethylene-Octene-Copolymer (EOC-g-VTMS) by Response Surface Methodology. *Polymer* **2020**, *12*, 2798.
(45) Bäuerle, T.; Ulitzsch, S.; Lorenz, A.; Rebner, K.; Chassé, T.; Kandelbauer, A.; Lorenz, G. Effects of process parameters on silane

https://doi.org/10.1021/acsomega.3c03098
ACS Omega 2023, 8, 30273−30284

grafting of liquid ethylene-propylene copolymer by reactive extrusion as quantified by response surface methodology. *Polymer* **2020**, *202*, No. 122601.
(46) Kamiya, H.; Mitsui, M.; Takano, H.; Miyazawa, S. Influence of Particle Diameter on Surface Silanol Structure, Hydration Forces, and Aggregation Behavior of Alkoxide-Derived Silica Particles. *J. Am. Ceram. Soc.* **2000**, *83*, 287−293.
(47) Wang, R.; Wunder, S. L. Effects of Silanol Density, Distribution, and Hydration State of Fumed Silica on the Formation of Self-Assembled Monolayers of *n* -Octadecyltrichlorosilane. *Langmuir* **2000**, *16*, 5008−5016.
(48) Zhuravlev, L. T. The surface chemistry of amorphous silica. Zhuravlev model. *Colloids Surf., A* **2000**, *173*, 1−38.
(49) Poppe, T. Sintering of highly porous silica-particle samples: analogues of early Solar-System aggregates. *Icarus* **2003**, *164*, 139−148.
(50) Kang, S.-J. L. *Sintering:Densification, Grain Growth, and Microstructure*, 1st ed.; Elsevier Butterworth-Heinemann; Elsevier Science & Technology, 2005.
(51) Rahaman, M. N. *Ceramic Processing and Sintering*, Second edition; Materials engineering, Vol. *23*; CRC Press, 2017, DOI: 10.1201/9781315274126.
(52) Plumeré, N.; Ruff, A.; Speiser, B.; Feldmann, V.; Mayer, H. A. Stöber silica particles as basis for redox modifications: particle shape, size, polydispersity, and porosity. *J. Colloid Interface Sci.* **2012**, *368*, 208−219.
(53) Levy, D.; Zayat, M. *The sol-gel handbook*:Volume 1: Synthesis and Processing : Volume 2: Characterization and Properties of Sol-Gel Materials : Volume 3: Application of Sol-Gel Materials; Wiley-VCH, 2015, DOI: 10.1002/9783527670819.
(54) Park, S. K.; Kim, K. D.; Kim, H. T. Preparation of silica nanoparticles: determination of the optimal synthesis conditions for small and uniform particles. *Colloids Surf., A* **2002**, *197*, 7−17.
(55) Bogush, G. H.; Zukoski, C. F. Studies of the kinetics of the precipitation of uniform silica particles through the hydrolysis and condensation of silicon alkoxides. *J. Colloid Interface Sci.* **1991**, *142*, 1−18.

Recommended by ACS

Role of Hydrophobic Attraction and Hydrophobic Nanoconfined Channels in the Spray Drying Process for Synthesizing Hollow Microspheres from Silica Sol
Shaolei Zhao, Ting-Jie Wang, *et al.*
AUGUST 22, 2023
INDUSTRIAL & ENGINEERING CHEMISTRY RESEARCH
READ

Porous Polymer Particles with Tunable Surface Roughness by Combining Phase Separation and Interfacial Instability
Shanqin Liu, Huajie Wang, *et al.*
JANUARY 23, 2023
ACS APPLIED POLYMER MATERIALS
READ

New Lyotropic Complex Fluid Structured in Sheets of Ellipsoidal Micelles Solubilizing Fragrance Oils
Vera Tchakalova, Antonio Martins Figueiredo Neto, *et al.*
JULY 31, 2023
ACS OMEGA
READ

Versatility of the Preparation Method for Macroporous Cryogel Particles Utilizing the Inverse Leidenfrost Effect
Hayato Takase, Hiroshi Umakoshi, *et al.*
DECEMBER 19, 2022
ACS OMEGA
READ

Get More Suggestions >

https://doi.org/10.1021/acsomega.3c03098
ACS Omega 2023, 8, 30273−30284

Supporting Information

Sol-gel-controlled size and morphology of mesoporous silica microspheres using hard templates

Julia C. Steinbach [1,2], Fabio Fait [1,2], Hermann A. Mayer[2] and Andreas Kandelbauer [1,3,]*

[1] Process Analysis & Technology, Reutlingen Research Institute, Reutlingen University, Alteburgstraße 150, 72762 Reutlingen, Germany; julia.steinbach@reutlingen-university.de (J.C.S.); fabio.fait@reutlingen-university.de (F.F.)

[2] Institute of Inorganic Chemistry, University of Tübingen, Auf der Morgenstelle 18, 72076 Tübingen, Germany; hermann.mayer@uni-tuebingen.de (H.A.M.)

[3] Institute of Wood Technology and Renewable Materials, Department of Material Sciences and Process Engineering (MAP), University of Natural Resources and Life Sciences, Gregor-Mendel-Straße 33, 1180 Vienna, Austria

* Correspondence: andreas.kandelbauer@reutlingen-university.de; Tel.: +49-(0)7121-271-2009

Chemicals for the preparation of polystyrene seeds

Styrene (99 %) was purchased from Fisher Scientific GmbH (Schwerte, Germany). Polyvinylpyrrolidone K30 (PVP) and benzoyl peroxide (BPO, 75 %) were purchased from Sigma-Aldrich Chemie GmbH, Traufkirchen Germany. Sodium dodecyl sulfate (SDS, ≥ 99%) was purchased from Carl Roth GmbH + Co. KG (Karlsruhe, Germany). Ethanol 96% was purchased from VWR Chemicals (Darmstadt, Germany). All chemicals were used as delivered.

Preparation of polystyrene seed particles

Polystyrene seed particles (PS) were prepared in alcoholic media via dispersion polymerization[1]. 80 mL ethanol (96 %) and 20 mL styrene (99 %) were added in a three-necked round-bottom flask (250 mL). After the addition of 0.5 g benzoyl peroxide as initiator and 1.0 g polyvinylpyrrolidone k30 as stabilizer the suspension was sonicated for 10 min. The suspension was stirred with 120 rpm with a magnetic stirrer at room temperature for 30 minutes

while purging with Argon. To start the polymerization temperature was elevated to 70 ˚C for 24 h under reflux. The PS seed particles were centrifugated at 7500 rpm for 2 minutes. Then they were washed three times with ethanol and three times with deionized water to remove the reaction solution. The particles were freeze-dried under vacuum for 72 h. The particles were 1.95 µm in median size with a d_{90}/d_{10} = 1.09 (see Figure S. 1).

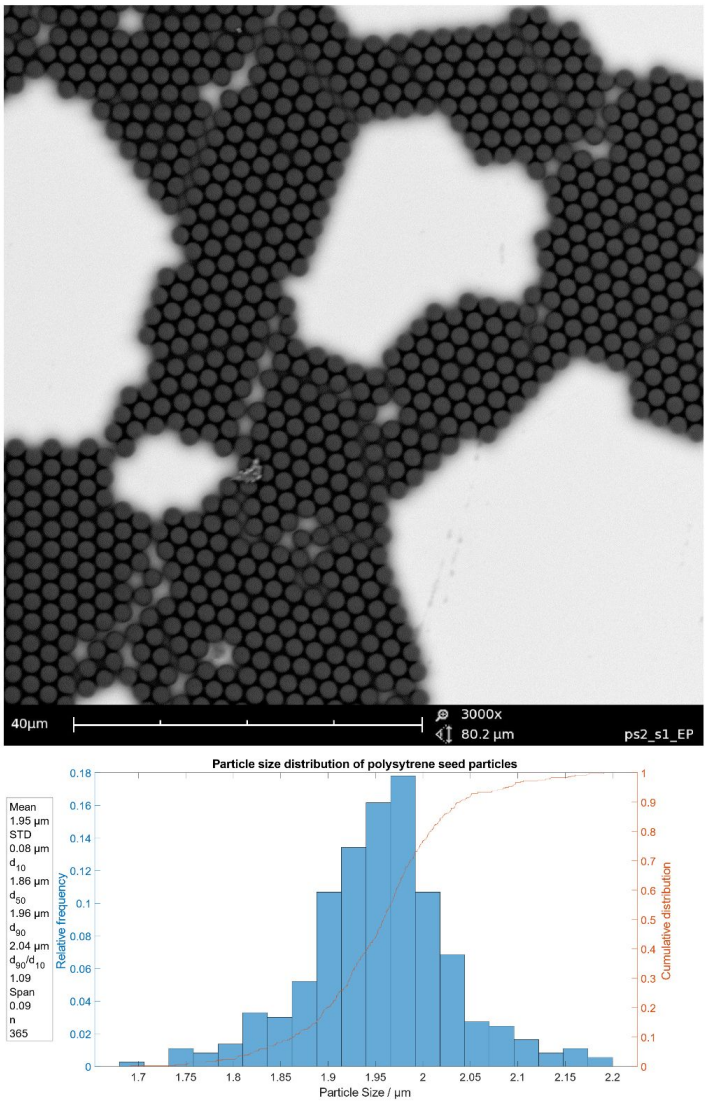


Figure S. 1. SEM image of polystyrene seed particles and corresponding particle size distribution and evaluation.

Preparation of hybrid beads

15 mL of a 2.0 g·L^{-1} SDS solution were prepared and 0.9 g monodisperse polystyrene seeds (1.95 µm, of d_{90}/d_{10} = 1.09) were added. The mixture was sonicated for 10 minutes in. 6.0 mL DBP and 450 mL of a 2.53 g·L^{-1} SDS solution (10 minutes at 5000 rpm) were homogenized and the emulsion was added to the seed particle suspension. The mixture was stirred at 200 rpm for 24 h at room temperature.

The organic phase consisting of 22.5 mL of each cyclohexanol, EDMA, GMA and toluene were homogenized together with 450 mL of SDS (3.33 g·L^{-1}), and 1.2 g of the initiator BPO for 10 minutes at 5000 rpm. The emulsion was added and the system stirred at 200 rpm for another 24 h. As stabilizer 450 mL of a PVA solution (23.3 g·L^{-1}) was added to the mixture. For polymerization the reaction mixture was stirred at 200 rpm for 24 h at 70 ˚C. The porous *p*(GMA-*co*-EDMA) particles were washed three times with ethanol and three times with water.

A mixture of 35 g of dried *p*(GMA-*co*-EDMA) particles and 1400 mL deionized water were sonicated for 15 min. Under stirring at 200 rpm, 0.256 mol of TEPA were added dropwise. The mixture was heated to 80 ˚C for 24 h. The functionalized particles were filtered off and washed three times with ethanol and water. The particles will be further referred to as p@TEPA.

2 g p@TEPA particles were dispersed in a mixture consisting of 2-propanol and water and sonicated for 5 minutes. The amount of added water was calculated in dependence of the stoichiometric ratio of $n(H_2O)/n(TEOS)$ according to the factor level setting of the FCD. The water content of the ammonia solution is thereby considered. As basic catalyst, a predefined amount of ammonia according to the FCD was added to the mixture under stirring. Then 21.5 mmol of TEOS was added and the mixture was stirred for 24 h at room temperature (550 rpm). The HB particles were separated from the reaction solution and washed three times with ethanol and water. The HBs were then dried at room temperature. **pH values after 24 h**

Table S. 1. pH values for the FCD samples 24 h after the start of the synthesis

	Factor level settings		
	A	**B**	**pH values**
	$n(H_2O)$/ n(TEOS)	**$n(NH_3)$ /mmol·L^{-1}**	
MPSM1	4	17.1	10.6
MPSM2	74	17.1	10.2
MPSM3	4	74.1	11.1
MPSM4	74	74.1	11.2
MPSM5	39	45.6	10.8

MPSM6	4	45.6	10.9
MPSM7	74	45.6	10.7
MPSM8	39	17.1	10.4
MPSM9	39	74.1	10.9
MPSM10	39	45.6	10.7
MPSM11	39	45.6	10.7
MPSM12	39	45.6	10.7
MPSM13	8	45.6	10.7
MPSM14	8	17.1	10.5
MPSM15	8	74.1	11.0

ANOVA Tables

Table S. 2. Analysis of variance (ANOVA) for the analysis of FCD design of the particle size

Source	Sum of Squares	df	Mean Square	F-value	p-value	
Model	101.25	3	33.75	130.54	< 0.0001	significant
A-n(H_2O)/n(TEOS)	56.42	1	56.42	218.21	< 0.0001	
B-c(NH_3)	11.69	1	11.69	45.21	< 0.0001	
A^2	23.14	1	23.14	89.49	< 0.0001	
Residual	2.84	11	0.2585			
Lack of Fit	2.39	8	0.2993	2.00	0.3076	not significant
Pure Error	0.4493	3	0.1498			
Cor Total	104.10	14				

Table S. 3. Analysis of variance (ANOVA) for the analysis of FCD design of specific surface area (SSA)

Source	Sum of Squares	df	Mean Square	F-value	p-value	
Model	$5.141 \cdot 10^5$	4	$1.285 \cdot 10^5$	55.95	< 0.0001	significant
A-n(H_2O)/n(TEOS)	$3.950 \cdot 10^5$	1	$3.950 \cdot 10^5$	171.95	< 0.0001	
B-c(NH_3)	$1.329 \cdot 10^5$	1	$1.329E \cdot 10^5$	57.88	0.0001	
A^2	$1.144 \cdot 10^5$	1	$1.144 \cdot 10^5$	49.81	0.0002	
B^2	40445.62	1	40445.62	17.61	0.0041	
Residual	16078.33	7	2296.90			
Lack of Fit	12137.34	4	3034.33	2.31	0.2588	not significant

Pure Error	3940.99	3	1313.66
Cor Total	$5.301 \cdot 10^5$	11	

Table S. 4. Analysis of variance (ANOVA) for the analysis of FCD design of pore diameter (PD)

Source	Sum of Squares	df	Mean Square	F-value	p-value	
Model	166.25	5	33.25	368.57	< 0.0001	significant
A-n(H_2O)/n(TEOS)	47.45	1	47.45	525.94	< 0.0001	
B-c(NH_3)	47.19	1	47.19	523.08	< 0.0001	
AB	2.53	1	2.53	28.02	0.0018	
A^2	9.12	1	9.12	101.07	< 0.0001	
A^2B	6.74	1	6.74	74.74	0.0001	
Residual	0.5413	6	0.0902			
Lack of Fit	0.2645	3	0.0882	0.9554	0.5145	not significant
Pure Error	0.2768	3	0.0923			
Cor Total	166.79	11				

Table S. 5. Analysis of variance (ANOVA) for the analysis of FCD design of the pore volume (V_p)

Source	Sum of Squares	df	Mean Square	F-value	p-value	
Model	0.4076	4	0.1019	9.01	0.0068	significant
A-n(H_2O)/n(TEOS)	0.1592	1	0.1592	14.07	0.0072	
B-c(NH_3)	0.2265	1	0.2265	20.02	0.0029	

A^2	0.0697	1	0.0697	6.16	0.0420	
B^2	0.1065	1	0.1065	9.42	0.0181	
Residual	0.0792	7	0.0113			
Lack of Fit	0.0664	4	0.0166	3.91	0.1459	not significant
Pure Error	0.0127	3	0.0042			
Cor Total	0.4868	11				

Appendix Figures

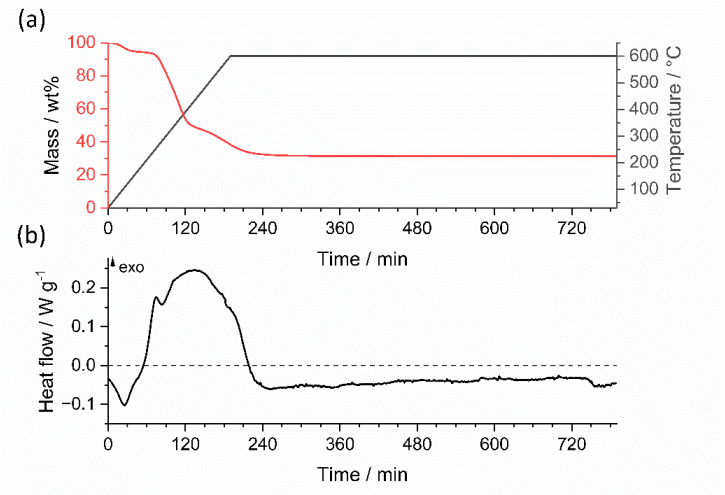


Figure S. 2. Thermogravimetric analysis trace of the calcination procedure. Heating rate: 3 k/min from 30 – 600 ˚C under 50 mL/min synthetic air followed by an isothermal degradation of the polymer at 600 ˚C for 10 h. a) Shows the relative mass conversion over the measurement duration and the temperature gradient.b) displays the heat flow over time.

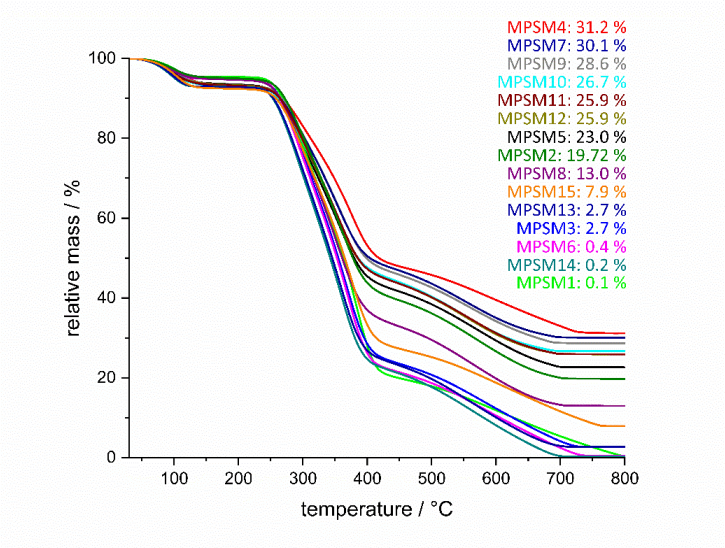


Figure S. 3. Thermogravimetric analysis traces displaying the relative mass loss during template removal of the hybrid beads. The residual mass correlated to the silica content of the hybrid material and the corresponding MPSMs. Heating rate: 5 K/min, from 30 – 800 °C under 50 mL/min synthetic air.

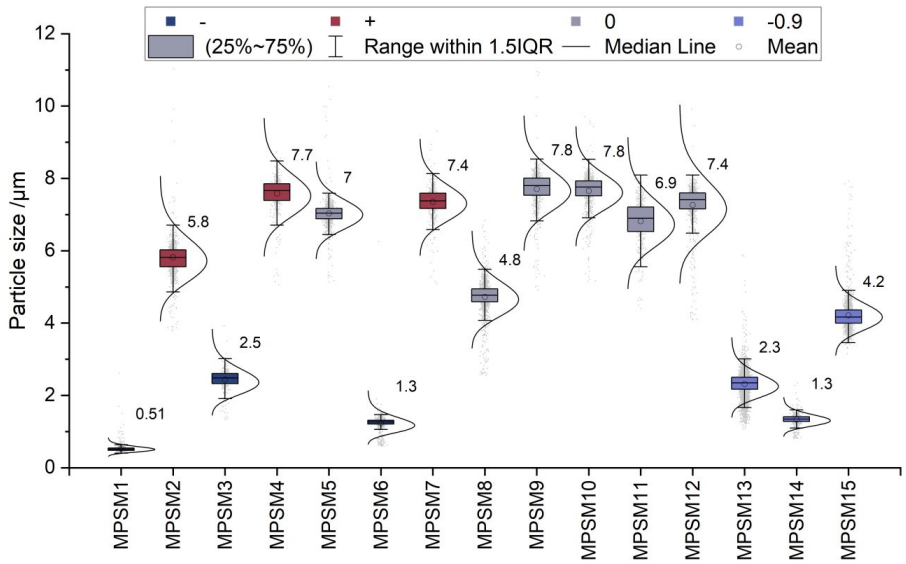


Figure S. 4. Box-Whisker-Plot with lognormal distribution curve of single values (light grey dots) for particle sizes of MPSM1–15. Box displays 1. and 3. quartile, whiskers display 1. and 3. quantile + 1.5 · interquartile range. Dark blue box coloration indicates low, red high, grey medium and light blue setting of n(H2O)/n(TEOS). Median particle sizes are given for each MPSM.

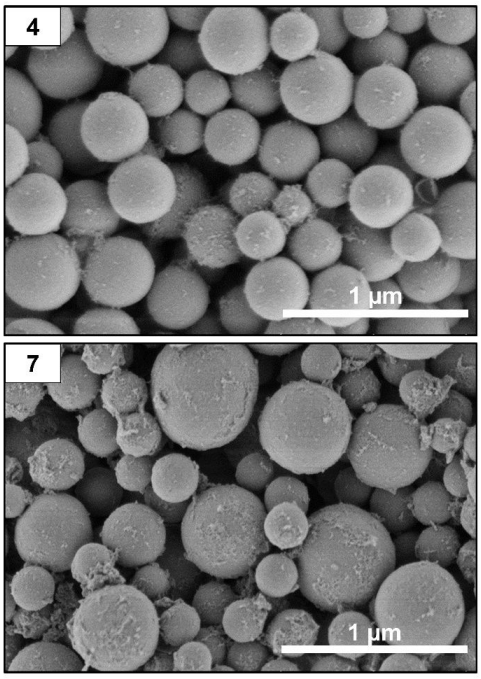


Figure S. 5. Non-porous secondary particles observed in the reaction regime III in the continuous phase during sol-gel processing. These particles were separated from the hybrid particles by filtration (Figure 1b). These secondary particles were observed in the preparation of the preceding HBs to form MPSM4 and MPSM7 after calcination.

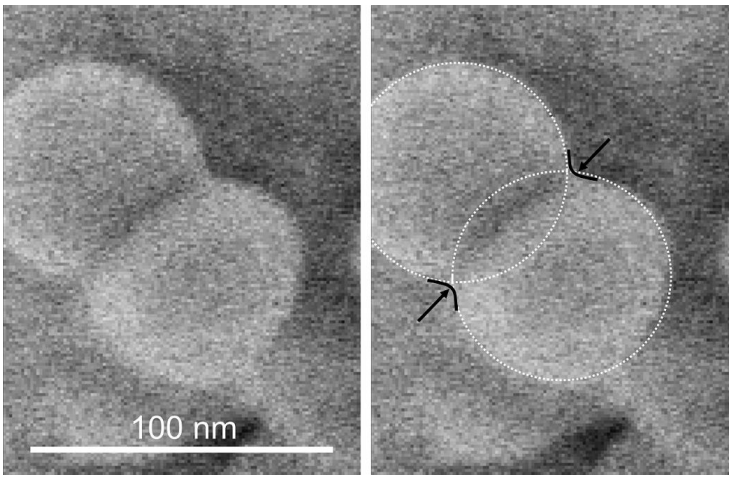


Figure S. 6. Neck formation between two silica nanoparticles after calcination. The decrease in radius indicates occurring shrinkage. On the right, the prior silica nanoparticle outline (dashed white circles) and the neck (solid black lines and black arrows) are highlighted for clarification.

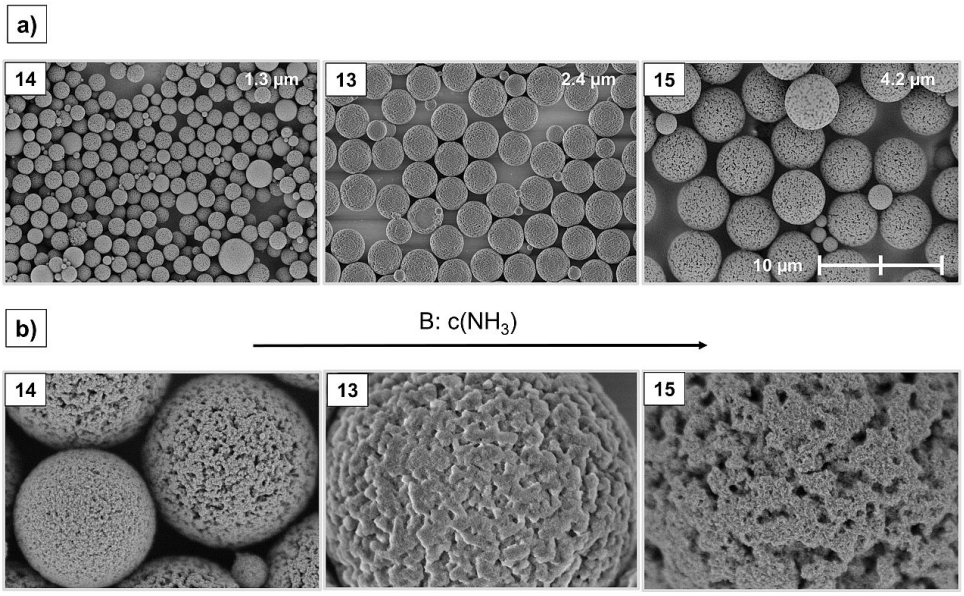


Figure S. 7. SEM image of the additional samples **MPSM13–15** prepared with $n(H_2O)/n(TEOS) = 8$ sorted by increasing $c(NH_3)$ (l.t.r.) at **a**) 5,000× and **b**) 50,000× magnification.

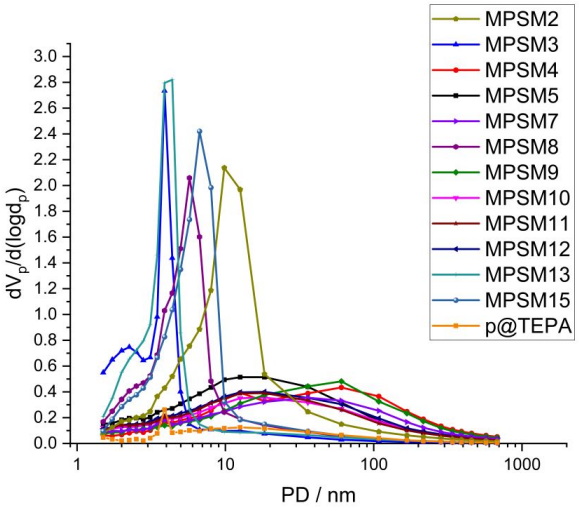


Figure S. 8. Pore size distribution of MPSMs and the corresponding p@TEPA template using the BJH method. The mean pore sizes are given in Table 2.

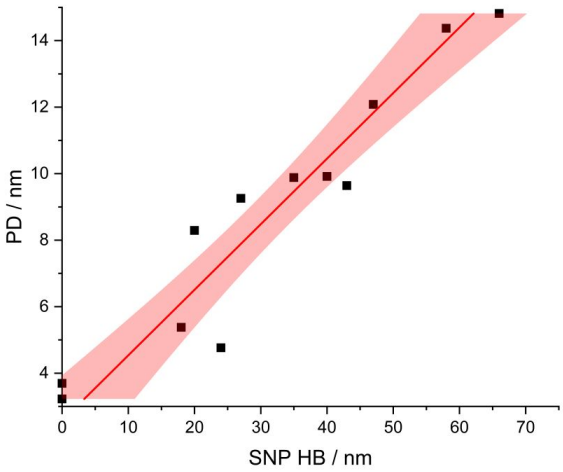


Figure S. 9. Linear regression of PD and the size of SNPs incorporated into the polymeric template. Shaded areas indicate 95% confidence intervals. $R^2_{adjusted} = 0.8986$

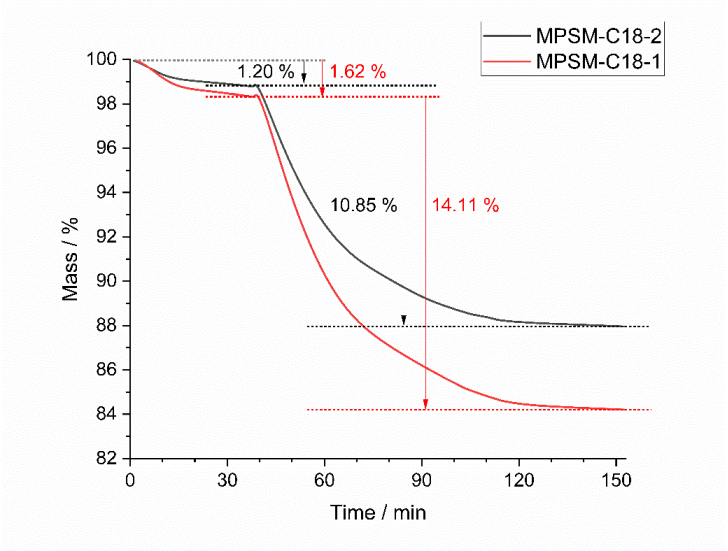


Figure S. 9. TGA traces for the materials MPSM-C_{18}-1 and -2. The first mass loss can be attributed to the desorption of surface bound water[2], while the second mass loss reflects the thermal degradation of the C_{18} functionalization until mass constancy of the residual silica. Heating rate: 5 K/min, from 30 – 800 °C under 50 mL/min synthetic air. Comparing the mass losses of the two materials for both steps, the mass loss of MPSM-C_{18}-2 is about 75 % (74.1 % for water loss and 76.9 % for the degradation of the C18 functionalization) of the mass loss of MPSM-C_{18}-1. This ratio is also reflected in the surface area ratio of the materials (MPSM-C_{18}-1: 246 m^2g^{-1} and MPSM-C_{18}-2: 186 m^2g^{-1}; 75.6 %).

Inverse size exclusion chromatography characterization of columns MPSM-C_{18}-1 and MPSM-C18-2

Table S. 6. Pore size, Pore volume and specific surface area determined by inverse size exclusion[1]

	Pore size / nm	Pore volume / cm^3/g	SSA / m^2/g
MPSM-C_{18}-1	23.1	0.77	134
MPSM-C_{18}-2	25.7	0.80	125

References

(1) Steinbach, J. C.; Fait, F.; Wagner, S.; Wagner, A.; Brecht, M.; Mayer, H. A.; Kandelbauer, A. Rational Design of Pore Parameters in Monodisperse Porous Poly(glycidyl methacrylate-co-ethylene glycol dimethacrylate) Particles Based on Response Surface Methodology. Polymers 2022, 14 (3). DOI: 10.3390/polym14030382.

(2) Zhuravlev, L. T. The surface chemistry of amorphous silica. Zhuravlev model. Colloids Surf. A 2000, 173 (1-3), 1–38. DOI: 10.1016/S0927-7757(00)00556-2.

12 Experimenteller Teil

12.1 Allgemeine Arbeits- und Analysemethoden

12.1.1 Ausrüstung und Arbeitstechniken

Für die Synthesen wurden entsprechend der Vorschrift ein Magnetrührer (RCT basic, *IKA®-Werke* GmbH & Co. KG) oder ein KPG-Rührer (*Heidolph Instruments* GmbH & Co. KG) verwendet. Die Filtration der Partikel erfolgte über Filterpapier (MN 85/70, ∅ 90 mm, *Macherey-Nagel* GmbH & Co. KG) mit Büchner-Trichter oder über P3-/P4-Glasfritten. Zur Darstellung der homogenen Emulsionen wurde ein Labormischer der Firma *Silverson* genutzt. Die analytische Hochleistungsflüssigkeitschromatographie wurde auf einem System der Agilent 1100 Serie (*Agilent Technologies*) durchgeführt, welches mit einer quaternären Pumpe mit Entgaser, einem automatischen Probeentnahmesystem, einem Säulenofen, einem Diodenarray- und einem Fluoreszenzdetektor ausgestattet ist. Die Steuerung des Geräts, die Datenerfassung und die automatische Datenanalyse wurden mit der OpenLAB CDS (Rev. C.01.07 SR3 Software, *Agilent Technologies*) durchgeführt.
Funktionalisierte Partikel wurden mit Aceton als Slurry und MeOH/H_2O (85/15, v.%/v.%) als Druckmedium in 250 × 4.6 mm Stahlsäulen mit Hilfe eines Füllrohrs und einer pneumatischen Pumpe (*Knauer* GmbH) gepackt. Die Auftrennung der Analyten erfolgte entsprechend den in Publ. **I**, Publ. **III** und Publ. **IV** beschriebenen Methoden.

12.1.2 Chemikalien und Lösungsmittel

Für Partikelsynthesen verwendete Lösungsmittel wurden mit Reinheitsgrad HPLC-grade erworben und ohne weitere Aufreinigung eingesetzt. Wasserfreies Toluol wurde über ein *Solvent Purification System* (SPS-800, *MBraun*) erhalten und unter Argon-Atmosphäre gelagert. 1,1-Diphenylethylen, Natriumnitrit, Polyvinylalkohol (87-89 % hydrolysiert, M_W: 88,000 − 97,000 g/mol), Polyvinylpyrrolidon K_{30} (M_W: 40,000 g/mol), Octadecyltrimethoxysilan, Tetramethoxysilan, Tetraethoxysilan, Trimethylammoniumchlorid und Vinyltriethoxysilan wurden von der *abcr GmbH* genutzt. Ammoniak (28 − 30 % wässrige Lsg.), Tetrabutoxysilan und Tetrapropoxysilan wurden bei *alfa aesar*, Ethylenglycoldimethacrylat bei *Acros Organics* und Cyclohexanol und Natriumlaurylsulfat bei *Carl Roth* erworben. Acetonitril, 1-Butanol, HPLC-Wasser, Tetraethylenpentamin und Styrol wurden bei *fisher scientific* eingekauft. (3-Aminopropyl)triethoxysilan, Dibenzoylperoxid, Dibutylphthalat, Ethanol, Glycidylmethacrylat, Methanol, 2-Propanol,Triethylamin und Salzsäure wurden von *Sigma-Aldrich* bezogen. Der Proteinstandard H2899 (Ribonuklease A, Cytochrome C, Holo-Transferrin, Apomyoglobin), das *D,L*-Aminosäuren-Analysekit (Alanin, Arginin, Asparaginsäure, Glutaminsäure, Glycin, Isoleucin, Leucin, Norvalin, Tryptophan, Tyrosin, Valin) und die Vitaminmixtur (Thiaminhydrochlorid (Vit. B_1),

Nicotinamid (Vit. B_3), D-Pantothensäure Hemicalciumsalz (Vit. B_5), Folsäure (Vit. B_9) und Cyanocobalamin (Vit. B_{12})) wurden ebenfalls bei *Sigma-Aldrich* erworben.

12.1.3 Charakterisierung der Partikeleigenschaften

Elementaranalyse
Die Elementaranalysen wurden an einem *Elementar* Vario MICRO CUBE von Mohammad Ghani an der Universität Tübingen gemessen und ausgewertet.

IR-Spektroskopie
Die Aufnahme der IR-Spektren erfolgte an einem *Bruker* Vertex 70 FT-IR-Spektrometer. Zur Probenpräparation wurden 10 mg Partikel und 30 mg KBr vermörsert und mit der DRIFT-Methode vermessen. Die Auswertung erfolgte mit Hilfe der OPUS Software (*Bruker Corporation*).

NMR-Spektroskopie
^{13}C- und ^{29}Si-NMR-Spektren im Festkörper wurden an einem *Bruker* Avance III HD-300WB Spektrometer mit ZrO_2-Rotoren (4 mm) bei Rotationsgeschwindigkeiten von 8 kHz (^{13}C) bzw. 5 kHz (^{29}Si) aufgenommen. Die Messfrequenzen betrugen 75.47 MHz (^{13}C) und 59.63 MHz (^{29}Si). Die Spektren wurden für ^{13}C auf Adamantan und für ^{29}Si auf Octakis(trimethylsiloxy)silsesquioxan (Q_8M_8) als externe Standards referenziert. Die Kontaktzeiten der Cross-Polarization Magic Angle Spinning (CP/MAS)-Aufnahmen betrugen 2000 µs (^{13}C) und 5000 µs (^{29}Si) und die Relaxationszeiten 4 s (^{13}C) bzw. 2 s (^{29}Si). Die ^{29}Si-NMR-Messungen mit Hochleistungsprotonenentkopplung (HPDEC) hatten Kontaktzeiten von 9000 µs und Relaxationszeiten von 30 s. Die Auswertung der NMR-Spektren erfolgte mit Hilfe der TopSpin Software (*Bruker Corporation*).

Rasterelektronenmikroskopie
Rasterelektronenmikroskopaufnahmen (REM) der Partikel wurden an einem *Hitachi* SU8030 mit kalter Feldemissionskathode von Elke Nadler an der Universität Tübingen durchgeführt. Zur Probenpräparation wurden homogene Partikelsuspensionen in EtOH mittels *spin coating* auf Si-Wafer vorgelegt. Die Auswertung der Partikelgrößen und Dispersität über REM-Aufnahmen erfolgte mit Hilfe eines im Arbeitskreis entworfenen MATLAB-Skripts.[111] Für die Angaben wurden Durchmesser von mindestens ≥ 300 Partikeln bestimmt. Die durchschnittliche Partikelgröße wird als d_{50} und die Dispersität der Partikel als d_{90}/d_{10} angegeben.

Stickstoffadsorptionsmessungen
Stickstoffadsorptionsmessungen wurden an einem BELSORP MiniX (*Microtrac Retsch* GmbH) durchgeführt. Polymer- und Hybrid-Partikel wurden bei 30 °C für 24 h und Si-

lica-Partikel bei 300 °C für 3 h bis zu einem Endvakuum von etwa 2 x 10^{-2} mbar entgast, um mögliche physiosorbierte Substanzen zu eliminieren und einen reproduzierbares Gleichgewicht zu erreichen.[114] Die Proben wurden mit dem BELSORP VACII (*Microtrac Retsch* GmbH) evakuiert. Die N_2-Adsorptions- und Desorptionsisothermen wurden bei 77 K aufgenommen und mit der Software BELMaster 7 ausgewertet. Die spezifische Oberfläche a_{BET} wurde nach der Brunauer-Emmet-Teller-Methode (BET) berechnet.[115] Die Porengrößenverteilung wurde mit der Barrett-Joyner-Halenda-Methode (BJH) aus den Desorptionsisothermen unter Verwendung der Harkins-Jura-Standardisotherme bestimmt.[116] Als Wert für die Porengröße Φ wird der Median der Porengrößenverteilung verwendet. Das Porenvolumen V_P wurde aus einer Einzelpunktadsorption bei $p/p_0 = 0.95$ ermittelt.

Thermogravimetrische Analyse

Die thermogravimetrischen Analysen (TGA) wurden an einer TGA/DSC I von *Mettler Toledo* durchgeführt. Die Proben wurden in einem 900 µL Al_2O_3-Tiegel unter Zuleitung synthetischer Luft (50 $^{mL}/_{min}$) mit einer Heizrate von 5 $^{K}/_{min}$ vermessen. Die relative Masse des verbleibenden Rückstandes korreliert mit der Menge an SiO_2.

12.2 Partikelnomenklatur

Tabelle 4: Nomenklatur der Partikel in dieser Arbeit mit den entsprechenden Bezeichnungen in den Veröffentlichungen.

	Bezeichnung in der Dissertation	Bezeichnung in der Veröffentlichung
Publ. **I**	**P1**	**P1**
	P2	**P2**
	P3	**P3**
	P4	**P4**
	P5	**P5**
	P6	**P6**
	HB1	**HB1**
	HB2	**HB2**
	HB3	**HB3**
	HB4	**HB4**
	HB5	**HB5**
	HB6	**HB6**
	MPSM1	**MPSM1**
	MPSM2	**MPSM2**
	MPSM3	**MPSM3**
	MPSM4	**MPSM4**
	MPSM5	**MPSM5**
	MPSM6	**MPSM6**
Publ. **III**	**HB7**	**HB1**
	HB8	**HB2**
	HB9	**HB3**
	HB10	**HB4**
	MPSM7	**MPSM1**
	MPSM8	**MPSM2**
	MPSM9	**MPSM3**
	MPSM10	**MPSM4**
Publ. **IV**	**HB11**	**HB1a**
	HB12	**HB1b**
	HB13	**HB1c**
	HB14	**HB1d**
	MPSM11	**MPSM1a**
	MPSM12	**MPSM1b**
	MPSM13	**MPSM1c**
	MPSM14	**MPSM1d**
	HB15	**HB2a**
	HB16	**HB2b**
	HB17	**HB2b**
	HB18	**HB2d**
	MPSM15	**MPSM2a**
	MPSM16	**MPSM2b**
	MPSM17	**MPSM2c**
	MPSM18	**MPSM2d**
	HB19	**HB1e**
	HB20	**HB1f**
	MPSM19	**MPSM1e**
	MPSM20	**MPSM1f**

12.3 Synthesen

12.3.1 Synthese monodisperser Polystyrol-Partikel

Die Synthese monodisperser Polystyrol-Partikel erfolgt in Anlehnung an Xia *et al.*,[102] Srisopa[117] und Wagner.[33]

PS1

20 mL Styrol, 0.5 g Dibenzoylperoxid, 1.0 g Polyvinylpyrrolidon (PVP-K_{30}) und 80 mL EtOH werden in einem 250 mL Dreihalskolben mit ovalem Rührstab (25 mm) vorgelegt und im Ultraschallbad dispergiert. Die Lösung wird für 30 min mit Argon inertisiert. Die Reaktionslösung wird für 24 h bei 70 °C gerührt (120 rpm). Die Partikel werden durch Zentrifugation (2 min, 5500 rpm) von der Reaktionslösung entfernt, jeweils dreimal mit EtOH und H_2O gewaschen und für sieben Tage gefriergetrocknet.

REM: $d_{50} = 1.94\,\mu m$, $^{d_{90}}/_{d_{10}} = 1.06$

PS2

13.2 mL Styrol, 0.5 g Dibenzoylperoxid, 1.44 g Polyvinylpyrrolidon (PVP-K_{30}) und 108.6 mL MeOH werden in einem 250 mL Dreihalskolben mit ovalem Rührstab (25 mm) vorgelegt und im Ultraschallbad dispergiert. Die Lösung wird für 30 min mit Argon inertisiert. Die Reaktionslösung wird für 24 h bei 70 °C gerührt (120 rpm). Die Partikel werden durch Zentrifugation (5 min, 7000 rpm) von der Reaktionslösung entfernt, jeweils dreimal mit EtOH und H_2O gewaschen und für sieben Tage gefriergetrocknet.

REM: $d_{50} = 1.06\,\mu m$, $^{d_{90}}/_{d_{10}} = 1.12$

PS3 und PS4

20 mL Styrol, 0.5 g Dibenzoylperoxid, 1.0 g Polyvinylpyrrolidon (PVP-K_{30}) und 80 mL EtOH werden in einem 250 mL Dreihalskolben mit ovalem Rührstab (25 mm) vorgelegt und im Ultraschallbad dispergiert. Die Lösung wird für 30 min mit Argon inertisiert. Die Reaktionslösung wird bei 70 °C gerührt (120 rpm). Nach 1.5 h werden 0.4 mL 1,1-Diphenylethylen in 40 mL EtOH zugegeben und weitere 22.5 h bei 70 °C gerührt (120 rpm). Die Partikel werden durch Zentrifugation (5 min, 7000 rpm) von der Reaktionslösung entfernt, jeweils dreimal mit EtOH und H_2O gewaschen und für sieben Tage gefriergetrocknet.

REM: **PS3**: $d_{50} = 1.07\,\mu m$, $^{d_{90}}/_{d_{10}} = 1.17$; **PS4**: $d_{50} = 1.41\,\mu m$, $^{d_{90}}/_{d_{10}} = 1.10$

12.3.2 Synthese poröser *p*(GMA-*co*-EDMA) Template

Die Darstellung poröser *p*(GMA-*co*-EDMA) Template (**P**) erfolgt nach einer modifizierten Synthese von Xia *et al.*[102] und Wagner.[33]

P1 – P6

0.3 g **PS1**, 0.1 g SDS und 5 mL H_2O werden in einem 250 mL Dreihalskolben mit ovalem Rührstab (35 mm) vorgelegt und im Ultraschallbad dispergiert. 0.38 g SDS und 2 mL Dibutylphthalat werden separat in 150 mL für 15 min homogenisiert (4500 rpm). Anschließend wird die Suspension in den Dreihalskolben überführt und für 24 h gerührt (200 rpm). Das Volumenverhältnis von Glycidylmethacrylat zu Ethylenglycoldimethacrylat und von Monomeren zu Porogenen bei einem Gesamtvolumen von 30 mL organischer Phase wurde entsprechend Tab. 5 eingesetzt. Die Monomer- und Porogenmischung, 0.4 g BPO und 0.5 g SDS werden in 150 mL H_2O für 15 min homogenisiert (4500 rpm). Anschließend werden beide Suspensionen in ein 500 mL Dreihalskolben überführt und für 24 h gerührt (200 rpm). 3.5 g Polyvinylalkohol werden in 150 mL H_2O bei 50 °C gelöst. Die PVA-Lösung wird zur Suspension gegeben und für 20 min mit Argon inertisiert. Das Reaktionsgemisch wird bei 70 °C für 24 h gerührt (200 rpm). Die Partikel werden von der Reaktionslösung getrennt, jeweils dreimal mit EtOH und H_2O gewaschen und für 24 h getrocknet.

Tabelle 5: Ansatzgrößen und Partikeleigenschaften der Template **P1 – P6**.

	GMA/EDMA [v.%/v.%]	Monomer/Porogen [v.%/v.%]	d_{50} [µm]	d_{90}/d_{10}	Φ [nm]	V_P $[\frac{mL}{g}]$	a_{BET} $[\frac{m^2}{g}]$
P1	20/80	50/50	7.89	1.09	8.0	0.29	270
P2	40/60	50/50	7.76	1.17	12.6	0.19	123
P3	60/40	50/50	7.50	1.13	21.1	0.09	43
P4	80/20	50/50	7.34	1.19	35.4	0.03	15
P5	40/60	25/75	7.58	1.25	27.9	0.25	132
P6	40/60	75/25	7.87	1.17	8.4	0.06	31

P7 und P11

0.3 g **PS1**, 0.1 g SDS und 5 mL H_2O werden in einem 250 mL Dreihalskolben mit ovalem Rührstab (35 mm) vorgelegt und im Ultraschallbad dispergiert. 0.38 g SDS und 2 mL Dibutylphthalat werden separat in 150 mL für 15 min homogenisiert (4500 rpm). Anschließend wird die Suspension in den Dreihalskolben überführt und für 24 h gerührt (200 rpm). 6 mL GMA, 9 mL EDMA, 11 mL Toluol, 4 mL Cyclohexanol, 0.4 g BPO und 0.5 g SDS werden in 150 mL H_2O für 15 min homogenisiert (4500 rpm). Anschließend werden beide Suspensionen in ein 500 mL Dreihalskolben überführt und für 24 h gerührt (200 rpm). 3.5 g Polyvinylalkohol werden in 150 mL H_2O bei 50 °C gelöst. Die PVA-Lösung wird zur Suspension gegeben und für 20 min mit Argon inertisiert. Das Reaktionsgemisch wird bei 70 °C für 24 h gerührt (200 rpm). Die Partikel werden von der Reaktionslösung getrennt, jeweils dreimal mit EtOH und H_2O gewaschen und für 24 h getrocknet.

Tabelle 6: Ansatzgrößen und Partikeleigenschaften der Template **P7** und **P11**.

	GMA/EDMA [v.%/v.%]	Monomer/Porogen [v.%/v.%]	d_{50} [µm]	d_{90}/d_{10}	Φ [nm]	V_P [$\frac{mL}{g}$]	a_{BET} [$\frac{m^2}{g}$]
P7	40/60	50/50	7.62	1.22	16.2	0.20	121
P11	40/60	50/50	7.99	1.17	15.4	0.22	125

P8

0.3 g **PS4**, 0.1 g SDS und 5 mL H_2O werden in einem 250 mL Dreihalskolben mit ovalem Rührstab (35 mm) vorgelegt und im Ultraschallbad dispergiert. 0.38 g SDS und 2 mL Dibutylphthalat werden separat in 150 mL für 15 min homogenisiert (4500 rpm). Anschließend wird die Suspension in den Dreihalskolben überführt und für 24 h gerührt (200 rpm). 6 mL GMA, 9 mL EDMA, 16.5 mL Toluol, 6 mL Cyclohexanol, 0.4 g BPO und 0.5 g SDS werden in 150 mL H_2O für 15 min homogenisiert (4500 rpm). Anschließend werden beide Suspensionen in ein 500 mL Dreihalskolben überführt und für 24 h gerührt (200 rpm). 3.5 g Polyvinylalkohol werden in 150 mL H_2O bei 50 °C gelöst. Die PVA-Lösung wird zur Suspension gegeben und für 20 min mit Argon inertisiert. Das Reaktionsgemisch wird bei 70 °C für 24 h gerührt (200 rpm). Die Partikel werden von der Reaktionslösung getrennt, jeweils dreimal mit EtOH und H_2O gewaschen und für 24 h getrocknet.

Tabelle 7: Ansatzgröße und Partikeleigenschaften von Templat **P8**.

	GMA/EDMA [v.%/v.%]	Monomer/Porogen [v.%/v.%]	d_{50} [µm]	d_{90}/d_{10}	Φ [nm]	V_P [$\frac{mL}{g}$]	a_{BET} [$\frac{m^2}{g}$]
P8	40/60	40/60	6.00	1.16	14.3	0.24	148

P9 und P10

0.3 g **PS2** bzw. **PS3**, 0.1 g SDS und 5 mL H_2O werden in einem 250 mL Dreihalskolben mit ovalem Rührstab (35 mm) vorgelegt und im Ultraschallbad dispergiert. 0.38 g SDS und 2 mL Dibutylphthalat werden separat in 150 mL für 15 min homogenisiert (4500 rpm). Anschließend wird die Suspension in den Dreihalskolben überführt und für 24 h gerührt (200 rpm). 6 mL GMA, 9 mL EDMA, 16.5 mL Toluol, 6 mL Cyclohexanol, 0.4 g BPO und 0.5 g SDS werden in 150 mL H_2O für 15 min homogenisiert (4500 rpm). Anschließend werden beide Suspensionen in ein 500 mL Dreihalskolben überführt und für 24 h gerührt (200 rpm). 3.5 g Polyvinylalkohol werden in 150 mL H_2O bei 50 °C gelöst. Die PVA-Lösung wird zur Suspension gegeben und für 20 min mit Argon inertisiert. Das Reaktionsgemisch wird bei 70 °C für 24 h gerührt (200 rpm). Die Partikel werden von der Reaktionslösung getrennt, jeweils dreimal mit EtOH und H_2O gewaschen und für 24 h getrocknet.

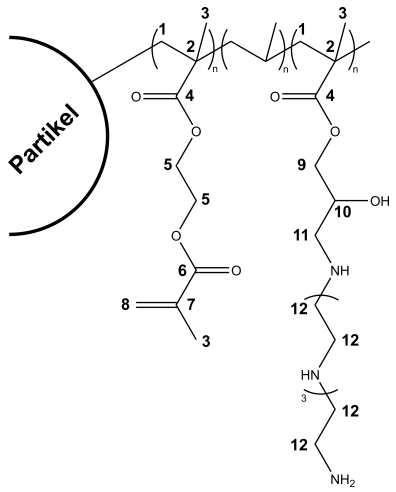
Tabelle 8: Ansatzgröße und Partikeleigenschaften von Templat **P9** und **P10**.

	GMA/EDMA [v.%/v.%]	Monomer/Porogen [v.%/v.%]	d_{50} [µm]	d_{90}/d_{10}	Φ [nm]	V_P [$\frac{mL}{g}$]	a_{BET} [$\frac{m^2}{g}$]
P9	40/60	40/60	4.54	1.08	13.1	0.18	107
P10	40/60	40/60	4.07	1.19	11.2	0.21	131

12.3.3 Aminofunktionalisierung von *p*(GMA-*co*-EDMA) Templaten

TEPA-Funktionalisierung

Die Synthese von Tetraethylenpentamin funktionalisierten Polymerpartikeln (**P@TEPA**) erfolgt nach Xia *et al.*[102] 10 g *p*(GMA-*co*-EDMA)-Partikel und 400 mL H_2O werden in einem 500 mL Dreihalskolben mit ovalem Rührstab (35 mm) vorgelegt und im Ultraschallbad dispergiert. Unter Rühren der Suspension (200 rpm) werden 15 mL Tetraethylenpentamin hinzugegeben. Das Reaktionsgemisch wird bei 80 °C für 24 h gerührt. Die Partikel werden von der Reaktionslösung getrennt, jeweils dreimal mit H_2O und EtOH gewaschen und für 24 h bei 70 °C getrocknet.



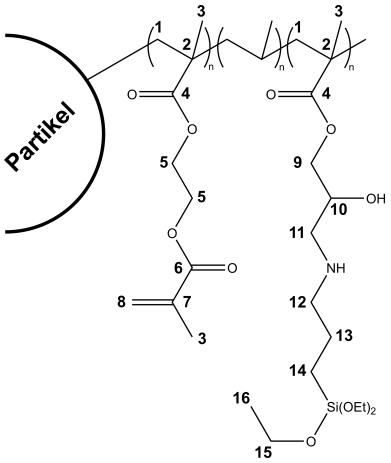
^{13}C-NMR (75.47 MHz, CP/MAS, 8 kHz rot.): δ (in ppm) = 18.0 (C-3), 45.0 (C-1), 55.1 (C-2, C-5, C-12), 63.2 – 69.3 (C-9, C-10, C-11), 127.4 (C-8), 136.1 (C-7), 167.1 (C-6), 176.6 (C-4).

EA: 57.63 % C, 7.68 % H, 2.75 % N.

IR (DRIFT): $\tilde{\nu}$ (in cm^{-1}) = 908 (ν_{Epoxid}), 1160 ($\nu_{\text{C-NH}}$), 1162 ($\nu_{\text{C-O-C}}$), 1265 ($\nu_{\text{C-NH}}$), 1458 ($\delta_{\text{C-H, aliph.}}$), 1735 ($\nu_{\text{C=O}}$), 2825 – 2890 ($\nu_{\text{C-H, aliph.}}$), 3100 – 3500 ($\nu_{\text{OH, NH}}$).

APTES-Funktionalisierung

Die Synthese von (3-Aminopropyl)triethoxysilan funktionalisierten Polymerpartikeln (**P@APTES**) erfolgt in Anlehnung an Grama *et al.*[118] 10 g *p*(GMA-*co*-EDMA)-Partikel und 300 mL MeOH werden in einem 500 mL Dreihalskolben mit ovalem Rührstab (35 mm) vorgelegt und im Ultraschallbad dispergiert. Unter Rühren der Suspension (200 rpm) werden 105 mL (3-Aminopropyl)triethoxysilan hinzugegeben. Das Reaktionsgemisch wird bei 60 °C für 24 h gerührt. Die Partikel werden von der Reaktionslösung getrennt, jeweils dreimal mit H_2O und EtOH gewaschen und für 24 h bei 70 °C getrocknet.



^{13}C-NMR (75.47 MHz, CP/MAS, 8 kHz rot.): δ (in ppm) = 9.6 (C-16), 18.0 (C-3, C-18), 22.6 (C-15), 44.9 (C-1, C-14), 55.2 (C-2, C-17), 62.5 – 69.3 (C-9, C-12, C-13), 126.9 (C-8), 136.3 (C-7), 166.7 (C-6), 176.9 (C-4).

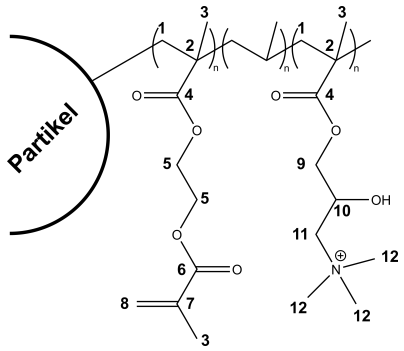
^{29}Si-NMR (59.63 MHz, CP/MAS, 5 kHz rot.): δ (in ppm) = − 42 (T^0), − 50 (T^1), − 58 (T^2), − 65 (T^3).

EA: 56.50 % C, 7.45 % H, 1.04 % N.

IR (DRIFT): $\tilde{\nu}$ (in cm^{-1}) = 906 (ν_{Epoxid}), 960 ($\nu_{\text{Si-OH}}$), 1158 ($\nu_{\text{C-NH}}$), 1163 ($\nu_{\text{C-O-C}}$), 1259 ($\nu_{\text{C-NH}}$), 1261 ($\nu_{\text{Si-O-Si}}$), 1454 ($\delta_{\text{C-H, aliph.}}$), 1732 ($\nu_{\text{C=O}}$), 2842 − 2989 ($\nu_{\text{C-H, aliph.}}$), 3109 − 3525 ($\nu_{\text{OH, NH}}$).

TMA-Funktionalisierung

Die Synthese von Trimethylammonium funktionalisierten Polymerpartikeln (**P@TMA**) erfolgt nach Chen *et al.*[119] 10 g *p*(GMA-*co*-EDMA)-Partikel, 125 mL MeOH und 250 mL H_2O werden in einem 500 mL Dreihalskolben mit ovalem Rührstab (35 mm) vorgelegt und im Ultraschallbad dispergiert. Unter Rühren der Suspension (200 rpm) werden 20 g Trimethylammoniumchlorid und 8.35 g NaOH hinzugegeben. Das Reaktionsgemisch wird bei 50 °C für 24 h gerührt. Die Partikel werden von der Reaktionslösung getrennt, mit H_2O und EtOH gewaschen bis das Filtrat neutral ist und für 24 h bei 70°C getrocknet.



^{13}C-NMR (75.47 MHz, CP/MAS, 8 kHz rot.): δ (in ppm) = 18.9 (C-3), 45.1 (C-1), 54.6 (C-2, C-5, C-12), 63.9 – 69.4 (C-9, C-10, C-11), 127.7 (C-8), 177.3 (C-4).
EA: 54.23 % C, 7.96 % H, 1.85 % N.
IR (DRIFT): $\tilde{\nu}$ (in cm^{-1}) = 912 (ν_{Epoxid}), 1162 ($\nu_{\text{C-NH}}$), 1165 ($\nu_{\text{C-O-C}}$), 1263 ($\nu_{\text{C-NH}}$), 1454 ($\delta_{\text{C-H, aliph.}}$), 1481 ($\nu_{\text{N-CH}_3}$), 1728 ($\nu_{\text{C=O}}$), 2947 – 2993 ($\nu_{\text{C-H, aliph.}}$), 3097 – 3572 ($\nu_{\text{OH, NH}}$).

12.3.4 Sol-Gel-Prozess in Anwesenheit aminofunktionalisierter *p*(GMA-*co*-EDMA)-Template

Die Darstellung von *p*(GMA-*co*-EDMA)/SiO_2 Hybrid-Partikeln (**HB**) erfolgt in Anlehnung an Xia *et al.*[102] und Wagner.[33]

HB1 – HB6

5 g **P1-6@TEPA**-Partikel, 270 mL 2-Propanol und 30 mL H_2O werden in einem 500 mL Dreihalskolben vorgelegt und im Ultraschallbad dispergiert. Der Aufbau wird mit einer KPG-Rührwelle und Rührblatt (90 mm) versehen. Anschließend werden 12.5 mL TEOS und 1.25 mL wässrige Ammoniaklösung (28-30 %) zugegeben und die Reaktionslösung bei RT für 24 h gerührt (130 rpm). Die Partikel werden von der Reaktionslösung getrennt, jeweils dreimal mit H_2O und EtOH gewaschen und 24 h bei 70 °C getrocknet.

Tabelle 9: Partikeleigenschaften der Hybrid-Partikel **HB1 – HB6**.

	d_{50} [µm]	d_{90}/d_{10}	SiO_2 wt. [%]
HB1	8.23	1.05	30.3
HB2	8.31	1.05	30.0
HB3	8.09	1.04	29.9
HB4	8.16	1.05	30.2
HB5	8.20	1.08	30.1
HB6	8.78	1.08	-

HB7 – HB10

5 g **P7@APTES**-Partikel, 270 mL MeOH (**HB7**), EtOH (**HB8**), 2-PrOH (**HB9**) oder n-BuOH (**HB10**) und 30 mL H_2O werden in einem 500 mL Dreihalskolben vorgelegt und im Ultraschallbad dispergiert. Der Aufbau wird mit einer KPG-Rührwelle und Rührblatt (90 mm) versehen. Anschließend werden 12.5 mL TEOS und 1.25 mL wässrige Ammoniaklösung (28-30 %) zugegeben und die Reaktionslösung bei RT für 24 h gerührt (130 rpm). Die Partikel werden von der Reaktionslösung getrennt, jeweils dreimal mit H_2O und EtOH gewaschen und 24 h bei 70 °C getrocknet.

Tabelle 10: Partikeleigenschaften der Hybrid-Partikel **HB7 – HB10**.

	d_{50} [µm]	d_{90}/d_{10}	SiO_2 wt. [%]
HB7	8.16	1.09	24.6
HB8	8.43	1.06	35.9
HB9	8.34	1.07	35.2
HB10	8.43	1.08	40.1

HB11 – HB14

1 g **P8@TEPA**-Partikel, 60 mL 2-Propanol und 7.5 mL H_2O werden in einem 100 mL Dreihalskolben mit ovalem Rührstab (20 mm) vorgelegt und im Ultraschallbad dispergiert. 2.4 mL TMOS (**HB11**), TEOS (**HB12**), TPOS (**HB13**) oder TBOS (**HB14**) und 0.2 mL wässrige Ammoniaklösung (28-30 %) werden zugegeben und die Reaktionslösung bei RT für 24 h gerührt (200 rpm).

HB15 – HB18

1 g **P8@TEPA**-Partikel und 67.5 mL H_2O werden in einem 100 mL Dreihalskolben mit ovalem Rührstab (20 mm) vorgelegt und im Ultraschallbad dispergiert. 2.4 mL TMOS (**HB15**), TEOS (**HB16**), TPOS (**HB17**) oder TBOS (**HB18**) werden zugegeben und die Reaktionslösung bei RT für 24 h gerührt (200 rpm). Anschließend werden 0.2 mL wässrige Ammoniaklösung (28-30 %) hinzugefügt und bei RT weitere 24 h gerührt (200 rpm).

HB19 und HB20

1 g **P8@TEPA**-Partikel, 60 mL 2-Propanol und 7.5 mL H_2O werden in einem 100 mL Dreihalskolben mit ovalem Rührstab (20 mm) vorgelegt und im Ultraschallbad dispergiert. 2.4 mL TEOS, 1.5 mL TMOS (**HB19**) oder TPOS (**HB20**) und 0.2 mL wässrige Ammoniaklösung (28-30 %) werden zugegeben und die Reaktionslösung bei RT für 24 h gerührt (200 rpm).
Die Partikel werden von der Reaktionslösung getrennt, jeweils dreimal mit H_2O und EtOH gewaschen und 24 h bei 70 °C getrocknet.

Tabelle 11: Partikeleigenschaften der Hybrid-Partikel **HB11 – HB20**.

	d_{50} [µm]	d_{90}/d_{10}	SiO_2 wt. [%]
HB11	6.29	1.13	37.8
HB12	6.28	1.15	29.9
HB13	6.27	1.16	17.7
HB14	6.26	1.12	6.6
HB15	6.68	1.05	33.4
HB16	6.24	1.15	35.6
HB17	6.05	1.12	0.1
HB18	6.07	1.13	0.1
HB19	6.21	1.14	43.0
HB20	6.18	1.16	33.8

HB23

5 g **P11@TMA**-Partikel, 270 mL 2-Propanol und 30 mL H_2O werden in einem 500 mL Dreihalskolben vorgelegt und im Ultraschallbad dispergiert. Der Aufbau wird mit einer KPG-Rührwelle und Rührblatt (90 mm) versehen. Anschließend werden 12.5 mL TEOS und 1.25 mL wässrige Ammoniaklösung (28-30 %) zugegeben und die Reaktionslösung bei RT für 24 h gerührt (130 rpm). Die Partikel werden von der Reaktionslösung getrennt, jeweils dreimal mit H_2O und EtOH gewaschen und 24 h bei 70 °C getrocknet.

HB24 – 26

5 g **P11@TEPA**- (**HB24**), **P11@APTES**- (**HB25**) bzw. **P11@TMA**-Partikel (**HB26**), 240 mL 2-Propanol und 40 mL H_2O werden in einem 500 mL Dreihalskolben vorgelegt und im Ultraschallbad dispergiert. Der Aufbau wird mit einer KPG-Rührwelle und Rührblatt (90 mm) versehen. Anschließend werden 1.25 mL wässrige Ammoniaklösung zugegeben und die Reaktionslösung bei RT gerührt (130 rpm). Mit einer Dosierpumpe werden 125 mL TEOS-Lösung (10% in 2-PrOH) mit einer Geschwindigkeit von 12 $^{mL}/_{h}$ zugetropft. Nach vollendeter Zugabe wird die Reaktionslösung bei RT für weitere 12 h gerührt (130 rpm). Die Partikel werden von der Reaktionslösung getrennt, jeweils dreimal mit H_2O und EtOH gewaschen und 24 h bei 70 °C getrocknet.

Tabelle 12: Partikeleigenschaften der Hybrid-Partikel **HB21** – **HB26**.

	d_{50} [µm]	d_{90}/d_{10}	SiO_2 wt. [%]
HB21	8.09	1.18	31.3
HB22	8.55	1.07	31.8
HB23	8.28	1.07	32.8
HB24	8.22	1.14	28.6
HB25	8.28	1.07	32.0
HB26	8.22	1.14	30.2

12.3.5 Kalzinierung von *p*(GMA-*co*-EDMA)/SiO_2-Hybrid-Partikel

Die dargestellten *p*(GMA-*co*-EDMA)/SiO_2-Hybrid-Partikel **HB** werden für 10 h bei 600 °C unter Zuleitung synthetischer Luft kalziniert, um das Polymer vollständig zu entfernen. Daraus resultieren mesoporöse Silica-Partikel (**MPSM**).

Tabelle 13: Partikeleigenschaften der Silica-Partikel **MPSM1** – **MPSM26**.

	d_{50} [µm]	d_{90}/d_{10}	Φ [nm]	V_P [$\frac{mL}{g}$]	a_{BET} [$\frac{m^2}{g}$]
MPSM1	6.59	1.24	15.4	0.71	342
MPSM2	6.83	1.24	19.2	0.56	252
MPSM3	7.03	1.26	23.0	0.22	139
MPSM4	7.12	1.19	72.4	0.12	68
MPSM5	6.30	1.14	12.1	0.88	383
MPSM6	8.22	1.06	-	-	-
MPSM7	5.82	1.22	4.7	0.73	573
MPSM8	7.36	1.14	20.3	0.46	309
MPSM9	7.12	1.21	20.3	0.48	317
MPSM10	7.69	1.10	23.5	0.49	247
MPSM11	6.02	1.07	23.6	0.50	271
MPSM12	5.54	1.21	11.3	0.84	389

Tabelle 14: Fortsetzung von **Tabelle 13**.

	d_{50} [µm]	d_{90}/d_{10}	Φ [nm]	V_P [$\frac{mL}{g}$]	a_{BET} [$\frac{m^2}{g}$]
MPSM13	3.65	1.20	8.8	0.62	339
MPSM14	2.20	1.44	4.0	0.68	637
MPSM15	5.91	1.10	15.7	0.87	390
MPSM16	6.03	1.13	24.9	0.67	346
MPSM17	0.82	1.45	-	-	-
MPSM18	0.54	1.78	-	-	-
MPSM19	5.93	1.13	23.4	0.45	242
MPSM20	5.01	1.22	17.1	0.77	364
MPSM23	7.67	1.10	17.4	0.73	441
MPSM24	6.84	1.10	16.3	0.69	348
MPSM25	7.14	1.12	16.8	0.66	420
MPSM26	7.10	1.16	14.3	0.86	530

12.3.6 Funktionalisierung der mesoporösen Silica-Partikel

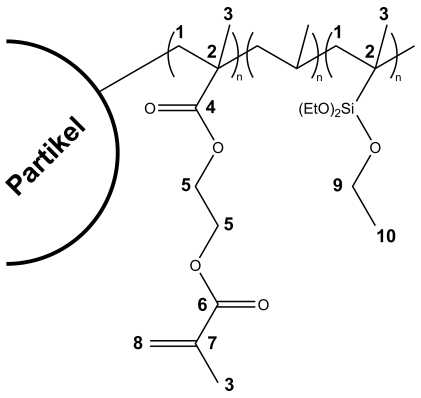
5 g **MPSM** und 600 mL Salzsäure (3.7 %) werden in einem 1000 mL Dreihalskolben vorgelegt und im Ultraschallbad dispergiert. Der Aufbau wird mit einer KPG-Rührwelle und Rührblatt (90 mm) versehen. Die Reaktionslösung wird bei 100 °C für 3 h gerührt (130 rpm). Die Partikel werden von der Reaktionslösung entfernt, jeweils mit EtOH und H_2O gewaschen, bis die Waschlösung neutral ist und 24 h bei 70 °C getrocknet.
5 g rehydroxylierte MPSM und 75 mL Toluol werden in einem 250 mL Dreihalskolben vorgelegt und im Ultraschallbad dispergiert. Der Aufbau wird mit einer KPG-Rührwelle und Rührblatt (90 mm) versehen. 25 mL Octadecyltrimethoxysilansilan und 0.5 mL Triethylamin werden zugegeben und die Reaktionslösung bei 100 °C für 24 h gerührt (130 rpm). Die Partikel werden von der Reaktionslösung entfernt, dreimal mit Toluol und EtOH und zweimal mit MeOH gewaschen und 24 h bei 70 °C getrocknet.

12.3.7 Synthese mesoporöser Silica-Partikel auf Basis von Vinyltriethoxysilan

Die Darstellung von *p*(VTEOS-*co*-EDMA) Templaten erfolgt in Anlehnung an WAGNER.[33]

V-PB1 – V-PB4

0.3 g **PS1**, 0.1 g SDS und 5 mL H_2O werden in einem 250 mL Dreihalskolben mit ovalem Rührstab (35 mm) vorgelegt und im Ultraschallbad dispergiert. 0.38 g SDS und 2 mL Dibutylphthalat werden separat in 150 mL für 15 min homogenisiert (4500 rpm). Anschließend wird die Suspension in den Dreihalskolben überführt und für 24 h gerührt (200 rpm). 6 mL VTEOS, 9 mL EDMA, 11 mL Toluol, 4 mL Cyclohexanol, 0.4 g BPO und 0.5 g SDS werden in 150 mL H_2O für 15 min homogenisiert (4500 rpm). Anschließend werden beide Suspensionen in ein 500 mL Dreihalskolben überführt und für 24 h gerührt (200 rpm). 3.5 g Polyvinylalkohol werden in 150 mL H_2O bei 50 °C gelöst. Die PVA-Lösung und 0 mg (**V-PB1** u. **V-PB2**), 135 mg (**V-PB3**) bzw. 270 mg (**V-PB4**) $NaNO_2$ werden zur Suspension gegeben und für 20 min mit Argon inertisiert. Das Reaktionsgemisch wird bei 70 °C für 24 h gerührt (200 rpm). Die Partikel werden von der Reaktionslösung getrennt, jeweils dreimal mit EtOH und H_2O gewaschen und für 24 h getrocknet.



^{13}C-NMR (75.47 MHz, CP/MAS, 8 kHz rot.): δ (in ppm) = 17.7 (C-3), 22.4 (C-10), 45.1 (C-1), 55.6 (C-2), 59.2 (C-5), 62.0 (C-9), 128.0 (C-8), 136.7 (C-7), 166.5 (C-6), 176.8 (C-4).

^{29}Si-NMR (59.63 MHz, CP/MAS, 5 kHz rot.): δ (in ppm) = − 44 (T^1, polym.), − 49 (T^2, polym.), − 55 (T^3, polym.), − 70 (T^2, unpolym.), − 79 (T^3, unpolym.).

IR (DRIFT): $\tilde{\nu}$ (in cm^{-1}) = 958 ($\nu_{\text{Si-OH}}$), 1149 ($\nu_{\text{C-O-C}}$), 1259 ($\nu_{\text{Si-O-Si}}$), 1458 ($\delta_{\text{C-H, aliph.}}$), 1602 ($\nu_{\text{C=C}}$), 1737 ($\nu_{\text{C=O}}$), 2952 − 2999 ($\nu_{\text{C-H, aliph.}}$), 3061 ($\nu_{CH_2}$), 3446 − 3633 ($\nu_{\text{OH}}$).

V-HB1, V-HB3 und V-HB4

5 g *p*(VTEOS-*co*-EDMA)-Templat **V-PB**, 270 mL 2-Propanol und 30 mL H_2O werden in einem 500 mL Dreihalskolben vorgelegt und im Ultraschallbad dispergiert. Der Aufbau wird mit einer KPG-Rührwelle und Rührblatt (90 mm) versehen. Anschließend werden 12.5 mL TEOS und 1.25 mL wässrige Ammoniaklösung (28-30 %) zugegeben und die Reaktionslösung bei RT für 24 h gerührt (130 rpm). Die Partikel werden von der Reaktionslösung getrennt, jeweils dreimal mit H_2O und EtOH gewaschen und 24 h bei 70 °C getrocknet.

V-MPSM1, V-MPSM3 und V-MPSM4

Die dargestellten *p*(VTEOS-*co*-EDMA)/SiO_2-Hybrid-Partikel **V-HB** werden für 10 h bei 600 °C unter Zuleitung synthetischer Luft kalziniert, um das Polymer vollständig zu entfernen. Daraus resultieren mesoporöse Silica-Partikel (**V-MPSM**).

13 Literatur

[1] F. Fait, J. C. Steinbach, A. Kandelbauer, H. A. Mayer, *Microporous Mesoporous Mater.* **2023**, *351*, 112482.

[2] J. C. Steinbach, F. Fait, S. Wagner, M. Wagner Alexandra Brecht, H. A. Mayer, A. Kandelbauer, *Polymers* **2022**, *14*, 382.

[3] F. Fait, J. C. Steinbach, H. A. Mayer, A. Kandelbauer, *J. Chrom. A* **2023**, *1705*, 464190.

[4] F. Fait, S. Wagner, J. C. Steinbach, H. A. Mayer, A. Kandelbauer, *Int. J. Mol. Sci.* **2023**, *24*, 11729.

[5] J. C. Steinbach, F. Fait, H. A. Mayer, A. Kandelbauer, *Int. J. Mol. Sci.* **2022**, *23*, 14977.

[6] J. C. Steinbach, F. Fait, H. A. Mayer, A. Kandelbauer, *ACS Omega* **2023**, *8*, 30273 – 30284.

[7] R. Nageswara Rao, V. Nagaraju, *J. Pharm. Biomed. Anal.* **2003**, *33*, 335–377.

[8] I. Slowing, J. Viveroescoto, C. Wu, V. Lin, *Adv. Drug Deliv. Rev.* **2008**, *60*, 1278–1288.

[9] B. Zhang, Z. Luo, J. Liu, X. Ding, J. Li, K. Cai, *J. Control Release* **2014**, *192*, 192–201.

[10] H. Mekaru, J. Lu, F. Tamanoi, *Adv. Drug Deliv. Rev.* **2015**, *95*, 40–49.

[11] D. P. Bentz, P. E. Stutzman, *Cem. Concr. Res.* **1994**, *24*, 1044–1050.

[12] Z. Bajja, W. Dridi, A. Darquennes, R. Bennacer, P. Le Bescop, M. Rahim, *Constr. Build Mater.* **2017**, *132*, 85–93.

[13] S. Kwon, T. Adachi, W. Araki, A. Yamaji, *Acta Mater.* **2006-07**, *54*, 3369–3374.

[14] Q. Li, X. Li, U. R. Cho, *Elastomers and Composites* **2018**, *53*, 57–66.

[15] C. Blasco, P. Vazquez-Roig, M. Onghena, A. Masia, Y. Picó, *J. Chrom. A* **2011**, *1218*, 4892–4901.

[16] M. Pedrouzo, F. Borrull, E. Pocurull, R. M. Marcé, *J. Sep. Sci.* **2011**, *34*, 1091–1101.

[17] W. Peysson, E. Vulliet, *J. Chrom. A* **2013**, *1290*, 46–61.

[18] S. Bayen, X. Yi, E. Segovia, Z. Zhou, B. C. Kelly, *J. Chrom. A* **2014**, *1338*, 38–43.

[19] M. Huang, H. Ma, M. Niu, F. Hu, S. Wang, L. Li, C. Lv, *J. Sep. Sci.* **2018**, 1232–1239.

[20] W. Stöber, A. Fink, E. Bohn, *J. Colloid Interface Sc.* **1968**, *26*, 62–69.

[21] E. D. E. R. Hyde, A. Seyfaee, F. Neville, R. Moreno-Atanasio, *Ind. Eng. Chem. Res.* **2016-08-24**, *55*, 8891–8913.

[22] S.-L. Chen, P. Dong, G.-H. Yang, J.-J. Yang, *J. Colloid Interface Sci.* **1996**, *180*, 237–241.

[23] J. H. Zhang, P. Zhan, Z. L. Wang, W. Y. Zhang, N. B. Ming, *J. Mater. Res.* **2003**, *18*, 649–653.

[24] K. Nozawa, H. Gailhanou, L. Raison, P. Panizza, H. Ushiki, E. Sellier, J. P. Delville, M. H. Delville, *Langmuir* **2005**, *21*, 1516–1523.

[25] H. Nakabayashi, A. Yamada, M. Noba, Y. Kobayashi, M. Konno, D. Nagao, *Langmuir* **2010**, *26*, 7512–7515.

[26] C. T. Kresge, M. E. Leonowicz, W. J. Roth, J. C. Vartuli, J. S. Beck, *Nature* **1992**, *359*, 710–712.

[27] N. K. Raman, M. T. Anderson, C. J. Brinker, *Chem. Mater.* **1996**, *8*, 20.

[28] L. Zhang, L. Jin, B. Liu, J. He, *Front. Chem.* **2019**, *7*, 22.

[29] M. Mesa, L. Sierra, B. López, A. Ramirez, J.-L. Guth, *Solid State Sci.* **2003**, *5*, 1303–1308.

[30] J. P. Hanrahan, A. Donovan, M. A. Morris, J. D. Holmes, *J. Mater. Chem.* **2007**, *17*, 3881.

[31] A. Ahmed, R. Clowes, E. Willneff, H. Ritchie, P. Myers, H. Zhang, *Ind. Eng. Chem. Res.* **2010**, *49*, 602–608.

[32] U. Meyer, R. A. Caruso, A. Larsson, H.-P. Hentze, *Adv. Mater.* **2002**, 5.

[33] S. Wagner, *Doktorarbeit* **2021**, Eberhard Karls Universität, Tübingen.

[34] J. He, C. Yang, X. Xiong, B. Jiang, *J. Polym. Sci. A Polym. Chem.* **2012**, *50*, 2889–2897.

[35] H. Xia, Q. Bai, G. Wan, F. Yang, J. Wang, *Mater. Lett.* **2016**, *180*, 19–22.

[36] J. Chen, L. Zhu, L. Ren, C. Teng, Y. Wang, B. Jiang, J. He, *Appl. Bio Mater.* **2018**, *1*, 604–612.

[37] J. Bai, Q. Zhu, C. Tang, J. Liu, Y. Yi, Q. Bai, *J. Chrom. A* **2022**, *1675*, 463165.

[38] R. D. Badley, W. T. Ford, F. J. McEnroe, R. A. Assink, *Langmuir* **1990**, *6*, 792–801.

[39] K. Albert, R. Brindle, P. Martin, I. D. Wilson, *J. Chrom. A* **1994**, *665*, 253–258.

[40] K. Vrancken, K. Possemiers, P. Van Der Voort, E. Vansant, *Colloids Surf. A Physicochem. Eng. Asp.* **1995**, *98*, 235–241.

[41] F. Gritti, G. Guiochon, *J. Chrom. A* **2007**, *1166*, 30–46.

[42] J. S. Baker, J. C. Vinci, A. D. Moore, L. A. Colón, *J. Sep. Science* **2010**, *33*, 2547–2557.

[43] D. Cabooter, A. Fanigliulo, G. Bellazzi, B. Allieri, A. Rottigni, G. Desmet, *J. Chrom. A* **2010**, *1217*, 7074–7081.

[44] K. K. Unger, R. Skudas, M. M. Schulte, *J. Chrom. A* **2008**, *1184*, 393–415.

[45] R. Hayes, A. Ahmed, T. Edge, H. Zhang, *J. Chrom. A* **2014**, *1357*, 36–52.

[46] H. Claessens, M. Vanstraten, *J. Chrom. A* **2004**, *1060*, 23–41.

[47] B. Leader, Q. J. Baca, D. E. Golan, *Nat. Rev. Drug. Discov.* **2008**, *7*, 21–39.

[48] M. A. Alossaimi, M. A. Alzeer, F. M. Abdel Bar, M. H. ElNaggar, *Pharmaceuticals* **2022**, *15*, 1184.

[49] A. Staub, S. Comte, S. Rudaz, J.-L. Veuthey, J. Schappler, *Electropheresis* **2010**, *31*, 3326–3333.

[50] J. F. Carpenter, S. J. Prestrelski, A. Dong, *Eur. J. Pharm. Biopharm.* **1998**, *45*, 231–238.

[51] W. William Wilson, *J. Struct. Biol.* **2003**, *142*, 56–65.

[52] C. Bertucci, M. Pistolozzi, A. De Simone, *Anal. Bioanal. Chem.* **2010**, *398*, 155–166.

[53] A. Oliva, J. Farina, M. Llabres, *CPA* **2007**, *3*, 230–248.

[54] A. Staub, D. Zurlino, S. Rudaz, J.-L. Veuthey, D. Guillarme, *J. Chrom. A* **2011**, *1218*, 8903–8914.

[55] C. E. Bakis, L. C. Bank, V. L. Brown, E. Cosenza, J. F. Davalos, J. J. Lesko, A. Machida, S. H. Rizkalla, T. C. Triantafillou, *J. Compos. Constr.* **2002**, *6*, 73–87.

[56] N. Miletić, Z. Vuković, A. Nastasović, K. Loos, *J. Mol. Catal. B Enzym.* **2009**, *56*, 196–201.

[57] F. Reymond, C. Vollet, Z. Plichta, D. Horák, *Biotechnol. Progress* **2013**, *29*, 532–542.

[58] T. Ellingsen, O. Aune, J. Ugelstad, S. Hagen, *J. Chrom. A* **1990**, *535*, 147–161.

[59] B. Frolund, K. Keiding, *Appl. Microbiol. Biotechnol.* **1994**, *41*, 708–716.

[60] M. W. H. Roberts, C. M. Ongkudon, G. M. Forde, M. K. Danquah, *J. Sep. Sci.* **2009**, *32*, 2485–2494.

[61] K. Lungfiel, A. Seubert, *J. Chrom. A* **2014**, *1358*, 117–127.

[62] M. T. Gokmen, F. E. Du Prez, *Prog. Polym. Sci.* **2012**, *37*, 365–405.

[63] K. N. N. Jayachandran, P. R. Chatterji, *J. Macromol. Sci. C* **2001**, *41*, 79–94.

[64] S. Watanabe, T. Kobayashi, H. Sumitomo, M. Murata, Y. Masuda, *Polym. Bull.* **2010**, *65*, 543–550.

[65] E. Vivaldo-Lima, P. E. Wood, A. E. Hamielec, A. Penlidis, *Ind. Eng. Chem. Res.* **1997**, *36*, 939–965.

[66] E. J. Hukkanen, R. D. Braatz, *Sens. Actuators B Chem.* **2003**, *96*, 451–459.

[67] J. Ugelstad, K. H. Kaggerud, F. K. Hansen, A. Berge, *Makromol. Chem.* **1979**, *180*, 737–744.

[68] J. Ugelstad, P. Mørk, K. Herder Kaggerud, T. Ellingsen, A. Berge, *Adv. Colloid Interface Sci.* **1980**, *13*, 101–140.

[69] J. Ugelstad, A. Berge, T. Ellingsen, R. Schmid, T.-N. Nilsen, P. Mørk, P. Stenstad, E. Hornes, Ø. Olsvik, *Prog. Polym. Sci.* **1992**, *17*, 87–161.

[70] J.-W. Kim, K.-D. Suh, *Polymer* **2000**, *41*, 6181–6188.

[71] S. T. Camli, E. Unsal, S. Senel, A. Tuncel, *J. Appl. Polym. Sci.* **2004**, *92*, 3685–3696.

[72] V. Šmigol, F. Švec, *J. Appl. Polym. Sci.* **1992**, *46*, 1439–1448.

[73] M. B. Tennikov, D. Horak, F. Svec, *J. Chrom. A* **1989**, *475*, 187–194.

[74] M. Petro, F. Svec, J. M. Fréchet, *Anal. Chem.* **1997**, 3131–3139.

[75] J. Hradil, E. Králová, M. J. Beneš, *React. Funct. Polym.* **1997**, *33*, 263–273.

[76] F. Svec, J. M. Fréchet, *J. Chrom. A* **1995**, 89–95.

[77] B. Gong, J. Zhu, L. Li, K. Qiang, L. Ren, *Talanta* **2006**, *68*, 666–672.

[78] D. Hérault, C. Saluzzo, M. Lemaire, *React. Funct. Polym.* **2006**, 567–577.

[79] A. Wale, K. Mulani, S. Deshpande, C. Rajan, S. Ponrathnam, *J. Polym. Res.* **2021**, *28*, 287.

[80] C. M. Hansen, *Hansen Solubility Parameters: A User's Handbook*, CRC-Press, 2. Auflage, **2007**.

[81] J.-W. Kim, K.-D. Suh, *J. Ind. Eng. Chem.* **2008**, *14*, 1–9.

[82] U. Schubert, *The Sol-Gel Handbook: Synthesis, Characterization and Applications*, Wiley-VCH, 1. Auflage, **2015**.

[83] C. J. Brinker, G. W. Scherer, *Sol-Gel Science: The physics and chemistry of sol-gel processing*, Elsevier - Academic Press, 1. Auflage, **1990**.

[84] R. K. Iler, *The Chemistry of Silica: Solubility, Polymerization, Colloid and Surface Properties and Biochemistry of Silica*, Wiley, 1. Auflage, **1979**.

[85] W. T. Grubb, *J. Am. Chem. Soc.* **1954-07**, *76*, 3408–3414.

[86] V. K. LaMer, R. H. Dinegar, *J. Am. Chem. Soc.* **1950**, *72*, 4847–4854.

[87] T. Matsoukas, E. Gulari, *J. Colloid Interface Sci.* **1988**, *124*, 252–261.

[88] T. Matsoukas, E. Gulari, *J. Colloid Interface Sci.* **1989**, *132*, 13–21.

[89] G. Bogush, C. Zukoski, *J. Colloid Interface Sci.* **1991**, *142*, 1–18.

[90] G. Bogush, C. Zukoski, *J. Colloid Interface Sci.* **1991**, *142*, 19–34.

[91] J. Bailey, M. Mecartney, *Colloids Surf.* **1992**, *63*, 151–161.

[92] M. T. Harris, R. R. Brunson, C. H. Byers, *J. Non Cryst. Solids* **1990**, *121*, 397–403.

[93] S. Sadasivan, A. K. Dubey, Y. Li, D. H. Rasmussen, *J. Sol-Gel Sci. Technol.* **1998**, *12*, 10.

[94] O. Malay, I. Yilgor, Y. Z. Menceloglu, *J. Sol-Gel Sci. Technol.* **2013**, *67*, 351–361.

[95] A. Van Blaaderen, J. Van Geest, A. Vrij, *J. Colloid Interface Sci.* **1992**, *154*, 481–501.

[96] J. Maisch, *Doktorarbeit* **2016**, Eberhard Karls Universität, Tübingen.

[97] A. Van Helden, J. Jansen, A. Vrij, *J. Colloid Interface Sci.* **1981**, *81*, 354–368.

[98] G. Bogush, M. Tracy, C. Zukoski, *J. Non Cryst. Solids* **1988**, *104*, 95–106.

[99] H. Giesche, *J. Eur. Ceram.* **1994**, *14*, 189–204.

[100] Y. Han, Z. Lu, Z. Teng, J. Liang, Z. Guo, D. Wang, M.-Y. Han, W. Yang, *Langmuir* **2017**, *33*, 5879–5890.

[101] K. Chen, T. Tsuchiya, J. Mackenzie, *J. Non Cryst. Solids* **1986**, *86*, 227–237.

[102] H. Xia, G. Wan, J. Zhao, J. Liu, Q. Bai, *J. Chrom. A* **2016**, *1471*, 138–144.

[103] K. Hosoya, J. M. J. Fréchet, *J. Polym. Sci. A Polym. Chem.* **1993-07**, *31*, 2129–2141.

[104] S. Dubinsky, J. I. Park, I. Gourevich, C. Chan, M. Deetz, E. Kumacheva, *Macromolecules* **2009**, *42*, 1990–1994.

[105] I. Halász, P. Vogtel, *Angew. Chem. Int. Ed. Engl.* **1980**, *19*, 24–28.

[106] G. Socrates, *Infrared and Raman Characteristic Group Frequencies: Tables and Charts, 3rd Edition | Wiley*, John Wiley & Sons Inc, 3. Auflage, **2004**.

[107] D. V. Goeddel, D. G. Kleid, F. Bolivar, H. L. Heyneker, D. G. Yansura, R. Crea, T. Hirose, A. Kraszewski, K. Itakura, A. D. Riggs, *Porc. Natl. Acad. Sci.* **1979**, *76*, 106–110.

[108] M. Woodruff, *Chromatogr.* **2016**, 48–51.

[109] B. M. Wagner, S. A. Schuster, B. E. Boyes, J. J. Kirkland, *J. Chrom. A* **2012**, *1264*, 22–30.

[110] J. J. Kirkland, S. A. Schuster, W. L. Johnson, B. E. Boyes, *J. Pharm. Anal.* **2013**, *3*, 303–312.

[111] J. C. Steinbach, *unveröffentliche Doktorarbeit* **2023**, Eberhard Karls Universität, Tübingen.

[112] I. S. Stefanović, M. V. Pergal, B. M. Ekmeščić, D. D. Maksin, A. B. Nastasović, Z. P. Miladinović, Z. M. Vuković, D. M. Micić, *Ind. Eng. Chem. Res.* **2015**, *54*, 6902–6911.

[113] Q. C. Wang, F. Švec, J. M. J. Fréchet, *J. Polym. Sci. A Polym. Chem.* **1994**, *32*, 2577–2588.

[114] F. Rouquerol, J. Rouquerol, K. S. W. Sing, P. L. Llewellyn, G. Maurin, *Adsorption by powders and porous solids: principles, methodology and applications*, Elsevier - Academic Press, 2. Auflage, **2014**.

[115] S. Lowell, J. E. Shields, M. A. Thomas, M. Thommes, *Characterization of Porous Solids and Powders: Surface Area, Pore Size and Density*, Springer Dordrecht, 1. Auflage, **2004**.

[116] M. Thommes, K. Kaneko, A. V. Neimark, J. P. Olivier, F. Rodriguez-Reinoso, J. Rouquerol, K. S. Sing, *Pure Appl. Chem.* **2015**, *87*, 1051–1069.

[117] A. Srisopa, *Talanta* **2016**, *147*, 358–363.

[118] S. Grama, Z. Plichta, M. Trchová, J. Kovářová, M. Beneš, D. Horák, *React. Funct. Polym.* **2014**, *77*, 11–17.

[119] J. Chen, L. Zhu, L. Ren, C. Teng, Y. Wang, B. Jiang, J. He, *Appl. Bio Mater.* **2018**, *1*, 604–612.